Electronic Thesis and Dissertation Repository

10-20-2017 2:30 PM

Development of Nanomaterials for Lithium-Ion Batteries by Atomic Layer Deposition

Biqiong Wang, *The University of Western Ontario*

Supervisor: Prof. Xueliang Sun, *The University of Western Ontario*
Co-Supervisor: Prof. Tsun-Kong Sham, *The University of Western Ontario*
A thesis submitted in partial fulfillment of the requirements for the Doctor of Philosophy degree in Mechanical and Materials Engineering
© Biqiong Wang 2017

Follow this and additional works at: https://ir.lib.uwo.ca/etd

Part of the Nanoscience and Nanotechnology Commons, and the Other Materials Science and Engineering Commons

Recommended Citation

Wang, Biqiong, "Development of Nanomaterials for Lithium-Ion Batteries by Atomic Layer Deposition" (2017). *Electronic Thesis and Dissertation Repository*. 4978.
https://ir.lib.uwo.ca/etd/4978

This Dissertation/Thesis is brought to you for free and open access by Scholarship@Western. It has been accepted for inclusion in Electronic Thesis and Dissertation Repository by an authorized administrator of Scholarship@Western. For more information, please contact wlswadmin@uwo.ca.

Abstract

Lithium ion batteries (LIBs) have been the dominant candidate in the field of energy storage. The ever-growing demand of high energy and power density, longer battery life, and more assured safety level has geared the development of LIBs towards all-solid-state batteries (ASSBs). The solid-state nature allows more flexibility in battery design and higher area capacity to be obtained within limited space. Moreover, replacing liquid electrolytes with solid-state electrolytes (SSEs) is a most effective approach to achieve safer battery system. In addition, ASSBs hold great promise in the actual fabrication of microbatteries for microelectronics. Therefore, a technique which can synthesize materials in a precisely controlled manner is extremely critical. Atomic layer deposition (ALD) strikes as a thin film deposition technique which is capable of depositing ultrathin, uniform, conformal and pinhole-free thin films over various complex structures.

In this thesis, we reported the fabrication of nanomaterials by ALD as electrodes and SSEs for next-generation batteries. More focus has been put on the development of SSEs. Amorphous lithium phosphate (LPO) was deposited by a simplified route of reaction. The composition of the as-prepared thin films was analyzed and an acceptable ionic conductivity was obtained.

Based on the first SSE developed, a nanocomposite as anode material for LIBs was rationally designed combining ALD procedures of TiO_2 and LPO. Carbon nanotubes were utilized as an electronically conductive scaffold. The detailed structure of the nanocomposite was investigated. Excellent electrochemical performance was obtained.

Furthermore, another SSE, lithium silicate, was developed by ALD. The composition of the as-deposited thin films can be adjusted by changing the lithium to silicon subcycle ratio. The relation of composition and deposition temperature was studied. And a stoichiometry close to lithium orthosilicate demonstrated the best ionic conductivity.

The third system explored by ALD as SSEs was lithium niobium oxide. Similarly, the atomic ratio between Li and Nb was tuned by the subcycle number. The local structure was studied. The ionic conductivity was also assessed, exceeding 10^{-8} S cm at room temperature.

In summary, ALD has been proven to be a promising technique to develop electrode and SSE materials for the next-generation ASSBs.

Keywords

Co-Authorship Statement

1.

Title: Atomic Layer Deposition of Lithium Phosphates as Solid-State Electrolytes for All-Solid-State Microbatteries

Authors: B. Wang, J. Liu, Q. Sun, R. Li, T.-K. Sham, and X. Sun

The final version of this manuscript has been published in **Nanotechnology**, 2014, 25, 504007

Biqiong Wang carried out all the experiments and drafted the paper.

Jian Liu gave suggestions on the methodologies and modified the manuscript.

Qian Sun helped discuss the results and reviewed the manuscript.

Ruying Li helped organize the experiment.

T.-K. Sham is the co-supervisor and helped with the synchrotron results.

Xueliang Sun is the supervisor, helped organize the whole story and gave funding supports.

2.

Title: Titanium Dioxide/Lithium Phosphate Nanocomposite Derived from Atomic Layer Deposition as a High-Performance Anode for Lithium Ion Batteries

Authors: B. Wang, J. Liu, Q. Sun, B. Xiao, R. Li, T.-K. Sham, and X. Sun

The final version of this manuscript has been published in **Adv. Mater. Interfaces**, 2016, 3, 1600369

Biqiong Wang carried out all the experiments and drafted the paper.

Jian Liu helped with the in-situ XRD setup and modified the manuscript.

Qian Sun helped discuss the results and review the manuscript.

Biwei Xiao helped measure the Synchrotron data.

Ruying Li helped organize the experiment.

T.-K. Sham is the co-supervisor and helped with the synchrotron results.

Xueliang Sun is the supervisor, helped organize the whole story and gave funding supports.

3.

Title: Atomic Layer Deposited Lithium Silicates as Solid-State Electrolytes for All Solid-State Batteries

Authors: B. Wang, J. Liu, M. N. Banis, Q. Sun, Y. Zhao, R. Li, T.-K. Sham, and X. Sun

The final version of this manuscript has been published in **ACS Appl. Mater. Interfaces**, 2017, 9, 31786

Biqiong Wang carried out all the experiments and drafted the paper.

Jian Liu helped discuss the results and modify the manuscript.

Mohammad Norouzi Banis helped measure part of the synchrotron results.

Qian Sun helped discuss the results and review the manuscript.

Yang Zhao helped discuss the results.

Ruying Li helped organize the experiment.

T.-K. Sham is the co-supervisor and helped with the synchrotron results.

Xueliang Sun is the supervisor, helped organize the whole story and gave funding supports.

4.

Title: Atomic Layer Deposition of Lithium Niobium Oxides as Potential Solid-State Electrolytes for Lithium Ion Batteries

Authors: B. Wang, Y. Zhao, M. N. Banis, Q. Sun, K. Adair, R. Li, T.-K. Sham, and X. Sun

The final version of this manuscript has been submitted for publishing.

Biqiong Wang carried out all the experiments and drafted the paper.

Yang Zhao helped discuss the results and modify the manuscript.

Mohammad Norouzi Banis helped measure part of the synchrotron results.

Qian Sun helped discuss the results and review the manuscript.

Keegan Adair helped polishing the manuscript.

Ruying Li helped organize the experiment.

T.-K. Sham is the co-supervisor and helped with the synchrotron results.

Xueliang Sun is the supervisor, helped organize the whole story and gave funding supports.

Acknowledgments

The work included in this thesis was accomplished in Dr. Sun's Nanomaterials and Energy group and in Dr. Sham's group at the University of Western Ontario in London, Canada. Herein, I would like to express my deepest gratitude to every individual who have been helping me throughout the past five years.

First and foremost, I would like to thank my supervisors: Dr. Xueliang (Andy) Sun and Dr. Tsun-Kong Sham for their exceptional guidance and constant support during my five years of graduate study. I was lucky enough to join Dr. Sun's group first and then got to be co-supervised by Dr. Sham a term later. When I initially started as a master student here, I basically knew nothing on how to do research. It was them who constantly shared their insightfulness and set the role models as a serious researcher. They impressed me with their great dedication and enthusiasm to their work and inspired me both academically and mentally. The decision to transfer to Ph. D. degree came so naturally and has made my great adventure here in Western.

Secondly, I will be forever thankful to Mrs. Ruying (Kathy) Li, Dr. Sun's wife and a research engineer in our group. She truly cared for me not only in my work, but also in my life. Her generous help was with me since my day-one in the group. During my years away from home, she was like my family and supported me with her gentle and loving heart.

I would also like to sincerely thank my advisory committee members Dr. Jun Yang in Department of Mechanical and Materials Engineering and Dr. Zhifeng Ding in Department of Chemistry for their valuable advices at every stage of my Ph. D. work. Special thanks to my doctoral thesis examination board members, Dr. Liying Jiang, a professor in the Department of Mechanical and Materials Engineering at UWO, Dr. Hamidreza Abdolvand, a professor in the Department of Mechanical and Materials Engineering at UWO, and Dr. Yong Yang, a professor in the Department of Chemistry at Xiamen University, for their careful examinations and important suggestions on this thesis.

Next I would like to thank all current and former members in Dr. Sun's and Dr. Sham's group at Western. Especially, I would like to give my thanks to Dr. Jian Liu, Dr. Mohammad

Last but not least, I would like to express my heartfelt gratitude to my family. To Dr. Kai Gao: you are the best thing ever happened to me in my life. Thank you for sharing every single moment, bright or blue. Thank you for always having faith in me even when I doubted myself. Thank you for bringing the best out of me and making me a better person. It's been a memorable journey and hope we could make it a lifelong one. To my dearest parents, Mr. Zengdong Wang and Dr. Qinghua Lu: I have been away from our sweetest home for nine years and you are the persons I have been missing the most. You let me go to experience the fullest of my life and you are always there giving me the warmest comfort and unconditional love whenever I look back. I apologize for not being able to keep you company when you

needed. Please allow me to say: Thank you for everything, I love you so much and I'm proud of having you as my parents. I hope I could be the daughter you will be proud of one day. To myself: "In the end, it's not the years in your life that count. It's the life in your years."

Biqiong Wang

June 20, 2017

Table of Contents

List of Tables

List of Figures

xv

List of Abbreviations

2D: Two-dimensional

3D: Three-dimensional

A

AAO: Anodic aluminum oxide

AB: Acetylene black

ALD: Atomic layer deposition

ALE: Atomic layer epitaxy

APS: Advanced Photon Source

ASSB: All-solid-state battery

B

BE: Binding energy

BO: Bridging oxygen

C

CCEM: Canadian Centre for Electron Microscopy

CE: Coulombic efficiency

CFI: Canada Foundation for Innovation

CIHR: Canadian Institutes of Health Research

CLS: Canadian Light Sources

CNTs: Carbon nanotubes

CPE: Constant phase element

CRC: Canada Research Chair

CV: Cyclic voltammetry

CVD: Chemical vapor deposition

D

DEC: Diethyl carbonate

DEPA: Diethyl phosphoramidate

DSC: Differential scanning calorimetry

E

EC: Ethylene carbonate

EDS: Energy dispersive spectroscopy

EIS: Electrochemical impedance spectroscopy

EMC: Ethylmethy carbonate

EXAFS: Extended X-ray absorption fine structure

EV: Electric vehicle

F

FLY: Fluorescence yield

G

GPC: Growth per cycle

H

HEG: High energy grating

HEV: Hybrid electric vehicle

HRTEM: High resolution transmission electron microscopy

J

JCPDS: Joint committee on powder diffraction standards

L

LEG: Low energy grating

LFP: Lithium iron phosphate

LIB: Lithium ion battery

LINAC: Linear accelerator

LiPON: Lithium phosphorus oxynitride

LMO: Lithium manganese oxide

LNMO: Lithium nickel manganese oxide

LLTO: Lithium lanthanum titanate

LLZO: Lithium lanthanum zirconium oxide

LNO: Lithium niobium oxide

LPO: Lithium phosphate

LSO: Lithium silicate

LiO^{t}Bu: Lithium tert-butoxide

LiHMDS: Lithium hexamethyldisilazide

M

MEG: Medium energy grating

MEMS: Microelectromechanical systems

N

Nb(EtO)$_5$: Niobium ethoxide

NBO: Non-bridging oxygen

NCNT: Nitrogen-doped carbon nanutube

NMC: Lithium nickel manganese cobalt oxide

NMP: N-Methyl-2-pyrrolidone

NRC: National research council

NSERC: National science & engineering research center

O

ORF: Ontario research fund

ORNL: Oak Ridge National Laboratory

P

PAN: Poly(acrylonitrile)

PHEV: Plug-in hybrid electric vehicle

PLD: Pulsed laser deposition

PMMA: Poly(methyl methacrylate)

PVD: Physical vapor deposition

PVDF: Polyvinylidene fluoride

R

RF: Radio frequency

RT: Room temperature

<center>**S**</center>

SEI: Solid electrolyte interphase

SEM: Scanning electron microscopy

SGM: Spherical grating monochromator

SIMS: Secondary ion mass spectrometry

SR: Synchrotron radiation

SU: Structural unit

SXRMB: Soft X-ray microcharacterization beamline

<center>**T**</center>

TDMAP: Trisdimethylaminophosphorus

TEY: Total electron yield

TEOS: Tetraethylorthosilane

TEM: Transmission electron microscopy

TFLB: Thin film solid-state lithium ion battery

TGA: Thermogravimetric analysis

TLPO: Titanium/lithium phosphate nanocomposite

TMA: Trimethyl aluminum

TMPO: Trimethyl phosphate

TTIP: Titanium tetra-isopropoxide

U

UWO: University of Western Ontario

UV: Ultraviolet

V

VLS-PGM: Variable line spacing plane grating monochromator

VTOP: Vanadium tri-isopropoxide

X

XANES: X-ray absorption near edge structure

XAS: X-ray absorption spectroscopy

XAFS: X-ray absorption fine structure

XPS: X-ray photoelectron spectroscopy

XRD: X-ray diffraction

Chapter 1

1 Introduction

1.1 Introduction to Lithium-Ion Batteries (LIBs)

The dependence of modern civilization on fossil fuels has led to problematic consequences like air pollution and CO_2 emission which creates global warming. Moreover, with the rapid depletion of the limited sources of fossil fuels, there is an urging demand to seek alternative renewable and environmental benign energy sources. Clean energy like solar radiation, wind, and waves are intermittent sources that are variable in time and diffuse in space. Therefore it is essential to develop an energy storage system which can store and deliver the energy with high conversion efficiency.[1,2] Lithium ion batteries (LIBs) have been the dominant candidate in the market since it was commercially released in 1991 by Sony, Japan. The high volume and gravimetric energy density has revolutionized the applications of portable electronic device like mobile phones, laptops, and tablets. Later, LIBs found their way into, and spurred the expanding market of electric vehicles (EVs) and hybrid electric vehicles (HEVs), due to their good performance and long cycling life.[3-7]

1.1.1 Fundamentals of LIBs

A battery consists of one or more interconnected electrochemical cells each providing a current at a voltage for a time interval Δt. For an individual rechargeable LIB cell, energy is stored and released by means of charge and discharge process. Each LIB is composed of three functional components, the anode and cathode, separated by an electrolyte which could be either a liquid or a solid.[8-11] Figure 1.1 shows a schematic illustration of the working principle of a LIB, where lithium ions (Li^+) diffuse inside the cell through the ionic conductive electrolyte, generating electricity in the external circuit.[9] Taking the widely communalized $LiCoO_2$/C (graphite) system for example, Li^+ are extracted from the $LiCoO_2$ by electrochemical oxidation, transported through the electrolyte and separator, and then intercalated into C (graphite) in the charging process. Simultaneously,

electrons are provided by the external electric power supply from the cathode to the anode, when electrical energy is stored in the form of chemical energy. While being discharged, the lithium ions are transferred in the opposite direction from the anode to the cathode. At the same time, electrons are continuously generated at the anode side by chemical redox reactions and driven to the cathode, delivering electricity for the load.[9,10] LIBs are also referred to as rocking-chair batteries, as lithium ions rock back and forth between the anode and cathode electrodes when the LIB cell is charged and discharged.[12]
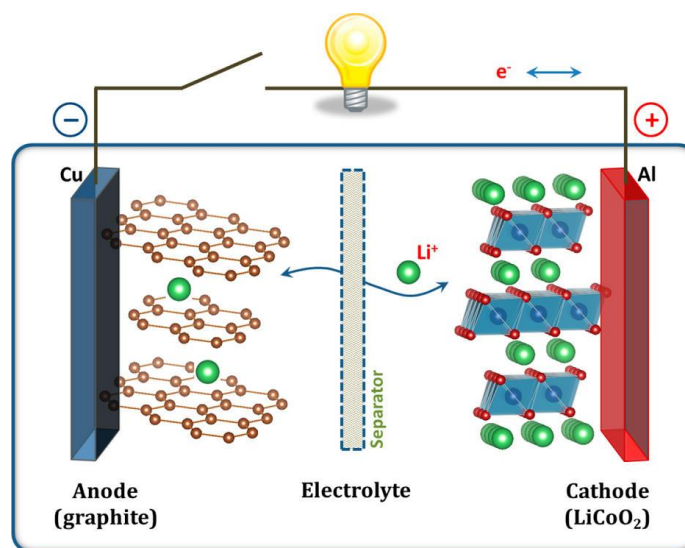
Figure 1.1 Schematic illustration of charging and discharging of a Li-ion battery (LiCoO$_2$/Li$^+$ electrolyte/graphite) [9]

The performance of battery is evaluated by several critical parameters including capacity, current rate, cyclic capabilities, power density and energy density. Capacity defines the amount of charge that can be stored or released during charge and discharge processes with mAh unit. Specific capacity is the capacity per mass or per surface area. Current rate (also known as C-rate) represents the rate at which the battery is fully charged/discharged. For instance, *nC* means that an electrode reaches its fully charged/discharge state in *1/n* hours. Cyclic capability or cyclability measures the stability of the discharge capacity versus cycles (noting one electrochemistry cycle is comprised of one charging and one discharging process). The term 'power density' reflects the rate performance of the battery which describes the energy delivery speed with a unit of W kg^{-1}, while energy

density equals to the voltage multiplied by capacity representing the amount of energy that can be stored.[3,5] The overall performance of the battery highly relies on the properties of each components, namely the anode, cathode, and electrolyte.

1.1.2   Development and Challenges of LIBs

Within the past two decades, LIBs have been a propelling technology in the market of not only portable electronics but also electric vehicles. To fulfill the growing needs for high performance batteries, tremendous efforts have been focused on achieving improved battery systems with longer cycle life, higher energy density, and higher safety level at lower cost.[10,11,13] As discussed above, the selection of the anode, cathode and electrolyte materials will affect the battery performance. In regards of the electrode materials, they are required to possess high rate capability as well as high reversible capacity. In addition, the voltage difference between the cathode and anode determines the energy density of the battery. Therefore, ideal electrode materials should provide the following properties: (1) fast electrochemical reaction kinetics involving Li^+ and electrons; (2) high ionic diffusivity and electronic conductivity; (3) short diffusion length for Li^+ and electrons; and (4) robust structure for rapid intercalation and de-intercalation of Li^+.[14]

The research for advanced electrode materials has been marching during the past few years. Figure 1.2 summarizes the materials of choice at present for cathode and anode in the plot of voltage versus capacity.[14] Some of the materials have been evolved into practical fabrication of batteries in LIB industry. However, challenges come along with the intrinsic properties of the materials and the nature of the electrochemical reactions.

For cathodes, well-known materials include olivine polyanions $LiMPO_4$ (M = Fe, Co, Ni, and Mn),[15] and layered oxides [$LiCoO_2$, $LiMnO_2$, $LiNi_{0.5}Mn_{0.5}O_2$, $LiNi_{1/3}Co_{1/3}Mn_{1/3}O_2$ (NMC)],[16] and spinel oxides ($LiMn_2O_4$, $LiNi_{0.5}Mn_{1.5}O_4$).[17] These cathode materials normally have a limited capacity due to the limited accommodation sites for lithium ion and their rate capability mostly depends on the conductivity, related with the dimensionality of lithium ion transport in their crystal structures.[14] Besides, the cathode materials normally suffer from severe side reactions with HF which is generated during cycling, leading to metal dissolution and sabotaged battery performance.[17] Seeking

electrode materials with high voltage or discharge capacity like lithium-rich NMC, or applying protective surface modifications onto the cathode are considered as two effective approaches to resolve these issues. For instance, our previous work have demonstrated that with atomic layer deposited $AlPO_4$ coating, the lithium-rich layered material, $Li_{1.2}Mn_{0.54}Co_{0.13}Ni_{0.13}O_2$ exhibited highly stable cycling performance with improved thermal stability and capacity retention.[18]
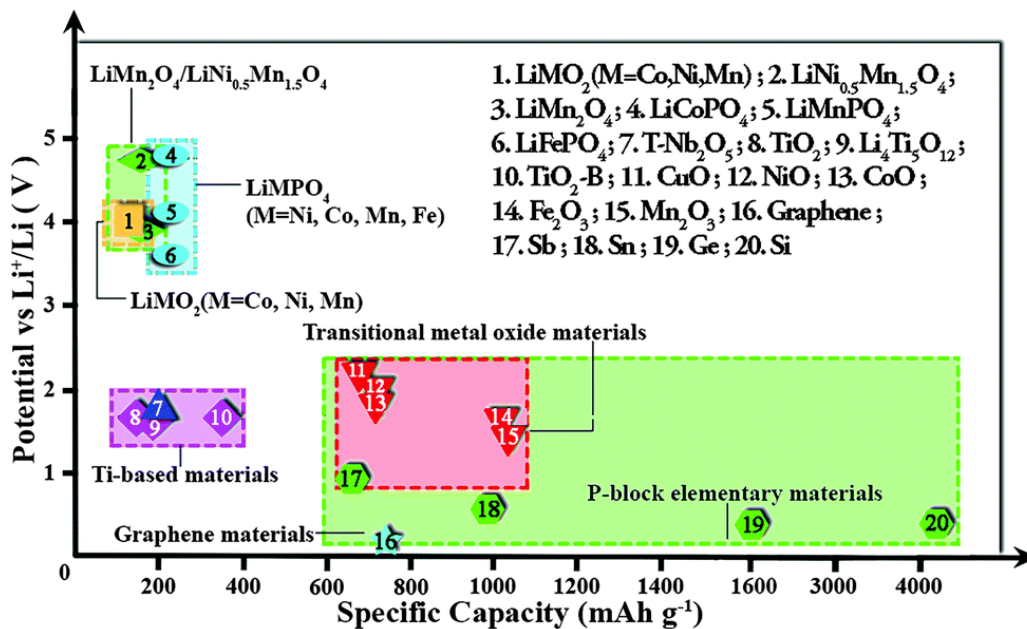
Figure 1.2 Voltage versus capacity chart for anode and cathode materials for LIB application [14]

As for anode materials, diverse alternatives have been sprung up to replace graphite, which can be categorized into three kinds based on the reaction mechanisms between lithium ions and the materials, namely intercalation, conversion, and alloy reaction.[14] Each class presents their own advantages and disadvantages. Intercalation materials like graphene and carbon nanotubes provide fast lithium ion reaction kinetics and are able to maintain structural integrity upon cycling. But the theoretical capacity is not comparable with the alloy reaction class. Nevertheless, Si and Sn as the representative materials of the alloy category, having a theoretical capacity as high as 4200 and 960 mA h g^{-1} respectively. However, they have significant drawbacks like large volume changes, giving rise to pulverization and devastatingly compromising the performance of

LIBs.[14,19,20] Strategies like novel nanostructural design and constraining surface coatings have been applied to solve the problems. Wang et al. in our group have reported sandwiched structure composed of carbon coated SnO_2 nanorod grafted on graphene, which showed ultrahigh reversible specific capacity (1420 mA h g^{-1}) and excellent rate capability.[21]

In addition to the challenges associated with the material properties, desirable LIBs should address other concerns, especially those related with safety. Battery failure might result in overheating or gas releasing and cause catastrophic fires or explosions, which must be avoided in practical applications in every aspect.[22] Henceforth, both incremental advances in today's lithium ion technology and conceptual innovations and approaches are demanded to achieve high-performance, inexpensive, and safe battery system.

1.1.3   All-Solid-State Batteries

Promising avenues have been developed as the solutions to the aforementioned problems. Among them, all-solid-state Li batteries have attracted great interest. Existing LIBs, apart from the storage and active components, applies considerable amount of auxiliary materials. The organic liquid electrolytes used in conventional LIBs have inevitable intrinsic drawbacks such as flammability and risks of leakage, which could lead to detrimental accidents. Besides, the dissolution of electrolytes, severe side reactions with the cathode during cycling, and the formation of dendrites of Li on the anode side, can also be problematic.[23,24] To surmount these issues, a nonflammable solid electrolyte can replace the liquid one, which is the principle underlying an all-solid-state battery (ASSB). Compared to liquid-electrolyte ones, ASSBs are considered to have more assured safety level, longer cycle life, higher energy density, and less constraints on packaging and state-of-charge monitoring circuits.[23–26] With the unparalleled advantages, a rapidly increasing trend in the research of ASSBs has emerged.
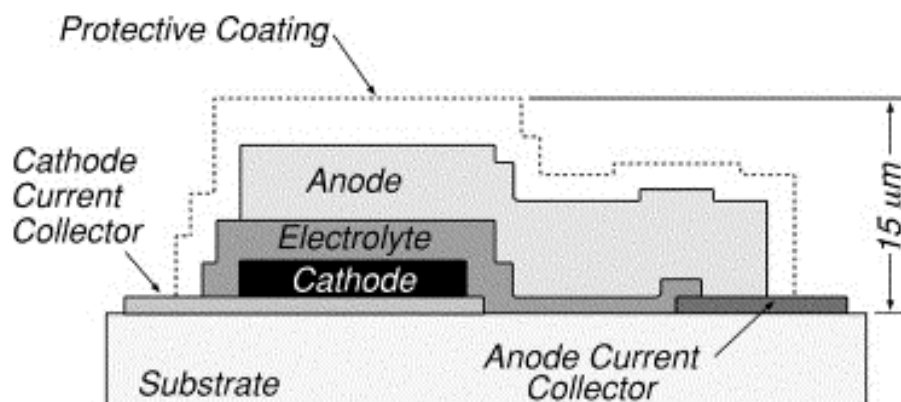
Figure 1.3 Schematic cross-section of a thin-film lithium battery [29]

Planar design was the starting point to fabricate ASSB. The thin-film solid-state Li (ion) battery (TFLB) is assembled from a few thin film components acting as current collector, cathode, electrolyte, anode, and optional protection sealing layers. The first appearance of TFLBs dates back to early 1980s,[27] approximately ten years after the first demonstration of metallic Li batteries. Most of the early studies on TFLBs employed thin film oxide or sulfide glass electrolyte like Li_2O-SiO_2-P_2O_5.[27] Later, the most classic model of TFLB was composed of successively deposited $LiCoO_2$, LiPON, and metallic Li as cathode, electrolyte, and anode materials, respectively.[28] The design by Oak Ridge National Laboratory (ORNL) has been the basic model for building two-dimensional (2D) planar laboratorial and commercial TFLBs later, as presented in Figure 1.3.[27,29] As the earliest commercialized ASSBs, TFLB has been shown to be promising in wide applications including tiny scale electronic applications such as microelectromechanical systems (MEMS), system-on-chips (SoCs), and implantable medical devices.[6,25,30,31] Some typical materials selected for the fabrication of commercial TFLB product are summarized in Table 1.1. Generally, the performances of the state-of-the-art 2D TFLBs are already sufficient for many conventional applications, while improvements are still urged for further applications where high energy/power density output or cycling under extreme temperatures are required.

Table 1.1: Typical thin film batteries [25]

Anode	Electrolyte	Cathode	Voltage (V)	Current ($\mu A/cm^2$)	Capacity
Li	$Li_{3.6}Si_{0.6}P_{0.4}O_4$	TiS_2	2.5	16	45–150 $\mu Ah/cm^2$
Li	$Li_{3.6}Si_{0.6}P_{0.4}O_4$	TiS_2	2.5	16–30	–
Li	$Li_{3.6}Si_{0.6}P_{0.4}O_4$	WO_3–V_2O_5	1.8–2.2	16	60–92 Ah/cm^2
Li	$LiBO_2$	In_2Se_3	1.2	0.1	–
Li	Li_2SO4–Li_2O–B_2O_3	TiS_xO_y	2.6	1–60	40–15 $\mu Ah/cm^2$
Li	Li_2S–SiS_2–P_2S_5	V_2O_5–TeO_2	2.8–3.1	0.5–2	–
LiV_2O_5	LiPON	V_2O_5	3.5–3.6	10	6 $\mu Ah/cm^2$
V_2O_5	LiPON	$LiMn_2O_4$	3.5–1	>2	18 $\mu Ah/cm^2$
Li/LiI	LiI–Li_2S–P_2S_5–P_2O_5	TiS_2	1.8–2.8	300	70 mAh/cm^3
Li	LiBP, LiPON	$LiMn_2O_4$	3.5–4.5	70	100 mAh/g
Li	$Li_{6.1}V_{0.61}Si_{0.39}O_{5.36}$	$MoO_{2.89}$	2.8	20	60 $\mu Ah/cm^2$
Li	$Li_{6.1}V_{0.61}Si_{0.39}O_{5.36}$	$LiMn_2O_4$	3.5–5	10	33.3 $\mu Ah/cm^2$
Li	LiPON	$LiMn_2O_4$	4.5–2.5	2–40	11–81 $\mu Ah/cm^2$
Cu	LiPON	$LiCoO_2$	4.2–3.5	1–5	130 $\mu Ah/cm^2$
Li	LiPON	$LiCoO_2$	4.2–2.0	50–400	35 $\mu Ah/cm^2$
Li	LiPON	$Li_x(Mn_yNi_{1-y})_{2-x}O_2$	4–3.5	1–10	100 mAh/g
Li	LiPON	$LiMn_2O_4$	4–5.3	10	10–30 $\mu Ah/cm^2$
Li	LiPON	Li–V_2O_5	1.5–3	2–40	10–20 $\mu Ah/cm^2$
SiSnON	LiPON	$LiCoO_2$	2.7–4.2	~5000	340–450 mAh/g
Li	LiPON	$LiMn_2O_4$	4.3–3.7	~800	45 $\mu Ah/(cm^2$-$\mu m)$
SnO	$Li_{6.1}V_{0.61}Si_{0.39}O_{5.36}$	$LiCoO_2$	2.7–1.5	10–200	4–10 $\mu Ah/cm^2$

Therefore, three-dimensional (3D) ASSB has drawn enormous attention recently. High energy density can be achieved within limited volume without much loss of the power density due to the shortened diffusion length, which benefits the miniaturization of the final devices.
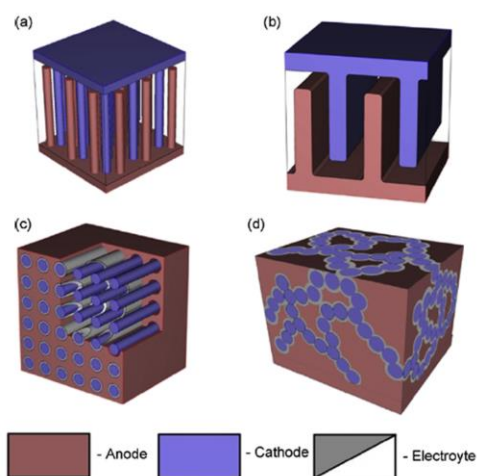
Figure 1.4 Different 3D architectures: (a) interdigitated rod electrodes, (b) interdigitated plates or 3D-trench, (c) concentric tube design, and (d) 3D aperiodic sponge [34]

A few prototype designs have been reported.[32–38] Figure 1.4 presents four architectures for 3D micro-ASSBs.[34] Besides, Song et al. proposed a novel strategy to fold the planner battery to a compacted 3D stack, resulting in significantly increased areal energy densities.[39,40]

1.1.4   Solid-State Electrolytes (SSEs)

The primary difference between a conventional LIB and an all-solid-state one is the solid-state electrolyte (SSE), which provides multiple benefits like thermal and electrochemical stability, longer cycle life, and higher energy density. The foremost features of a SSE are a high lithium ion conductivity and negligible electronic conductivity at operating temperatures (preferably ambient temperature). Furthermore, the SSE should be chemically stable against the electrodes and the thermal expansion coefficient should match with that of both electrodes. A wide electrochemical stability window is also required, as well as excellent mechanical properties. For scaling-up industrial production, these solid state lithium ion conductors should be environmentally benign, non-toxic, easy to prepare, and low cost materials.[42–44]
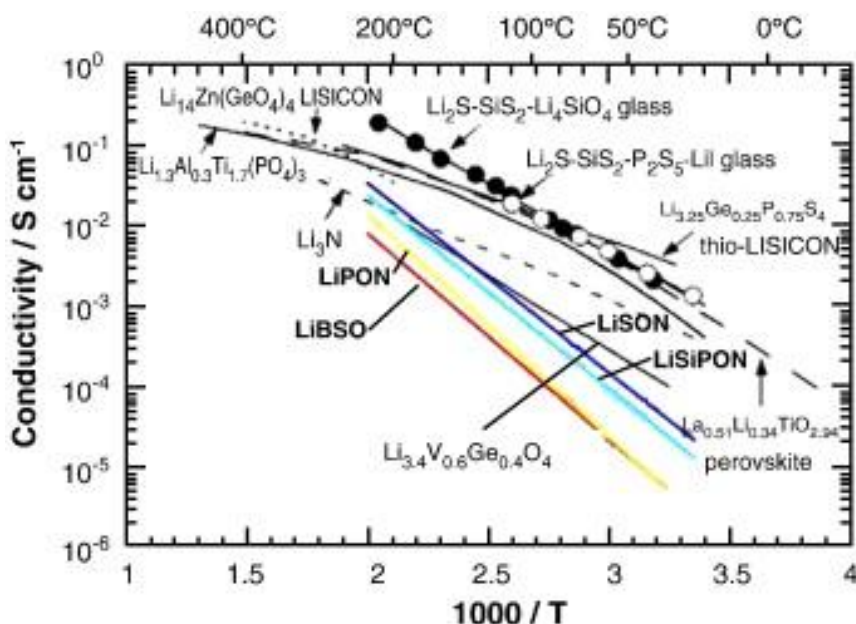
Figure 1.5 Arrhenius plot of ionic conductivity of important crystalline and amorphous inorganic solid lithium ion conductors [42]

The solid-state electrolytes employed in LIBs belong mainly to two classes of materials, which are lithium-ion conductive polymers and inorganic ceramics. For the former class, materials like poly(acrylonitrile) (PAN), poly(vinylidene fluoride) (PVDF), poly(methyl methacrylate) (PMMA) have been extensively studied and widely used in all-solid-state polymer LIBs.[44] Herein, this section will focus on the recent development of inorganic solid lithium ion conductors. According to the structure of the materials, the inorganic solid state electrolytes for LIBs falls into two main categories: crystalline lithium ion conductors and amorphous ones. Figure 1.5 summarizes most of the popular inorganic solid lithium ion conductors.[42]
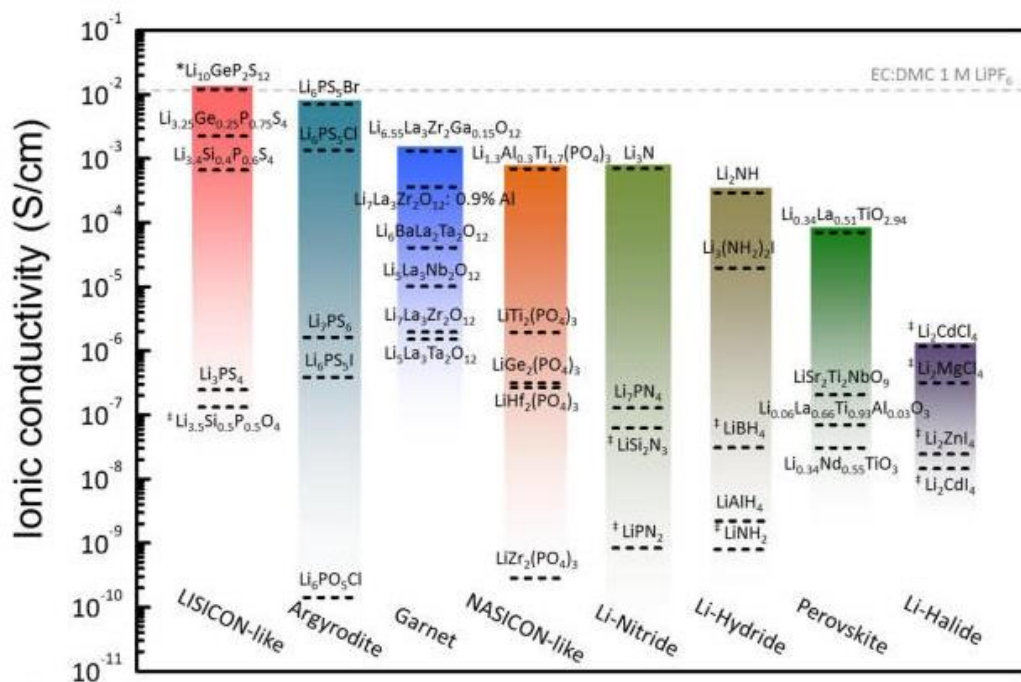
Figure 1.6 Reported total ionic conductivity of SSE at room temperature, including LISICON-like (LISICON, thio- LISICON), argyrodite, garnet, NASICON-like, Li-nitride, Li-hydride, perovskite, and Li-halide [43]

For the crystalline SSE, considerable researches have been dedicated to the following systems: LISICON-like (lithium superionic conductor),[45] argyrodites,[46] garnets,[47] NASICON-like (sodium superionic conductor), lithium nitrides, lithium hydrides, perovskites, and lithium halides. Within a given family of structures, the ionic

conductivity can be tuned by adjusting the structure and composition of the materials.[42,43,48] In crystalline SSEs, lithium ion transportation generally depends on the concentration and distribution of "Frenkel" and "Schottky" defects . Schottky defects generally occur when cations and anions in the ionic crystal conductors have the similar atomic diameters. Diffusion of lithium ions, however, is mostly related to the mechanisms based on Frenkel defects. Several ionic diffusion mechanisms are proposed, including the simple vacancy mechanism and relatively complicated diffusion mechanisms, such as the divacancy mechanism, interstitial mechanism, interstitial–substitutional exchange mechanism and the collective mechanism.[49,50]

Although some of the crystalline SSEs, as shown in Figure 1.6,[43] have been proven to have superior ionic conductivity comparable to that of liquid electrolyte (ethylene carbonate/dimethyl carbonate with 1 M LiPF$_6$ $\approx 10^{-2}$ S cm^{-1} highlighted with the dashed grey line), they are restricted by certain properties when applied in ASSBs. For instance, the sulfides in LISICON-like family have ionic conductivities as high as 10^{-2} S cm^{-1} but they have low oxidation stability and poor compatibility with cathode materials. Their extreme sensitivity toward moisture poses significant challenges in the fabrication process.[44,51] The NASICON type have also been intensively exploited, particularly the LiTi$_2$(PO$_4$)$_3$ system, the ionic conductivity of which can reach 10^{-3} S cm^{-1}. The ionic conductivity can be further enhanced by substituting Ti with other metals in the form of Li$_{1+x}$M$_x$Ti$_{2-x}$(PO$_4$)$_3$ (M = Al, Cr, Ga, Fe, Sc, In, Lu, Y or La) system, where M = Al have provided the best ionic conductivity.[52] Nevertheless, the reduction of Ti^{4+} on contact with lithium metal is an issue that cannot be neglected.[44]

Another type of inorganic SSE includes amorphous systems (also known as glass systems). Similar to the diffusion process in a crystal structure, the ionic transportation in glassy materials is initiated by a 'hopping' of ions from its initial site to the neighboring sites and then collectively diffusing on a macroscopic scale. There are some criteria that determine the overall ion diffusion kinetics. First, the number of equivalent sites available for the mobile ions (Li$^+$) to occupy should be sufficient. Second, the energy barrier between the adjacent available sites should be low enough for the ions to migrate from one site to another. A continuous pathway should be formed by connected available sites

for the ions to diffuse through.[50,53] In other words, the interaction between the charge carrier (Li^+) and the structural skeleton plays the most important role. Compared to the crystalline SSE, the glass electrolytes have some unique advantages such as isotropic ionic conduction, no grain boundaries, and tunable ionic conductivity based on wide range of compositions.[42] Most commonly studied oxide systems include $Li_2O-P_2O_5-B_2O_3$ and $Li_2O-SiO_2-Al_2O_3$, where P−O and Si−O thread as the skeleton called the network former while B_2O_3 and Al_2O_3 act as the network modifier to increase the ionic conductivity.[54] Later, it was found that replacing the oxygen with sulfur provides more weakly bonded Li ions and the sulfide glass SSE yields much improved ionic conductivity. A typical sulfide glass, $Li_2S-P_2S_5-LiI$, shows ionic conductivity of 10^{-4} S cm^{-1} at room temperature, in which P_2S_5 is the network former and LiI is the network modifier.[55,56] Despite the high ionic conductivity, this group of SSE is very air-sensitive, which increases the cost of production. The voltage window is also limited, making it not suitable for high voltage cathodes in some cases.[57]

One specific system of glass SSE that is worth mentioning is the oxynitrides, lithium phosphorous oxynitride (LiPON) in particular. LiPON exhibits fairly good ionic conductivity as high as 10^{-6} S cm^{-1}, as well as a relatively stable electrochemical window (> 5.5 V). It was developed by Bates et al in 1990s and later studies demonstrated that the presence of N in the network plays a critical role in the film stability and ionic conductivity.[58–61] So far, LiPON has been the most widely studied candidate in this group which has been applied in ASSBs.[62,63]

Three major methods have been employed for fabrication of thin films to implement solid-state electrolytes into ASSBs including chemical reaction, electro-chemical reaction or physical deposition. More specifically, the most popular deposition techniques are atomic layer deposition (ALD), solution deposition (Sol-gel), chemical vapor deposition (CVD), electrostatic coating, sputtering, thermal evaporation, pulsed laser deposition (PLD) etc.

1.2   Atomic Layer Deposition (ALD)

Atomic layer deposition (ALD) has emerged as an essential technique for thin film deposition for a wide range of applications. ALD provides unparalleled advantages compared to other thin film fabrication techniques such as chemical vapor deposition, physical vapor deposition, and sputtering, due to its conformality and control over materials thickness and composition. This technique was introduced as atomic layer epitaxy (ALE) by Suntola and Antson in 1970s for the first time in Finland. Tuomo Suntola as one of the pioneers in this field demonstrated some of the first ALE processes in 1974.[64] ZnS was deposited for flat panel displays.[65] The first literature paper on ALE was published in 1980 in Thin Solid Films. The first ALE device was an electroluminescent display which operated in the Helsinki airport from 1983 to 1998. As for the apparatus, the first reactor for ALE was a model F-120 from Microchemistry in 1988.[66]

The term "ALE" was popularly used until approximately 2000, when the use of the term "ALD" has become more common. Other names have been used including molecular layer epitaxy and binary reaction sequence chemistry. The reason behind changing from the term ALE to ALD is because of the nature of the self-limiting surface reactions. The direction of the sequential chemical reactions did not necessarily take place epitaxially to the underlying substrates during the thin films growth. As a matter of fact, some of the films grown were in amorphous phase. Therefore, the term ALD is now in common use. The use of ALD has become dominant with the practitioners in many fields.

1.2.1 Mechanisms
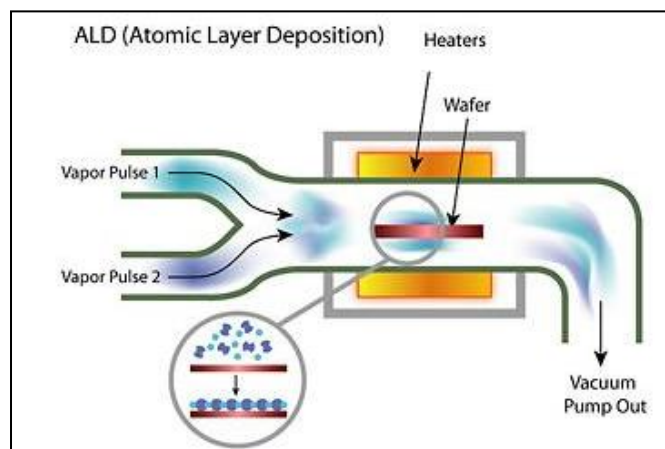
Figure 1.7 Schematic setup of a binary ALD deposition system [67]

A typical ALD process involves sequential alternating pulses of gaseous chemical precursors into the reaction chamber. A schematic diagram of a typical binary ALD reaction system is illustrated in Figure 1.7.[67] The individual chemical vapor reacts with the substrates, which is called 'half-reactions' composing only part of the material synthesis. The reactions generally take place under vacuum (<1 Torr) where the precursor is introduced in the chamber for a designated period of time and then purged out until the pressure of the chamber drops to the base line. An inert carrier gas (typically N_2 or Ar) is used to remove the excess precursor and the reaction by-products. This is to make sure that no excess residuals remain in the chamber to block the pipeline. Then the next precursor is pulsed in and purged out to allow the complete reaction. The surface reaction is self-limiting so that no more than one monolayer of the species forms on the surface. After the counter half-reaction, up to one layer of the desired material is formed. [Figure 1.8 (a-e)] The full cycle consisting of two half-reactions is repeated for multiple times to reach the desired thickness of the thin films. [Figure 1.8(f)]
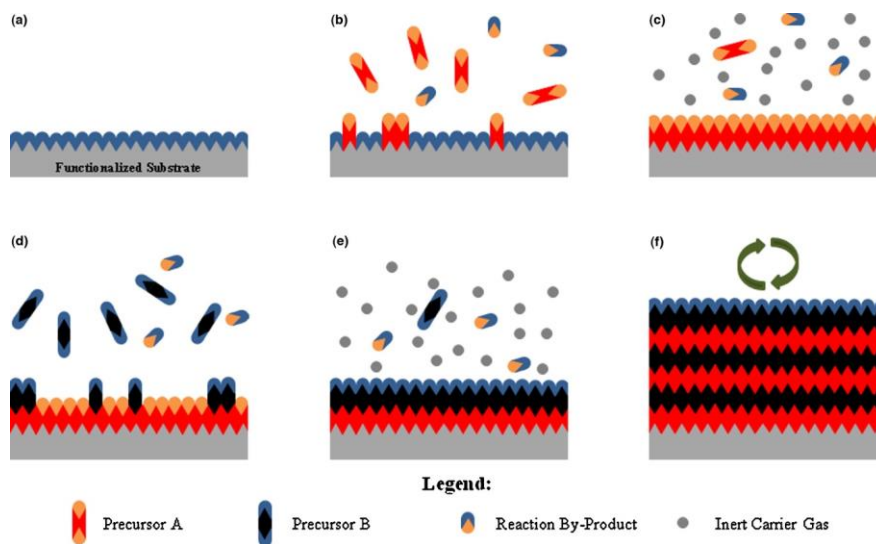
Figure 1.8 Schematic of ALD procedure: (a) the surface of the naturally functionalized substrate; (b) precursor A pulsed in, reacting with the surface; (c) excess precursor A and side products of the reaction purged out with inter carrier gas; (d) precursor A pulsed in, reacting with the surface; (e) excess precursor B and side products of the reaction purged out with inter carrier gas; (f) repeating step (b)-(e) until the desired thickness is reached [76]

Taking the model compound Al_2O_3 as an example as shown in Figure 1.9, the precursors typically used are trimethylaluminum [$Al(CH_3)_3$, TMA] and water. The first report of the ALD Al_2O_3 using TMA and water dates back to the late 1980s.[68,69] It is a model system to demonstrate the ALD process owing to the extremely efficient and readily available surface reactions. In a CVD process, the TMA and H_2O reaction can be described by an overall reaction:

$$2Al(CH_3)_3 + 3H_2O \rightarrow Al_2O_3 + 6CH_4 \qquad (1)$$

In comparison, the ALD procedure consists of two half-reactions, suggested as follow:

$$AlOH* + Al(CH_3)_3\ (g) \rightarrow Al{-}O{-}Al(CH_3)_2* + CH_4\ (g) \qquad (2a)$$

$$Al{-}O{-}Al(CH_3)_2* + 2H_2O\ (g) \rightarrow Al{-}O{-}Al(OH)_2* + 2CH_4\ (g) \qquad (2b)$$

where the asterisks denote the species attached on the substrate surface by chemisorption and (g) the gaseous phase of the precursors or byproducts.
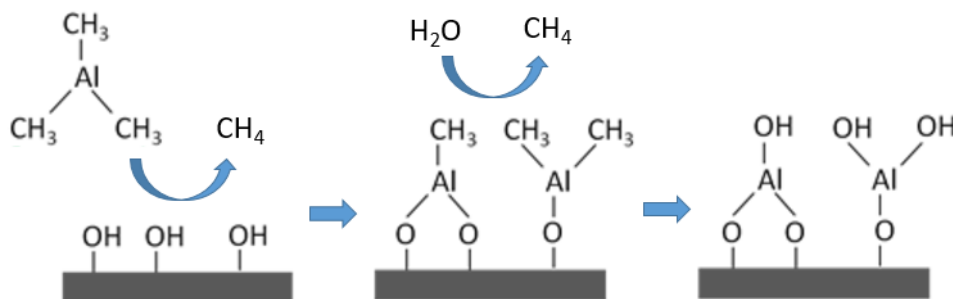
Figure 1.9 A model ALD process of depositing Al₂O₃ using TMA and water as precursors

Upon supplying of TMA as the aluminum source, the bond between the Al atom and the carbon ligand breaks, as well as the bond between the oxygen and hydrogen in the hydroxyl function (–OH). Consequently, an Al−O bond forms and the released H atoms react with the −CH₃ ligands forming CH₄ as the byproduct. Then the gaseous CH₄ and unreacted TMA are purged out, completing the first half-reaction. Afterwards, the oxidant, H₂O is pulsed in. Similarly, the remaining Al–CH₃ bonds will break and be replaced by the hydroxyl group, with CH₄ as the byproducts forming, which finishes the second half-reaction. Thus, ALD operates cyclically and proceeds in a layer by layer manner.

For an ALD process, there are three critical parameters that jointly determine the deposition features. First and foremost is the substrate. As illustrated in Figure 1.8 and 1.9, the surface of the substrate has to be uniformly functionalized to initiate the reaction, where the first half-reaction take place at the reactive sites.[70] The growth is self-limiting because all the surface functional groups (reaction sites) are saturated after the first half-reaction and new layer has been formed. Accordingly, the newly formed layer during the first half-reaction provide the reaction sites for the second half-reaction to occur. Sequentially, the next precursor reacts with the new functional ligands and terminates when there is no site to react with, creating a new layer with reactive sites for the following reactions. The combined effects of the two half-reactions provides well-

controlled growth of the desired material in a layer by layer manner. Therefore, the ability of the substrates to be functionalized and the number of the reactive sites on the surface greatly affect the thin film growth.
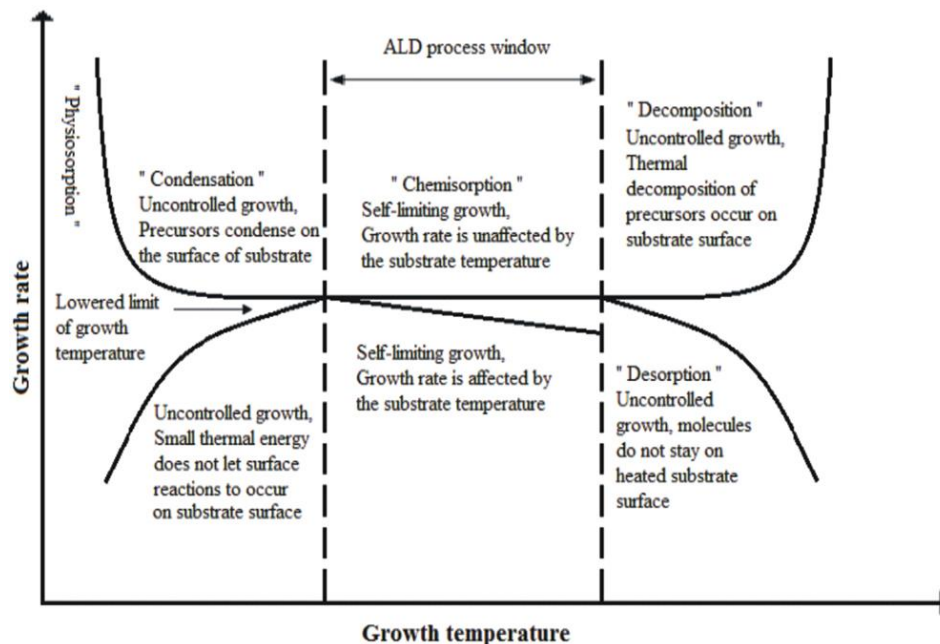
Figure 1.10 Schematic of possible behaviors for the ALD growth per cycle versus temperature showing the ALD window [71]

The second determining factor is temperature, which is closely related with the deposition of the targeting materials in the following aspects. During an ALD process, chemisoption rather than physisorption of the precursors is necessary to sustain ALD characteristics.[71] Hence the ALD deposition temperature should be adjusted to minimize the physisoption of the ligands. In other words, if the temperature is too low, the precursor materials may desorb without a complete half-reaction or even condense a liquid or solid on the surface, resulting in an increased growth rate. Alternatively, the thermal energy may not be sufficient to initiate the reaction and thus a lower growth rate might be observed. As plotted in Figure 1.10, there is an inevitable relationship between the selected deposition temperature and the growth behavior.[72] Above a certain temperature, the precursors might be decomposed before reaction, leading to a larger growth rate. Another possibility is that the precursor may be desorbed which means the

molecules tend not to stay on the heated substrate surface and thereby give rise to a decreased growth rate. An appropriate temperature range where successful ALD growth can be achieved is called "ALD window".[72] Typically, the temperature window for an ALD process is much lower than their CVD analog, even down to room temperature.[73]

Another key factor is the precursor. The most important consideration is that sufficient vapor must be provided to saturate all the reactive sites on the substrate. The concentration of the precursors in their gaseous phase must exceed a threshold value so that a continuous monolayer coverage can be obtained.[74,75] The sublimation temperature must ensure that the vapor pressure of the precursor is high enough and decomposition does not occur. The dose of the precursor can be controlled by the pulse time since the time scale for the chemisorptions is usually milliseconds.[75,76] The fractional coverage is gradually increased with the partial pressure of the precursor until a threshold pressure is reached where the coverage levels off to 100%. Therefore, the effect of pulse time of the precursors on the growth rate is studied in an ALD process to determine the empirical value needed for a saturated growth. Properties of the precursors must be taken into careful consideration as well as the cost of the precursors. The expected byproducts must be properly dealt with for the maintenance of the system and safety precautions must be taken.

1.2.2   Characteristics

The unique reaction mechanisms impart distinct characteristics of ALD. One of the main features is the excellent uniformity and conformality of the deposited films in comparison with other techniques including solution-based methods (sol-gel), PVD, and CVD. Figure 1.11 shows the schematic diagram of the deposition of thin films on complex substrates comparing sol-gel, PVD, CVD, and ALD techniques.[77] It is clearly illustrated that in PVD, the source material generally comes from a certain direction and the full coverage cannot be achieved over the non-planar substrates. Although CVD is also a gas-phase based method where gaseous reactants can diffuse into the delicate architectures of the substrates, uneven deposition is often delivered and the rate of the growth is uncontrollable. Similarly, solution-based method gives full coverage but no uniformity.

Only ALD can prepare ultra-uniform and conformal thin films on complex 3D substrates due to the nature of the reactions.
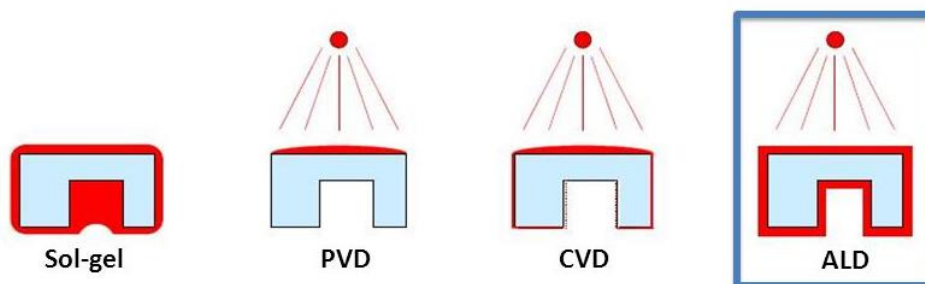
Figure 1.11 Schematics of deposition of thin films over complex substrates by sol-gel, PVD, CVD, and ALD [77]

Not only a much smaller surface roughness can be expected, the conformality extends to substrates with high-aspect-ratio or nanoscale dimensions. Some representative electron microscopy images are exemplified in Figure 1.12.[78] For instance, helical oxide nanotubes fabricated by ALD onto carbon nanocoils well maintain the curvature features of the templates [Figure 1.12 (b)]. Anodic aluminum oxide (AAO) templates were used as template to synthesize the core-shell nanotubes [Figure 1.12 (c, f, j)]. By alternating ALD process of metals and Al_2O_3, the template and the sacrificial layer (Al_2O_3) was later etched to achieve the patterned core-shell nanostructure. Despite the fact that ALD growth take place in a slow fashion, the precise thickness control in turn ensures the suitability of this technique for the fabrication of delicate devices like microelectronics. In addition, because no surface sites are left behind during film growth, the films tend to be very continuous and pinhole-free, which is another essential assessment in the actual fabrication of devices. ALD processing is also extendible to large substrates and multiple substrates in parallel. The precursors fill in all space regardless of substrate geometry since they are vaporized gas phase molecules. Thus, larger scale of production can be achieved using larger size of reaction chamber.
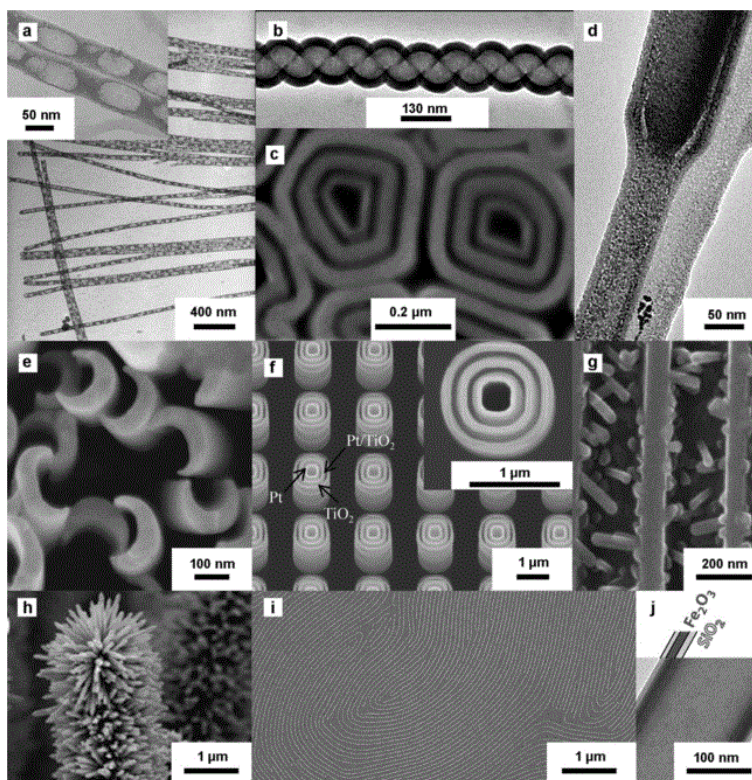
Figure 1.12 ALD deposition on complex nanostructure: (a) titania/silica hybrid nanowires containing linear mesocage arrays; (b) Al₂O₃ helical nanotubes; (c) Nested coaxial multiwalled nanotubes; (d) Diameter modulations in magnetic iron oxide nanotubes; (e) Au crescent-shaped half-nanotubes; (f) Highly ordered arrays of nested semiconductor/metal nanotubes; (g) TiO₂ nanorods in 3D-confined space; (h) Hierarchical ZnO nano- architectures; (i) Nanoscopic patterned materials with tunable dimensions; (j) Multilayered core/shell nanowires [78]

In addition, relatively low deposition temperature is another asset for ALD, which is typically less than 400 ºC versus 600-1000 ºC for CVD. Room-temperature deposition has been reported for some compounds. SiO_2 has been successfully synthesized by ALD at room temperature using $SiCl_4$ and water.[79] Numerous studies have reported depositions below 100 ºC, such as Al_2O_3,[68,71] ZrO_2,[80] ZnO,[81] TiO_2,[82] SnO_2,[83] Pd,[84] and Cu.[85] The low-temperature condition makes ALD applicable to heat-sensitive substrates such as polymers and biomaterials.

Furthermore, the composition of the deposited materials can be adjusted by varying the ALD recipes. In the macroscale, the as-prepared materials should have a stoichiometry close to the theoretical value. However, the atomic ratio can experience variations due to the different deposition temperatures. Groner et al. reported that the O/Al ratios of the ALD Al_2O_3 from TMA and water varied from 1.34 to 1.70 in the temperature range 33–177 ° C, revealed by Rutherford backscattering spectrometry (RBS).[86] The selection of precursors for the same element could also affect the outcome composition. Hämäläinen et al. demonstrated successful deposition of amorphous lithium silicate thin films from lithium hexamethyldisilazide [LiHMDS, $Li(N(SiMe_3)_2)$] and ozone, with a stoichiometry close to lithium metasilicate ($Li_{2.0}SiO_{2.9}$).[87] Interestingly, in this thesis, different precursors were used to deposit lithium silicate including lithium tert-butoxide [LiO^{t}Bu, $(CH_3)_3COLi$] and tetraethyl orthosilicate [TEOS, $Si(OC_2H_5)_4$]. The as-prepared thin films possess a composition close to lithium orthosilicate (Li_4SiO_4) instead. For more complicated compounds like ternary systems, the concept of "subcycle" is employed. Each subcycle is responsible for one of the elements. A full ALD cycle consists of different subcycles. And the composition of the final product can be tuned by changing the subcycle ratio within one full ALD cycle.
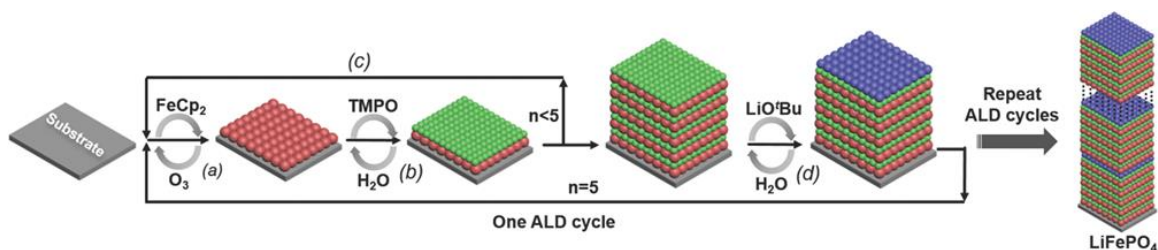
Figure 1.13 Atomic layer deposition of amorphous LiFePO$_4$ at 300 °C using FeCp$_2$ and O$_3$, TMPO, H$_2$O, and LiO^{t}Bu. (a) Sequential pulse of FeCp$_2$ and O$_3$ leading to the growth of a Fe$_2$O$_3$ layer (red); (b) sequential pulse of TMPO and H$_2$O leading to deposition of a PO$_x$ layer (green); (c) steps (a) and (b) are repeated for 5 times; (d) sequential pulse of LiO^{t}Bu and H$_2$O leading to formation of Li$_2$O layer (blue). One ALD cycle for the growth of amorphous LiFePO$_4$ consists of steps (a)–(d). [88]

A typical example is the ALD process for LiFePO$_4$, carried out by Jiu et al. As shown in Figure 1.13, (a) represents the subcycle for Fe using ferrocene (FeCp$_2$) ozone (O$_3$), (b) is

the subcycle for P using trimethylphosphate (TMPO) and water, and (d) illustrates the subcycle for Li with LiO^{t}Bu and water. The final recipe involves one full ALD cycle composed of 5 times of step (a) followed by (b) and only one subcycle of step (d). The growth of such compounds is rather complex. In other words, the number of subcycles for each element does not necessarily gives the exact corresponding atomic ratio and can only be determined experimentally.[88] The sequence of the subcycles also has some influences on the product, due to the fact that different subcycles might involve reaction terminating with different functional groups. Nevertheless, the capability of ALD to tune the composition of products is still attractive toward the synthesis of various materials.

1.3   Applications of ALD in LIBs

Owing to the advantages of ALD discussed in the previous sections, this technique has been considered as one of the promising approaches to fabricate all-solid-state batteries. Great efforts have been dedicated to the synthesis and surface engineering of various types of nanostructures for applications in LIBs. The first report of ALD technology in battery research was published in 2000 where V_2O_5 nanofibers were synthesized by ALD and electrochemically investigated as LIB cathodes.[89] However, the follow-up of this technique in LIBs did not occur until 2007 when it was used for surface functionalization in LIBs.[90] Since 2009, there have been more widespread appreciations of ALD for energy storage systems. The constantly rising number of publications in the past decade indicates that ALD has attracted world-wide interests, as shown in Figure 1.14.[91] The applications of ALD in the field of LIBs can be divided into three main categories: a) development of electrode materials, b) solid-state electrolytes, and c) surface coatings on electrodes. Table 1.2 has summarized some of the materials developed by ALD as battery components.[91] The following sections will focus on the recent progress of ALD applications in LIBs from the three perspectives.

Table 1.2: Summary of anodes, cathodes, and SSEs synthesized by ALD [91]

	Material	Substrate	Precursors	Temperature
Anode	TiO_2	Al nanorods	$TiI_4–H_2O$	200 °C
	TiO_2	Ni nanowires	$TiCl_4–H_2O$	120 °C
	TiO_2	graphene	$TiCl_4–H_2O$	120 °C
	TiO_2	peptide	$TTIP–NH_3/O_2$	140 °C
	SnO_2	graphene	$SnCl_4–H_2O$	200, 400 °C
	SnO_2	SS	$Sn(O^tBu)^5–O^-$ ions	200 °C
	Co_3O_4	TiN/Si	$CoCp_2$–plasma O_2	300 °C
	$Li_4Ti_5O_{12}$	NCNTs	$(LiO^tBu–H_2O)+(TTIP–H_2O)$	225 °C
	$Li_xTi_yO_z$	Si	$(LiO^tBu–H_2O)+(TTIP–H_2O)$	225 °C
	GaS_x	Si, CNTs	$Ga_2(NMe_2)_6–H_2S$	125–225 °C
Cathode	V_2O_5	Si, SS, AAO, CNTs	$VTOP–O_3$	170–185 °C
	V_2O_5	Si, glass, SS	$VO(thd)_2–O_3$	215 °C
	$FePO_4$	Si, glass, SS	$(Fe(thd)_3–O_3)+(TMP–H_2O/O_3)$	196–376 °C
	$LiCoO_2$	Si/SiO_2, Si/TiO_2/Pt	$(CoCp_2$–plasma $O_2)+(LiO^tBu$–plasma $O_2)$	325 °C
	$Li_xMn_2O_4$	Si, SS	$(Mn(thd)_3–O_3)+(Li(thd)–O_3)$	225 °C
	$LiFePO_4$	Si, CNTs	$5\times(FeCp_2–O_3–TMP–H_2O)+(LiO^tBu–H_2O)$	300 °C
Solid-state electrolyte	$(Li,La)_xTi_yO_z$	Si, glass	$(TiCl_4–H_2O)+(La(thd)_3–O_3)+(LiO^tBu–H_2O)$	225 °C
	$LiAlO_x$	Si, Teflon	$(LiO^tBu–H_2O)+(TMA–H_2O)$	225 °C
	Li_3PO_4	Si, glass	LiO^tBu or $LiHMDS–TMP$	225–350 °C
	Lithium silicate	Si	$LiHMDS–O_3$	150–400 °C
	$LiTaO_3$	Si	$(LiO^tBu–H_2O)+(Ta(OEt)_5–H_2O)$	225 °C
	$LiNbO_3$	Si, glass	$(LiHMDS–H_2O)+(Nb(OEt)_5–H_2O)$	235 °C
	Li_3N	Glass, Si, Ti	$LiHMDS–NH_3$	167 °C
	$LiSiAlO_2$	Si, Ge	$(TMA–H_2O)+(LiO^tBu–H_2O)+(TEOS–H_2O))$	290 °C

1.3.1   Fabrications of Electrode Materials

A battery cell has two electrodes, namely the anode and the cathode.

First, the focus will be given to the anode part. Based on their electrochemical reactions with lithium ions, anode materials can be categorized into three types, which are intercalation/de-intercalation (e.g. graphite, TiO_2, and $Li_4Ti_5O_{12}$), alloy/de-alloy (e.g. Si and Sn), and conversion (e.g. metal oxides, sulfides, and fluorides). Each category has its advantages and drawbacks.

The intercalation/de-intercalation based TiO_2 was among the earlier studies. TiO_2 exhibits only small volume changes, providing excellent mechanical stability, but suffers from relatively low electronic and ionic conductivities. Hence a few attempts have been demonstrated to fabricate novel structured TiO_2.[92] The crystallinity of the deposited TiO_2 can be tuned by changing the deposition temperature. Figure 1.14 depicts the schematic process of depositing TiO_2 on graphene nanosheets (GNSs).[73] 3D designs on Al nanorods and Ni nanowires presented significantly increased areal capacity. Hollow nanotubes and

core-shell structure also gave much higher electrochemical performance.[92,93] $TiCl_4$ (with H_2O) has been one of the popular precursors for growing TiO_2, but the generated corrosive byproduct (HCl) is harmful to the deposition system. Hence another precursor, titanium(IV) isopropoxide [TTIP, $Ti[OCH(CH_3)_2]_4$], has been the preferable choice. Another intercalation-based anode material, $Li_4Ti_5O_{12}$, known as a 'zero-strain' material, has also been successfully developed by ALD. The subcycle of Li_2O and TiO_2 were combined using LiO^{t}Bu and TTIP as Li and Ti sources, respectively.[94,95] The Li to Ti ratio was adjusted by the subcycle number. An amorphous lithium titanate thin film was obtained with a Li: Ti of 1.5. Post annealing was carried out to get the desired spinel phase between 650 to 900 $^\circ$C.[91] In order to improve the conductivity of these materials, a well-recognized strategy is to combine them with carbonaceous nanomaterials including graphene and CNTs.[96]
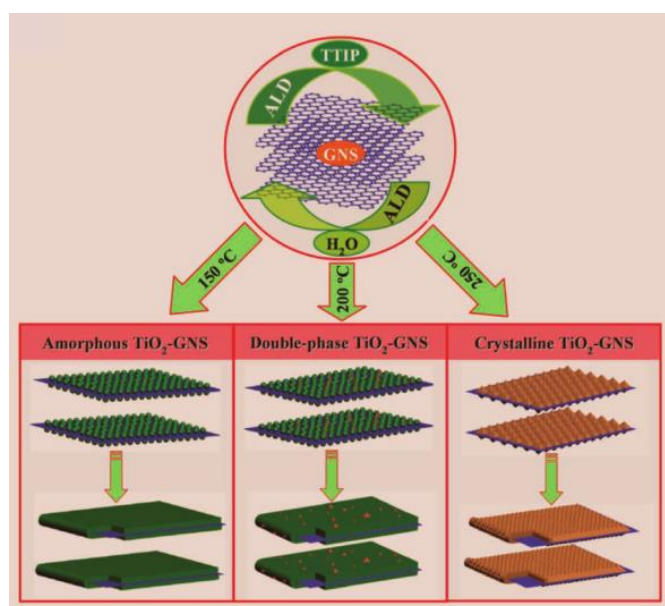
Figure 1.14 Schematic of ALD procedures for the growth of different phases of TiO_2 on GNSs [73]

The demand for high-capacity materials pushed the development of some conversion-based materials, such as SnO_2. Interestingly, both amorphous and crystallized phases have been proven to be electrochemically active in LIBs. Meng et al revealed that the phase of the as-prepared material by ALD can be tailored by controlling the deposition

temperature.[83,97] The nanocomposite concept can also be adopted to accommodate the large volume changes of this material during charge and discharge cycles. SnO_2 was deposited on GNSs and nitrogen-doped CNTs (NCNTs) by ALD from $SnCl_4$ and H_2O (Figure 1.15). Amorphous phase was obtained at lower temperatures as below 200 °C while rutile crystalline phase was observed at higher temperatures as above 400 °C. The reason was proposed to be due to the changes in the surface functional groups and reaction mechanisms at different deposition temperatures. Strikingly, the amorphous phase performed much better than the crystalline one as anodes for LIBs, showing a high capacity of ~800 mAh g^{-1} after 150 cycles (Figure 1.15).[83] Compared to amorphous phase, crystalline phase exhibited a gradual capacity drop, which might be due to the isotropic matrix of the amorphous phase and the fact that the flexible GNS support could better buffer the volume changes.
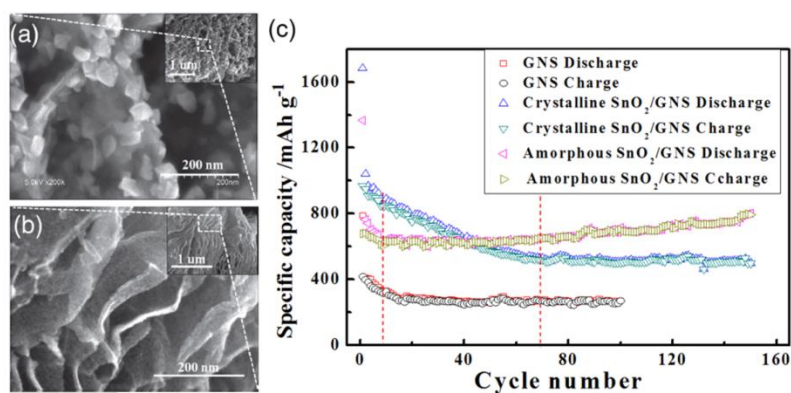
Figure 1.15 SEM of (a) crystalline and (b) amorphous SnO2 deposited on GNSs; (c) Cycling performance as anodes in LIBs [83]

Other materials like RuO_2,[98] Co_3O_4,[99] Fe_2O_3,[100,101] metal sulfides[102], and metal nitrides[103] have been fabricated by ALD as LIB anodes. Different from oxides, deposition of sulfides by ALD normally requires the use of H_2S as the counter reactants instead of water. The new ALD process for amorphous GaS_x used hexakis(dimethylamido)digallium and H_2S as precursors.[104] Other promising sulfides as LIB anode have been explored recently including MnS, Co_9S_8, and NiS_x. However, no studies on ALD elemental materials for energy storage have been reported so far.[102,105]

As for the cathodes, there are relatively fewer available processes compared to anodes. As mentioned above, the first cathode material developed was V_2O_5 from vanadium tri-isopropoxide [VTOP, $OV(OCH(CH_3)_2)_3$] and ozone in a temperature window of 170- 185 ^oC.[106] Another non-lithiated cathode material, amorphous $FePO_4$, was deposited using a combination of $Fe(thd)-O_3$ and $TMPO-H_2O/O_3$) at a temperature range of 196-376 ^oC.[107] However, non-lithiated cathodes are not applicable in full cells since they do not contain lithium.

lithium-containing cathode materials have been explored along with the development of lithium precursors.[108] The common approach is to combine the lithium subcycles with the other metal oxide subcycles. An ALD process for $LiCoO_2$ was later reported using $CoCp_2$ [Cobaltocene, $Co(C_5H_5)_2$], LiO^tBu, and O_2 plasma precursors at 325 ^oC.[109] Crystalline $LiCoO_2$ was obtained after annealing at 700 ^oC for 6 min. Although, the electrochemical performance can be optimized by tuning the Li to Co ratio, the experimental value was still lower than the theoretical value. $Li_xMn_2O_4$ was then synthesized by ALD with a recipe of $Mn(thd)_3-O_3$ and $Li(thd)-O_3$.[110] It is worth noting that the transformation from MnO_2 to $Li_xMn_2O_4$ could take place by post-treatment of ALD lithium oxide. The obtained $Li_xMn_2O_4$ exhibited 230 mAh g^{-1} at 50μA and 190 mAh g^{-1} at 200 μA with stable cycling performance over 550 cycles.

Impressively, a ternary cathode system, $LiFePO_4$ (LFP), was developed by Liu et al.[88] $LiFePO_4$ has been considered as a promising candidate due to its high energy density, low cost, high stability, and high safety. The challenges of developing such ALD recipe is related to tuning the surface chemistry and the stoichiometry. Amorphous lithium iron phosphate was grown at 300 ^oC using the procedure shown in Figure 1.13. The growth rate of a whole cycle on Si substrate was 0.9 nm/cycle. Olivine phase $LiFePO_4$ was acquired after annealing at 700 ^oC for 5 h in Ar. Figure 1.16 presents the SEM and HRTEM images of the annealed sample on CNTs. The CNTs substrate acted as an electronic conductive scaffold while benefited the rate capability of the composite electrode. It delivered a high capacity of ~70 mAh g^{-1} at 60C (1 min for each full charge and discharge cycle). A specific capacity of ~160 mAh g^{-1}, comparable to those obtained from other synthesis methods was observed. The authors also demonstrated ultra-long

testing duration up to 2000 cycles with no apparent degradation in performance. This work sheds light on the fabrication of complex cathode materials for next-generation LIBs.
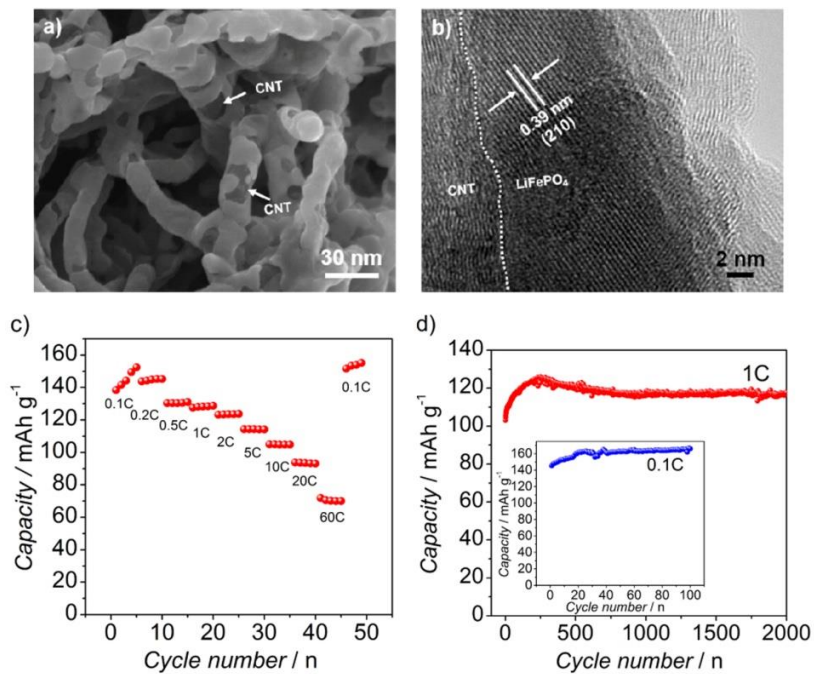
Figure 1.16 (a) SEM image and (b) HRTEM of crystalline LFP on CNTs; (c) rate capacitlity and (d) cycling performance of LFP on CNTs [88]

1.3.2 Fabrications of Solid-State Electrolytes

Solid-state electrolytes by ALD have experienced a rapid development in recent years. Researchers have devoted great efforts into this field. Lithium is an important constituent in inorganic SSEs for LIBs.[111] The first report of lithium-containing materials by ALD was conducted by one joint study from the researchers from Norway and Finland in 2009.[108] Several lithium-containing organics were evaluated as lithium precursors, including lithium β-diketonate Li(thd) (thd = 2,2,6,6-tetramethyl-3,5-heptanedionate), lithium alkoxide LiOᵗBu, lithium cyclopentadienyl LiCp (Cp = cyclopentadienyl), lithium alkyl n-butyllithium, and lithium amide lithium dicyclohexylamide. Lithium carbonate was obtained from Li(thd) and ozone in a temperature range of 185–300 ℃. In addition, lithium lanthanate thin films were grown by combining the Li(thd) process with a ALD

process for lanthanum oxide from La(thd)$_3$ and ozone. Thereafter, several studies have been performed, reporting the successful ALD processes of a few lithium-containing compounds. LiO^{t}Bu has become one of the most commonly used lithium precursors. The sublimation temperature is usually over 170 ^{o}C and the deposition temperature must be above 225 ^{o}C, otherwise condensation of the precursor and high amount of carbon impurity might be presented.[108,112,113] Cavanagh et al. demonstrated the growth of LiOH and Li$_2$CO$_3$ with LiO^{t}Bu and water/CO$_2$, stating the possibility of using ALD to fabricate an artificial solid-electrolyte interphase (SEI) layer to improve capacity retention during the battery cycling.[112] Based on the concept of combining subcycles, lithium lanthanum titanate (LLTO) and lithium aluminum oxide have been synthesized as potential SSEs.[113,114] Up to this point, only the amorphous Li$_2$O-Al$_2$O$_3$ system has been demonstrated to have electrochemical properties, with an ionic conductivity of 10^{-7} at 300 ^{o}C.[114] This value was not good enough for the actual application of SSE into LIBs.

Following the above, other glass systems have prepared by ALD such as lithium silicate and lithium phosphate.[87,115] A new lithium precursor was studied and later recognized as another popular choice for lithium source, which is lithium hexamethyldisilazide [LiHMDS, Li(N(SiMe$_3$)$_2$)]. Compared to LiO^{t}Bu, LiHMDS requires lower sublimation temperature at about 60 ^{o}C, which is more favorable. However, the more complex ligands of it can sometimes be problematic. It was used to directly react with ozone to form lithium silicates in a temperature window of 150- 400 ^{o}C. All the as-deposited films were amorphous except that deposited at 400 ^{o}C, where partial decomposition of LiHMDS was also observed. The one grown at 250 ^{o}C had a composition close to lithium metasilicate with the presence of hydrogen impurities (4.6%). Li$_3$N was also prepared from LiHMDS reacting with NH$_3$.[116] The crystalline state of Li$_3$N depended on the deposition conditions and varied from amorphous to a phase mixture of α-Li$_3$N and β-Li$_3$N. In the same study, it was proved to be possible to deposit lithium carbonate from LiHMDS as well, although a small amount of Si impurities was present. Østreng et al. reported ALD of ferroelectric LiNbO$_3$ using LiHMDS, niobium ethoxide [Nb(OEt)$_5$, Nb(OC$_2$H$_5$)$_5$], and water at 235 ^{o}C.[117]

It was not until 2013 when Liu et al. tried out the electrochemical measurement again for the system lithium tantalate SSE.[118] Tantalum(V) ethoxide [Ta(OEt)$_5$, Ta(OC$_2$H$_5$)$_5$] and water were employed for the Ta$_2$O$_5$ subcycle. The source temperature for Ta(OEt)$_5$ was also very high (190 $^\circ$C). The recipe selected for the later impedance measurement consisted of 1 × Li$_2$O+6 × Ta$_2$O$_5$. A through-plan setup of lithium tantalite thin films sandwiched between two Au electrodes was used to measure the ionic conductivity, which reached 2 × 10^{-8} S cm^{-1} at room temperature. Another glass system, Li$_x$Al$_y$Si$_z$O by ALD was studied by Perng and Cho et al.[119] A more complex setup was used for the impedance measurement, employing two-point hanging mercury drop electrodes (HMDE) connected to an HP 4284A LCR meter. The HMDEs were replaced by metal contacts; 800 μm diameter dots comprised of a 10 nm adhesion layer of Ti followed by 100 nm of Pt were e-beam deposited onto the LASO-coated ITO samples. Tungsten probes controlled by the probe station made contact to the dots under light pressure. The room temperature ionic conductivity for the as-deposited films was in the range of 10^{-7} to 10^{-9} S cm^{-1} depending upon the Li content in the films
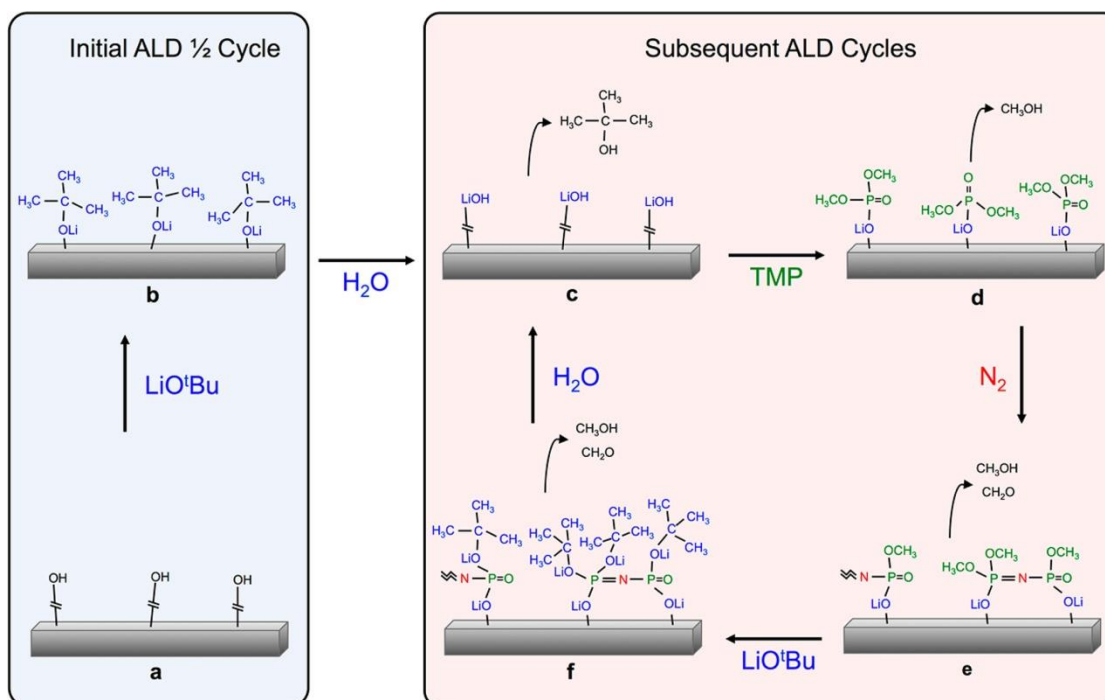
Figure 1.17 Schematic of proposed ALD LiPON process chemistry: (a) Hydroxyl terminated substrate; (b) metastable surface after the LiO^{t}Bu pulse; (c) H$_2$O pulse

removes the tert-butanol ligands and forms LiOH on the surface; (d) TMP reacts with surface LiOH through ligand exchange reaction, evolving CH₃OH; (e) N₂ plasma cross-links phosphorous atoms and evolve CH₃OH and CH₂O; (f) LiOᵗBu reacts with −OCH₃ ligands and evolves both CH₂OH and CH₂O [120]

More recently, a big jump in this field has been the successful development of lithium phosphorousoxynitride (LiPON) by ALD. The first report came in 2015, by Kozen et al. from University of Maryland.[120] An Ultratech Fiji F200 ALD system coupled with plasma was used, where LiOᵗBu and TMP (a.k.a TMPO) were used as precursors. Same precursors were used for the growth of lithium phosphate. The key difference here is the cross-linking process conducted by the N₂ plasma, thereby creating a nitrogen-doped phosphate network. Reaction mechanism proposed is described in Figure 1.17. Detailed XPS study showed the successful incorporation of N into the system. The ionic conductivity of the as-prepared thin films reached as high as $(1.45 \pm 3) \times 10^{-7}$ S cm⁻¹ at room temperature. Consistent with previous studies, the ionic conductivity increased with the increasing nitrogen content in the thin films. The thin film was proved to be functional in a coin cell with sputter-deposited amorphous silicon anodes on copper current collectors.

How to introduce P−N bond has always been the bottleneck in developing ALD LiPON. In thermal ALD, NH₃ has been applied as N source, like in the ALD procedure for Li₃N. However, according to the literatures, NH₃ almost exclusively undergoes a nucleophilic substitution at the carbon of the methyl ester group instead of cleaving the P−O bonds to form the required P−N bonds. Therefore, Nisula et al. choose an alternative approach, where a nitrogen-containing phosphorus precursor was utilized. LiHMDS and diethyl phosphoramidate $H_2NP(O)(OC_2H_5)_2$ (DEPA) reacted with each other at deposition temperatures from 230–350 °C.[121] The source temperature for DEPA was 87 °C. One drawback of this approach is that the N content in the films could hardly be tuned. Room-temperature ionic conductivities were determined for the films deposited at 290 and 330 °C using EIS. The one prepared at higher temperature exhibited a much better ionic conductivity at room temperature, which was 6.6×10^{-7} S cm⁻¹ with an activation energy of 0.55 eV. Inspired by this work, Shibata et al. utilized LiOᵗBu instead of LiHMDS and

another nitrogen containing phosphorus precursor, trisdimethylaminophosphorus [P(N(CH$_3$)$_2$)$_3$, TDMAP].[122] Furthermore, the use of H$_2$O, O$_3$, and other intensively oxidative substances was taken place by oxygen gas (100%) to suppress complete oxidation and promote nitriding. NH$_3$ was used for nitriding. The source temperature for TDMAP was rather low (30–40 °C) and the deposition temperature ranged from 400 to 500 °C. The compositional ratio was concentrated in a range of approximately Li/P ~ 1:4, O/P ~ 2:5, and N/P ~ 0:0.2. A comparable ionic conductivity of 3.7×10^{-7} S cm^{-1} was obtained with an activation energy of 0.57 eV.
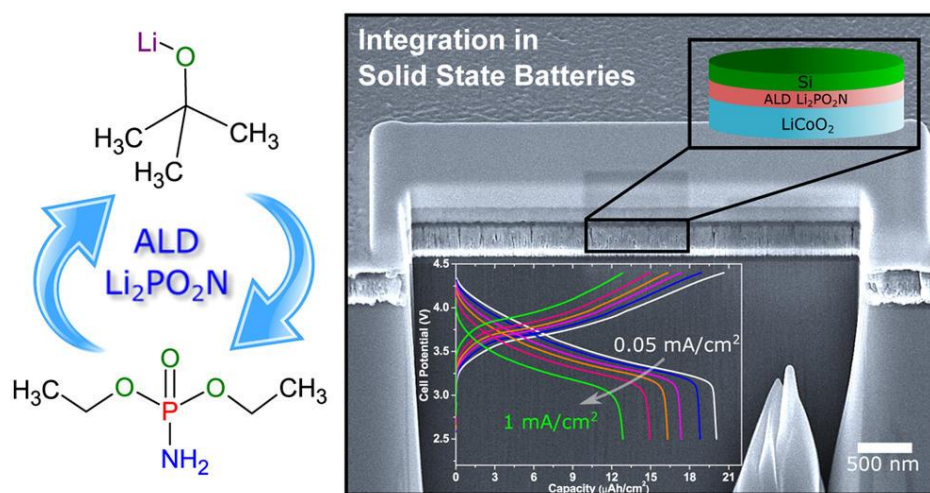
Figure 1.18 Schematic of ALD procedure for LiPON, rate performance of the battery measured in the inset panel, and the cross-section SEM image of the integrated device [123]

Similarly, an ALD procedure using LiO^{t}Bu and DEPA (Figure 1.18) was later carried out by Pearse et al.[123] A stoichiometry close to Li$_2$PO$_2$N was obtained at a deposition temperature of 300 °C, presenting an ionic conductivity of ~6.5 ×10^{-7} S cm^{-1} at 35 °C. The LiPON SSE was integrated into a full thin film battery using LiCoO$_2$ as the cathode and Si as the anode operating at up to 1 mA cm^{-2}. This work demonstrated the successful fabrication and operation of thin film batteries with ultrathin (<100 nm) SSE by ALD.

1.3.3   Surface Modifications of Electrodes

Interfacial reactions between the electrodes and liquid electrolytes are inevitable in battery systems, which might lead to unfavorable results that can compromise the overall performance of LIBs. For instance, SEI formed on the anode can consume lithium ions permanently, which will reduce columbic efficiency of the battery. For the cathode, HF generated in the electrolyte during cycling will give rise to metal dissolution of cathode materials, resulting in rapid degradation of the performance. Surface coating has been considered as one of the most effective methods to protect the electrode surface and thus suppress the unwanted reactions.
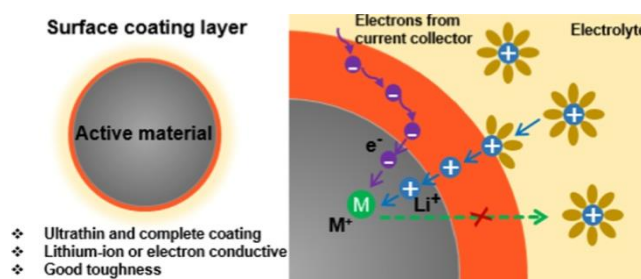
Figure 1.19 Schematic of an ideal surface coating on the active electrode material [91]

An ideal surface coating should feature one or more of the following characteristics. First, full coverage should be ensured in order to completely protect the electrode materials. The coating layer also must be ultrathin to prevent blocking the transportation of lithium ions and electrons through the coating layer, as illustrated in Figure 1.19. In addition, the coating layer should be conductive either ionically or electronically to allow better dynamics of the electrochemical reactions. Besides, the surface coating should have either high flexibility and toughness to buffer or constrain the volume changes.

Apart from the conventional coating methods used for LIBs like solution-based methods, ALD provides a more controllable deposition of the coating layer. Complete and uniform coatings with precise thickness control can be achieved via ALD. The surface coating process is time-consuming, non-destructive to electrode and easy to scale up for large batch productions.[91] With the growing awareness of the advantages of this technique,

ALD has been extensively applied as a coating method for LIBs, on both the anodes and cathodes.

ALD coatings on the anodes mainly deal with the problems from the formation of SEI, which is crucial to the cycling life of the battery. On one hand, it forms to protect the electrode from decomposition of the electrolyte. However, SEI is one of the reasons for irreversible capacity losses, which becomes even more severe in anode with large volume changes during cycling (Si, Sn, and SnO_2).[19,20] The pulverization of the electrodes during cycling gives fresh electrode surface to form a new SEI layer which is not desirable.

Therefore, one function of the ALD coating is to serve as an artificial SEI layer such as on graphite[124] and $Li_4Ti_5O_{12}$.[125] Binary oxides like TiO_2 and Al_2O_3 on graphite were shown to have positive effect on suppressing SEI formation and improved the specific capacity. At higher operation temperatures, the artificial SEI was more stable than the natural one. ZrO_2 has been applied onto $Li_4Ti_5O_{12}$, where EIS test justified that the resistance across the SEI layer was greatly reduced due to the ultrathin surface coating.[125]

The other function of the ALD coating is to alleviate the serious pulverization of the anodes. For instance, multiple coatings including TiO_2, TiN, and Al_2O_3 have been coated on Si nanotubes, among which TiO_2 coated one was found to have the best performance.[126] Wang et al. coated different cycles of Al_2O_3 on SnO_2. Optimal thickness for different particle sizes of SnO_2 can be found. Cycling stability and columbic efficiency are significantly improved for the tin based system. The coating layer restricted the active material and thus less cracking happened during cycling to minimize the new SEI formation from the newly exposed surfaces.[127]

On the cathode side, the ALD coating is aimed to tackle the problems caused by the side reactions with the liquid electrolytes. The generated HF can easily dissolve the metal components in the cathode materials and dramatic degradation will shorten the battery life time. $LiCoO_2$ as the dominant cathode materials was put on trial first. Deep extraction of Lithium at voltages above 4.2 V will lead to loss of Co^{4+} into the electrolyte, resulting in deterioration of the structure and loss of performance.[15,17] Al_2O_3, TiO_2, and ZrO_2 with a coating thickness less than 1 nm have been reported to be effective in protecting the

surface. Comparing these three, coated Al_2O_3 showed the best cycling stability and capacity retention while ALD coated ZrO_2 gave the best rate capacity, especially at higher current densities.[128] Some other typical cathode materials include $LiNi_{1/3}Mn_{1/3}Co_{1/3}O_2$ (NMC),[129] $LiNi_{0.5}Mn_{1.5}O_4$,[130,131] and lithium-rich systems ($Li_{1.2}Ni_{0.15}Mn_{0.55}Co_{0.1}O_2$ and $Li_{1.2}Ni_{0.13}Mn_{0.54}Co_{0.13}O_2$).[132] These high-capacity and high-voltage (4.5-4.8 V vs Li^+/Li) cathode materials can provide higher energy densities, however, still suffering from Mn dissolution through a disproportionate reaction, $2Mn^{3+}$ $\rightarrow$ Mn^{4+} + Mn^{2+}. More importantly, the generated Mn^{2+} would migrate through the separator and deposit onto the anode, blocking the ion transportation and damaging the SEI layer. The ultrathin ALD coatings act as a physical barrier between the cathode and the electrolyte and therefore improve the battery performance.[129]
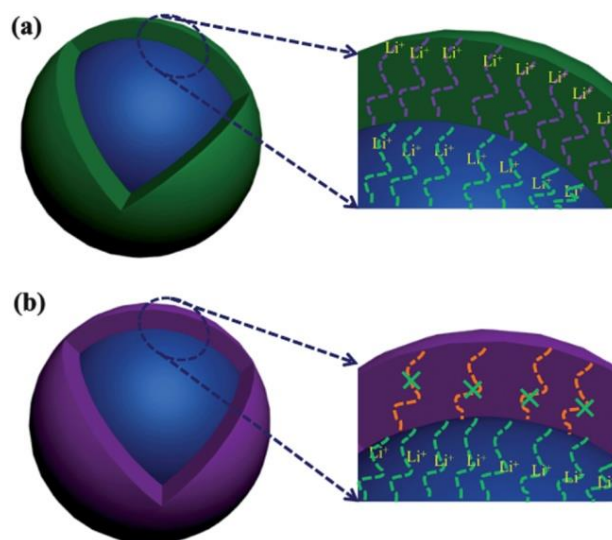
Figure 1.20 Schematic of (a) SSE coating (green) and (b) metal oxide coating (purple) [129]

Furthermore, lithium-conductive coating layers were demonstrated to be able to further enhance battery performance compared to simple oxide coatings. Li and his colleagues applied ALD lithium tantalate SSE on NMC.[129] The ionically conductive coating is expected to allow the diffusion of Li ions through the coatings and provide better battery dynamics as shown in Figure 1.20, which is supported by the acquired electrochemical performances. Both the stability and rate capability were greatly improved, especially at

higher cutoff voltages up to 4.8 V and a high working temperature (55 °C). Similar concept has been reported, such as ALD $LiAlO_2$ coating on $LiNi_{0.5}Mn_{1.5}O_4$.[130,131] This approach has been a promising direction to improve the cathode performance for LIBs.

1.4 Synchrotron Radiation

1.4.1 Overview

Synchrotron radiation (SR) is so named because it was first observed at synchrotrons, which are large and complex machines built for high-energy physics experiments. Charged particles are accelerated up to relativistic speeds, i.e. the particle velocity (v) approaches the speed of light (c). The accelerated charge particles are directed around curved paths by magnetic fields to that electromagnetic radiation is generated. Synchrotron radiation research has evolved substantially over the last few decades. Dating back to 1970s, the new emerging field of synchrotron radiation research was entirely parasitic on the high-energy physics experiments.[133] After the pioneer work at Tantalus which was among the first operational synchrotron radiation sources for photon research and later Sayer et al. who made the acceptable theory for the Extended X-ray Absorption Fine Structure (EXAFS), many synchrotron facilities have been built around the world.[133] Dedicated second generation facilities, such as NSLS (US), BESSY I (Germany), KEK (Japan), and Aladdin (US), came into service in 1980s. Compared to the first generation, the charged particles were changed from relatively massive protons to electrons, which radiate much more efficiently (for a given particle energy). These were oriented toward using the radiation produced at bending magnets. Upon the developing of instrumentation, third generation sources were built to accommodate insertion devices like wigglers and undulators, which generate light through undulating electrons by linear packed alternating magnetic fields. Facilities, like APS (US), ALS (US), ESRF (France), SPRING 8 (Japan), and CLS (Canada), produce light with many orders of magnitude brighter. The size of synchrotron facilities could be huge, for example, SPRING 8 has a circumference of 1436 m and APS is 1104 m in circumference.[133] Figure 1.21 shows the general layout of a modern SR facility.[134] Over

60 rings of various sizes widely distributed in the Americas, Europe, and Asia; and Australia has its own.
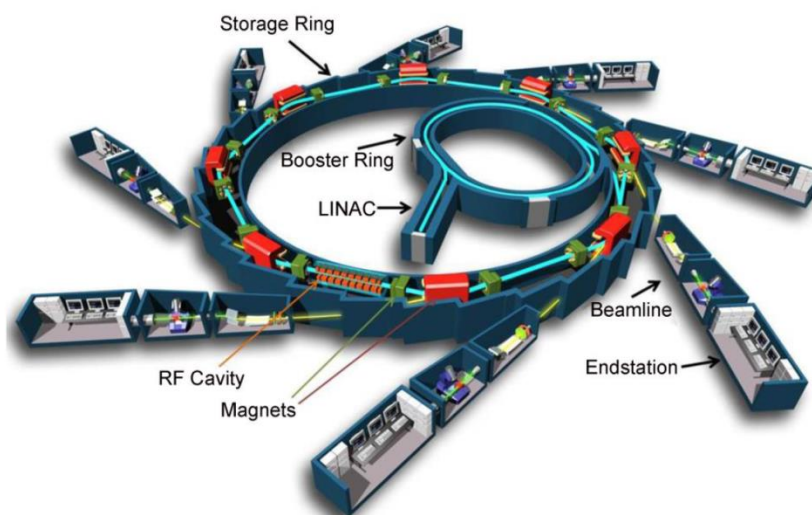
Figure 1.21 Schematic layout of a modern SR facility [134]

First, electrons are generated by a heated metal oxide cathode (electron gun) and then injected into the linear accelerator (LINAC), which can accelerate the electrons to 99.9998% of the speed of light with the energy to the order of MeV. After that, the electrons are injected into the booster ring where dipole magnets are used to direct travelling electrons around the booster ring. In the meantime, quadrupole magnets can focus and defocus the electrons, keep them in the desired orbit and maintain the stability of the electron beam. When the energy of the electrons reach a certain value (GeV), they are transferred into the storage ring. The electrons will then circulate in the storage ring for a few hours at nearly the speed of light. By rapid deflecting the directions of high energy electrons using wigglers/undulators, the tangential direction of the big storage ring emits the synchrotron radiation. The wiggler can produce a continuum of radiation that can be regarded as the superposition of the bending magnet radiation with higher flux, whereas the undulator takes advantage of the phasing/interference effects to produce more collimated, synchrotron light. The energy loss will be replenished by the radio-frequency (RF) cavity. Each beamline directs the beam from storage ring using mirrors, slits and monochromators for different energy range at each end station.

Overall, SR holds many advantages over laboratory X-ray sources, such as tenability, brightness, polarization, and time structure.[134] The energy range extends from IR to hard X-ray. The flux of SR can reach as high as 12 orders of magnitude of that of the traditional X-ray source. The highly-collimated beam of SR can give much higher spectral resolution. Furthermore, the generated beam is linearly polarized in the plane of orbit and elliptically polarized out of the orbit plane. In addition, the RF cavity produces bunched electrons as pulsed wave with a few nanoseconds between pulses and thus time-resolved spectroscopy is available. All the above characteristics of SR make it powerful in studying materials science in various fields.

1.4.2   X-ray Absorption Fine Structure

X-ray absorption fine structure (XAFS) has developed alongside the growth of synchrotron radiation research. It benefits the XAFS experiment enormously since XAFS requires an X-ray beam of finely tunable energy. XAFS spectroscopy is a unique tool for studying the local structure around the selected elements that are contained within a material at atomic and molecular level. It can be applied not only to crystals, but also to materials that possess little or no long-range translational order. The versatility allows it to be utilized in various disciplines.

The term "XAFS" is a broad one, which refers to several techniques, including EXAFS (Extended X-ray Absorption Fine Structure), XANES (X-ray Absorption Near Edge Structure), NEXAFS (Near Edge XAFS), and SEXAFS (Surface EXAFS). Different terminology and techniques may be employed, particularly in the low-energy (soft X-ray) and high-energy (hard-X-ray) regimes, although the fundamental physics is basically the same. In this thesis, researches are only focused on the low and medium energy ranges.[135]

The basic physical quantity measured in XAFS is the X-ray absorption coefficient (μ), describing how strongly X-rays are absorbed as a function of X-ray energy. It can be described by the equation: $\mu \approx \frac{\rho Z^4}{AE^3}$, where ρ is the sample density, Z is the atomic number, A is the atomic mass, and E is the X-ray energy. Generally, μ decreases with increasing E, meaning the X-rays become more penetrating. Sudden increases, which is

called X-ray absorption edges, occur at specific energies and are characteristics of the absorbing atoms in the material.
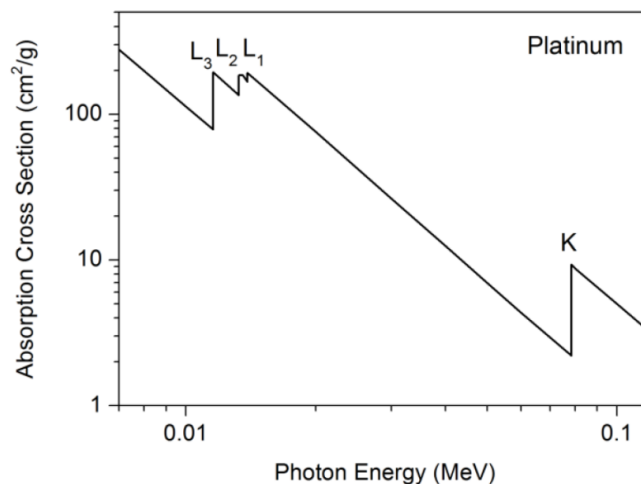
Figure 1.22 Log-log plot of X-ray absorption cross section (σ) of platinum as a function of X-ray photon energy (E) [136]

Figure 1.22 plots the K- and L-edges of Pt. Note that the nomenclature of an absorption edge comes from the shell name of the core-electron that is being excited. Accordingly, excitations of the Pt 1s (K-shell), 2s (L_1-shell), $2p_{1/2}$ (L_2-shell) and $2p_{3/2}$ (L_3-shell) electrons correspond to the Pt K-edge, L_1-edge, L_2-edge and L_3-edge, respectively. The cross-section, σ, as y axis shown in Figure 1.23, is a quantity proportional to μ.[136] The electrons from the low-energy bound states in the atoms are excited with enough X-ray photon energy. Then the "photoelectron" wave scatters from the atoms around the absorbing atom, creating interferences between the outgoing and scattered parts of the photoelectron wave function. The interferences lead to a variation in the X-ray absorption probability (proportional to the measurable μ). After proper interpretation, characteristic information can be provided on the structure, atomic number, structural disorder, and thermal motions of neighboring atoms using a tunable synchrotron light source to scan the photon energy across the absorption edge.[136]

An XAFS spectrum is typically divided into two regimes, XANES and EXAFS, depending on the behaviors of electron scattering which is related to the kinetic energy of

electrons. In this thesis, only studies on the XANES region are involved, which is generally from 20 eV below to 50 eV above the absorption edge.[137]
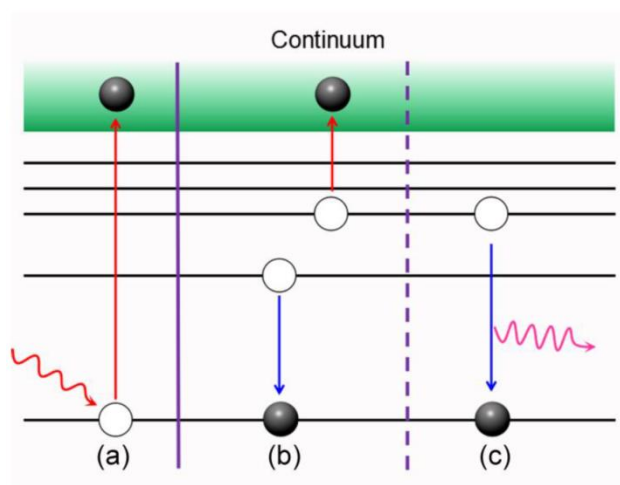
Figure 1.23 Schematics of a core-electron excitation by X-ray and the subsequent de-excitation processes: (a) The presence of a photoelectron and a core-hole upon X-ray excitation; (b) Auger process; and (c) X-ray fluorescence process [138]

Absorption event takes place when an incident photon on a sample interacts with electrons, gives up all its energy, and disappears in the process. The transitions of electrons from lower energy levels to higher energy levels creates core-holes at the lower levels [Figure 1.23(a)], which are later filled by transitions of electrons from higher levels down to lower ones. The de-excitations involve two competing processes. The energy is either released radiatively by kicking off an electron in an "Auger process" [Figure 1.23(b)], or by emitting fluorescence radiation at a lower energy than the incident photon [Figure 1.23(c)]. It is worth noting that the de-excitation following an absorption event can be complicated because of a possible sequence of single- and multiple-electron processes. Photons generally are emitted at X-ray, UV-visible, and infrared wavelengths. In addition, electrons may be ejected from the atoms and heat pulses may be generated. Therefore different detection modes have been developed while the most common ones are fluorescence and electron yield detection, which were used in this thesis.[138,139]

1.5 Thesis Objectives

As has been thoroughly reviewed, the challenges that the field of lithium-ion batteries are facing could be resolved by the development of all-solid-state batteries. Atomic layer deposition has been considered as one of the promising techniques to accomplish the fabrication of ASSBs. Therefore, the general objective of this thesis is to develop nanostructured materials as components (electrodes and solid-state electrolytes) for the next-generation lithium-ion batteries via atomic layer deposition. The specific objectives are the following.

(1) To develop a phosphorus-based glass system by ALD as SSEs for lithium ion batteries. The synthesis of lithium phosphate thin films is carried out. The correlation between the deposition temperature and the properties of the thin films is studied. The ionic conductivity of the system is evaluated.

(2) To synthesize novel structured nanocomposites as the anode materials for lithium ion batteries. A hybrid nanostructured material based on titanium oxide and lithium phosphate is designed. Detailed investigation on both the structure and the electrochemical performance of the nanocomposite is carried out.

(3) To exploit another non-metal based material, namely silicon-based system as SSEs for ASSBs. Lithium silicate thin films are developed by ALD. The mechanism of the thin film growth is studied. XANES study is applied to reveal the local electronic structure of the thin films and ionic conductivity is assessed as one important property of SSE.

(4) To explore an ALD process of a metal-based glass system as a SSE, which is lithium niobium oxide. Thin films are prepared and the ALD procedure is studied. A relationship between the ALD process parameter (subcycle number) and the local electronic structure is established by XANES study. Again, the ionic conductivity is measured at last.

1.6 Thesis Organization

This thesis includes seven chapters and satisfies the requirements for "Integrated-Article form" as outlined in the Thesis Regulation Guide by the School of Graduate and Postdocoral Sudies (SGPS) of the University of Western Ontario. Specifically, the thesis is organized as follows:

Chapter 1 gave a general background of lithium ion batteries including its working principles, recent development and challenges currently faced in this field. One proposed solution was all-solid-state batteries. Recent progress made on ASSB was reviewed, followed by a summary on the solid-state electrolytes. Atomic layer deposition as the fabrication technique was introduced in details from the aspects of fundamentals and applications in LIBs. Synchrotron radiation as another important technique applied in the thesis was introduced as well.

Chapter 2 listed the methodologies including detailed synthesis route and apparatus used such as structural characterizations, synchrotron-based techniques, and electrochemical measurements.

Chapter 3 presented the study of ALD deposited lithium phosphate thin films as SSE for LIBs. The ALD process was demonstrated. The growth of the thin films is monitored. The relations of the deposition temperature to the chemical composition and electrochemical properties were studied, proving that lithium phosphate by ALD was applicable to LIBs as SSE.

Chapter 4 reported a novel nanocomposite developed by ALD as anode materials for LIBs. The approach of combining ALD processes of TiO_2 and lithium phosphate generated a novel structure, which was investigated through several characterization techniques. It was revealed that nanocrystals of TiO_2 embedded in amorphous lithium phosphate matrix were achieved on CNTs skeletons. Excellent electrochemical performances demonstrated that the nanocomposite was a promising anode material.

Chapter 5 studied a silicon-based SSE system by ALD. The ALD recipes for lithium silicate thin films were described. The effect of deposition temperature and subcycle number on the local electronic structure was unveiled by XANES studies. Their influence on the ionic conductivity was also illustrated. Herein, another potential SSE material were prepared by ALD successfully.

Chapter 6 focused on the work of another metal-based glass system as SSE. Lithium niobium oxide thin films were deposited via ALD. Varying subcycle number ratio of Li to Nb consequently changed the growth rate, the chemical composition, and most interestingly, the local electronic structures. XANES measurements were performed, indicating a correlation between the lithium incorporation amount and the octahedral unit structures. The good lithium ion conductivity observed suggested the great potential of this material as either a SSE or interfacial engineering materials in ASSBs.

Chapter 7 summarized the results and conclusions of the work and points out the possible future directions of the following work in the future

References

1   K. Tomabechi, *Energies*, 2010, **3**, 686–695.

2   George Crabtree, *Nature*, 2015, **526**, 592.

3   V. Etacheri, R. Marom, R. Elazari, G. Salitra and D. Aurbach, *Energy Environ. Sci.*, 2011, 3243–3262.

4   P. P. R. M. L. Harks, F. M. Mulder and P. H. L. Notten, *J. Power Sources*, 2015, **288**, 92–105.

5   N. Nitta, F. Wu, J. T. Lee and G. Yushin, *Mater. Today*, 2015, **18**, 252–264.

6   Y. Wang, B. Liu, Q. Li, S. Cartmell, S. Ferrara, Z. D. Deng and J. Xiao, *J. Power Sources*, 2015, **286**, 330–345.

7   L. Ji, Z. Lin, M. Alcoutlabi and X. Zhang, *Energy Environ. Sci.*, 2011, **4**, 2682.

8   J. B. Goodenough and K.-S. Park, *J. Am. Chem. Soc.*, 2013, **135**, 1167–1176.

9   J. B. Goodenough and Y. Kim, *Chem. Mater.*, 2010, **22**, 587–603.

10   A. Manthiram, *J. Phys. Chem. Lett.*, 2011, **2**, 176–184.

11   E. M. Erickson, C. Ghanty and D. Aurbach, *J. Phys. Chem. Lett.*, 2014, **5**, 3313–3324.

12   D. Linden and T. B. Reddy, in *Handbook of Batteries*, McGraw-Hill publisher, 4th edn., 2010, p. 35.1.

13   M. Armand and J.-M. Tarascon, *Nature*, 2008, **451**, 652–7.

14   Y. Tang, Y. Zhang, W. Li, B. Ma and X. Chen, *Chem. Soc. Rev.*, 2015, **44**, 5926–5940.

15   M. S. Islam and C. A. J. Fisher, *Chem. Soc. Rev.*, 2014, **43**, 185–204.

16   J. Lee, A. Urban, X. Li, D. Su, G. Hautier and G. Ceder, *Science (80-.).*, 2014, **343**, 519–522.

17   B. Xu, D. Qian, Z. Wang and Y. S. Meng, *Mater. Sci. Eng. R Reports*, 2012, **73**, 51–65.

18   B. Xiao, B. Wang, J. Liu, K. Kaliyappan, Q. Sun, Y. Liu, G. Dadheech, M. P. Balogh, L. Yang, T. K. Sham, R. Li, M. Cai and X. Sun, *Nano Energy*, 2017, **34**, 120–130.

19   L. Liu, F. Xie, J. Lyu, T. Zhao, T. Li and B. G. Choi, *J. Power Sources*, 2016, **321**, 11–35.

20   J.-Y. Li, Q. Xu, G. Li, Y.-X. Yin, L.-J. Wan and Y.-G. Guo, *Mater. Chem. Front.*, , DOI:10.1039/C6QM00302H.

21   D. Wang, J. Yang, X. Li, D. Geng, R. Li, M. Cai, T.-K. Sham and X. Sun, *Energy Environ. Sci.*, 2013, **6**, 2900.

22   J. Cho, Y.-W. Kim, B. Kim, J.-G. Lee and B. Park, *Angew. Chemie Int. Ed.*, 2003, **42**, 1618–1621.

23   K. Takada, *Acta Mater.*, 2013, **61**, 759–770.

24   C. Sun, J. Liu, Y. Gong, D. P. Wilkinson and J. Zhang, *Nano Energy*, 2017, **33**, 363–386.

25   Y. N. Zhou, M. Z. Xue and Z. W. Fu, *J. Power Sources*, 2013, **234**, 310–332.

26   J. G. Kim, B. Son, S. Mukherjee, N. Schuppert, A. Bates, O. Kwon, M. J. Choi, H. Y. Chung and S. Park, *J. Power Sources*, 2015, **282**, 299–322.

27   K. Kanehori, K. Matsumoto, K. Miyauchi and T. Kudo, *Solid State Ionics*, 1983, **9–10**, 1445–1448.

28   B. Wang, J. B. Bates, F. X. Hart, B. C. Sales, R. A. Zuhr and J. D. Robertson, *J. Electrochem. Soc.*, 1996, **143**, 3203.

29   J. B. Bates, N. J. Dudney, B. Neudecker, A. Ueda and C. D. Evans, *Solid State Ionics*, 2008, **135**, 33–45.

30   J. M. Tarascon and M. Armand, *Nature*, 2001, **414**, 359–67.

31   S. Pan, J. Ren, X. Fang and H. Peng, *Adv. Energy Mater.*, 2016, **6**, 1–19.

32   J. W. Long, B. Dunn, D. R. Rolison and H. S. White, *Chem. Rev.*, 2004, **104**, 4463–92.

33   A. A. Talin, D. Ruzmetov, A. Kolmakov, K. McKelvey, N. Ware, F. El Gabaly, B. Dunn and H. S. White, *ACS Appl. Mater. Interfaces*, 2016, **8**, 32385–32391.

34   S. Ferrari, M. Loveridge, S. D. Beattie, M. Jahn, R. J. Dashwood and R. Bhagat, *J. Power Sources*, 2015, **286**, 25–46.

35   K. Gerasopoulos, E. Pomerantseva, M. Mccarthy, A. Brown, C. Wang, J. Culver and R. Ghodssi, *ACS Nano.*, 2012, **6**, 6422–6432.

36   C. Liu, E. I. Gillette, X. Chen, A. J. Pearse, A. C. Kozen, M. A. Schroeder, K. E. Gregorczyk, S. B. Lee and G. W. Rubloff, *Nat. Nanotechnol.*, 2014, **9**, 1031–1039.

37   J. Song, X. Yang, S.-S. Zeng, M.-Z. Cai, L.-T. Zhang, Q.-F. Dong, M.-S. Zheng, S.-T. Wu and Q.-H. Wu, *J. Micromechanics Microengineering*, 2009, **19**, 45004.

38   M. Roberts, P. Johns, J. Owen, D. Brandell, K. Edstrom, G. El Enany, C. Guery, D. Golodnitsky, M. Lacey, C. Lecoeur, H. Mazor, E. Peled, E. Perre, M. M. Shaijumon, P. Simon and P.-L. Taberna, *J. Mater. Chem.*, 2011, **21**, 9876–9890.

39   Z. Song, T. Ma, R. Tang, Q. Cheng, X. Wang, D. Krishnaraju, R. Panat, C. K. Chan, H. Yu and H. Jiang, *Nat. Commun.*, 2014, **5**, 1–6.

40   Z. Song, X. Wang, C. Lv, Y. An, M. Liang, T. Ma, D. He, Y.-J. Zheng, S.-Q. Huang, H. Yu and H. Jiang, *Sci. Rep.*, 2015, **5**, 10988.

41   V. Zadin, H. Kasemägi, A. Aabloo and D. Brandell, *J. Power Sources*, 2010, **195**, 6218–6224.

42   P. Knauth, *Solid State Ionics*, 2009, **180**, 911–916.

43   J. C. Bachman, S. Muy, A. Grimaud, H. H. Chang, N. Pour, S. F. Lux, O. Paschos, F. Maglia, S. Lupart, P. Lamp, L. Giordano and Y. Shao-Horn, *Chem. Rev.*, 2016, **116**, 140–162.

44   A. Manthiram, X. Yu and S. Wang, *Nat. Rev. Mater.*, 2017, **2**, 16103.

45   E. Rangasamy, Z. Liu, M. Gobet, K. Pilar, G. Sahu, W. Zhou, H. Wu, S. Greenbaum and C. Liang, *J. Am. Chem. Soc.*, 2015, **137**, 1384–1387.

46   H. J. Deiseroth, S. T. Kong, H. Eckert, J. Vannahme, C. Reiner, T. Zaiβ and M. Schlosser, *Angew. Chemie - Int. Ed.*, 2008, **47**, 755–758.

47   V. Thangadurai, S. Narayanan and D. Pinzaru, *Chem. Soc. Rev.*, 2014, **43**, 4714.

48   J. B. Goodenough and P. Singh, *J. Electrochem. Soc.*, 2015, **162**, A2387–A2392.

49   R. P. Buck, *Sensors and Actuators*, 1981, 137–196.

50   J. B. Goodenough, *Annu. Rev. Mater. Res.*, 2003, **33**, 91–128.

51   N. Kamaya, K. Homma, Y. Yamakawa, M. Hirayama, R. Kanno, M. Yonemura, T. Kamiyama, Y. Kato, S. Hama, K. Kawamoto and A. Mitsui, *Nat. Mater.*, 2011, **10**, 682–686.

52   A. M. Cruz, E. B. Ferreira and A. C. M. Rodrigues, *J. Non. Cryst. Solids*, 2009, **355**, 2295–2301.

53   T. Minami, a Hayashi and M. Tatsumisago, *Solid State Ionics*, 2006, **177**, 2715–2720.

54   Z. Xiao, J. Zhou, Y. Wang and M. Luo, *Open Mater. Sci. J.*, 2011, **5**, 45–50.

55   R. Mercier, J. P. Malugani, B. Fahys and G. Robert, *Solid State Ionics*, 1981, **5**, 663–666.

56   H. Tsukasaki, S. Mori, H. Morimoto, A. Hayashi and M. Tatsumisago, *Sci. Rep.*, 2017, **7**, 4142.

57   K. Takada, N. Aotani, K. Iwamoto and S. Kondo, *Solid State Ionics*, 1995, **79**, 284–287.

58   Y. Su, J. Falgenhauer, A. Polity, T. Leichtweiß, A. Kronenberger, J. Obel, S. Zhou, D. Schlettwein, J. Janek and B. K. Meyer, *Solid State Ionics*, 2015, **282**, 63–69.

59   D. W. Murphy, P. A. Christian, F. J. DiSalvo, C. Tsang, A. Dananjay, J. Kim, A. Manthiram, H. I. Schlesinger, H. C. Brown, A. E. Finholt, J. R. Gilbreath, H. R. Hoekstra, E. K. Hyde, J. Amer, X. Yu, J. B. Bates, G. E. Jellison and F. X. Hart, *J. Electrochem. Soc. Sci. This J. Carides, J. V. Waszczak, ibid. Inorg. Chem. Chem. Soc. This J.*, 1997, **144965**, 150–1115.

60   J. B. Bates, N. J. Dudney, G. R. Gruzalski, R. A. Zuhr and A. Choudhury, *J.*

Power Sources, 1993, **44**, 103–110.

61   C. S. Nimisha, K. Y. Rao, G. Venkatesh, G. M. Rao and N. Munichandraiah, *Thin Solid Films*, 2011, **519**, 3401–3406.

62   N. Suzuki, S. Shirai, N. Takahashi, T. Inaba and T. Shiga, *Solid State Ionics*, 2011, **191**, 49–54.

63   F. Mũnoz, *J. Power Sources*, 2012, **198**, 432–433.

64   R. L. Puurunen, *Chem. Vap. Depos.*, 2014, **20**, 332–344.

65   G. N. Parsons, J. W. Elam, S. M. George, S. Haukka, H. Jeon, W. M. M. (Erwin) Kessels, M. Leskelä, P. Poodt, M. Ritala and S. M. Rossnagel, *J. Vac. Sci. Technol. A Vacuum, Surfaces, Film.*, 2013, **31**, 50818.

66   S. M. George, *Chem. Rev.*, 2010, **110**, 111–31.

67   Schematic setup of a binary ALD deposition system, http://encyclopedia.che.engin.umich.edu/Pages/Reactors/CVDReactors/CVDReactors.html, (accessed 20 July 2006).

68   G. S. Higashi and C. G. Fleming, *Appl. Phys. Lett.*, 1989, **55**, 1963–1965.

69   C. Soto, *J. Vac. Sci. Technol. A Vacuum, Surfaces, Film.*, 1991, **9**, 2686.

70   J. E. Crowell, *J. Vac. Sci. Technol. A Vacuum, Surfaces, Film.*, 2003, **21**, S88–S95.

71   R. L. Puurunen, *J. Appl. Phys.*, 2005, **97**, 121301.

72   M. R. Saleem, R. Ali, M. B. Khan, S. Honkanen and J. Turunen, *Front. Mater.*, 2014, **1**, 1–15.

73   X. Meng, X.-Q. Yang and X. Sun, *Adv. Mater.*, 2012, **24**, 3589–615.

74   V. Miikkulainen, M. Leskelä, M. Ritala and R. L. Puurunen, *J. Appl. Phys.*, 2013, **113**, 21301.

75   M. Leskelä and M. Ritala, *Angew. Chemie - Int. Ed.*, 2003, **42**, 5548–5554.

76   R. W. Johnson, A. Hultqvist and S. F. Bent, *Mater. Today*, 2014, **17**, 236–246.

77   S. K. Panda and H. Shin, in *atomic layer deposition of nanostructured materials*, eds. N. Pinna and K. Mato, Wiley-VCH publisher, 2012.

78   C. Marichy, M. Bechelany and N. Pinna, *Adv. Mater.*, 2012, **24**, 1017–32.

79   J. W. Klaus, O. Sneh and S. M. George, *Science*, 1997, **278**, 1934–1936.

80   B. H. Lee, S. Cho, J. K. Hwang, S. H. Kim and M. M. Sung, *Thin Solid Films*, 2010, **518**, 6432–6436.

81   Y.-M. Chang, S.-R. Jian, H.-Y. Lee, C.-M. Lin and J.-Y. Juang, *Nanotechnology*, 2010, **21**, 385705.

82   M. Knez, A. Kadri, C. Wege, U. Gösele, H. Jeske and K. Nielsch, *Nano Lett.*, 2006, **6**, 1172–1177.

83   X. Li, X. Meng, J. Liu, D. Geng, Y. Zhang, M. N. Banis, Y. Li, J. Yang, R. Li, X. Sun, M. Cai and M. W. Verbrugge, *Adv. Funct. Mater.*, 2012, **22**, 1647–1654.

84   M. J. Weber, A. J. M. Mackus, M. A. Verheijen, V. Longo, A. A. Bol and W. M. M. Kessels, *J. Phys. Chem. C*, 2014, **118**, 8702–8711.

85   Z. Li, A. Rahtu and R. G. Gordon, *J. Electrochem. Soc.*, 2006, **153**, C787.

86   M. D. Groner, F. H. Fabreguette, J. W. Elam and S. M. George, *Chem. Mater.*, 2004, **16**, 639–645.

87   J. Hämäläinen, F. Munnik, T. Hatanpää, J. Holopainen, M. Ritala and M. Leskelä, *J. Vac. Sci. Technol. A Vacuum, Surfaces, Film.*, 2012, **30**, 01A106.

88   J. Liu, M. N. Banis, Q. Sun, A. Lushington and R. Li, *Adv. Mater.*, 2014, 6472–6477.

89   J. Badot, S. Ribes, E. Yousfi, V. Vivier, J. P. Pereira-Ramos, N. Baffier and D. Lincot, *Electrochem. Solid-State Lett.*, 2000, **3**, 485–488.

90   M. Q. Snyder, S. A. Trebukhova, B. Ravdel, M. C. Wheeler, J. DiCarlo, C. P. Tripp and W. J. DeSisto, *J. Power Sources*, 2007, **165**, 379–385.

91   J. Liu and X. Sun, *Nanotechnology*, 2015, **26**, 24001.

92   W. Wang, M. Tian, A. Abdulagatov, S. M. George, Y. Lee and R. Yang, *Nano Lett.*, 2012, **12**, 655–660.

93   S. Kim, T. H. Han, J. Kim, H. Gwon, H. Moon, S. Kang, S. O. Kim and K. Kang, *ACS Nano.*, 2009, **3**, 1085–1090.

94   V. Miikkulainen, O. Nilsen, M. Laitinen, T. Sajavaara and H. Fjellvåg, *RSC Adv.*, 2013, **3**, 7537–7542.

95   X. Meng, J. Liu, X. Li, M. N. Banis, J. Yang, R. Li and X. Sun, *RSC Adv.*, 2013, **3**, 7285.

96   C. Ban, M. Xie, X. Sun, J. J. Travis, G. Wang, H. Sun, A. C. Dillon, J. Lian and S. M. George, *Nanotechnology*, 2013, **24**, 424002.

97   M. Knez, K. Nielsch and L. Niinistö, *Adv. Mater.*, 2007, **19**, 3425–3438.

98   S. K. Park, R. Kanjolia, J. Anthis, R. Odedra, N. Boag, L. Wielunski and Y. J. Chabal, *Chem. Mater.*, 2010, **22**, 4867–4878.

99   M. E. Donders, H. C. M. Knoops, M. C. M. van, W. M. M. Kessels and P. H. L. Notten, *J. Electrochem. Soc.*, 2011, **158**, G92.

100   X. Lv, J. Deng, B. Wang, J. Zhong, T. K. Sham, X. Sun and X. Sun, *Chem. Mater.*, 2017, **29**, 3499–3506.

101   A. B. F. Martinson, M. J. Devries, J. A. Libera, S. T. Christensen, J. T. Hupp, M. J. Pellin and J. W. Elam, *J. Phys. Chem. C*, 2011, **115**, 4333–4339.

102 N. P. Dasgupta, X. Meng, J. W. Elam and A. B. F. Martinson, *Acc. Chem. Res.*, 2015, **48**, 341–348.

103 H. Kim, *J. Vac. Sci. Technol. B Microelectron. Nanom. Struct.*, 2003, **21**, 2231.

104 X. Meng, J. Libera and T. Fister, *Chem. ….*

105 X. Meng, X. Wang, D. Geng, C. Ozgit-Akgun, N. Schneider and J. W. Elam, *Mater. Horiz.*, 2017, **4**, 133–154.

106 L. Cathodes, X. Chen, H. Zhu, Y. Chen, Y. Shang, A. Cao, L. Hu and C. E. T. Al, *ACS Nano*, 2012, 7948–7955.

107 K. B. Gandrud, A. Pettersen, O. Nilsen and H. Fjellvåg, *J. Mater. Chem. A*, 2013, **1**, 9054–9059.

108 M. Putkonen, T. Aaltonen, M. Alnes, T. Sajavaara, O. Nilsen and H. Fjellvåg, *J. Mater. Chem.*, 2009, **19**, 8767–8771.

109 M. E. Donders, H. C. M. Knoops, W. M. M. Kessels and P. H. L. Notten, *ECS Trans.*, 2011, **41**, 321–330.

110 V. Miikkulainen, A. Ruud, E. Østreng, O. Nilsen, M. Laitinen, T. Sajavaara and H. Fjellvåg, *J. Phys. Chem. C*, 2014, **118**, 1258–1268.

111 V. Thangadurai and W. Weppner, *Ionics (Kiel).*, 2006, **12**, 81–92.

112 A. S. Cavanagh, Y. Lee, B. Yoon and S. M. George, *ECS Trans.*, 2010, **33**, 223–229.

113 T. Aaltonen, M. Alnes, O. Nilsen, L. Costelle and H. Fjellvåg, *J. Mater. Chem.*, 2010, **20**, 2877–2881.

114 T. Aaltonen, O. Nilsen, A. Magras and H. Fjellv, *Chem. Mater.*, 2011, 4669–4675.

115 J. Hamalainen, J. Holopainen, F. Munnik, T. Hatanpaa, M. Heikkila, M. Ritala and M. Leskela, *J. Electrochem. Soc.*, 2012, **159**, A259–A263.

116   E. Østreng, P. Vajeeston, O. Nilsen and H. Fjellvåg, *RSC Adv.*, 2012, **2**, 6315–6322.

117   E. Østreng, H. H. Sønsteby, T. Sajavaara, O. Nilsen and H. Fjellvåg, *J. Mater. Chem. C*, 2013, **1**, 4283–4290.

118   J. Liu, M. N. Banis, X. Li, A. Lushington, M. Cai, R. Li, T.-K. Sham and X. Sun, *J. Phys. Chem. C*, 2013, **117**, 20260–20267.

119   Y.-C. Perng, J. Cho, D. Membereno, N. Cirigliano, B. Dunn and J. P. Chang, *J. Mater. Chem. A*, 2014, **2**, 9566–9573.

120   A. C. Kozen, A. J. Pearse, C. Lin, M. Noked and G. W. Rublo, *Chem. Mater.*, 2015, **27**, 5324–2331.

121   M. Nisula, Y. Shindo, H. Koga and M. Karppinen, *Chem. Mater.*, 2015, **27**, 6987–6993.

122   S. Shibata, *J. Electrochem. Soc.*, 2016, **163**, 2555–2562.

123   A. J. Pearse, T. E. Schmitt, E. J. Fuller, F. El-Gabaly, C. F. Lin, K. Gerasopoulos, A. C. Kozen, A. A. Talin, G. Rubloff and K. E. Gregorczyk, *Chem. Mater.*, 2017, **29**, 3740–3753.

124   Y. S. Jung, A. S. Cavanagh, L. A. Riley, S. H. Kang, A. C. Dillon, M. D. Groner, S. M. George and S. H. Lee, *Adv. Mater.*, 2010, **22**, 2172–2176.

125   J. Liu, X. Li, M. Cai, R. Li and X. Sun, *Electrochim. Acta*, 2013, **93**, 195–201.

126   E. M. Lotfabad, P. Kalisvaart, A. Kohandehghan, K. Cui, M. Kupsta, B. Farbod and D. Mitlin, *J. Mater. Chem. A*, 2014, **2**, 2504–2516.

127   D. Wang, J. Yang, J. Liu, X. Li, R. Li, M. Cai, T.-K. Sham and X. Sun, *J. Mater. Chem. A*, 2014, **2**, 2306.

128   X. Li, J. Liu, X. Meng, Y. Tang, M. N. Banis, J. Yang, Y. Hu, R. Li, M. Cai and

X. Sun, *J. Power Sources*, 2014, **247**, 57–69.

129   X. Li, J. Liu, M. N. Banis, A. Lushington, R. Li, M. Cai and X. Sun, *Energy Environ. Sci.*, 2014, **7**, 768–778.

130   J. S. Park, X. Meng, J. W. Elam, C. Wolverton, C. Kim and J. Cabana, *Chem. Mater.*, 2014, 3128–3134.

131   X. Xiao, D. Ahn, Z. Liu, J. H. Kim and P. Lu, *Electrochem. commun.*, 2013, **32**, 31–34.

132   M. Bettge, Y. Li, B. Sankaran, N. D. Rago, T. Spila, R. T. Haasch, I. Petrov and D. P. Abraham, *J. Power Sources*, 2013, **233**, 346–357.

133   D. E. Sayers, E. A. Stern and F. W. Lytle, *Phys. Rev. Lett.*, 1971, **27**, 1204–1207.

134   Schematic layout of a modern SR facility, https://commons.wikimedia.org/wiki/File:Schéma_de_principe_du_synchrotron.jpg, (accessed 1 June 2017).

135   G. Bunker, in *Introduction to XAFS*, Cambridge University Press, 1st edn., 2010, pp. 42–51.

136   G. Bunker, in *Introduction to XAFS*, Cambridge University Press, 1st edn., 2010, p. 2.

137   G. Henderson and D. R. Baker, *Synchrotron radiation: earth, environmental and materials sciences applications*, 2002.

138   M. O. Krause and J. H. Oliver, *J. Phys. Chem. Ref. Data*, 1979, 329.

139   G. Bunker, in *Introduction to XAFS*, Cambridge University Press, 1st edn., 2010, p. 13.

Chapter 2

2   Experimental Apparatus and Characterization Techniques

2.1   Experimental Methods

2.1.1   Apparatus
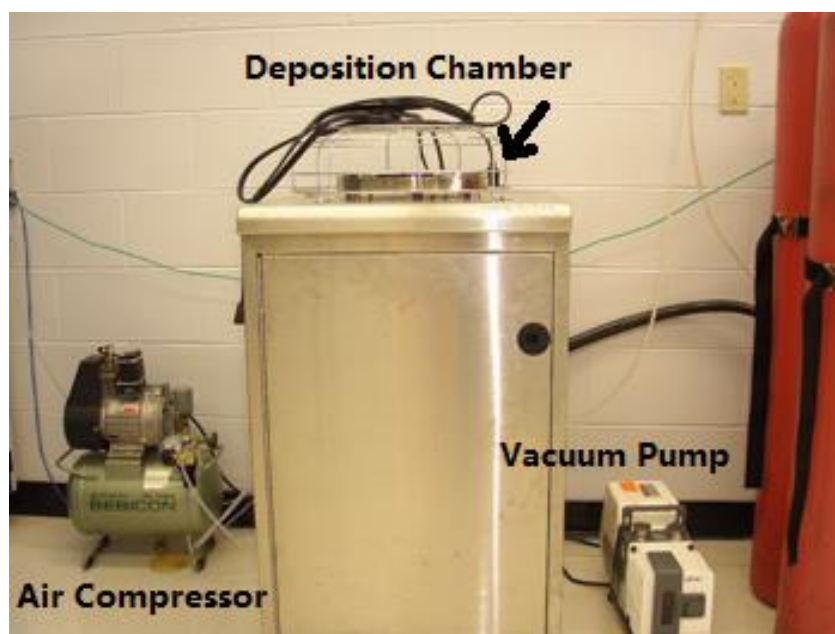
Figure 2.1 A Picture of Savannah 100 ALD system (Cambridge Nanotech, USA)

Synthesis of thin films using atomic layer deposition (ALD) techniques was performed in Savannah 100 ALD system (Ultratech/Cambridge Nanotech., USA). A picture of Savannah 100 ALD system used in Dr. Sun's laboratory is shown in Figure 2.1. A screenshot of the software that controls the ALD process is presented in Figure 2.2. This Cambridge ALD system is composed of a reaction chamber, a manifold, precursor bubblers, two traps, a vacuum pump, an electronic-box for controlling the system, and a computer. The deposition temperature in the reaction chamber could vary from 80 to 350

ºC. The precursor bubblers could be heated up to 200 ºC to provide sufficient vapors for ALD processes by using heating jackets. The system operating pressure was about 0.9-1 Torr sustained by the vacuum pump. Nitrogen gas (99.999% in purity) was used as a carrying gas at a flowing rate of 20 sccm.

All parameters for ALD processes were controlled by LABVIEW program installed in the desktop, and an example of the program in an exposure mode is presented in Figure 2.2. The left upper panel illustrates the sequences of an ALD process. The lower part shows the real-time monitoring of the system pressure. All the temperatures (the heating jackets and the deposition system) were controlled on the right panel.
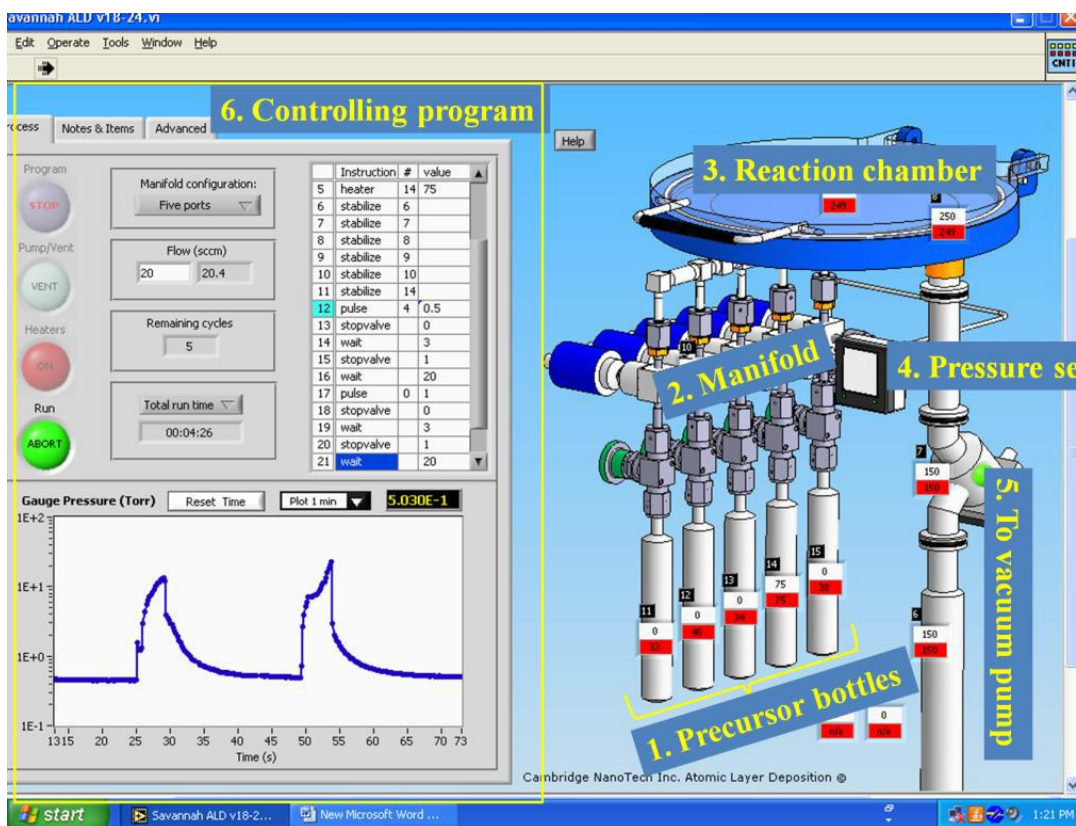
Figure 2.2 A screen snapshot showing the monitoring software of Savannah 100 ALD system and its setup

2.1.2   Synthesis Process

2.1.2.1   Substrate Preparation

Before the ALD process, Silicon (100) substrates were cleaned using a stepwise acetone, ethanol, and water rinse procedure, and then blown dry by N_2. Commercial carbon nanotubes (CNTs) powders were refluxed in nitric acid (HNO_3, 70%) for 3 h at 120 ^{o}C to remove the residual catalyst from the growth of CNTs and functionalize the surface of CNT. The treated CNTs were dispersed in ethanol and washed in ultrasonic bath. Then the solution was casted on Al foil and loaded in the ALD chamber for deposition.

2.1.2.2   ALD Process of Lithium Phosphate Thin Films

Lithium tert-butoxide [LiO^tBu, $(CH_3)_3COLi$] was used as lithium source and trimethylphosphate [TMPO, $(MeO)_3PO$] as phosphate source. The source temperature for LiO^tBu and TMPO was 180 and 75 ^{o}C, respectively. The system pipelines were maintained at 190 ^{o}C in order to prevent the condensation of the precursors. The lithium phosphates were deposited at four different temperatures, i.e. 250, 275, 300, and 325 $^{\circ}C$. LiO^tBu and TMPO were pulsed into the chamber alternatively with the same pulse time duration separated by a 15 s nitrogen purge. A pulse time of 1, 2, and 4 s were used. Morphology, structure, and composition characterizations were conducted on lithium phosphate films deposited on Si(100) substrates, while electrochemical impedance characterization was carried out on lithium phosphate film on Au-coated glass.

2.1.2.3   ALD Process of TiO2/Lithium Phosphate Nanocomposite

TiO_2/lithium phosphate composite thin films (TLPO) was deposited using TTIP ($Ti(OCH(CH_3)_2)_4$) and water for TiO_2 subcycle and LiO^tBu [$(CH_3)_3COLi$] and TMPO [$(MeO)_3PO$] for lithium phosphate (LPO) subcycle. Source temperatures for TTIP, LiO^tBu, and TMPO were 80, 180, and 75 ^{o}C, respectively, while H_2O was kept at room temperature (RT). The deposition of the nanocomposite was carried out at 250 ^{o}C. The chosen temperature was in the overlapped temperature range of the ALD windows of TiO_2 and LPO to achieve ALD growth and prevent precursors from decomposing.

Additionally, the manifold was heated to 180 ºC to avoid condensation of precursors. Nitrogen was used as the carrier gas. One ALD cycle consisted of two subcycles of TiO_2 and LPO. The overall sequence was the following: $2 \times$ [TTIP, (x s pulse/ 10 s purge) - H_2O (0.5 s pulse/15 s purge)] + [LiO^tBu, (2 s pulse/15 s purge) - TMPO (2 s pulse/ 15 s purge)]. The recipe of LPO subcycle was directly taken from our previous work. Different pulse times of TTIP (1, 2, and 4 s) were used to verify the ALD process. Si (100) wafers and CNTs powders were used as substrates for the deposition of TLPO.

2.1.2.4   ALD Process of Lithium Silicate Thin Films

Lithium silicate thin films were deposited using nitrogen as the carrier and purging gas. The ALD subcycles of Li_2O and SiO_2 were combined. The Li_2O subcycle consisted of lithium tert-butoxide [LiO^tBu, $(CH_3)_3COLi$] as lithium source and H_2O as oxidant while tetraethylorthosilane (TEOS) and water were precursors for the SiO_2 ALD subcycle. LiO^tBu and TEOS were sublimed at a source temperature of 170 and 65 °C respectively. The system pipeline was maintained at 190 °C to prevent the condensation of the precursors. Four different deposition temperatures were carried out, i.e. 225, 250, 275, and 300 °C, while the pulse time of LiO^tBu, TEOS, and water remained at 1, 2, and 1 s respectively. One subcycle of Li_2O and one subcycle of SiO_2 composed of one full ALD cycle. 10 s of nitrogen purge was used subsequently after each precursor.

2.1.2.5   ALD Process of Lithium Niobium Oxide Thin Films

Lithium niobium oxide thin films were deposited in the Savannah 100 ALD system (Cambridge Nanotech Inc.). For deposition of ternary compounds, the lithium subcycle and niobium subcycle were combined, using lithium tert-butoxide [LiO^tBu, $(CH_3)_3COLi$] and niobium ethoxide [$Nb(OEt)_5$, Et= $–CH_2CH_3$] for Li and Nb sources, respectively. Deionized water was used as the oxidant for both subcycles and nitrogen as the carrier and purging gas. LiO^tBu and $Nb(OEt)_5$ were sublimed at 170 and 155 °C, respectively. The system pipeline was held at 190 °C to avoid the condensation of the precursors. All the depositions were performed at a temperature of 235 °C. All the precursors were pulsed in for 1 s, followed by 15 s of nitrogen purge.

2.2   Characterization Techniques

2.2.1   Physical Characterizations

To study the physical and chemical properties of the synthesized materials, a variety of analytical techniques were applied, including SEM, EDS, (HR)TEM, XRD, XPS, and XAS. This section briefly reviews these techniques.

The morphology of the materials was observed using high-resolution scanning electron microscope (SEM, Hitachi S-4800) equipped with energy dispersive X-ray spectroscopy (EDS), as shown in Figure 2.3. The SEM was operated at 5 kV in order to observe morphologies of samples while EDS was operated at 20 kV to give the elemental compositions. The magnification of Hitachi S-4800 is in a range of $\times 20$ to $\times 800,000$.
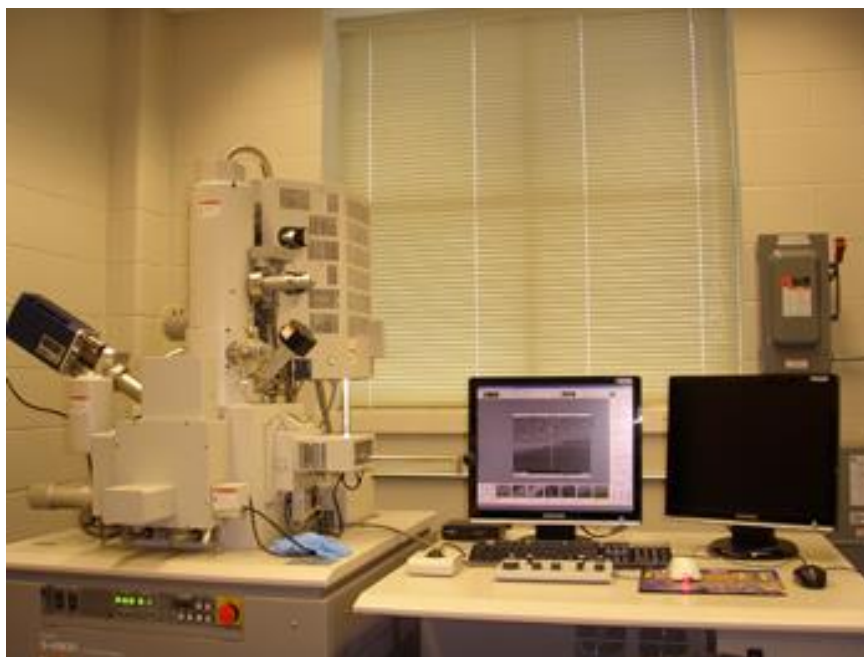
Figure 2.3 A picture of field emission scanning electron microscope (Hitachi S-4800)

Transmission electron microscope (TEM) was used to obtain detailed structural information of the synthesized samples. A Hitachi H-7000 transmission electron microscope has a resolution of 0.4 nm at 125 kV, a picture of which is shown in Figure 2.4.

Figure 2.4 Instrument of a Hitachi H-7000 transmission electron microscope

A JEOL 2010F high-resolution TEM (Figure 2.5) located at the Canadian Centre for Electron Microscopy (CCEM) at McMaster University was used to observe the fine structures of the samples. The instrument was operated at 200 kV.

Figure 2.5 A picture of JEOL 2010F high-resolution TEM

X-ray diffraction (XRD) was used to provide the phase information of the prepared materials. The XRD pattern of the samples were collected on a Bruker D8 Advance Diffractometer using Cu Kα radiation at 40 kV and 40 mA. This system is coupled with a low-angle kit to analyze thin films samples, which could be of a thickness smaller than one micrometer. Figure 2.6 presents the photo of the XRD instrument in our laboratory.

Figure 2.6 A Bruker D8 Advance Diffractometer XRD

X-ray photoelectron spectroscopy (XPS) was used to analyze the chemical composition by detecting the amount of the escaped electrons from the surface of the samples at a certain excitation energy. Kratos AXIS Ultra Spectrometer at Surface Science Western uses a monochromated Al Ka (1486.6 eV) source while the synchrotron XPS at Canadian Light Source (CLS) on Variable Line Spacing Plane Grating Monochromator (VLS PGM) has a tunable excitation energy from 130 to 230 eV which is suitable for detecting light elements like Li.

Figure 2.7 A SDT Q600 Thermogravimetric/Differential Scanning Calorimetry Analyzer

The thermal properties of the materials were determined by a Thermo Instruments SDT Q600 Thermogravimetric (TGA)/Differential Scanning Calorimetry (DSC) analyzer as shown in Figure 2.7.
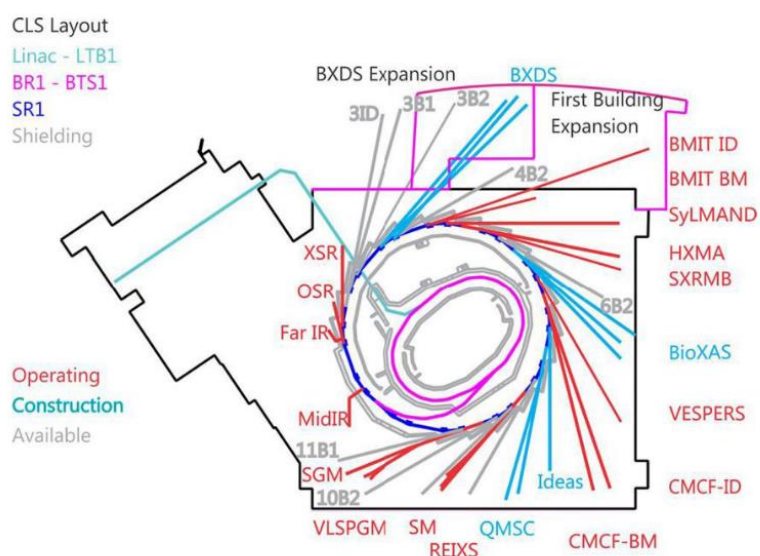
Figure 2.8 The schematic layout of the CLS beamlines (courtesy of Canadian Light Source Inc.) [1]

A most essential characterization technique employed in the thesis is X-ray absorption spectroscopy (XAS). All the XAS measurements were conducted in Canadian Light Source (CLS) in Canada's national Synchrotron light source facility located in Saskatoon, Saskatchewan, Canada. CLS is a third generation synchrotron source and it facilitates a 250 MeV electron linear accelerator (LINAC), a booster ring to increase the electron beam energy to 2.9 GeV, and a main storage ring which operates at a current of 500 mA. The radio frequency (RF) cavity operates at 500 MHz to restore the electrons energy loss. Figure 2.8 shows a schematic layout and a picture of the CLS experimental hall. [1] Currently there are 14 operating beamlines, the photon energy of which ranges from Far infrared (IR) to hard X-ray. In this thesis, two beamlines were used for XAS measurements, including Spherical Grating Monochromator (SGM) beamline and Soft X-ray Microcharacterization Beamline (SXRMB).
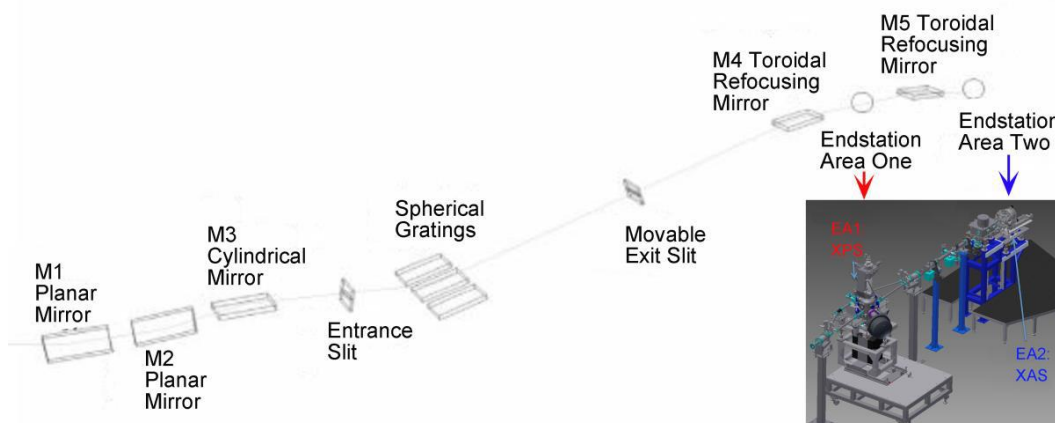
Figure 2.9 The layout of SGM beamline at CLS. [2,3]

The SGM beamline (11ID-1) at CLS covers the energy range from 250 – 2000 eV using a undulator source, the layout of which is shown in Figure 2.9. [2,3] Three diffraction gratings, the low (LEG), medium (MEG), and high energy gratings (HEG), are designed to tune the energy for different ranges, which are 250 – 700 eV, 450 – 1250 eV, and 740 – 2000 eV, respectively. The spot size of the beamline is 1000 μm × 100 μm (horizontal × vertical), with an energy resolution ($E/\Delta E$) of ~5000 (below 1500 eV). The beamline flux (photons/s at 100 mA) is 10^{12} at 250 eV and reaches 10^{11} up to 1900 eV. As presented in Figure 2.9, two endstations (EA_1 and EA_2) are built in the beamline, of which EA_1 is used

for X-ray photoemission while EA_2 for XAS studies. All the XAS measurements at SGM beamline in this thesis were performed in endstation EA_2.
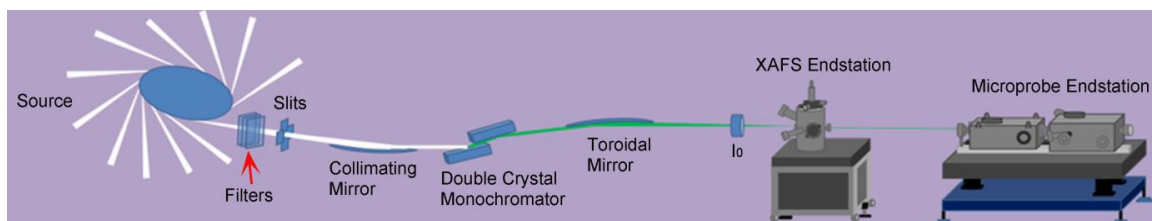
Figure 2.10 The layout of SXRMB beamline at CLS [4]

The SXRMB beamline (06B1-1) at CLS is a bending magnet based beamline, providing a medium energy range of 1.7 – 10 keV. The two endstations illustrated in Figure 2.10 are X-ray absorption fine structure (XAFS) endstation and microprobe endstation.[4] The common beamline operation conditions include an energy resolution ($E/\Delta E$) of 3000 using InSb (111) crystal (energy range: 4 – 10 keV) and 10000 using Si (111) crystal (energy range: 1.7 – 4 keV). All the XAS studies in the thesis were conducted at the XAFS endstation, which has a beam spot size (horizontal $\times$ vertical) of ~1 mm $\times$ 4 mm and a flux (photons/s at 100 mA) over 10^{11}.

2.2.2 Electrochemical Characterizations

Figure 2.11 A picture of the glovebox used for battery assembly

The battery cycling performance and rate capability testing are presented in Chapter 4. The anode materials synthesized were mixed with acetylene black and polyvinylidene fluoride (PVDF) using a ratio of 8:1:1 with N-methyl-2-pyrrolidone (NMP) as the solvent. The slurry was casted on Al foil and dried in vacuum oven kept at 80 ºC overnight. The electrodes were prepared by cutting the dried sheet into a round shape with a diameter of 13 mm. The electrolyte was a mix of $LiPF_6$ dissolved in ethylene carbonate (EC): diethyl carbonate (DEC): ethyl methyl carbonate (EMC) of 1:1:1 volume ratio and the separator used was polypropylene Celgard 2400. Li metal was used as the counter electrode. All the components were assembly into a CR2032 coin cell in a highly pure argon-filled glovebox (Figure 2.11) with strictly controlled oxygen and water level below 1 ppm. The assembled cells were then taken out and cycled in an Arbin BT2000 battery test station (Figure 2.12).

Figure 2.12 An Arbin BT2000 battery test station

Cyclic voltammetry (CV) presented in Chapter 4 and electrochemical impedance spectroscopy (EIS) for all the later chapters were acquired on a multichannel VMP3

Potentiostat/Galvanostat/EIS system. The CV tests are conducted at a scan rate of 0.1 mVs^{-1} over specific voltage ranges. And the EIS curves were collected within a certain temperature range with the tested samples placed in an oven.
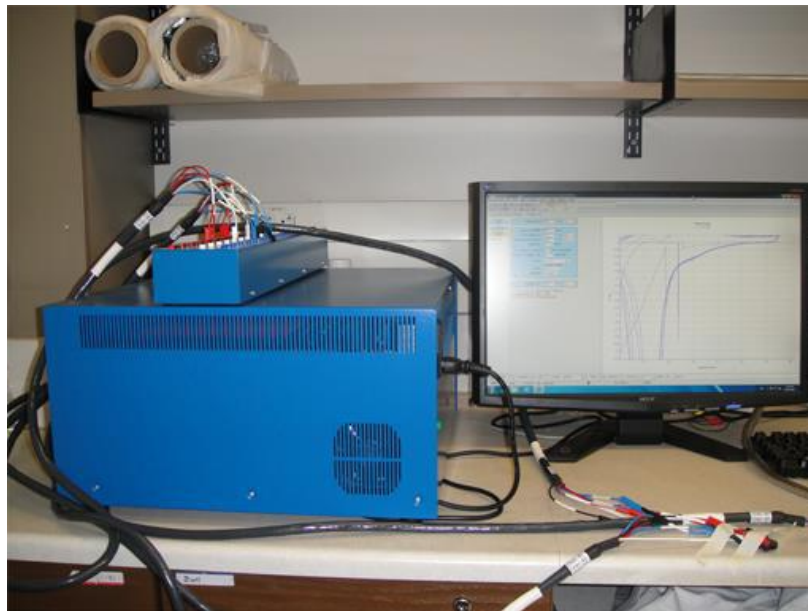
Figure 2.13 A picture of the multichannel potentiostat VMP3

References

1. Adapted from: http://www.lightsource.ca/beamlines.html. in Jun. 2017

2. Adapted from: http://sgm.lightsource.ca/. in Jun. 2017

3. T. Regier, J. Paulsen, G. Wright, I. Coulthard, K. Tan, T. K. Sham, and R. I. R. Blyth, *AIP Conf. Proc.* 2007, **879**, 473

4. Adapted from: http://sxrmb.lightsource.ca/about/. in Jun. 2017

Chapter 3

3 Atomic Layer Deposition of Lithium Phosphates as Solid-State Electrolytes for All-Solid-State Microbatteries*

Atomic layer deposition (ALD) has been shown as a powerful technique to build 3-dimensional (3D) all-solid-state microbattery, because of its unique advantages in fabricating uniform and pinhole-free thin films in 3D structures. The development of solid-state electrolyte by ALD is a crucial step to achieve the fabrication of 3D all-solid-state microbattery by ALD. In this work, lithium phosphate solid-state electrolytes were grown by ALD at four different temperatures (250, 275, 300, and 325 $^{\circ}$C) using two precursors (lithium tert-butoxide and trimethylphosphate). A linear dependence of film thickness on ALD cycle number was observed and uniform growth was achieved at all four temperatures. The growth rate was 0.57, 0.66, 0.69, and 0.72 Å/cycle at deposition temperatures of 250, 275, 300, and 325 $^{\circ}$C, respectively. Furthermore, X-ray photoelectron spectroscopy confirmed the compositions and chemical structures of lithium phosphates deposited by ALD. Moreover, the lithium phosphate thin films deposited at 300 $^{\circ}$C presented the best ionic conductivity of 1.73×10^{-8} S/cm at 323 K with ~0.51 eV activation energy based on the electrochemical impedance spectroscopy. The ionic conductivity was calculated to be 3.3×10^{-8} S/cm at 26 $^{\circ}$C (299 K).

---

*Note: This work has been published.

3.1   Introduction

Microelectronic devices play a continuously and increasingly indispensible role in our daily life, such as medical implants, micro sensors, and microelectromechanical systems (MEMS). The continually downscaling of the products requires the on-board power supply device to be of smaller dimensions, higher energy and power density [1]. Microbattery is the preferable energy devices for such applications. In particular, the all-solid state lithium-ion microbattery has been of continuous interest as an efficient energy storage system [2,3]. Comparing to liquid-electrolyte-based microbatteries, all-solid-state microbatteries offer several advantages. First, more flexibility is provided in battery design and management. Secondly, miniaturized size extends the applications on microelectronic devices. Thirdly and more importantly, the inherent problems coming with liquid electrolytes including the release of heat during cycling, inflammability of the electrolyte, and the potential leakage could all lead to severe safety hazards. Some significant issues plaguing the development of batteries such as the degradation effect and the safety problem can be expected to be well resolved through all-solid-state microbatteries [4,5].

During the past decade, great effort has been devoted to developing two-dimensional (2D) thin film all-solid-state micro lithium ion batteries (micro-LIBs) [5–8]. A typical thin film all-solid-state LIB, which has similar structure as commercial LIBs, is composed of thin film positive electrode (e.g. $LiCoO_2$ [4,5]), solid-state electrolyte (e.g. nitrogen-doped lithium phosphate (LIPON) [7,8]) and negative electrode (e.g. metallic lithium [5] and TiO_2 [6]). Among these components, the thin film solid-state electrolytes play the most critical roles. Different techniques have been developed to deposit thin film solid-state electrolytes, including radio frequency (RF) magnetron sputtering [8], chemical vapor deposition (CVD) [7], pulsed layer deposition (PLD) [9], and atomic layer deposition (ALD) [10].

However, the miniaturization of power sources and demands on high power and energy density expose the limitations of such designs [11]. The three-dimension (3D) microbatteries are desirable to achieve higher performance. A most significant advantage

of 3D microbatteries over 2D thin film batteries is that it has much higher specific surface area which provides higher energy density while it keeps short diffusion path, giving better power density [12,13]. The challenges in fabricating 3D microbatteries mainly lie in the narrow battery assemblies, implying rather complicated designs in small footprint architecture [14]. Conventional techniques for depositing thin films such as RF sputtering or CVD are not suitable in such delicate 3D structures below micro scale. Problems include non-uniform deposition, failure of interface because of cracking or roughness of the surface, giving rise to short circuit and failure of batteries [15].

ALD stands out from all the other approaches in depositing conformal and pin-hole free thin films on 3D high-aspect-ratio substrates [16]. ALD is a vapor-phase deposition process, and the precursors are pulsed into the reaction chamber in sequence and the growth of the thin films are dictated by the self-terminating gas-solid surface reactions [16]. With film growth taking place in a cyclic manner, the saturation reaction conditions gives a self-limiting growth mechanism, which offers exquisite thickness control at atomic level and adjustable stoichiometric composition. Given a large area for deposition, the process is easy to scale up with high conformity and reproducibility [17]. Substrates of high aspect ratio can also be applied because of the excellent step coverage and the growth of the film, which is independent of the geometry due to the nature of the gas phase precursors in ALD processes [18–21]. The aforementioned advantages make ALD the unique method to fabricate thin film electrolyte for 3D microbatteries. Cheah et al. [22] reported that a nanostructured 3D TiO_2 electrode prepared by ALD exhibited ten times higher areal capacity than the 2D counterpart. Another group used biological scaffolds of high aspect ratio as substrates and synthesized Ni/TiO_2 nanocomposite anodes via ALD. The Ni/TiO_2 electrodes presented excellent capacity and rate capability, and extremely low capacity fading [23]. More recently, ALD (depositing V_2O_5 as cathodes) combined with micromachining was applied in 3D microbatteries. The hierarchical 3D micro- and nanostructured electrodes exhibited 3-fold increase in energy density compared with nanosturctures alone due to the enlarged surface area [24].

Even though no full 3D all-solid-state micro-LIBs has been manufactured by ALD yet, the application of ALD in fabricating key battery components (the anode, cathode, and

solid-state electrolyte) has been intensively investigated. Recently, a few cases of anode (such as SnO_2, TiO_2) [22,25–27] and cathode (like V_2O_5, $LiCoO_2$) [28,29] materials of LIBs has been successfully developed. Another crucial component in all-solid-state LIBs is solid-state electrolyte. Available materials containing lithium have been developed. Recently the successful synthesis of Li_2O was reported by Aaltonen et. al [30], which promoted the rapid progress in the study of solid-state electrolytes derived by ALD. Aaltonen et al. [31] grew lithium lanthanum titanate (LLT) from lithium turt-butoxide, $TiCl_4$, $La(thd)_3$ (thd=2,2,6,6-tetramethyl-3,5-heptanedione)), ozone, and water. Later on, Li_2O-Al_2O_3 ($LiAlO_x$) was prepared by combining ALD subcycles of Li_2O and Al_2O_3 using lithium tert-butoxide, TMA and water as precursors [32,33]. This material was lately used as a coating material for increased interracial stability in high voltage LIBs [34]. Other lithium containing compounds include lithium silicate [35], lithium niobate [36], lithium tantalate [10], lithium nitride [37], and $Li_xAl_ySi_zO$ [38].

In order to be employed in all-solid-state microbatteries, ionic conductivity is an important parameter for solid-state electrolytes, but was seldom reported in previous studies. The lithium-ion conductivity could reach 1×10^{-7} S/cm at 300 $^{\circ}$C for Li_2O-Al_2O_3 after being annealed at 700 $^{\circ}$C for 5 h [33]. However, the drastic post heat treatment could cause severe damage to electrode materials or problems like cracking could occur when the solid-state electrolyte is used in LIBs, which is fatal to the battery system. Therefore, it is an approachable strategy to explore materials with high ionic conductivity without post-annealing treatment using ALD. Moreover, an easy ALD process is more favorable for the real application in 3D microbatteries.

Apart from the above materials, Li_3PO_4 has proved to be a promising candidate as solid-state electrolyte due to its good ionic conductivity of 7×10^{-8} S/cm at 25 $^{\circ}$C in amorphous thin film structures [39]. Furthermore, it is clearly evident that amorphous Li_3PO_4 exhibits a higher ionic conductivity (6.6×10^{-8} S/cm at 25 $^{\circ}$C) than its crystalline counterpart (4.2×10^{-18} S/cm at 25 $^{\circ}$C) [39,40]. This implies that the film prepared by the relatively mild ALD process has a lower risk of fracturing and can be readily employed in LIB either as solid-state electrolyte. Hämäläinen et al. established a thorough ALD process for synthesizing Li_3PO_4, which contains two precursors (lithium tert-butoxide and trimethylphosphate)

avoiding the complication of ALD sub cycles when applied in 3D microbatteries. However, no electrochemical results were shown in this work [41]. Herein, we carry out the ALD process of Li_3PO_4, and optimize the ALD process in terms of the electrochemical performance of the Li_3PO_4 thin film electrolytes. The lithium phosphate thin films produced by ALD are featured with not only extremely conformal and uniform deposition with well-tuned composition, but also moderate lithium ion conductivity in the order of 10^{-7} S/cm at 50 ºC, without any additional post treatment process. In summary, lithium phosphate deposited by ALD is an ideal candidate as thin film electrolyte in 3D all-solid-state micro-LIBs.

3.2 Experimental

All the lithium phosphate thin films were grown on silicon (100) or glass substrates in a Savannah 100 ALD system (Cambridge Nanotech Inc.). Lithium tert-butoxide [LiO^{t}Bu, $(CH_3)_3COLi$] was used as lithium source and trimethylphosphate [TMPO, $(MeO)_3PO$] as phosphate source. The source temperature for LiO^{t}Bu and TMPO was 180 and 75 ºC, respectively. The system pipelines were maintained at 190 ºC in order to prevent the condensation of the precursors. The lithium phosphates were deposited at four different temperatures, i.e. 250, 275, 300, and 325 ℃. LiO^{t}Bu and TMPO were pulsed into the chamber alternatively with the same pulse time duration separated by a 15 s nitrogen purge. Different pulse times of 1, 2, and 4 s were used. Morphology, structure, and composition characterizations were conducted on lithium phosphate films deposited on the Si(100) substrates, while electrochemical impedance characterization was carried out on lithium phosphate film on Au-coated glass.

Film thicknesses were measured from the fresh-cut cross-sections using field-emission scanning electron microscopy (FESEM, Hitachi-4800). Five different spots of each film were randomly selected and the average thickness was taken to obtain the final thickness. The compositions of the lithium phosphates were determined by X-ray photoelectron spectroscopy (XPS) using a Kratos Axis Ultra Al (alpha) spectrometer. The depth distribution of the elements in the films was studied by secondary ion mass spectrometry (SIMS) using a Cameca IMS-6f ion microprobe. An area of 250×250 mm2 was

sputtered by a negative oxygen beam. The depth scales were obtained by measuring the SIMS craters with a Tencor P-10 surface profilometer.

Electrochemical impedance spectra (EIS) of the lithium phosphate thin film on glass were evaluated on a CHI electrochemistry workstation in a frequency range of 200 kHz-100 Hz. A sandwich structure of Au-thin film electrolyte-Au on glass substrate was designed for the EIS measurements. Au layers were deposited by sputtering. The sputtering processes were carried out in a Polaron sputtering system under 2 kV for 9 min with a current of 25 mA, to achieve a thickness of 50 ± 5 nm of Au. The thickness of lithium phosphate thin film was 130 ± 10 nm. The geometric areas of the thin film electrolytes between the two Au electrodes were 4 mm$\times$ 4 mm. Temperature was elevated from 323 K to 403 K (10 K step) and the samples were maintained at each temperature for 20 min for stabilization before acquiring the spectra.

3.3   Results and Discussion

Lithium phosphate thin films grown using 2000 ALD cycles at 250 ℃ (LPO250), 275 ℃ (LPO275), 300 ℃ (LPO300), and 325 ℃ (LPO325) have been examined by SEM, and the results are displayed in Figure 3.1. From the cross-section views in Figure 3.1, it can be seen that the lithium phosphate film is uniformly deposited on the Si substrate at all the deposition temperatures, giving an ultra flat surface on the substrate. The thicknesses of LPO250, LPO275, LPO300, and LPO325 are measured to be 112, 133, 137, and 154 nm, respectively. Figure 3.2 displays the film thickness of lithium phosphate film as a function of ALD cycle number at each deposition temperature. It is obvious that the film thickness of lithium phosphate is linearly proportional to the number of ALD cycles, indicating the self-limiting behavior of the ALD process. After fitting the data in Figure 3.2, the growth per cycle of lithium phosphate film is calculated to be 0.57, 0.66, 0.69, and 0.74 Å/cycle at the deposition temperatures of 250, 275, 300, and 325 ℃, respectively. The deposition temperature dependence of the growth rates was plotted in Figure 3.2(b), from which one can see that the film is deposited faster at elevated temperatures, in accordance with the literatures [41,42]. The reason could be that higher temperature promotes the ligands exchange process in the ALD process. The reactivity

between LiO^{t}Bu and TMPO is higher at elevated temperature. More reactions lead to higher growth rate. The growth rates of lithium phosphate in this work are lower than the reported ones (0.7 – 1 Å/cycle) in the similar temperature range (225 – 300 °C). In our work, LPO250 and LPO300 have a growth rate of 0.57 and 0.74 Å/cycle, respectively, while it was reported 0.7 and 1 Å/cycle at the same temperatures [41]. It can be explained by the less pulse time (2 s) of both of the precursors (LiO^{t}Bu and TMPO) applied in our work. Shorter (1 s) and longer pulse time (4 s) were used at 300 °C and the growth rate was shown in Figure 3.2(b). With 4 s of pulse time, the growth rate reaches 0.94 Å/cycle. In addition, the growth rate with 2 s of pulse time is also in accordance with the reported one [41]. The growth rate increased with the pulse time of LiO^{t}Bu. No full saturation was observed with 4 s of pulse time. The reason is that this system is not an ideal ALD process. No normal oxidizer like H_2O, O_2, and O_3 was used. More ligands exchange occurs when exposed to the reactants for longer time, providing larger growth rate. The decomposition of LiO^{t}Bu is reported to take place at 350 °C [41]. When the temperature reached 325 °C, a slight color change observed in the deposition chamber indicates that there might be a degree of decomposition of LiO^{t}Bu. Therefore, LPO325 was not further tested in the following electrochemical measurements.
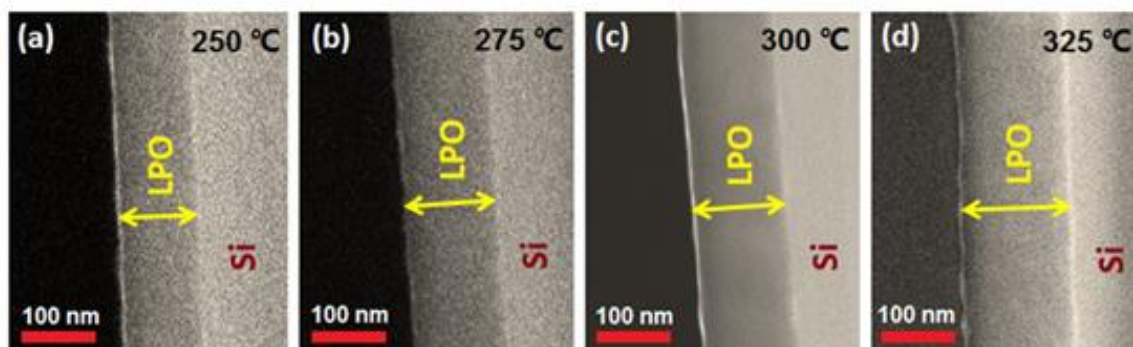
Figure 3.1 Cross-section SEM pictures of the ALD deposited lithium phosphate thin films on Si(100) substrates at (a) 250 °C (LPO250), (b) 275 °C (LPO275), (c) 300 °C (LPO300), and (d) 325 °C (LPO325), after 2000 ALD cycles
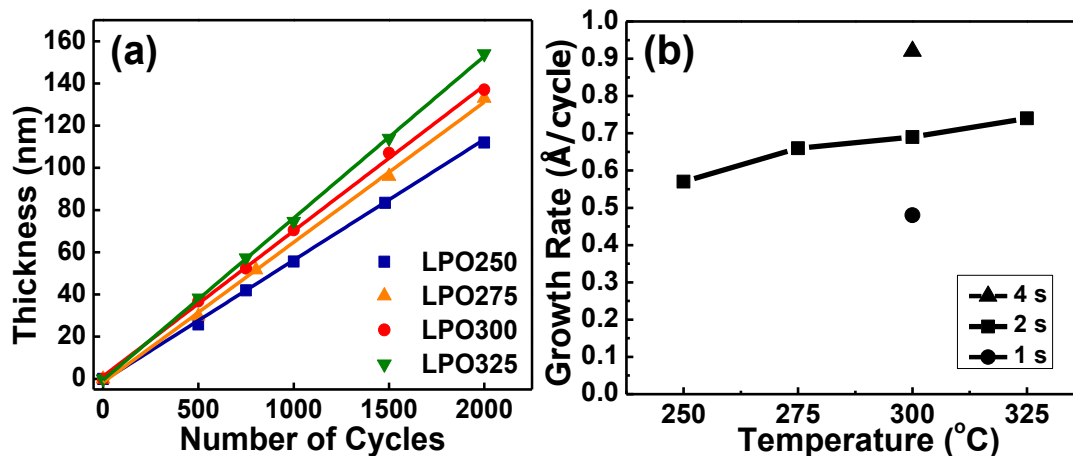
Figure 3.2 (a) Thickness of the lithium phosphate thin films as a function of the number of ALD cycles; (b) the thin film growth rates as a function of deposition temperature

XPS measurements were carried out in order to determine the chemical composition of the ALD deposited lithium phosphate thin films, and the results are presented in Figure 3.3. The XPS survey in Figure 3.3(a) shows that lithium phosphate thin films contain Li, P, C, and O elements (the atomic percentages listed in table SI-1). For LPO250 and LPO300, the atomic ratio of Li to P elements is calculated to be 3.33 and 2.80 respectively, which are close to that of standard Li_3PO_4. In the slow scan of Li 1s shown in Figure 3.3(b), the peak position of Li 1s locates at ~55.26 eV, which corresponds well to that of standard Li_3PO_4 [43]. There is no observable shift in Li 1s for $Li_{2.80}PO_z$ and $Li_{3.33}PO_z$ (55.26 eV for $Li_{2.80}PO_z$ and 55.52 eV for $Li_{3.33}PO_z$), indicating the single chemical environment of Li (Li–O) in both of the lithium phosphate thin films. The P 2p spectra can be fitted into a set of doublet P $2p_{1/2}$ and P $2p_{3/2}$, which are centered at about 134.04 and 133.20 eV, respectively. No evident shift is observed between the spectra of LPO250 and LPO300. Assigning the P 2p in phosphate in reference to the standard spectra of Li_3PO_4 (2p peak at 133.2 eV) [43], the result reveals that P in the lithium phosphate films shares a similar chemical state as that in standard Li_3PO_4. Furthermore, deconvolution of O 1s peak in Figure 3.3(d) consists of two components located at 532.69 eV and 531.25 eV for both LPO250 and LPO300. The former belongs to the oxygen in organics at higher binding energy (532.69 eV), and the latter corresponds to

the oxygen in phosphates, which is consistent with the conclusion from the spectra of P 2p and agrees with the standard O peaks of Li_3PO_4 (at 531.1 eV) [43]. Also, carbon is detected in all thin films prepared (Figure 3.3(a)). The carbon detected on the surface exists in forms of O–C=O (288.80 eV), C=O (287.80 eV), C–OH, C–O–C (286.30 eV), and C–C, C–H (284.80 eV) in both C 1s spectra of LPO250 and LPO300. Besides, a trace of carbonate (290.04 eV) was found in LPO250 (see Figure 3.SI-1). The organic carbon might be resulted from the residual ligands from ALD precursors, which could not be efficiently removed by purging and is commonly observed in XPS. The source of the carbonate is the reaction between Li_2O in the lithium-containing films and CO_2 when the thin films are exposed to ambient air [33].The reason that carbonate is only detectable in LPO250 rather than LPO300 can be due to the higher content of lithium on the surface (see Figure 3.SI-3), which reacts with ambient carbon dioxide more readily. Therefore, it can be concluded that lithium phosphate prepared by ALD has similar chemical structure as standard Li_3PO_4.
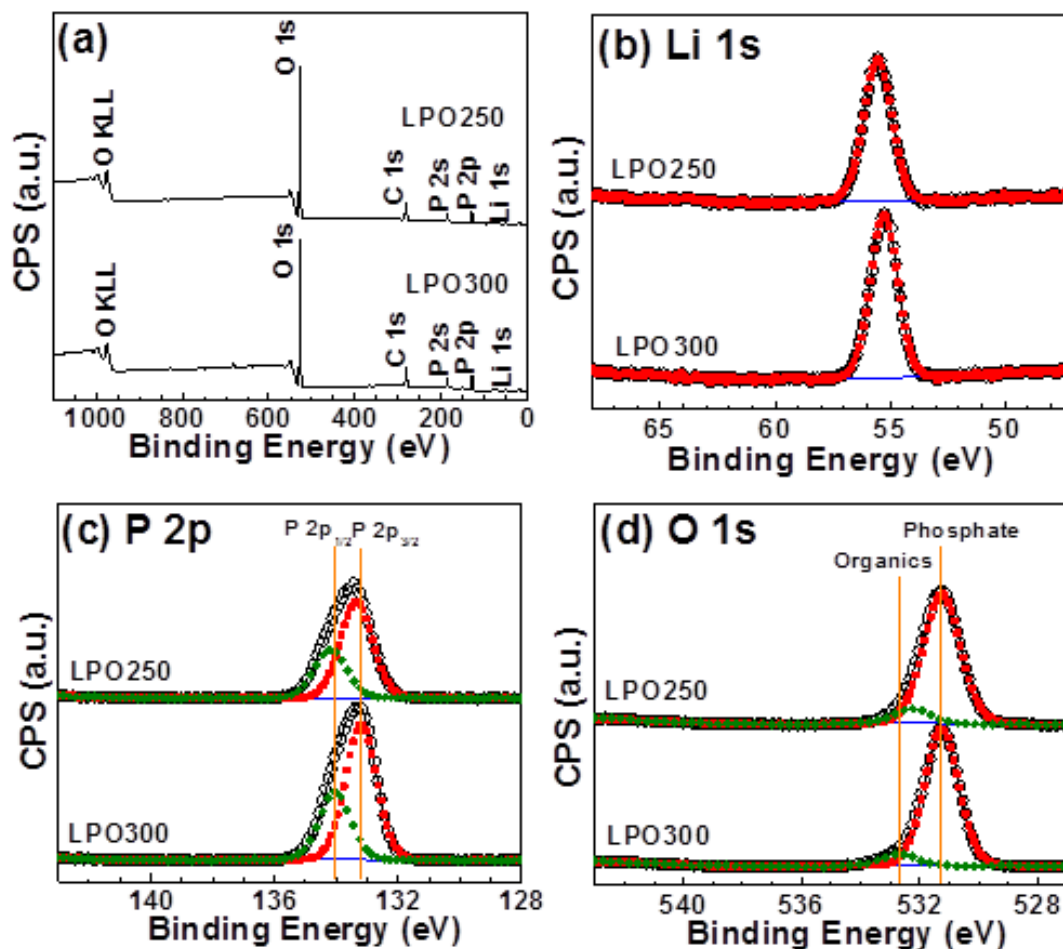
Figure 3.3 (a) XPS survey of the lithium phosphate thin films LPO250 and LPO 300 deposited on Si (100); deconvolution of (b) Li 1s (c) P 2p and (d) O 1s spectra

Lithium-ion conductivities of the lithium phosphate thin films LPO250, LPO275, and LPO300 were measured using electrochemical impedance spectroscopy. Figure 3.4 displays the Cole-Cole plots obtained at temperatures between 323 and 403 K and the Arrhenius plot of the ionic conductivities of the deposited thin films.
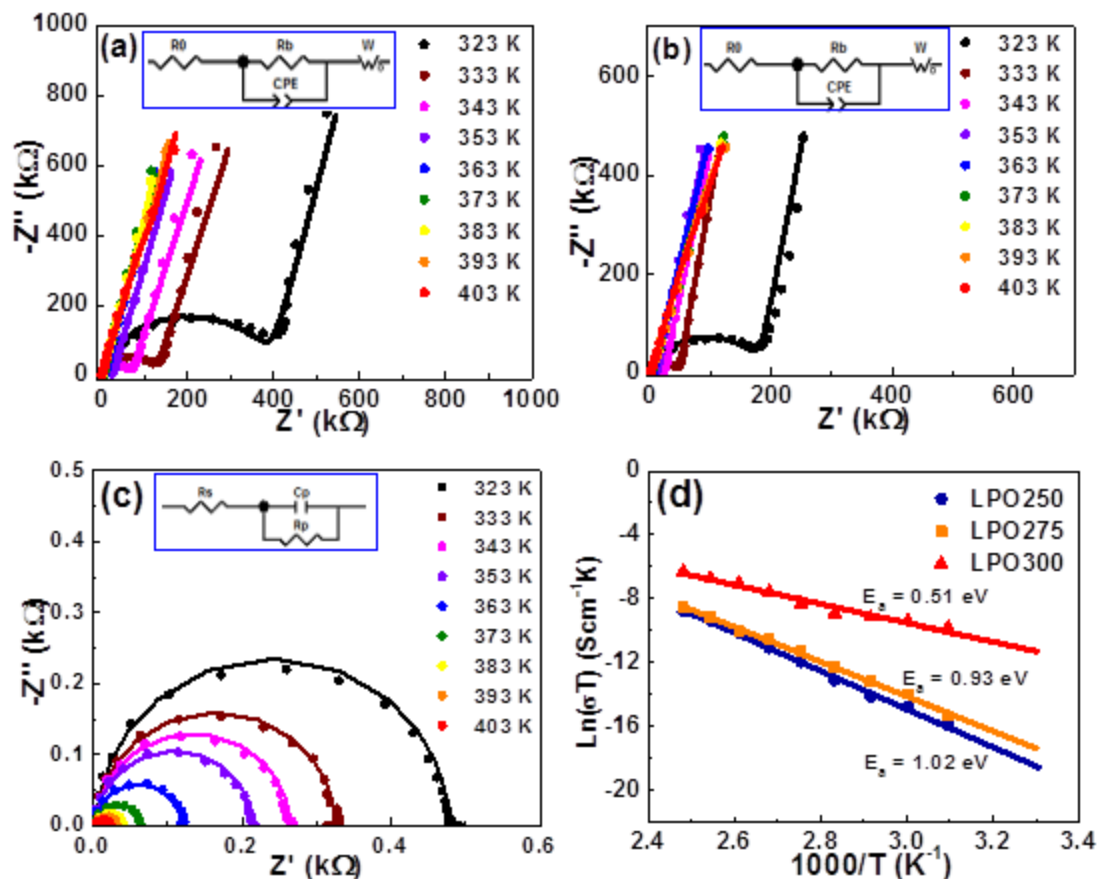
Figure 3.4 Impedance plots of lithium phosphate thin films (a) LPO250, (b) LPO275, and (c) LPO300 measured at different temperatures (insets are the equivalent circuits employed for simulation); (d) Arrhenius plots of the ionic conductivity of the lithium phosphate films measured between 323 and 403 K. (Scattered points are measured value and lines are fitted results.)

The complex impedance plots in Figure 3.4(a) and 4(b) are composed of one semicircle in the high-frequency region and one linear tail at lower frequency. The semicircle is addressed to the bulk resistance of lithium phosphate solid-state electrolytes, while the linear tail is due to the polarization at electrode-electrolyte interface [10]. The insets depict the equivalent circuits used to resolve the Cole-Cole plots, where R_0 denotes the high-frequency limiting resistance of the electrodes, and R_b represents for the bulk resistance. CPE stands for constant-phase element. A CPE is commonly used in a model in place of a capacitor, considered to be the resultant bulk capacitance of the lithium phosphate

solid-state electrolyte. W in the circuit is the finite length Warburg element, which occurs when charge carrier diffuses through the solids [44]. In this case, lithium ion is the charge carrier. Since Au applied as the electrode material is ionic blocking (open circuit diffusion), the behavior thus observed is typical of an ionic conductor in nature [44]. The ionic conductivity of the lithium phosphate thin films was evaluated by substituting the empirical R_b values into the equation below [10]:

$$\sigma = d/(AR_b) \tag{1}$$

where σ is the ionic conductivity, d is the thickness of the lithium phosphate thin film, and A is the geometric area of the lithium phosphate thin film between the Au electrodes. Thin film LPO250 yields a resistance from 387.8 Ω to 381.2 kΩ, giving conductivity from 3.72×10^{-10} to 3.79×10^{-7} S/cm, at measuring temperatures between 323 and 403 K. From Figure 3.4(b), the resistance of LPO275 acquired within the same measuring temperature range (323 – 403 K) varies from 17854 Ω to 241.4 kΩ and thus its ionic conductivity falls between 6.85×10^{-10} and 5.06×10^{-7} S/cm.

For the lithium phosphate film deposited at 300 $^{\circ}$C, Figure 3.4(c) shows only complete symmetric semicircular arcs indicative of a parallel R-C network (Figure 3.4(c) inset) and no diffusion element is present at the lower frequency end [45,46]. No diffusion effects appear when only charge of a single sign is mobile (lithium ions of positive charge); this is an excellent approximation of solid-state electrolytes [44]. The resistance in Figure 3.4 reaches 0.47 kΩ even at 323 K and drops to 0.014 kΩ at 403 K. Therefore the calculated ionic conductivity of LPO300 is as high as 1.72×10^{-7} S/cm at 323 K and 4.50×10^{-5} S/cm at 403 K. these values are three orders higher than those of LPO250 and LPO275. Therefore, it is found that the increasing deposition temperature (within 250 – 300 $^{\circ}$C) in the ALD process provides higher ionic conductivity of lithium phosphate solid-state electrolyte.

Furthermore, the activation energies of the thin film electrolytes are calculated by plotting Ln(σT) against 1000/T according to the Arrhenius equation [46]:

$$\sigma T = A \exp[- E_a/(kT)] \tag{2}$$

where T is the absolute temperature, A is a pre-exponential factor, E_a is the activation energy, and k represents the Boltzmann constant. The value of activation energy can be extracted by linearly fitting the results in a ln plot. Figure 3.4(d) demonstrates that E_a of the lithium phosphate thin films LPO250, LPO275, and LPO300 are of ~1.02, ~0.93, and ~0.51 eV, respectively. Comparing the conductivities of lithium phosphate solid-state electrolytes prepared by ALD at 250, 275, and 300 ℃, it is found that ionic conductivity is reliant on deposition temperature. Higher temperature results in improved ionic conductivity in the ALD deposited lithium phosphate thin film system in this study. Referring to the previous studies, in this amorphous oxides system, when the ratio of Li to P is 1, metaphosphate structural units (SUs) are formed. SUs consist of oxygen tetrahedral [PO$_4$] connected in chains by bridging oxygen atoms. Tie chains are formed between SUs threading the entire volume. The ionic conductivity is related to the migration of lithium ions in the thin films. The oxygen shared by SUs are negatively charged and lithium ions are dissociated from the polar structural chemical units, hopping from one to another to achieve the migration [47]. Another factor is the lithium concentration in the thin films. As the current carrier, introducing more lithium content can efficiently improve the ionic conductivity [45,47]. In this study, LPO250 has a higher Li to P ratio but a much lower ionic conductivity compared to LPO300. Therefore, it could be explained that the former factor is dominant. Higher deposition temperature could lead to growth of number of terminal oxygen atoms and formation of shorter-chain SUs. In addition, the polarization of the structural chemical units is of higher degree, resulting in decreasing the tightness of fixation of lithium ions in the structure, which is beneficial to the mobility of lithium ions. Hence the ionic conductivity is improved owing to a drop in the activation energy of conductivity [45,47].

Extrapolation of the lines in Figure 3.4(d) reads an ionic conductivity of 3.3×10^{-8} S/cm at RT, for thin film LPO300. This result is superior than those of other ALD deposited solid-state electrolytes. For example, the ionic conductivity of Li_2O-Al_2O_3 was reported to be 1×10^{-7} S/cm at 573 K, with a rather high activation energy of 2.90 eV. At RT, the conductivity would drop dramatically. Besides, the as-prepared Li_2O-Al_2O_3 electrolyte had to be annealed at 700 ℃ prior to the measurement [33]. The post-treatment could be

detrimental when applied to real battery fabrication. The ultrathin coatings of $Li_{5.1}TaO_z$ and $LiAlO_2$ were applied to cathode materials of LIBs, exhibiting similar ionic conductivities to this work [34,48]. Nonetheless, the ALD process of preparing the $Li_{5.1}TaO_z$ and $LiAlO_2$ thin films employs water as a precursor. The little trace of residue of water could be hazardous to battery performance. This work conducted here is a water-free ALD process. Another system successfully synthesized is $Li_xAl_ySi_zO$. [38] Despite the fairly good ionic conductivity, the rather complicated ALD process combines the subcycles of three oxides (four precursors) comparing to lithium phosphate thin films which only needs two precursors to set off.

Table 3.1: Comparisons of lithium phosphates deposited by ALD and conventional methods

Solid-State Electrolyte	Substrate	Li^+ Conductivity (S/cm)	Activation Energy (eV)	Method	Ref.
$Li_{2.8}PO_z$	Si (100) glass	3.3×10^{-8} (at 299 K)	0.51	ALD	This work
$Li_{2.7}PO_{3.9}$	Sapphire Graphite Alumina Glass	6.6×10^{-8} (at 298 K)	0.68	RF sputtering	[39]
Polycrystallin □- Li_3PO_4	—	4.2×10^{-18} (at 298 K)	1.24	Solid state reaction	[40]

Overall, we managed to achieve an acceptable ionic conductivity with a much simplified ALD process. Its electrochemical property is either comparable to or better than the lithium phosphate films fabricated by other reported methods such as RF sputtering and solid state reaction [39,40]. Moreover, the ALD process is able to produce the films with ultra thin thickness, extreme uniformity, and application to micro-3D structures. Lithium phosphate solid-state electrolyte deposited by ALD can be of great potential in both the

application of all-solid-state micro-LIBs in future and as beneficial coating layers on the electrodes for LIBs.

3.4   Conclusions

In summary, lithium phosphate thin films were deposited at 250, 275, 300, and 325 $^{\circ}$C by ALD using LiO^{t}Bu and TMPO as precursors, without any additional oxidizer. Self-limiting growths of lithium phosphate thin film were achieved at all the temperatures. The growth rate of lithium phosphate thin films was 0.57, 0.66, 0.69, and 0.74 Å/cycle at 250, 275, 300, and 325 $^{\circ}$C, respectively. XPS analysis showed that the as-deposited films had similar chemical structure as that in standard Li$_3$PO$_4$, and a higher deposition temperature provided a lower Li to P and O to P ratio. Furthermore, the lithium-ion conductivities of the films were measured. Lithium phosphate films grown at 300 $^{\circ}$C exhibited the highest ionic conductivity of 1.73×10^{-7} S/cm at 323 K with an activation energy of 0.51 eV. The extrapolated ionic conductivity at RT was 3.3×10^{-8} S/cm. It is expected that the lithium phosphate thin films prepared by ALD can find potential applications as solid-state electrolytes for 3D all-solid-state micro-LIBs, which, as an emerging area, deserves more extensive investigation in the coming future.

Acknowledgement

References

1   M. Roberts, P. Johns, J. Owen, D. Brandell, K. Edstrom, G. El Enany, C. Guery, D. Golodnitsky, M. Lacey, C. Lecoeur, H. Mazor, E. Peled, E. Perre, M. M. Shaijumon, P. Simon and P.-L. Taberna, *J. Mater. Chem.*, 2011, **21**, 9876–9890.

2   J. B. Goodenough and K.-S. Park, *J. Am. Chem. Soc.*, 2013, **135**, 1167–1176.

3   J. B. Goodenough and Y. Kim, *Chem. Mater.*, 2010, **22**, 587–603.

4   J. F. M. Oudenhoven, L. Baggetto and P. H. L. Notten, *Adv. Energy Mater.*, 2011, **1**, 10–33.

5   J. B. Bates, N. J. Dudney, B. Neudecker, A. Ueda and C. D. Evans, *Solid State Ionics*, 2000, **135**, 33–45.

6   K. Takada, *Acta Mater.*, 2013, **61**, 759–770.

7   W. C. West, J. F. Whitacre, V. White and B. V. Ratnakumar, *J. Micromechanics Microengineering*, 2002, **12**, 58–62.

8   J. Song, X. Yang, S.-S. Zeng, M.-Z. Cai, L.-T. Zhang, Q.-F. Dong, M.-S. Zheng, S.-T. Wu and Q.-H. Wu, *J. Micromechanics Microengineering*, 2009, **19**, 45004.

9   S. Zhao, Z. Fu and Q. Qin, *Thin Solid Films*, 2002, **415**, 108–113.

10   J. Liu, M. N. Banis, X. Li, A. Lushington, M. Cai, R. Li, T.-K. Sham and X. Sun, *J. Phys. Chem. C*, 2013, **117**, 20260–20267.

11   M. Armand and J.-M. Tarascon, *Nature*, 2008, **451**, 652–7.

12   K. Sun, T.-S. Wei, B. Y. Ahn, J. Y. Seo, S. J. Dillon and J. a Lewis, *Adv. Mater.*, 2013, **25**, 4539–43.

13   J. H. Pikul, H. Gang Zhang, J. Cho, P. V Braun and W. P. King, *Nat. Commun.*, 2013, **4**, 1732.

14   R. K. Joshi and J. J. Schneider, *Chem. Soc. Rev.*, 2012, **41**, 5285–312.

15   X. Meng, X.-Q. Yang and X. Sun, *Adv. Mater.*, 2012, **24**, 3589–615.

16   S. M. George, *Chem. Rev.*, 2010, **110**, 111–31.

17   P. Chen, T. Mitsui, D. B. Farmer, J. Golovchenko, R. G. Gordon and D. Branton, *Nano Lett.*, 2004, **4**, 1333–1337.

18   R. G. Gordon, D. Hausmann, E. Kim and J. Shepard, *Chem. Vap. Depos.*, 2003, **9**, 73–78.

19   J. W. Elam, D. Routkevitch, P. P. Mardilovich and S. M. George, *Chem. Mater.*, 2003, 3507–3517.

20   R. Solanki and B. Pathangey, *Electrochem. Solid-State Lett.*, 2000, **3**, 479–480.

21   J. Liu, Y. Tang, B. Xiao, T.-K. Sham, R. Li and X. Sun, *RSC Adv.*, 2013, **3**, 4492.

22   S. K. Cheah, E. Perre, M. Rooth, M. Fondell, A. Hårsta, L. Nyholm, M. Boman, J. Lu, P. Simon and K. Edstro, *Nano Lett.*, 2009, **9**, 3230–3233.

23   K. Gerasopoulos, X. Chen, J. Culver, C. Wang and R. Ghodssi, *Chem. Commun. (Camb).*, 2010, **46**, 7349–51.

24   K. Gerasopoulos, E. Pomerantseva, M. Mccarthy, A. Brown, C. Wang, J. Culver and R. Ghodssi, *ACS Nano.*, 2012, **6**, 6422–6432.

25   X. Li, X. Meng, J. Liu, D. Geng, Y. Zhang, M. N. Banis, Y. Li, J. Yang, R. Li, X. Sun, M. Cai and M. W. Verbrugge, *Adv. Funct. Mater.*, 2012, **22**, 1647–1654.

26   S. Kim, T. H. Han, J. Kim, H. Gwon, H. Moon, S. Kang, S. O. Kim and K. Kang, *ACS Nano.*, 2009, **3**, 1085–1090.

27   X. Meng, Y. Zhong, Y. Sun, M. N. Banis, R. Li and X. Sun, *Carbon N. Y.*, 2011, **49**, 1133–1144.

28   J. C. Badot, A. Mantoux, N. Baffier, O. Dubrunfaut, D. Lincot and P. Cedex, *J. Mater. Chem.*, 2004, **14**, 3411–3415.

29   M. E. Donders, W. M. Arnoldbik, H. C. M. Knoops, W. M. M. Kessels and P. H. L. Notten, *J. Electrochem. Soc.*, 2013, **160**, A3066–A3071.

30   M. Putkonen, T. Aaltonen, M. Alnes, T. Sajavaara, O. Nilsen and H. Fjellvåg, *J. Mater. Chem.*, 2009, **19**, 8767–8771.

31   T. Aaltonen, M. Alnes, O. Nilsen, L. Costelle and H. Fjellvåg, *J. Mater. Chem.*, 2010, **20**, 2877–2881.

32   D. J. Comstock and J. W. Elam, *J. Phys. Chem. C*, 2013, **117**, 1677–1683.

33   T. Aaltonen, O. Nilsen, A. Magrasó and H. Fjellvåg, *Chem. Mater.*, 2011, 4669–4675.

34   J. S. Park, X. Meng, J. W. Elam, C. Wolverton, C. Kim and J. Cabana, *Chem. Mater.*, 2014, **26**, 3128–3134.

35   J. Hämäläinen, F. Munnik, T. Hatanpää, J. Holopainen, M. Ritala and M. Leskelä, *J. Vac. Sci. Technol. A*, 2012, **30**, 01A106.

36   E. Østreng, H. H. Sønsteby, T. Sajavaara, O. Nilsen and H. Fjellvåg, *J. Mater. Chem. C*, 2013, **1**, 4283–4290.

37   E. Østreng, P. Vajeeston, O. Nilsen and H. Fjellvåg, *RSC Adv.*, 2012, **2**, 6315–6322.

38   Y.-C. Perng, J. Cho, D. Membreno, N. Cirigliano, B. Dunn and J. P. Chang, *J. Mater. Chem. A*, 2014, **2**, 9566–9573.

39   J. B. Bates, N. J. Dudney, G. R. Gruzalski, R. A. Zuhr and A. Choudhury, *J. Power Sources*, 1993, **44**, 103–110.

40   B. Wang, B. C. Chakoumakos, B. C. Sales, B. S. Kwak and J. B. Bates, *J. Solid State Chem.*, 1995, **115**, 313–323.

41   J. Hamalainen, J. Holopainen, F. Munnik, T. Hatanpaa, M. Heikkila, M. Ritala and M. Leskela, *J. Electrochem. Soc.*, 2012, **159**, A259–A263.

42   J. Holopainen, F. Munnik, M. Heikkila, M. Ritala and M. Leskela, *J. Phys. Chem. C*, 2012, **116**, 5920–5925.

43   A. T. Appapillai, A. N. Mansour, J. Cho and Y. Shao-horn, *Chem. Mater.*, 2007, **89**, 5748–5757.

44   J. R. Macdonald, *Ann. Biomed. Eng.*, 1992, **20**, 289–305.

45   S. W. Martin and C. A. Angell, *J. Non. Cryst. Solids*, 1986, **83**, 185–207.

46   Y. W. Hu, I. D. Raistrick and R. A. Huggins, *J Electrochem Soc*, 1997, **124**, 1240–1242.

47   I. a. Sokolov, Y. P. Tarlakov, N. Y. Ustinov and A. A. Pronkin, *Russ. J. Appl. Chem.*, 2005, **78**, 741–746.

48   X. Li, J. Liu, M. N. Banis, A. Lushington, R. Li, M. Cai and X. Sun, *Energy Environ. Sci.*, 2014, **7**, 768.

Supporting Information
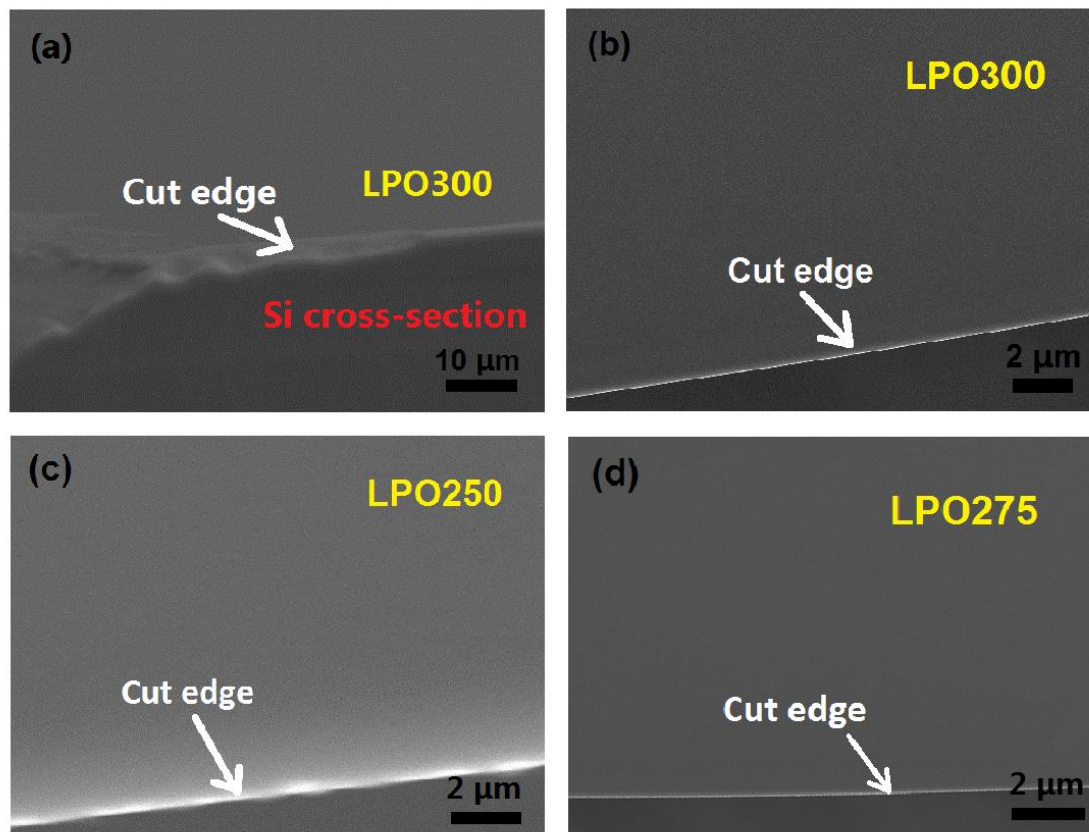
Figure 3.SI-1 Top-view SEM pictures of LPO250, LPO275, and LPO300 after 2000 ALD cycles. (a) Angled top-view of LPO300; Top-view of (b) LPO300, (c) LPO250, and (d) LPO275
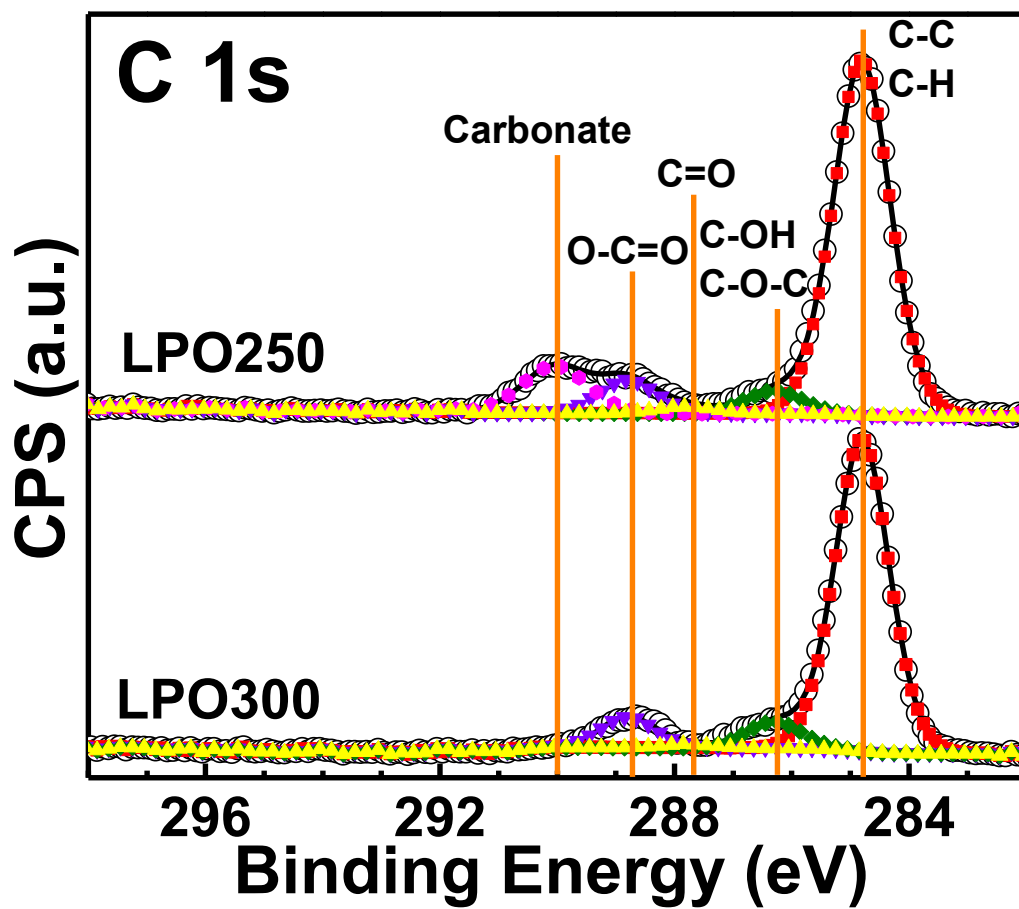
Figure 3.SI-2 XPS deconvolution of C 1s
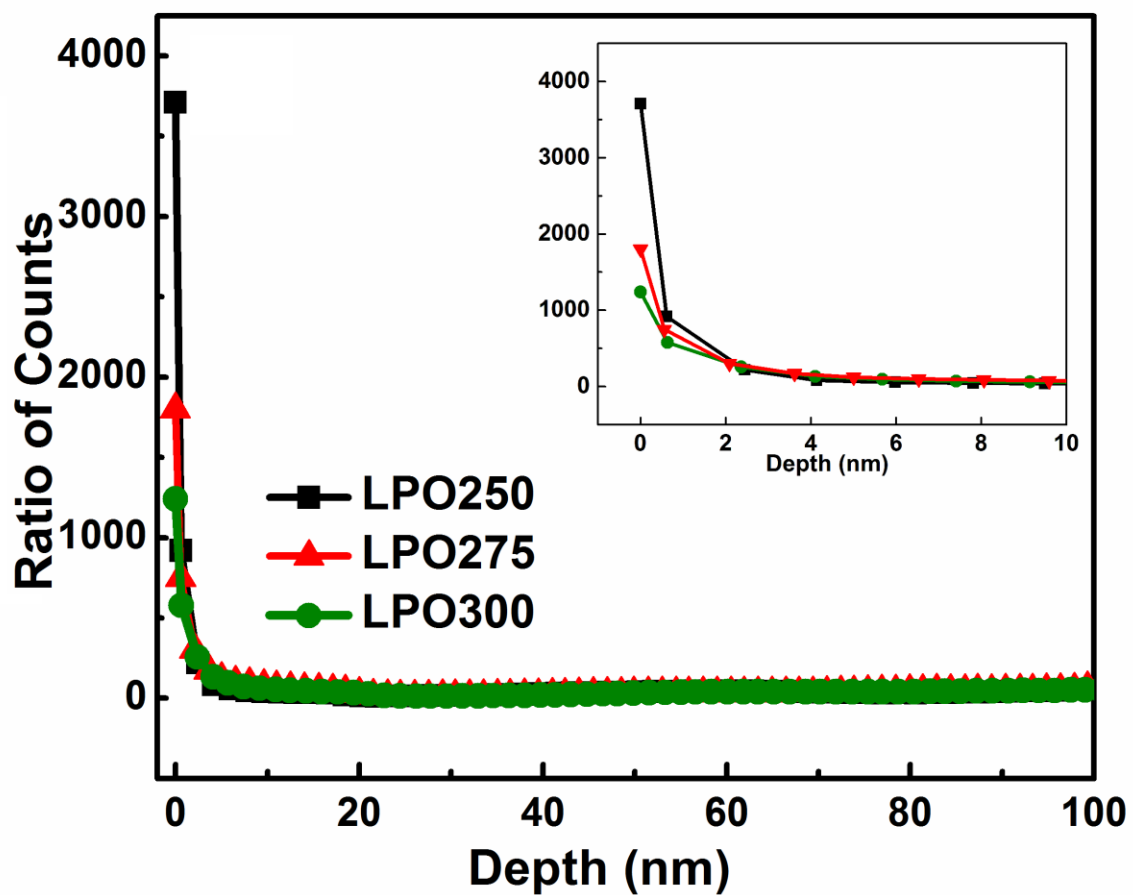
Figure 3.SI-3 SIMS depth profiles of the ratio of lithium to phosphous in LPO250, LPO275, and LPO300. The inset is the enlarged image of the first 10 nm
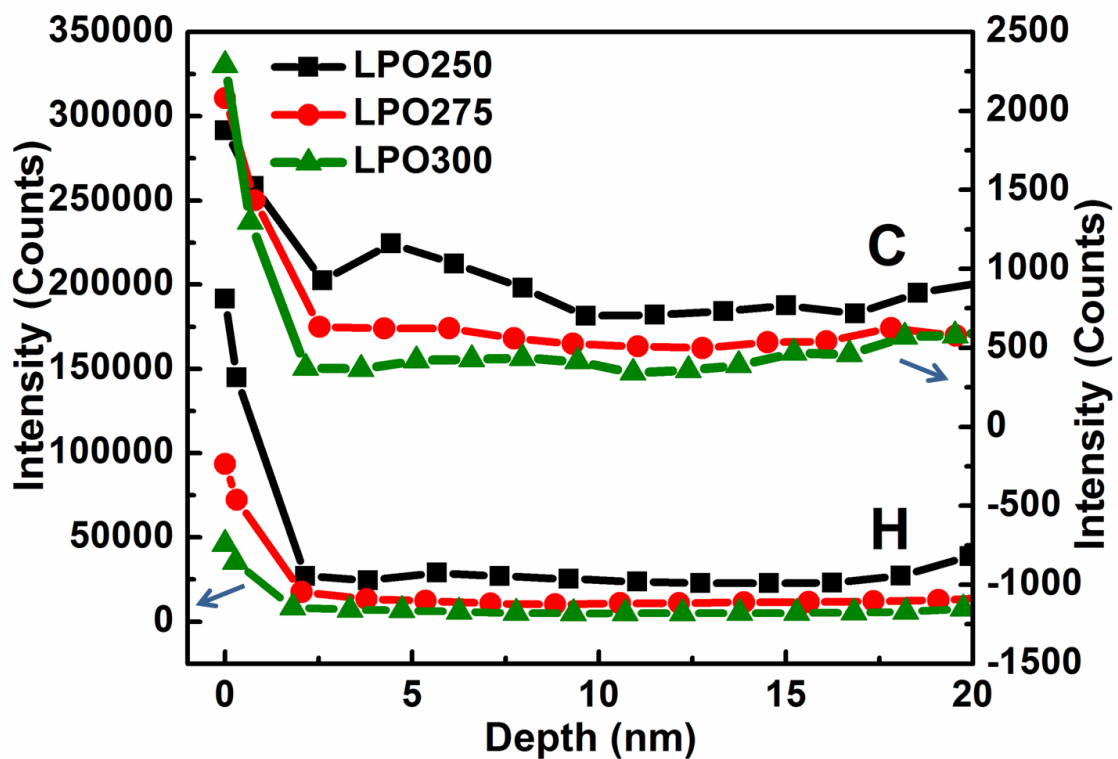
Figure 3.SI-4 SIMS depth profiles of carbon and hydrogen in LPO250, LPO275, and LPO300

Table 3.SI-1 Elemental compositions of the lithium phosphate thin films deposited at 250 and 300 ºC

Dep. Temp. (ºC)	Li (at%)	P (at%)	O (at%)	C (at%)	Li: P: O
250	22.0	6.6	49.1	22.0	3.3: 1: 7.4
300	24.6	8.8	45.0	20.7	2.8: 1: 5.1

Chapter 4

4   Titanium Dioxide/Lithium Phosphate Nanocomposite Derived from Atomic Layer Deposition as a High-Performance Anode for Lithium Ion Batteries*

Atomic layer deposition (ALD) is considered as a powerful technique to synthesize novel electrode materials for lithium-ion batteries (LIBs), because not only the compositions can be specifically designed to achieve higher battery performances, but also the materials can be deposited on various substrates for different purposes. Herein, a novel design of active material/electrolyte mixture electrode, i.e. titanium dioxide/lithium phosphate (TLPO) nanocomposite, has been successfully developed by ALD and deposited on carbon nanotubes substrates (CNTs@TLPO) at 250 ^{o}C, by combining the ALD recipes of TiO_2 and lithium phosphate (LPO). In the nanocomposite, anatase TiO_2 nanocrystals are embedded in a matrix of amorphous lithium phosphate. CNTs@TLPO has been examined as an anode material for LIBs, exhibiting a similar electrochemical response as anatase TiO_2 in the cyclic voltammetry testing. CNTs@TLPO presents an outstanding capacity of 204 mA h g^{-1} upon 200 cycles in charge and discharge cycling measurements, as well as a significantly improved rate capability compared with ALD deposited TiO_2 on CNTs (CNTs@T) without LPO ALD cycles. This work shows that the in-situ addition of solid-state electrolyte into active electrode materials is an efficient way to achieve high-performance electrode materials for LIBs by ALD.

4.1 Introduction

In recent years, lithium-ion batteries (LIBs) have been aggressively pursued for portable electronic devices. In order to reduce the dependence on fossil fuels at present, there has been a drastic expansion of the market of electric vehicles (EVs) and hybrid electric vehicles (HEVs), for whose applications LIBs are considered the most promising storage system due to their high energy density and long cycle life. Intensive studies have been focused on improving LIBs in the aspects of power and energy density, cycling lifetime, safety characteristics, and cost, in order to fulfill the ever-increasing demand of EVs and HEVs.[1,2] However, the state-of-the-art LIBs are still insufficient to meet the strict standard of future EVs in term of power output and driving distance. It is expected that the desired improvements on LIBs can be achieved by engineering novel architectures on current electrode materials and developing all-solid-state batteries.

TiO_2 has been studied extensively as an anode material for LIBs, since it is stable, environmentally benign and of low fabrication cost. It also delivers a high Li-insertion potential (~ 1.7 V versus Li/Li^+) and has a rather low self-discharge rate.[3–6] Considering electrochemical performance of different polymorphs of TiO_2, anatase TiO_2 is remarkable of its reversible uptake of 0.5 Li per formula unit, leading to a theoretical charge storage capacity of 167.5 mA h g^{-1}.[3,4] However, TiO_2 suffers from poor electronic conductivity and slow lithium-ion diffusion kinetics. The Li^+ ion diffusion coefficient in anatase TiO_2 is $\sim 10^{-13}$-10^{-17} cm^2 s^{-1}. The electronic conductivity of anatase is also low at $\sim 10^{-12}$ S cm^{-1}.[7] The problems can be addressed from two perspectives. First, TiO_2 can be combined with highly conductive materials, such as carbon nanotubes (CNTs) and graphene.[8–10] To further boost the electrochemical performance, a Li^+ ion conductive material can be applied to help facilitate ion transport. Li et al. reported improved battery performance by coating the electrode material with solid-state electrolyte.[11] The second approach to solving the problems is nanostructuring. The downsizing dimensions not only significantly reduce the ionic and electronic diffusion length but also provide a high surface area, giving high rate and cycling performances.[12]

Atomic layer deposition (ALD) is a gas-phase deposition technique and capable to uniformly deposit ultrathin TiO_2 on materials of high aspect ratios. ALD is featured by two sequentially cyclic self-limiting reactions. The saturated surface reactions allow the film to grow layer-by-layer, providing extremely precise control of thickness at atom level.[13] Owing to these advantages, many research groups have demonstrated that ALD can be employed for direct synthesis of nanosized electrode materials for LIBs, including metal oxides, sulfides, and lithium containing materials (like $LiCoO_2$ and $LiFePO_4$). [14–19]

Meanwhile, the deposition of TiO_2 by ALD has been well established.[20,21] $TiCl_4$ and titanium tetra-isopropoxide (TTIP, $Ti(OCH(CH_3)_2)_4$) are two most common titanium sources, with water as the most widely used oxidizer. Compared with $TiCl_4$, the usage of TTIP avoids the generation of corrosive HCl by-product or chlorine containing residues in the thin film deposited.[21] Previous studies have shown that the phase of TiO_2 can be tuned by changing the deposition temperature. Amorphous TiO_2 can be achieved at lower temperatures ($\sim 150\ ^{\circ}C$) while anatase phase is obtained at higher temperatures ($\sim 250\ ^{\circ}C$).[13,21] The application of ALD TiO_2 involves the deposition on different substrates like Ni, Au and Si to fabricate three-dimensional batteries.[22–27] Also, Amorphous TiO_2 by ALD has been deposited on nano carbon materials (CNTs and graphene) as an anode in LIBs.[7,28]

Recently, a new strategy to mix electrolyte into electrode materials has been proposed, in order to increase the ionic conductivy of the overall electrode and improve the performance of all-solid-state batteries.[29–33] ALD technique has been also recently applied to fabricate various solid-state electrolytes.[34–40] The ALD process of amorphous lithium phosphate (LPO) was reported, using lithium tert-butoxide [LiO^tBu, $(CH_3)_3COLi$] and trimethylphosphate [TMPO, $(MeO)_3PO$] to react directly without water. LPO was proved to be a promising candidate as a solid-state electrolyte with good ionic (Li^+) conductivity.[38] However, there has been still no report on in-situ building a mixed active electrode material/electrolyte with a single combined ALD process. Thus, we herein choose anode material TiO_2 and solid-state electrolyte LPO to verify the feasibility of this strategy in ALD electrodes for LIBs.

In this work, we developed a novel nanocomposite of anatase TiO_2/lithium phosphate (TLPO) on CNTs (denoted as CNTs@TLPO) by ALD. The ALD processes of TiO_2 and LPO were applied in sequence at 250 ℃ to create a continuous matrix of the nanocomposite. TLPO thin film was uniformly and conformally deposited on CNTs. The electrochemical performances of CNTs@TLPO as anode in LIBs was also compared with ALD-deposited anatase TiO_2 on CNTs (designated as CNTs@T).

4.2   Experimental

4.2.1   Deposition of TLPO by ALD

TLPO was deposited in a Savannah 100 ALD system (Ultratech/Cambridge Nanotech., USA) by using TTIP ($Ti(OCH(CH_3)_2)_4$) and water for TiO_2 subcycle and LiO^tBu [$(CH_3)_3COLi$] and TMPO [$(MeO)_3PO$] for LPO subcycle. Source temperatures for TTIP, LiO^tBu, and TMPO were 80, 180, and 75 ℃, respectively, while H_2O was kept at room temperature (RT). The deposition of the nanocomposite was carried out at 250 ℃. The chosen temperature was in the overlapped temperature range of the ALD windows of TiO_2 and LPO to achieve ALD growth and prevent precursors from decomposing. Additionally, the manifold was heated to 180 ℃ to avoid condensation of precursors. Nitrogen was used as the carrier gas. One ALD cycle consisted of two subcycles of TiO_2 and LPO. The overall sequence was the following: $2 \times$ [TTIP, (x s pulse/ 10 s purge) - H_2O (0.5 s pulse/15 s purge)] + [LiO^tBu, (2 s pulse/15 s purge) - TMPO (2 s pulse/ 15 s purge)]. The recipe of LPO subcycle was directly taken from our previous work.[38] Different pulse times of TTIP (1, 2, and 4 s) were used to verify the ALD process. Si (100) wafers and CNTs powders were used as substrates for the deposition of TLPO. Before the ALD process, Si wafers were cleaned by acetone, ethanol and water in sequence, followed by drying with flowing air. CNTs powders were refluxed in nitric acid (HNO_3, 70%) for 3 h at 120 ℃ to remove the residual catalyst from the growth of CNTs and functionalize the surface of CNT. The treated CNTs were dispersed in ethanol and washed in ultrasonic bath. Then the solution was casted on Al foil and loaded in the ALD chamber for deposition.

4.2.2 Physical Characterization of TLPO

The thickness, morphology, and compositions were determined by a field emission scanning electron microscope (FE-SEM, Hitachi S4800). Soft X-ray photoelectron spectroscopy (with a photon energy of 160 eV for Li 1s XPS and 210 eV for P 2p XPS) and X-ray absorption near-edge structure (XANES) spectroscopy were conducted at Canadian Light Source (CLS) on Variable Line Spacing Plane Grating Monochromator (VLS PGM) and Spherical Grating Monochromator (SGM) beamlines, respectively, in order to study the chemical states of the nanocomposite. Structural information was characterized by transmission electron microscopy (TEM, Hitachi 7000), high resolution transmission electron microscopy (HRTEM, JEOL 2010 FEG) and X-ray diffraction (XRD) system (Bruker D8 Advance, Cu-K$_\alpha$ X-ray source). High-temperature *In situ* XRD (HT-XRD) measurements (scan step of 0.02º per second) were conducted on CNTs@TLPO in air to study the temperature dependence of the phase transformation. Spectra were collected from 400 to 900 ºC with a diffraction angle of 10º to 60º. At each temperature, the sample was annealed for 1 hour before the measurement was taken in a period of 15 min.

4.2.3 Electrochemical Characterization of CNTs@TLPO

Electrochemical measurements were performed on CNTs@TLPO and CNTs@T. TLPO was deposited on CNTs using 300 ALD cycles of 2 × [TTIP, (1 s pulse/ 10 s purge) - H$_2$O (0.5 s pulse/ 15 s purge)] + [LiO^{t}Bu, (2 s pulse/ 15 s purge) - TMPO (2 s pulse/ 15 s purge)]. 600 ALD cycles of TiO$_2$ was selected to maintain the same total cycle number of TiO$_2$, using the recipe: [TTIP, (1 s pulse/ 10 s purge) - H$_2$O (0.5 s pulse/ 15 s purge)]. The loadings of CNTs@TLPO and CNTs@T were evaluated by thermogravimetric analysis (TGA, SDT Q600) from RT to 1000 ºC in air at a heating rate of 10 ºC min^{-1}. Energy dispersive spectroscopy (EDS) was done to estimate the content ratio of TiO$_2$ and LPO. Electrochemical performances were tested in coin-type half cells, using lithium foils as the counter electrode. CNTs@TLPO and CNTs@T were scraped gently off the Al foil and mixed with acetylene black, and polyvinylideneuoride (PVDF) with a weight ratio of 8: 1: 1 in Nmethylpyrrolidinone (NMP) solvent. The electrode was fabricated using a

slurry casting method.[11] Pure CNTs was fabricated into electrode using the same method and tested for comparison. The electrolyte was composed of 1 M LiPF$_6$ salt dissolved in ethylene carbonate (EC): diethyl carbonate (DEC): ethyl methyl carbonate (EMC) of 1: 1: 1 volume ratio. The cells were assembled in a glove box (Vacuum Atmosphere Company) under a dry argon atmosphere (moisture and oxygen level less than 1 ppm). Cyclic voltammetry (CV, 1- 3 V, 0.1 mV/s) and electrochemical impedance spectroscopy were measured on the versatile multichannel potentiostat 3/Z (VMP3). Charge-discharge characteristics at a constant current mode were tested at RT on Arbin BT-2000 Battery Tester, at different current rates (1C= 160 mA g^{-1}) in a voltage window of 1- 3 V. The specific capacity was calculated by dividing the obtained capacity with the weight of TLPO and TiO$_2$ deposited in the composite.

4.3   Results and Discussion
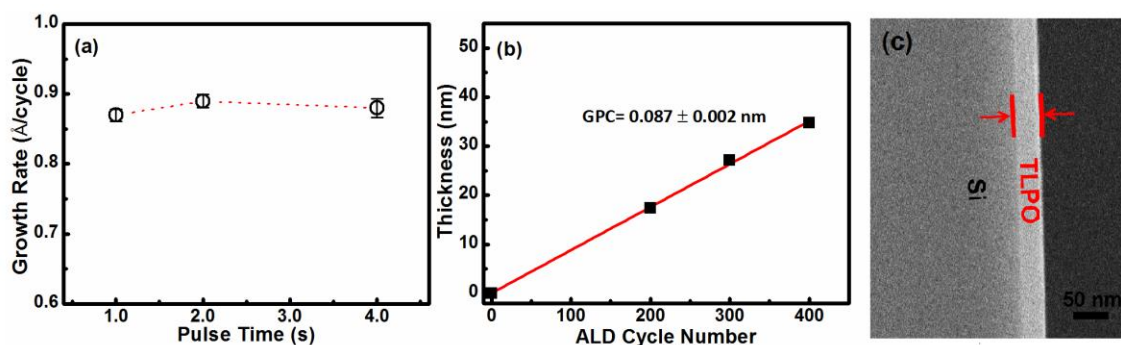
Figure 4.1 (a) Growth per cycle (GPC) of TLPO thin films as a function of TTIP pulse time; (b) Film thickness of TLPO as a function of ALD cycle number on a Si (100) substrate with a TTIP pulse time of 1s at 250 °C; (c) SEM image of cross-section of 400 ALD cycles of LTPO thin film deposited on the Si substrate

The ALD growth features of TLPO thin films were first characterized on standard Si (100) substrates. One ALD cycle consisted of two subcycles of TiO$_2$ and one of LPO in order to achieve higher ratio of TiO$_2$ as the active anode material. Keeping this ratio of subcycles, the effect of pulse time of TTIP on the growth rate of TLPO thin films at 250 °C is shown in Figure 4.1(a), with the pulse time of water kept at 0.5 s. The growth per cycle (GPC) of TLPO thin films remained constant while the pulse time of TTIP

increased, indicating a saturated growth was obtained. Thus, a pulse time of 1 s TTIP with 0.5 s H_2O was used in the subsequent experiments. Moreover, a linear relation between the film thickness and the ALD cycle number has been observed at 250 ºC, yielding a GPC of 0.087 nm in Figure 4.1(b). The self-limiting characteristics of TiO_2 and LPO subcycles were responsible for the linear cycle dependence. If simply assuming the GPC of LPO subcycle is ~ 0.057 nm/cycle, same as our previous result for ALD LPO thin film growth,[38] the growth rate of TiO_2 at 250 ºC could be estimated as 0.015 nm/cycle, which is relatively lower than the value (~ 0.024 nm/cycle) reported in previous study.[13] This could be due to the difference in the surface chemistry between the preceding and the succeeding subcycles, leading to a deviated GPC of one or each binary system in the combined ALD process.[34,36] In this case, it is reasonable to lower GPC of TLPO thin films than the linear combination of the GPC of TiO_2 and LPO. Besides, this result may also imply a strong interaction between the TiO_2 and LPO phases in the ALD TLPO thin films, which is expected to contribute a better ion transportation and exchange behavior in the electrode. SEM image of a cross section of TLPO thin film after 400 ALD cycles on Si substrate is displayed in Figure 4.1(c). It can be seen that TLPO thin film is uniformly deposited on the Si substrate, giving a flat surface on the substrate, with a thickness of about 35 nm.
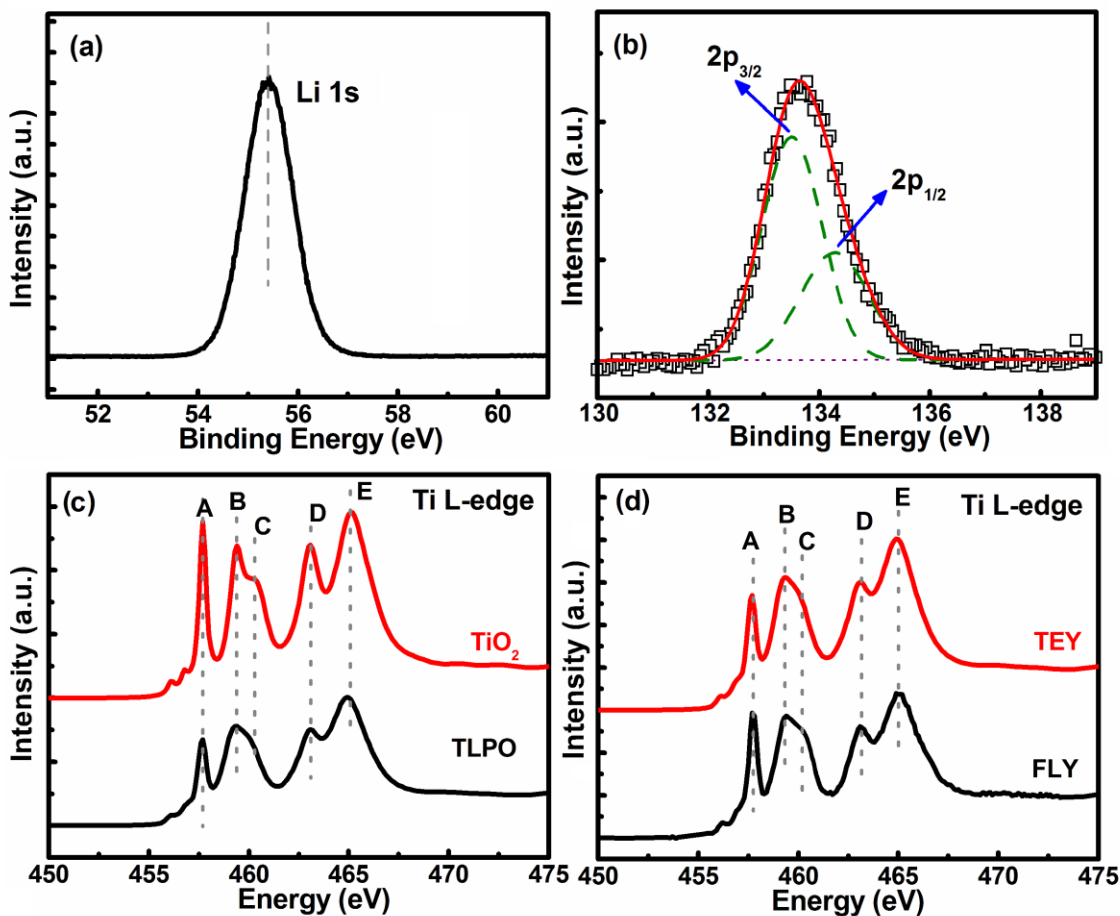
Figure 4.2 Photoelectron spectra of TLPO thin films deposited on the Si substrate: (a) Li 1s (the photon energy is 160 eV); (b) deconvolution of P $2p_{3/2,1/2}$ (with a photon energy of 210 eV); Ti $L_{3,2}$-edge XANES spectra: (c) TEY spectra of ALD deposited TLPO and TiO_2 thin films; (d) TEY and FLY spectra of TLPO as-deposited

The chemical states of the light elements in TLPO thin films were determined by X-ray photonelectron spectroscopy (XPS) using synchrotron radiation. The photon energies used for Li 1s and P 2p spectra were 160 and 210 eV, respectively. Due to the much lower energy of the excitation photons (often higher cross-section) and higher energy resolution than laboratory X-rays, soft X-ray XPS using synchrotron radiation is more sensitive to the variation of electronic states at the surface and enables us to study the core-level of lithium in greater details.[41] The Li 1s and P 2p XPS spectra of TLPO are presented in Figure 4.2. It is obvious that the Li 1s spectrum contains only one symmetric peak as shown in Figure 4.2(a), suggesting that Li is in the single chemical environment

of Li (Li-O) in the TLPO thin film. The peak position locates at 55.35 eV, which is in accordance with our previous work of ALD LPO.[42,43] The P 2p spectrum in Figure 4.2(b) can be fitted into a set of doublet, P $2p_{1/2}$ and $2p_{3/2}$, which are centered at 134.21 and 133.42 eV, respectively,[42–44] corresponding to the phosphorous in phosphate. This result is consistent with the spectrum of Li 1s. The XPS results confirmed the successful deposition of LPO in the nanocomposite TLPO. In addition, the LPO component in the TLPO thin films shared the same chemical states with the lithium phosphate thin films deposited by ALD at the same temperature (250 °C). [38]

X-ray absorption spectroscopy (XAS) was employed to study the local chemical environment of Ti by exciting the core electron to the previously unoccupied electronic states. Ti $L_{3,2}$-edge probes electron transition from Ti 2p to the conduction band of Ti 3d character (dipole selection rules). Spectra shown in Figure 4.2(c) were recorded in total electron yield (TEY) mode, which measures the total yield of photoelectrons, Auger electrons, and secondary electrons (dominant) upon X-ray excitation, revealing the information from the sample surfaces of a few nanometers.[45] A few characteristic features are observed and marked by vertical lines (Figure 4.2(c)). Peaks A, B, and C belong to the $2p_{3/2}$ to 3d transition (L_3-edge), while peaks D and E at a higher energy of a similar profile yet broadened, arise from the $2p_{1/2}$ to 3d transition (L_2-edge). At both edges, the crystal field splits the 3d band into t_{2g} (peaks A and D) and e_g (peaks B, C, and E) sub-bands. The e_g peak splitting (peaks B and C) results from the difference in local symmetry of the corresponding crystal phases.[46] The upper line represents the spectrum from ALD-deposited TiO_2 thin film at 250 °C and the lower one is from TLPO thin film. There is no evident energy shift between the onsets of edge jump the two spectra, suggesting that Ti in the two samples are of the same oxidation state (i.e., Ti^{4+}). The splitting of e_g band is well resolved in TiO_2 with peak B of a higher intensity than peak C, which is typical of anatase TiO_2. However, this feature is broadened in TLPO thin films, which can be associated with the loss of long-range order due to the effects of titanium interactions with second-neighboring atoms.[47] The addition of LPO component in the TLPO nanocomposite gives rise to the degradation of long-range order of TiO_2. Figure 4.2(d) compares the TEY and (X-ray fluorescence yield) FLY spectra of TLPO thin films. Differing from TEY, FLY measures the X-ray fluorescence emission which has two

orders of magnitude increase in attenuation length in the solid than electrons, collecting bulk sensitive information.[45] The key features in FLY resemble those in TEY, which is indicative of a consistent and uniform distribution of Ti with the same chemical states in as-prepared TLPO thin films.

To determine the crystal structure of CNTs@TLPO, XRD, transmission electron microscopy (TEM) and high resolution transmission electron microscopy (HRTEM) were employed and the results are shown in Figure 4.3. The diffraction peaks observed in Figure 4.3(a) locate at 26°, 43°, and 44° (labeled with ♥), corresponding (002), (100), and (101) planes of graphic carbon (JCPDS No. 08-415) from CNTs. The rest peaks (labeled with ♣) are assigned to anatase TiO_2 (JCPDS No. 21-1272). The two sharp peaks located at 25° and 48° belong to the (101) and (200) planes of anatase TiO_2. It is known that XRD provides overall collective information of the powder samples. Therefore it can be concluded that the ALD grown TiO_2 crystallized in the anatase phase, which is consistent with previous reports. [13,47] In contrast, no diffraction peak of Li_3PO_4 was found in the XRD pattern, indicating that the LPO component in TLPO is amorphous. In order to further track the LPO phase, an *in-situ* heating XRD measurement was carried out and the results are shown in Figure 4.3(b). The peaks addressed to Li_3PO_4 (JCPDS No. 15-760) are highlighted, which were absent in the RT XRD spectrum and started to appear at 500 ℃. Besides, the signals from the CNTs disappeared at elevated temperature (above 500 ℃), caused by the combustion of carbon content during *in-situ* heating in air. Both Li_3PO_4 and the anatase TiO_2 in the XRD patterns persisted till 1000 ℃. Moreover, annealing from 500 to 800 ℃ resulted in better crystallinity of both components. No noticeable phase transformation was detected during the heat treatment. When the temperature reached 1000 ℃, the patterns from either Li_3PO_4 or TiO_2 could not be discerned. The peaks were solely from the sample holders, which contained corundum Al_2O_3 (JCPDS no. 75-792) and quartz (JCPDS no. 79-1911, labeled with #). These *in-situ* XRD results doubtlessly prove the existence of the amorphous Li-P-O phase in the as grown TLPO thin films.
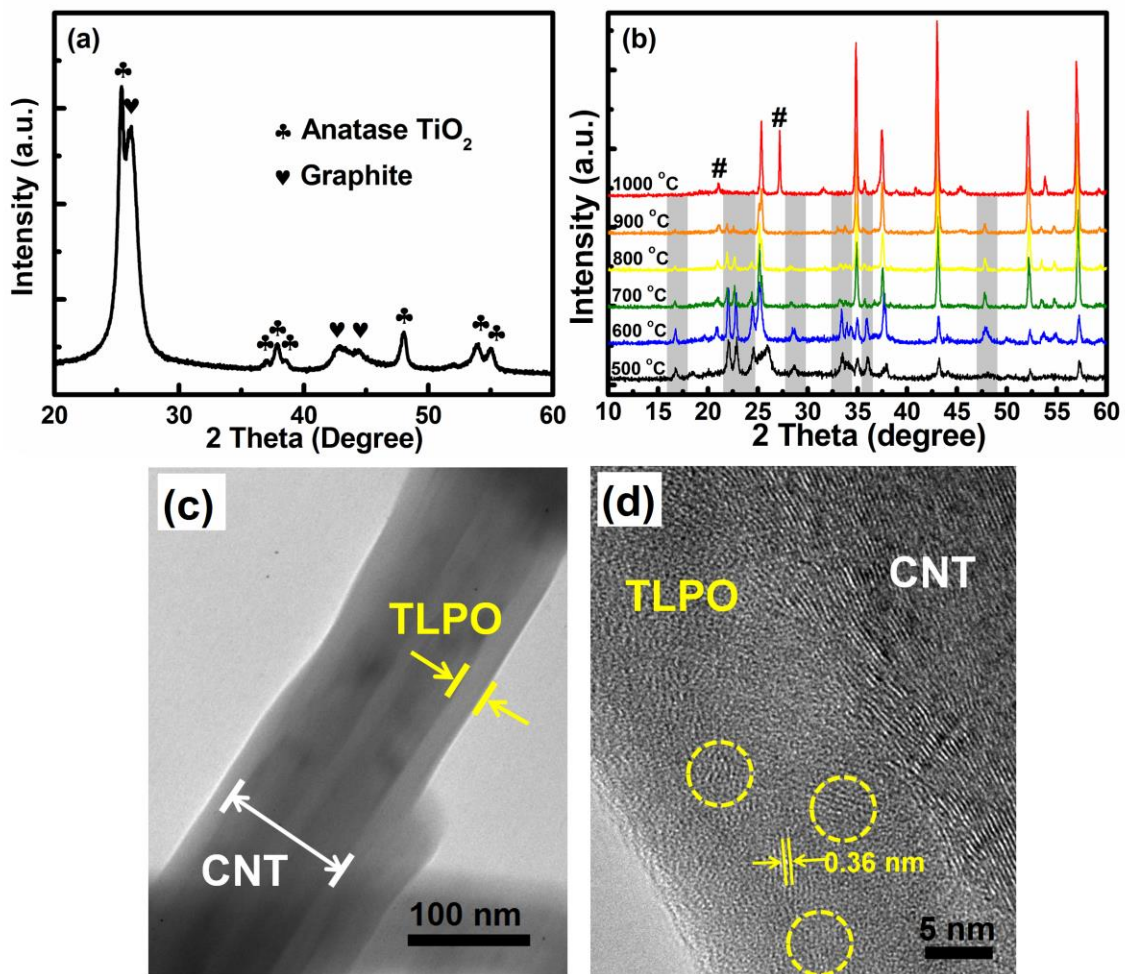
Figure 4.3 (a) XRD spectrum of TLPO/CNTs; (b) in-situ XRD spectra of TLPO/CNTs; (c) TEM image of CNTs@TLPO after 300 ALD cycles; (d) HRTEM image of the CNTs@TLPO after 300 ALD cycles

Microstructural information was provided by TEM and HRTEM as presented in Figure 4.3. The thickness of the as-prepared TLPO thin film on CNTs after 300 ALD cycles in Figure 4.3(c) were measured to be ~ 23 nm, which was very close to the calculated result (~ 26 nm) based on the GPC obtained on the Si substrate, indicating a similar ALD growing behavior on both substrates. The negligible deficiency could be explained by the high aspect ratio of CNTs. The amount of the precursors that diffused into the porous powder substrates could be a little less than that on the two-dimensional (2D) flat surface (Si). The hollow structure of multiwalled CNTs is clearly revealed, with the surface

evenly covered with TLPO thin films. Furthermore, the HRTEM image in Figure 4.3(d) discloses the detailed structure of the nanocomposite. Aligned lattices can be observed in the HRTEM image of CNT@TLPO, as some spots highlighted in the circled regions. The interplanar spacing of plane obtained from the pixel intensity profile of the selected regions is 0.36 nm, which matches the plane (101) of bulk anatase TiO_2.[8,48] Moreover, it is clearly shown that the nanocrystalline anatase TiO_2 randomly dispersed in the amorphous LPO matrix. It has been reported that ALD process at elevated temperatures resulted in anatase TiO_2.[13] The nucleation sites at the early stage of the ALD process, in this case, was highly possible to be affected by the roughness and the functional groups on the surface of the substrates (CNTs). Meanwhile, when the LPO ALD process was added, the continuous growth of TiO_2 was interrupted. Some available sites remained was taken by the growth of LPO component. Consequently when proceeding to the TiO_2 subcycle again, it tended to grow on favorable sites which most likely were some of the initial sites. Thus, after repeating this process, a nanocomposite with nanocrystal TiO_2 distributed in the amorphous LPO matrix was formed. To conclude the aforementioned discussions, TLPO nanocomposite was successfully synthesized via ALD by combining the subcycles of TiO_2 and lithium phosphate. The TLPO thin films could be evenly coated on CNTs. The as-prepared nanocomposite consisted of anatase TiO_2 nanocrystals wrapped in amorphous lithium phosphate matrix, as shown in the schematic diagram (Figure 4.5).
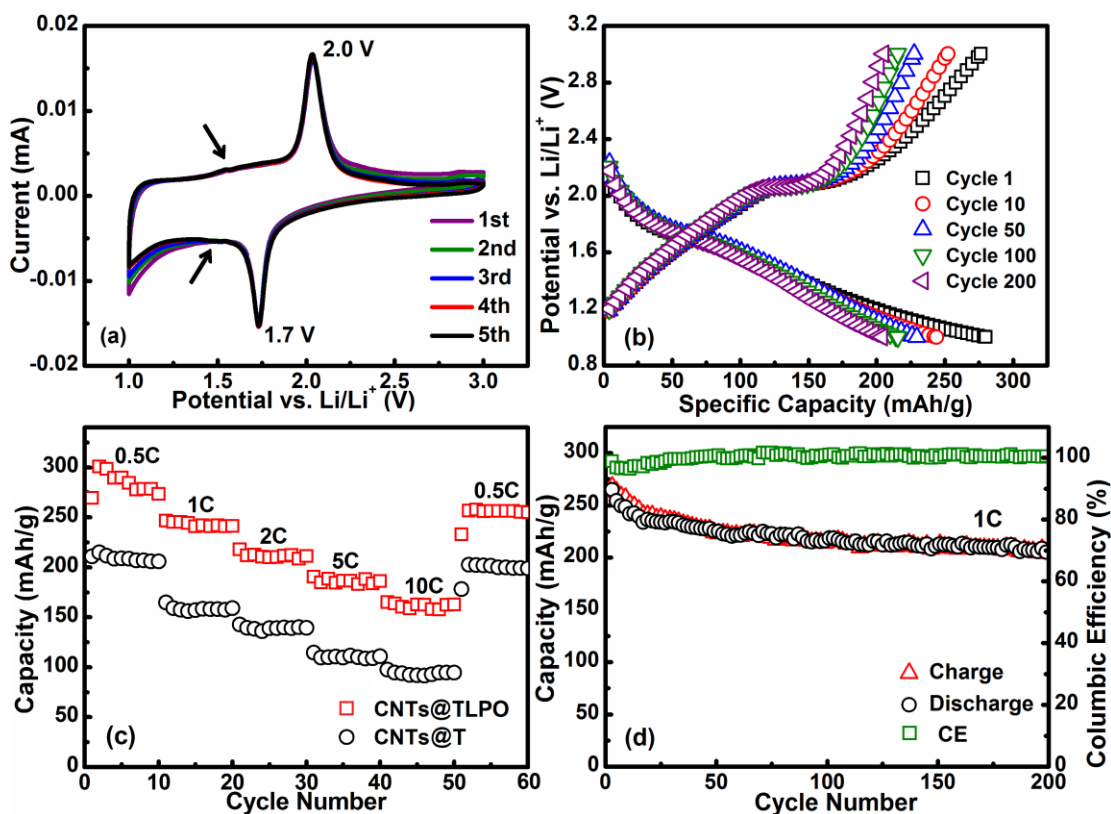
Figure 4.4(a) Cyclic voltammetry (CV) curves of TLPO/CNTs using a voltage window of 1.0-3.0 V versus Li/Li$^+$; (b) charge/discharge profiles of cycle 1, 50, 100, and 200 at a current density of 1C (160 mA/g) in a voltage window of 1.0-3.0 V; (c) rate capability of CNTs@TLPO at current density of 0.5, 1, 2, 5, and 10 C; (d) cycling stability of CNTs@TLPO at a current density of 1C (1.0-3.0 V)

Thermogravimetric analysis (TGA) was performed to analyze the weight percentage of CNTs@TLPO and T@CNTs. The results can be found in Figure 4.SI-1, yielding 45.2% and 67.1% loading of TLPO and TiO$_2$, respectively. The high mass loadings of the TLPO and TiO$_2$ are crucial to the successful implementation of ALD to deposit active materials on conductive substrates to fabricate electrodes for LIBs. Energy dispersive spectroscopy (EDS) results were also obtained to evaluate the content ratio of TiO$_2$ and LPO in the CNTs@TLPO sample (Figure 4.SI-2). Both signals from elements Ti and P were detected, giving an atomic ratio of 1.81, close to the subcycle number ratio of TiO$_2$ to LPO with reasonable of TiO$_2$ loading in the CNTs@TLPO nanocomposite.

Electrochemical measurements were then conducted on CNTs@TLPO and CNTs@T. Figure 4.4(a) displays cyclic voltammetry (CV) curs of CNTs@TLPO in the first five cycles. A pair of well-defined current peaks can be observed at 1.7 V (cathodic sweep) and 2.0 V (anodic sweep), which are the characteristic for the lithium-ion intercalation/deintercalation reaction in anatase TiO_2.[9] The voltage polarization between the two current peaks reflects the overpotential required for the transformation between TiO_2 and Li_xTiO_2 during lithiation/ delithiation. A 0.3 V difference in the CV for CNTs@TLPO is slightly reduced than the reported value for nanocrystalline TiO_2 (0.4 V),[3,49] presaging an easier transition between the two phases, which may have been benefited from the core-shell electron conduction from CNT and ionic diffusion from LPO electrolyte phase. In addition, the redox current peaks exhibited nearly no decrease after 5 CV cycles. Meanwhile, the ratio of anodic and cathode peak current was retained close to 1, indicating good reversibility and equilibrium redox system of CNTs@TLPO throughout the potential scan.[49] Interestingly, it can be observed that a pair of bumps appeared in the broad envelope region at lower potentials envelope at around 1.4/1.55 V. Similar phenomena have been reported before.[3,49–51] It was ascribed to the probably trace of another TiO_2 polymorph, which might cause extra contribution to capacity.[3,49–51] Turning to the charge-discharge voltage profiles, Figure 4.4(b) depicts the profiles of cycle 1, 10, 50, and 200 of CNTs@TLPO at the current rate of 1C (160 mA g^{-1}). The plateaus laid around the potential of 1.7/2.0 V, which matched the positions of the redox peaks in CV. Also, the plateaus and shapes of the charge/discharge curves well maintained even after 200 cycles of cycling, suggesting stable dynamics of the lithium insertion/extraction process.[8] The capacity for all the CNTs@TLPO and CNTs@T electrodes was calculated based on the loadings of TLPO and TiO_2 thin films, respectively. The initial discharge and charge capacities of CNTs@TLPO were 280.0 and 276.4 mA h g^{-1}, respectively. It should be noted that the applied voltage window was from 1 to 3 V, while the CNTs contributed negligible Li^+ storage in this voltage range (Figure 4.SI-3). Pure CNTs was also tested and it is confirmed that the specific capacity contribution from pure CNTs was negligible between 1 and 3 V (Figure 4.SI-4).[52]

To investigate the rate capability of CNTs@TLPO with CNTs@T as comparison, the electrodes were discharged and charged at various current rates, namely 0.5C, 1C, 2C, 5C,

and 10C, shown in Figure 4.4(c). Apparently, the capacity decreases with increasing current density (which is equivalent to power density when multiplied by the average discharge voltage). At the current rates of 0.5C, 1C, 2C, 5C, and 10C, CNTs@TLPO delivered a specific capacity of 273, 241, 211, 186, and 163 mA h g^{-1}, correspondingly, higher than many good works reported on anatase TiO$_2$ nanocomposites.[8,51,53] Moreover, the discharge/charge capacities resumed when the rate was reduced back to 0.5C. With respect to CNTs@T, CNTs@TLPO always demonstrated substantially improved specific capacity at all different current rate from 0.5C to 10C, which became even more distinguished at higher rate. For instance, at 10C, the specific capacity of TLPO reached 162.8 mA h g^{-1}, almost 2 times of that of CNTs@T. Both CNTs@TLPO and CNTs@T took advantage of the conductive carbon 'skeleton' as substrates for faster electron transportation (as shown in Figure 4.5) and the reduced diffusion path due to the nanoscale size of the active materials. Thus, the enhanced lithium diffusion kinetics of CNTs@TLPO compared to CNTs@T could be ascribed to the existence of LPO in the nanocomposite. LPO has proven to be a good solid-state electrolyte, which can efficiently transport lithium ions in and out the material.[38,54,55] Based previous structural analysis, the TiO$_2$ nanocrystals were dispersed in a matrix of LPO, 'immersed' in an ionic conductive material which could significantly increase the diffusion rate of Li$^+$, as shown in Figure 4.5. Electrochemical impedance spectroscopy (EIS) of CNTs@TLPO and CNTs@T electrodes was presented in Figure 4.SI-5. Both Nyquist plots consisted of a high-frequency semi-circle and a linear Warburg region at lower frequency. The high-frequency region was associated with the charge-transfer resistance related to Li$^+$ interfacial transfer. The lower charge-transfer resistance of CNTs@TLPO indicated a smaller ionic resistance and enhanced kinetics for CNTs@TLPO. It was further confirmed that the incorporation of Li$^+$ conducting material (LPO) into the nanocomposite helped achieve better Li$^+$ transport kinetics. At last, a stability test was carried out, as seen in Figure 4.4(d). With an initial discharge capacity of 280.0 and 276.4 mA h g^{-1}, CE of the first cycle was 101.3% while in the second cycle, the discharge capacity dropped to 265.0 mA h g^{-1} with a CE of 98.9%, indicating an irreversible capacity loss due to trapping of Li$^+$ inside the framework. Surprisingly, after the initial break-in cycles where CE decreases (typically three cycles) CE increased back during the

first 50 cycles and was sustained at about 100% afterwards. Former studies believed that in the break-in cycles the irreversible Li insertion sites were gradually filled and trace water was gradually oxidized and consumed at higher potentials and that the residue lithium remaining in the TiO_2 enhanced the electric conductivity,[56] thus improving the CE and decreasing the irreversible capacity accordingly. Furthermore, the discharge capacity was still retained at 204 mA h g^{-1} after 200 cycles, higher than that of the ALD deposited CNTs@T (149 mA h g^{-1}, shown in Figure 4.SI-6) under the same testing conditions. It is worth discussing that the specific capacity was even larger than the theoretical value (168 mA h g^{-1}) of anatase TiO_2 at 1C. Two postulations are proposed here. First, the matrix of LPO might act as a lithium storage media during the test, yielding higher capacity. Second, it has been well acknowledged that during the intercalation of Li^+, TiO_2 becomes Li_xTiO_2, where x is usually found to be 0.5 for anatase TiO_2, where the conventional theoretic capacity is reached. However, x could be close to 1 for amorphous TiO_2 and for very small anatase particles.[8,26,50,51] Apart from the biphasic transition from tetragonal to orthorhombic $Li_{0.5}TiO_2$, further insertion of Li^+ could form cubic $LiTiO_2$ with a higher capacity. In CNTs@TLPO, the nanocrystallines of TiO_2 were found to be around 5 nm (from Figure 4.3(d)), which might give rise to the formation of Li_xTiO_2 with x over 0.5 and therefore delivering a higher capacity.
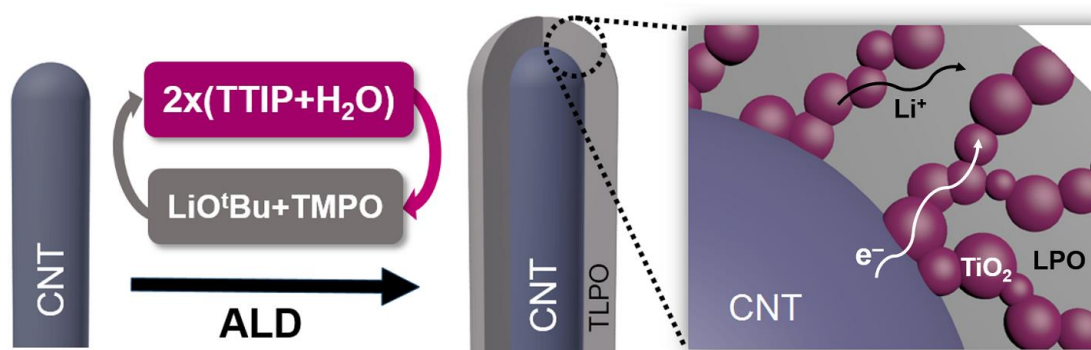
Figure 4.5 Schematic diagram of the fabrication process of CNTs@TLPO and the detailed structure of CNTs@TLPO

Overall, this study demonstrates that the incorporation of LPO solid-state electrolyte can significantly improve the performance of ALD TiO_2 electrodes. It can be expected that

applying and optimizing various choices of ALD electrolytes for ALD electrode materials can become a promising method to achieve high performance electrodes in future.

4.4   Conclusions

In summary, titanium dioxide/lithium phosphate nanocomposites (TLPO) have been successfully deposited using the ALD technique by combination of TTIP-H_2O and LiO^{t}Bu-TMPO subcycles. The overall growth can be well controlled in terms of film thickness. The two components TiO_2 and LPO were identified correspondingly, applying various techniques including UPS, XAS, XRD and HRTEM. LPO was determined to be amorphous while TiO_2 existed in the form of anatase nanocrystallines distributed in the LPO matrix. TLPO thin films were deposited on CNTs to be applied as anode materials for LIBs. Compared with ALD deposited TiO_2 single phase on CNTs as anodes, CNTs@TLPO exhibited exceptional rate capability especially at high current rates. The reason could be ascribed to the use of CNTs substrates and the adding of ionic conductive LPO component, which help achieve faster Li^+ diffusion kinetics. Furthermore, excellent cycling performance of CNTs@TLPO was obtained with a specific capacity of over 200 mA h g^{-1}, which could be contributed to the compositions, nanosized structure, the high surface area of the nanocomposite. The material designed here can be employed to form high power and high capacity electrode materials. Further, this work demonstrates that ALD can be employed to design and develop high-performance electrode materials for battery applications. It also holds great potential in fabricating all-solid-state batteries in future.

Ackowledgement

References

1   M. Armand and J.-M. Tarascon, *Nature*, 2008, 451, 652–7.

2   J. B. Goodenough and Y. Kim, *Chem. Mater.*, 2010, 22, 587–603.

3   J. S. Chen, Y. L. Tan, C. M. Li, Y. L. Cheah and D. Luan, *J. Am. Chem. Soc.*, 2010, 132, 6124–6130.

4   S. Kumar, S. Lee, W. Yoon and H. Shin, *J. Power Sources*, 2014, 249, 59–65.

5   Y. Tang, Y. Zhang, J. Deng, J. Wei, H. Le Tam, B. K. Chandran, Z. Dong, Z. Chen and X. Chen, *Adv. Mater.*, 2014, 6111–6118.

6   Y. Tang, Y. Zhang, J. Deng, D. Qi, W. R. Leow, J. Wei, S. Yin, Z. Dong, R. Yazami, Z. Chen and X. Chen, *Angew. Chem. Int. Ed.*, 2014, 53, 13488–13492.

7   M. Xie, X. Sun, C. Zhou, A. S. Cavanagh, H. Sun, T. Hu, G. Wang, J. Lian and S. M. George, *J. Electrochem. Soc.*, 2015, 162, 974–981.

8   H. Liu, W. Li, D. Shen, D. Zhao and G. Wang, *J. Am. Chem. Soc.*, 2015, 137, 13161–13166.

9   Y. Cheng, Z. Chen, H. Wu, M. Zhu and Y. Lu, *Adv. Funct. Mater.*, 2016, 1338–1346.

10   Y. Tang, Y. Zhang, X. Rui, D. Qi, Y. Luo, W. R. Leow, S. Chen, J. Guo, J. Wei, W. Li, J. Deng, Y. Lai, B. Ma and X. Chen, *Adv. Mater.*, 2016, 1567–1576.

11   X. Li, J. Liu, M. N. Banis, A. Lushington, R. Li, M. Cai and X. Sun, *Energy Environ. Sci.*, 2014, 7, 768.

12   S. K. Panda, Y. Yoon, H. Suk, W. Yoon and H. Shin, *J. Power Sources*, 2012, 204, 162–167.

13   X. Meng, D. Geng, J. Liu and R. Li, *Nanotechnology*, 2011, 22, 165602.

14   X. Li, X. Meng, J. Liu, D. Geng, Y. Zhang, M. N. Banis, Y. Li, J. Yang, R. Li, X. Sun, M. Cai and M. W. Verbrugge, *Adv. Funct. Mater.*, 2012, 22, 1647–1654.

15   N. P. Dasgupta, X. Meng, J. W. Elam and A. B. F. Martinson, *Acc. Chem. Res.*, 2015, 48, 341–348.

16   M. E. Donders, W. M. Arnoldbik, H. C. M. Knoops, W. M. M. Kessels and P. H. L. Notten, *J. Electrochem. Soc.*, 2013, 160, A3066–A3071.

17   J. Liu, M. N. Banis, Q. Sun, A. Lushington, R. Li, T.-K. Sham and X. Sun, *Adv. Mater.*, 2014, 37, 6472–6477.

18   X. Meng, X.-Q. Yang and X. Sun, *Adv. Mater.*, 2012, 24, 3589–615.

19   J. Liu and X. Sun, *Nanotechnology*, 2015, 26, 24001.

20   Y. Zhang, C. Guerra-nun, I. Utke, J. Michler, M. D. Rossell and R. Erni, *J. Phys. Chem. C*, 2015, 119, 3379–3387.

21   X. Meng, M. Norouzi, D. Geng, X. Li, Y. Zhang, R. Li, H. Abou-Rachid and X. Sun, *Appl. Surf. Sci.*, 2013, 266, 132–140.

22   W. Wang, M. Tian, A. Abdulagatov, S. M. George, Y. Lee and R. Yang, *Nano Lett.*, 2012, 12, 655–660.

23   J. Ye, A. C. Baumgaertel, Y. M. Wang, J. Biener and M. M. Biener, *ACS Nano.*, 2015, 9, 2194–2202.

24   E. Eustache, P. Tilmant, L. Morgenroth, P. Roussel, G. Patriarche, D. Troadec, N. Rolland, T. Brousse and C. Lethien, *Adv. Energy Mater.*, 2014, 4, 1301612.

25   S. K. Cheah, E. Perre, M. Rooth, M. Fondell, A. Hårsta, L. Nyholm, M. Boman, J. Lu, P. Simon and K. Edstro, *Nano Lett.*, 2009, 9, 3230–3233.

26   E. M. Lotfabad, P. Kalisvaart, K. Cui, A. Kohandehghan, M. Kupsta and D. Mitlin, *Phys. Chem. Chem. Phys.*, 2013, 15, 13646–13657.

27   S. Kim, T. H. Han, J. Kim, H. Gwon, H. Moon, S. Kang, S. O. Kim and K. Kang, *ACS Nano.*, 2009, 3, 1085–1090.

28   C. Ban, M. Xie, X. Sun, J. J. Travis, G. Wang, H. Sun, A. C. Dillon, J. Lian and S. M. George, *Nanotechnology*, 2013, 24, 424002.

29   G. Delaizir, V. Viallet, A. Aboulaich, R. Bouchet, L. Tortet, V. Seznec, M. Morcrette, J. M. Tarascon, P. Rozier and M. Dolle, *Adv. Funct. Mater.*, 2012, 22, 2140–2147.

30   S. Kinoshita, K. Okuda, N. Machida, M. Naito and T. Sigematsu, *Solid State Ionics*, 2014, 256, 97–102.

31   M. Nagao, A. Hayashi and M. Tatsumisago, *Electrochim. Acta*, 2011, 56, 6055–6059.

32   M. Nagao, A. Hayashi, M. Tatsumisago, T. Ichinose, T. Ozaki, Y. Togawa and S. Mori, *J. Power Sources*, 2015, 274, 471–476.

33   Y. Tang, Y. Zhang, W. Li, B. Ma and X. Chen, *Chem. Soc. Rev.*, 2015, 44, 5926–5940.

34   T. Aaltonen, M. Alnes, O. Nilsen, L. Costelle and H. Fjellvåg, *J. Mater. Chem.*, 2010, 20, 2877–2881.

35   Y.-C. Perng, J. Cho, D. Membreno, N. Cirigliano, B. Dunn and J. P. Chang, *J. Mater. Chem. A*, 2014, 2, 9566–9573.

36   J. Liu, M. N. Banis, X. Li, A. Lushington, M. Cai, R. Li, T.-K. Sham and X. Sun, *J. Phys. Chem. C*, 2013, 117, 20260–20267.

37   J. Hamalainen, J. Holopainen, F. Munnik, T. Hatanpaa, M. Heikkila, M. Ritala and M. Leskela, *J. Electrochem. Soc.*, 2012, 159, A259–A263.

38   B. Wang, J. Liu, Q. Sun, R. Li and T. Sham, *Nanotechnology*, 2014, 25, 504007.

39   M. Cui and P. S. Lee, *Chem. Mater.*, 2016, 28, 2934–2940.

40   Y. Cao, X. Meng and J. W. Elam, *ChemElectroChem*, 2016, 3, 1–7.

41   S. Tanaka, M. Taniguchi and H. Tanigawa, *J. Nucl. Mater.*, 2000, 287, 1405–1408.

42   Y. W. Hu, I. D. Raistrick and R. A. Huggins, *J Electrochem Soc*, 1997, 124, 1240–1242.

43   A. T. Appapillai, A. N. Mansour, J. Cho and Y. Shao-horn, *Chem. Mater.*, 2007, 89, 5748–5757.

44   Z. Jinli, W. Jiao, L. Yuanyuan, N. Ning, G. Junjie, Y. Feng and L. Wei, *J. Mater. Chem. A*, 2015, 3, 2043–2049.

45   L. Liu, J. Chan and T. Sham, *J. Phys. Chem. C*, 2010, 114, 21353–21359.

46   L. Liu, J. Li and T. Sham, *Can. J. Chem.*, 2015, 112, 106–112.

47   J. Liu, M. N. Banis, B. Xiao, Q. Sun, A. Lushington, R. Li, J. Guo, T. Sham and X. Sun, *J. Mater. Chem. A*, 2015, 3, 24281–24288.

48   W.-Q. Wu, H.-S. Rao, Y. Xu, Y.-F. Wang, C.-Y. Su and D.-B. Kuang, *Sci. Reports*, 2013, 3, 1892.

49   J. Wang, Y. Zhou, Y. Hu, R. O. Hayre and Z. Shao, *J. Phys. Chem. C*, 2011, 115, 2529–2536.

50   L. Kavan, M. Kalba, I. Exnar, V. Lorenzen, R. Nesper, M. Graetzel and J. Heyrovsky, *Chem. Mater.*, 2004, 16, 477–485.

51   N. Li, G. Liu, C. Zhen, F. Li, L. Zhang and H. Cheng, *Adv. Funct. Mater.*, 2011, 21, 1717–1722.

52   B. Xiao, X. Li, X. Li, B. Wang, C. Langford, R. Li and X. Sun, *J. Phys. Chem. C*, 2014, 118, 881–890.

53   D. Wang, D. Choi, J. Li, Z. Yang, Z. Nie, R. Kou, D. Hu, C. Wang, L. V Saraf, J. Zhang, I. A. Aksay and J. Liu, *ACS Nano.*, 2009, 3, 907–914.

54   J. B. Bates, N. J. Dudney, G. R. Gruzalski, R. A. Zuhr and A. Choudhury, *J. Power Sources*, 1993, 44, 103–110.

55   B. Wang, B. C. Chakoumakos, B. C. Sales, B. S. Kwak and J. B. Bates, *J. Solid State Chem.*, 1995, 115, 313–323.

56   B. A. R. Armstrong, G. Armstrong, J. Canales, R. García and P. G. Bruce, *Adv. Mater.*, 2005, 17, 2003–2006.

Supporting Information
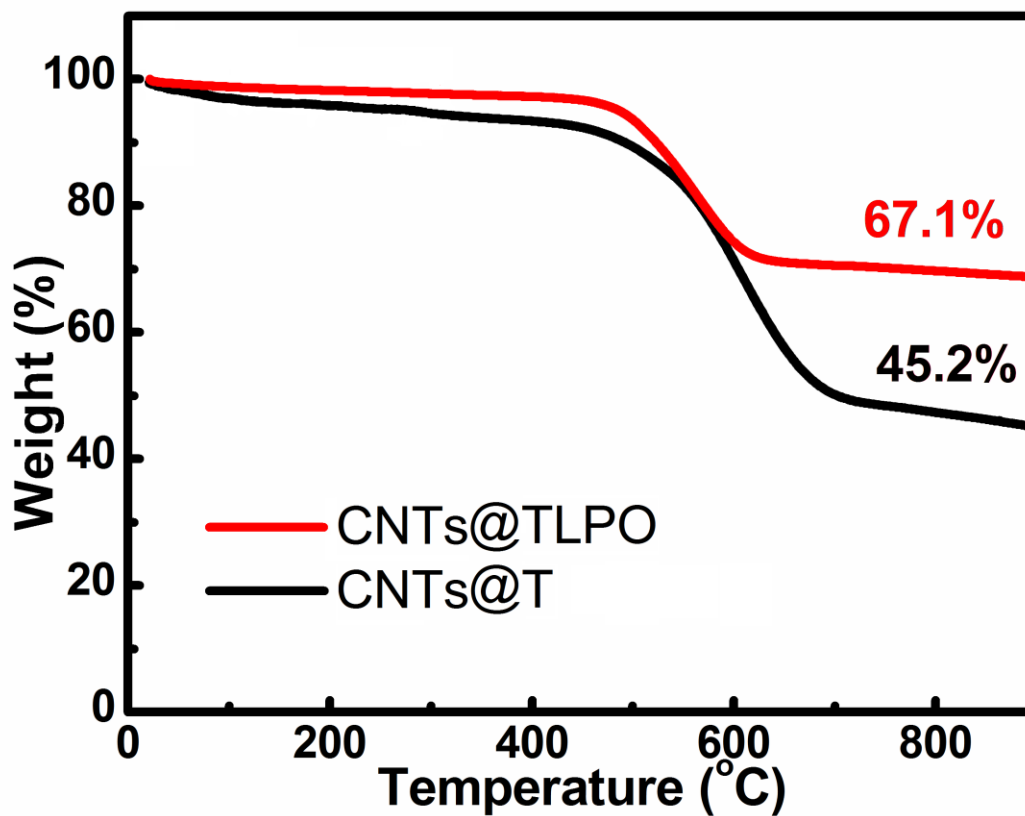
Figure 4.SI-1 TGA result for CNTs@TLPO and CNTs@T
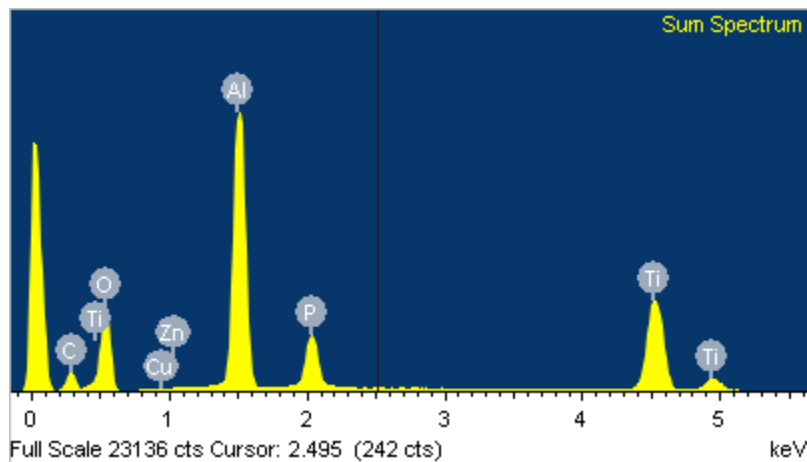
Figure 4.SI-2 EDS spectrum of TLPO/CNTs on an Al foil
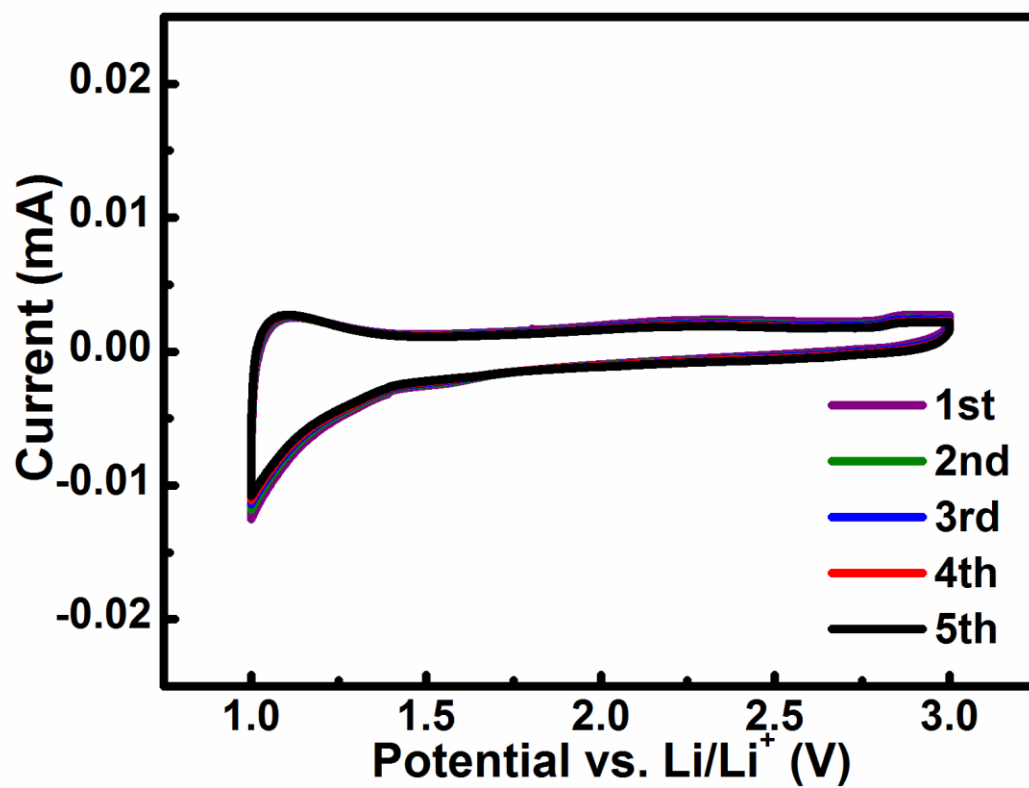
Figure 4.SI-3 Cyclic voltammetry (CV) curves of pure CNTs using a voltage window of 1.0-3.0 V versus Li/Li$^+$
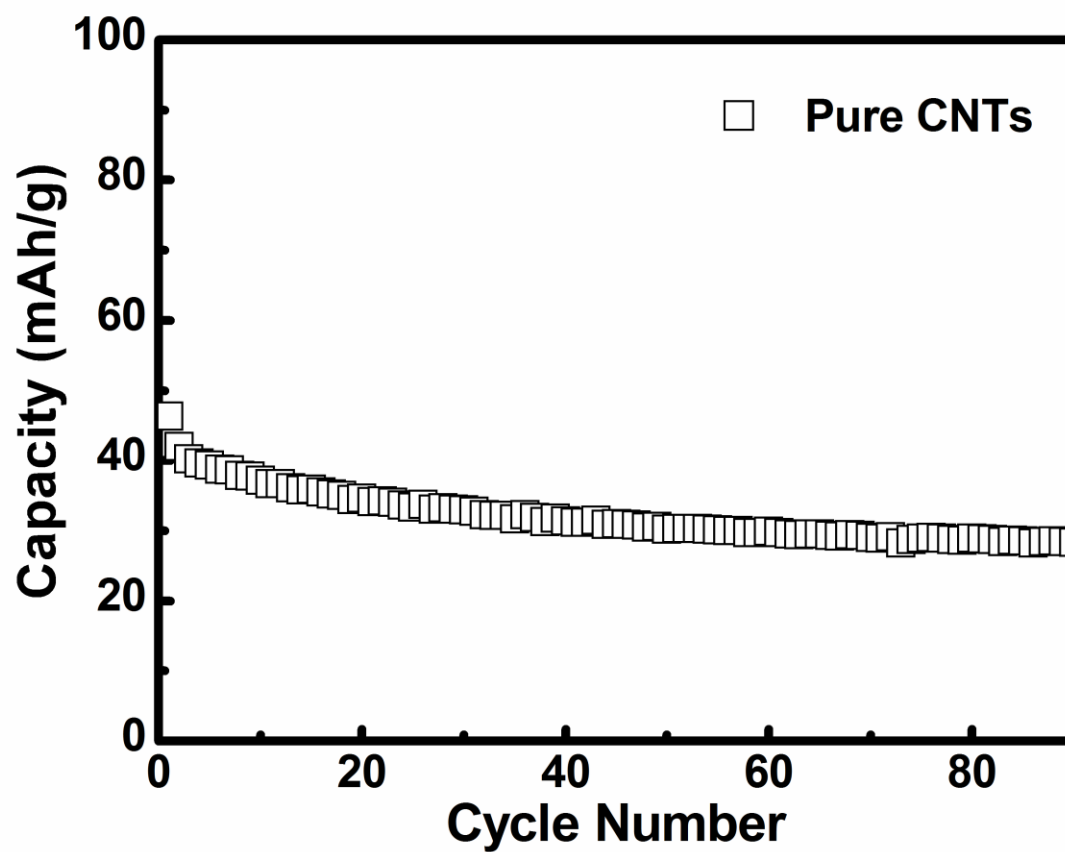
Figure 4.SI-4 Cycling stability of pure CNTs at a current density of 1C (1.0-3.0 V)
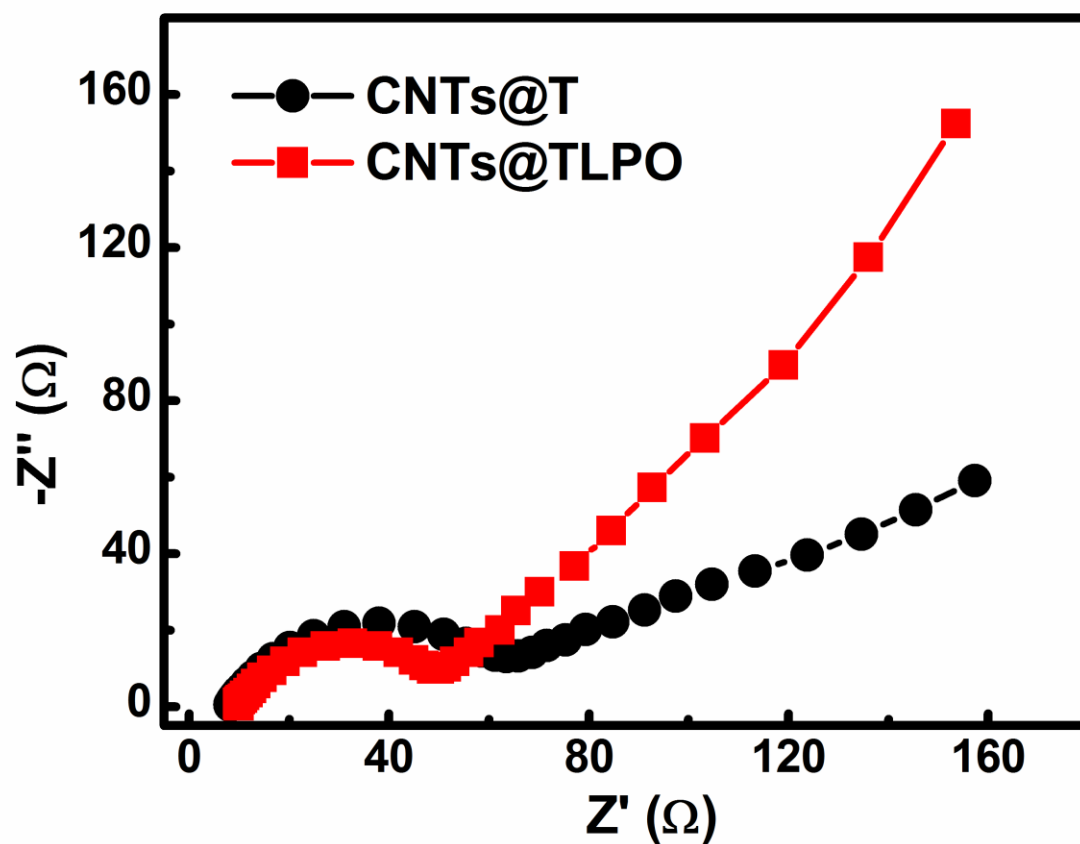
Figure 4.SI-5 Electrochemical impedance spectroscopy of the CNT@T and CNTs@TLPO electrodes; Z' and Z'' represent the real and virtual parts of the complex-value impedance, respectively
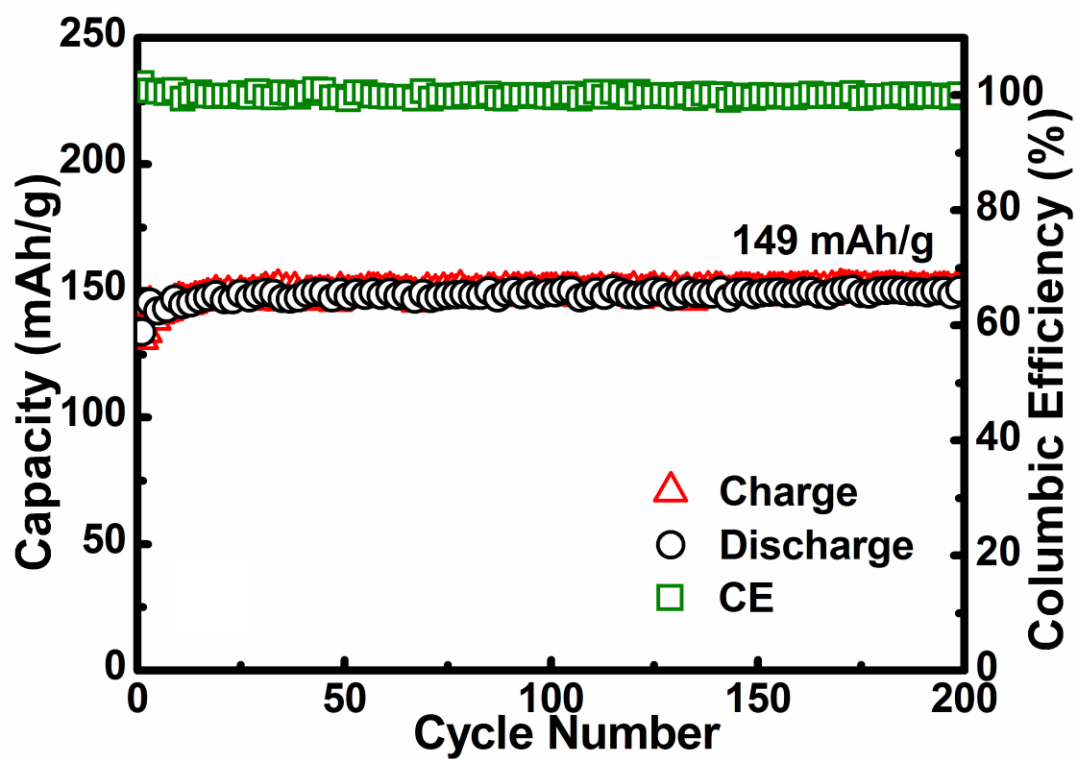
Figure 4.SI-6 Cycling stability of CNTs@T at a current density of 1C (1.0-3.0 V)

Chapter 5

5 Atomic Layer Deposited Lithium Silicates as Solid-State Electrolytes for All-Solid-State Batteries*

Development of solid-state electrolyte (SSE) thin films is a key toward the fabrication of all-solid-state batteries (ASSBs). However, it is challenging for conventional deposition techniques to deposit uniform and conformal SSE thin films in a well-controlled fashion. In this study, atomic layer deposition (ALD) was used to fabricate lithium silicate thin films as a potential SSE for ASSBs. Lithium silicates thin films were deposited by combining ALD Li_2O and SiO_2 subcycles using lithium tert-butoxide, tetraethylorthosilane, and H_2O as precursors. Uniform and self-limiting growth was achieved at temperatures between 225 and 300 °C. X-ray absorption spectroscopy analysis disclosed that the as-deposited lithium silicates were composed of SiO_4 tetrahedron structure and lithium oxide as the network modifier. X-ray photoelectron spectroscopy confirmed the chemical states of Li were the same with that in standard lithium silicate in the thin films. With one to one subcycle of Li_2O and SiO_2 the thin films had a composition close to Li_4SiO_4 whereas one more subcycle of Li_2O delivered a higher lithium content. The lithium silicate thin film prepared at 250 °C exhibited an ionic conductivity of 1.45×10^{-6} S cm^{-1} at 373 K. The high ionic conductivity of lithium silicate was due to the higher lithium concentration and lower activation energy.

---

*Note: This work has been published.

5.1 Introduction

Lithium ion batteries (LIBs) have led the revolutionary development of portable electronics in the past two decades due to their high energy density. Tremendous attention has also been directed toward improving LIBs to meet the stringent demands of hybrid electric vehicles (HEV), electric vehicles (EV), and grid energy storage systems. Deliberate and incremental progress has been made in optimizing the existing technology and the discovery of novel advanced battery materials.[1,2] One significant part of the research is ASSBs, where conventional liquid electrolyte is replaced by SSE. Liquid electrolytes carry inherent safety issues like flammability and risks of leakage, which will be eliminated by utilizing SSEs. In addition, the ASSBs provide more flexibility in battery design in order to pursue higher energy density and longer cycle life.[3–5] SSEs have primarily been incorporated in planar thin film batteries.[6,7] But the areal energy density is limited by the two dimensional design. The advent of 3D architecture enables increased energy storage in a small footprint area. Moreover, miniaturization of power sources can give rise to an enormous market expansion of microelectronics.[3,8] Despite a few 3D configurations proposed so far, it is still challenging to fabricate conformal electrodes and electrolytes in such design for 3D ASSBs.[9–12]

ALD has been widely used for depositing conformal pinhole-free thin films on high-aspect-ratio 3D structures. Vaporized precursors are sublimed and introduced into the deposition chamber alternatively. Saturated surface reactions based on the vapor-phase deposition dictate self-limiting film growths, therefore offering precise thickness control down to angstrom and tunable stoichiometry. The saturated and self-limiting surface reactions also ensure excellent coverage and uniformity on 3D substrates.[13–15] So far, various ALD processes have been established to synthesize different active materials as battery components.[7,16–18] Foremost, SSE is an indispensable component in ASSBs. Great efforts have been devoted to preparing lithium-containing thin films as SSEs by ALD, which remains to be challenging due to the limited choices of precursors and their different temperature windows.[15] Putkonen et al first reported successful synthesis of Li_2CO_3 by ALD after the evaluations of a few lithium organic compounds as lithium precursors, promoting the rapid progress of ALD in lithium containing systems.[19] Later

on, lithium lanthanum titanate was deposited by combining the subcycles of TiO_2 ($TiCl_4$-H_2O), La_2O_3 ($La(thd)_3$−O_3), and Li_2O (LiO^tBu−H_2O).[20] Other lithium-containing compounds, lithium phosphate, lithium silicate, and $LiNbO_3$,[21–27] have been deposited by applying the similar strategy of combining ALD processes to obtain multicomponent oxides. Besides, there have been significant progress in ALD synthesis of active electrode materials. As an example, we have reported that TiO_2/Li_3PO_4 nanocomposites by ALD presented outstanding electrochemical performance as anodes for LIBs.[28] Cathode materials including $LiFePO_4$, $LiCoO_2$, and lithium manganese oxides have also been developed via ALD.[7,16,29]

The ionic conductivity of SSEs must be evaluated before being used in all-solid-state lithium ion batteries. A protocol measurement of the ionic conductivity of thin films by ALD was first demonstrated by Aaltonen et al.[21] Li_2O-Al_2O_3 thin film presented an ionic conductivity at the order of 10^{-7} S cm^{-1} at 573 K after 5 h annealing at 700 °C.[21] The high temperature required in postannealing, however, can be detrimental to the thin films or the substrates (the electrodes), due to the occurrence of film cracking resulting from thermal stress. Henceforth, glassy SSEs have become promising candidates considering that the easy film formation does not require harsh post heat treatment. Moreover, high ionic conductivity can be achieved for the as-prepared thin films. Several systems have been selected and studied.[30–32] In our previous work, we have successfully developed lithium tantalate and lithium phosphate thin films with an ionic conductivity of 2×10^{-8} and 3.3×10^{-8} S cm^{-1} respectively at room temperature (RT).[31,32] Recently, lithium phosphorus oxynitride (LiPON) SSE has been synthesized by plasma enhanced ALD and thermal ALD. The ionic conductivity of LiPON was improved to the order of 10^{-7} S cm^{-1} at RT.[33–36]

Apart from the aforementioned glassy SSEs, lithium silicate glasses (Li_2O-SiO_2) possesses 'open' framework that allows isotropic lithium ion migration and thus promises good ionic conductivity. Ionic conductivity of lithium silicate ranges from 10^{-8} to 10^{-6} S cm^{-1} depending on the Li_2O and SiO_2 compositions.[37–40] Furthermore, lithium silicate is relatively stable in contact with lithium metal, thus avoiding possible reduction at negative electrode.[39,40] Hämäläinen et al established a process for lithium silicate with a

stoichiometry close to lithium metasilicate ($Li_{2.0}SiO_{2.9}$) using lithium hexamethyldisilazide [LiHMDS] as both lithium and silicon sources and ozone as the oxidant.[23] In this study, we achieved the lithium silicate (LSO) thin film growth with an alternative ALD recipe based on lithium tert-butoxide (LiO^{t}Bu), with tetraethylorthosilane (TEOS) as Si source. Local electronic structure of the ALD lithium silicate thin films was studied by X-ray absorption near edge structure (XANES). The ionic conductivity of the amorphous LSO deposited at different temperatures was evaluated.

5.2 Experimental

Lithium silicate thin films were deposited in a Savannah 100 ALD system (Cambridge Nanotech Inc.) with nitrogen as the carrier and purging gas. The ALD subcycles of Li_2O and SiO_2 were combined. The Li_2O subcycle consisted of lithium tert-butoxide [LiO^{t}Bu, $(CH_3)_3COLi$] as lithium source and H_2O as oxidant while tetraethylorthosilane (TEOS) and water were precursors for the SiO_2 ALD subcycle. LiO^{t}Bu and TEOS were sublimed at a source temperature of 170 and 65 °C respectively. The manifold was kept at 190 °C. Four different deposition temperatures were carried out, i.e. 225, 250, 275, and 300 °C, while the pulse time of LiO^{t}Bu, TEOS, and water remained at 1, 2, and 1 s respectively. One subcycle of Li_2O and one subcycle of SiO_2 composed of one full ALD cycle. 10 s of nitrogen purge was used subsequently after each precursor. Silicon (100) substrates were cleaned using a stepwise acetone, ethanol, and water rinse procedure, and then blown dry by N_2. Powder-based carbon nanotubes (CNTs) as substrates were refluxed in nitric acid (HNO_3, 70%) for 3 at 120 °C in order to remove the residual catalyst involved in the growth of CNTs. Then the treated CNTs were washed by deionized water, dispersed in ethanol, drop-casted on Al foil and dried overnight in air.

The cross section of thin films on Si substrates was observed using a field-emission scanning electron microscope (Hitachi-4800). The average thickness was measured and calculated from six randomly selected spots of each film. A Bruker D8 Advance X-ray diffraction (XRD) with Cu Kα X-ray source was employed to examine the crystal structure of the thin films on Si. X-ray photoelectron spectroscopy (XPS) [Kratos Axis

Ultra Al (alpha) spectrometer] was employed to obtain the stoichiometry of the lithium silicates on CNTs. All the XANES study in this work was conducted in Canadian Light Source (CLS) on the Soft X-ray Microcharacterization Beamline (SXRMB). A InSb (111) crystal monochromator was set up for measuring Si K-edge. Total electron yield (TEY) and X-ray fluorescence yield (FLY) spectra were collected. All XANES spectra were normalized to the incident photon flux.

For impedance testing, lithium silicates thin films were sandwiched between sputtered Au layers (~50 nm) on glass substrates. All the LSO thin films were deposited to be 130 ± 2 nm thick. The effective planar area of sandwiched SSE was 4×4 mm^2. Electrochemical impedance spectroscopy (EIS) was acquired by a CHI electrochemistry workstation. The testing frequency decreased from 200 kHz to 100 mHz within a temperature window of 303-373 K (10 K step).

5.3 Results and Discussion
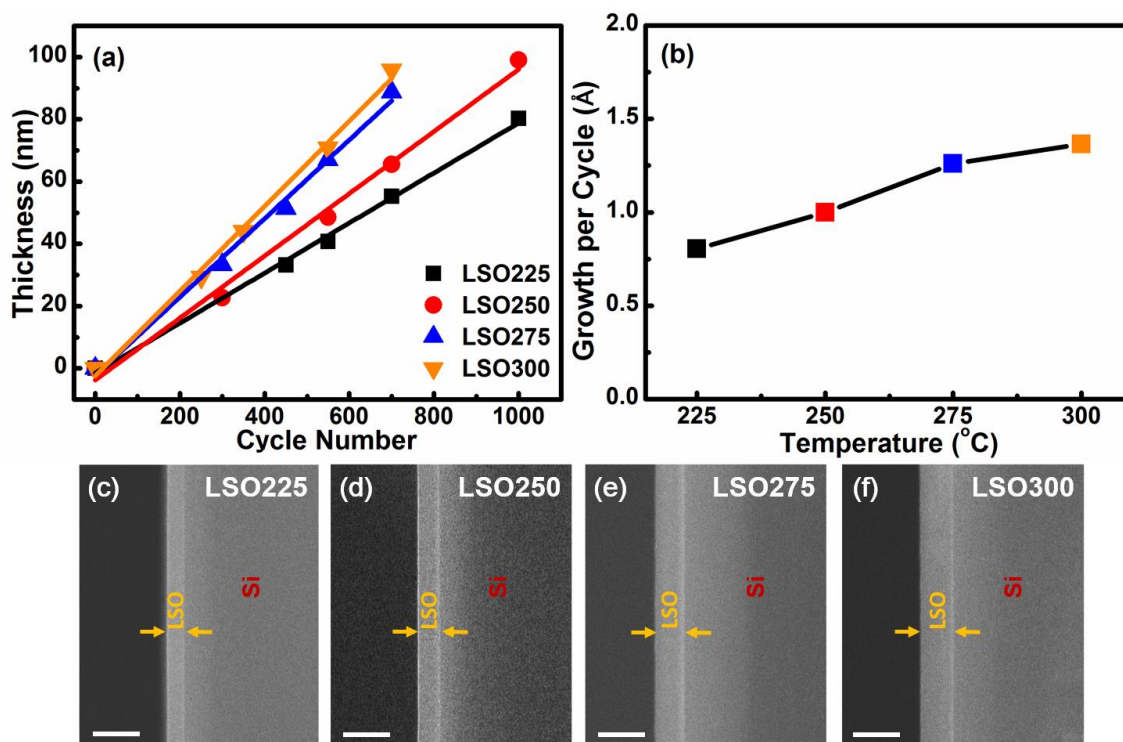
Figure 5.1 (a) Thickness of LSO thin films plotted against ALD cycle number; (b) growth per cycle of LSO at different deposition temperature; SEM pictures of the cross section of LSO thin films on silicon at (c) 225 ºC (LSO225), (d) 250 ºC (LSO250), (e) 275 ºC (LSO275), and (f) 300 ºC (LSO300) after 500 ALD cycles. The scale bar is 100 nm.

Lithium silicates thin films grown on silicon at 225 ºC (LSO225), 250 ºC (LSO250), 275 ºC (LSO275), and 300 ºC (LSO300) were examined by SEM. Figure 5.1(a) shows the film thickness plotted against the ALD cycle number, which exhibits a linear correlation after fitting the data. It is indicative of a self-saturated growth and thus a successful ALD process has been achieved at all four temperatures.[13] The cross-section views of lithium silicates thin films after 500 ALD cycles on Si substrates are displayed in Figure 5.1 (c-f). Uniform depositions can be seen at all four temperatures. The thicknesses of LSO225, LSO250, LSO275, and LSO300 thin films are measured to be 39, 49, 62, and 68 nm, respectively. ALD processes of SiO_2 using TEOS and water at low temperatures have

been reported only in the presence of the NH_3 catalyst.[41–43] The Si−OH* surface species are reported to have strong interactions with Lewis bases like ammonia and therefore the SiO−H chemical bond is weakened, making the oxygen a stronger nucleophile.[13,41] Interestingly, no deposition was observed when the SiO_2 subcycle was conducted solely without the Li_2O subcycle. This might be ascribed to the similar mechanism. By introducing the Li_2O subcycle, a Lewis base environment might be created to facilitate the ligands removal during the TEOS subcycle.[26,30,42] The slope of the linear fitting lines represents the growth per cycle (GPC), as shown Figure 5.1(b). A GPC of 0.80, 1.00, 1.26, and 1.36 Å is obtained for LSO225, LSO250, LSO275, and LSO300, respectively. A higher growth rate of lithium silicate is observed at a higher temperature. The reason could be that at elevated temperatures, the ligand exchange reaction is promoted and the reactivity of LiOⁱBu and TEOS is higher, leading to faster thin film growth.[13,23,31] When two subcycles of Li_2O were applied with one SiO_2 subcycle at 250 °C (denoted as LSO250-2), the GPC was increased to 2.57 Å [Figure 5. SI-1(a)]. The difference of GPC between LSO250 and LSO250-2 cannot be simply assigned to the extra one Li_2O subcycle considering its 'catalyzing effect' on the growth of SiO_2 proposed above. This mechanism makes it difficult to isolate the study of the growth of SiO_2. Hence, we only focused on the effect of different ALD parameters on the electronic structures and the electrochemical performances of deposited thin films.
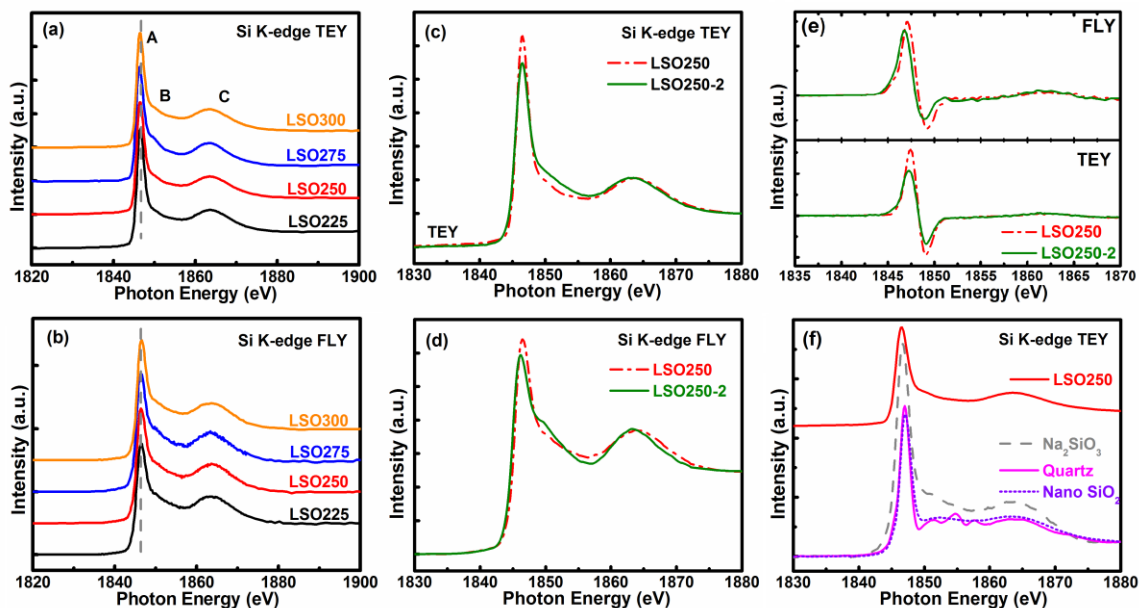
Figure 5.2 Si K-edge TEY XANES spectra at of lithium silicate thin films deposited (a) at different temperatures, (c) with different Li subcycle numbers, and (f) standard powders (Na$_2$SiO$_3$, quartz, and nano SiO$_2$). Si K-edge FLY XANES spectra at of lithium silicate thin films deposited (b) at different temperatures and (d) at 250°C with different Li subcycle number. (e) First-derivative spectra plotted from TEY and FLY spectra of LSO250 and LSO250-2

XANES at the Si K-edge was investigated the chemical environment of Si in the lithium silicate thin films. Si K-edge XANES involves the process that Si 1s electrons are excited into unoccupied states in the conduction band. The spectral features result from the dipole excitation of the core electrons to the bound and quasibound states, and are related to the local structure and bonding environment of the absorbing atom. The chemical change could be determined by the shift of edge jump threshold or the position of the first resonance (known as the whiteline).[44–50] Spectra in Figure 5.2 (a) and (c) were collected in total electron yield (TEY) mode while those in Figure 5.2 (b) and (d) were in fluorescence yield (FLY) mode. TEY measures the total yield of photoelectrons, Auger electrons, and secondary electrons (dominant), revealing the information from several nanometers deep from the surface due to the shallow electron escape depth. On the other hand, FLY detects outgoing fluorescent X-rays which has two orders of magnitude

increase in attenuation length in the solid than electrons, revealing bulk sensitive information.[47]

All the XANES spectra of the as-deposited thin films exhibited three main features, denoted as peak A, B, and C. First, comparing the four TEY spectra in Figure 5.2 (f), the whitelines of quartz SiO_2 and nano SiO_2 powders at 1846.8 eV agree well with the literature and can be attributed to the transition of Si 1s electrons to the antibonding 3p-like states (t_2) according to the dipole selection rules.[44–46] Below the edge, there is a weak shoulder peak arising from the forbidden transition from Si 1s to 3s-like states (a_1).[44,46] By introducing alkaline metals into the compound, the whiteline of LSO250 presented a red-shift of ~0.4 eV, consistent with the findings of Henderson et al.[45,48] A shift of the edge to lower energy in the spectra indicates a decrease in polymerization due to the addition of alkaline metal as a network modifier.[45,48] Besides, features in the spectrum of LSO250 resemble those for Na_2SiO_3 and standard lithium silicates in refs 45, 48, and 50, suggesting Si in the lithium silicate thin films exists in similar tetrahedral oxygen ligand environment.

Second, the TEY spectra in Figure 5.2 (a) show the same resonances A, B, and C. Peak A locates at the same position of 1846.4 eV, which is identified to be the 1s to t_2 transition for the four-coordinated Si. No shift is observable, which implies the same local structure Si^{4+} bonded with four oxygens on the surface in the thin films deposited at different temperatures.[45,48] The only peak B (~1849.4 eV) between A and C instead of the well-resolved features seen in quartz is present. Essentially spin forbidden transitions of Si 1s electrons to empty 3d states account for the features in this region, which is likely arising from local distortion. The alleviated distortion of the SiO_4 tetrahedron in amorphous systems and nano powders gives less chance for the overlapping of unoccupied 3p-like features with the 3d states, generating less symmetry-forbidden shape resonance. Therefore, the patterns are flattened out, indicating the amorphous nature of the thin film structures.[46,47] This was further verified by low-angle X-ray diffraction, where no diffraction patterns were found in the spectra, confirming the absence of long-range order.[28] Furthermore, the relative intensity of peak A to B remains almost the same for the four spectra. Based on Henderson and Li et al.'s work on the alkaline silicates, the

network modifier in our case is only Li_2O in the binary glass. The ratio of peak A to B implies similar Li_2O content in the thin films prepared at different temperatures.[45,46,48] The FLY spectra in Figure 5.2 (b) further substantiate the discussions above. The FLY XANES spectra suffer from the thickness effect, where the photon is self-absorbed by the thin films. The intensity of the whiteline is therefore reduced and all the features are broadened.[47] Nevertheless, a comparison between TEY and FLY spectra disclose similar electronic structure of Si at the surface and in the bulk of the LSO samples.

XANES spectra of LSO250 and LSO250-2 are compared in Figure 5.2 (c-e). First, peak A, B, and C experience a shift to lower energy in both TEY and FLY spectra when the ALD subcycle number of Li_2O increase from 1 to 2. The shift of ~ 0.3 eV is easily observable in the first derivative spectra shown in Figure 5.2 (e). By increasing the Li_2O subcycle number, higher Li to Si content ratio would be expected theoretically. The Li element is very electropositive, which will contribute more electrons toward Si. Si could exist in a chemical state a little lower than 4+ in the context of a Li-richer environment in LSO250-2, which can explain the red-shift of the whitelines as well as the edge jump. The shift also presages a possible lower degree of polymerization of SiO_4 tetrahedron, which is in good agreement with the effect of additional network modifier mentioned above.[45,46,48,50] The conclusion is further confirmed by the decrease of peak intensity of peak A to B from LSO250 to LSO250-2.[48,51,52] In addition, peak C is narrower and of higher intensity for LSO250-2 compared with LSO250. The higher lithium content might lead to an improvement in local order.[45,53]
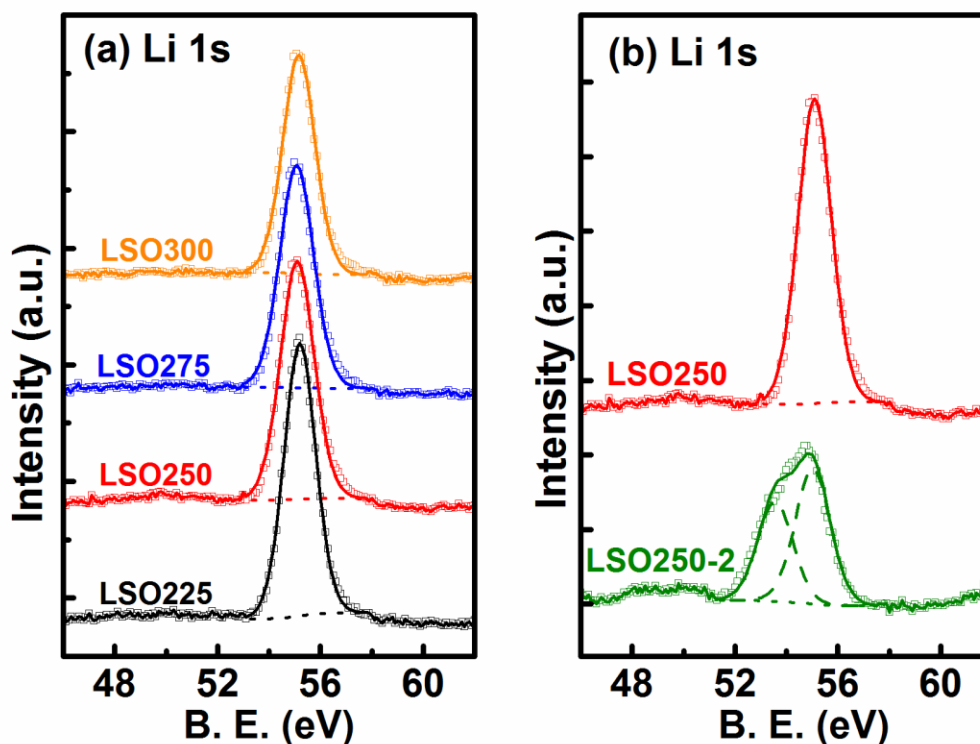
Figure 5.3 Deconvolution of Li 1s XPS spectra of lithium silicate thin films deposited (a) at different temperatures and (b) with different Li subcycle numbers

To further analyze the chemical compositions of LSO, XPS was conducted using CNTs as substrates instead of Si wafers to avoid the interference of the background Si signal. XPS survey scans are provided in the Supporting Information. The peaks for C 1s and some oxygen signals are from the CNTs substrates and the functional groups attached. Apart from it, the thin films consist of the elements Li, Si, and O. The atomic ratio of Li to Si is calculated from the atomic percentage and lists 3.25, 3.74, 3.57, 3.51, and 5.84 corresponding to LSO225, LSO250, LSO275, LSO300, and LSO0250-2, respectively. The four lithium silicate thin films with one subcycle of Li_2O resemble a close stoichiometry to Li_4SiO_4 considering the XPS and the XANES results.[54–56] With two subcycles of Li_2O, a much higher lithium content is obtained, which coincides very well with the conclusions from the XANES spectra. Figure 5.3 shows the Li 1s high resolution spectra with the deconvolution of the peaks. In Figure 5.3 (a), only one sharp and symmetric peak can be detected at 55.2 eV for all four spectra of thin films deposited at

the four temperatures, indicating there is solely one chemical state (Li−O) in each sample. The single peak can be designated to that of lithium silicate (Li_4SiO_4) referring to the literature.[54–56] Also, no evident shift of the peak position can be seen among the four spectra, which means the chemical state of Li in LSO is similar to that in standard Li_4SiO_4. Moreover, Figure 5.3 (b) includes the Li 1s XPS spectra of LSO250 and LSO250-2. Differing from the spectrum of LSO250, the deconvolution shows that another peak emerges at a lower energy of 53.6 eV except the one belonging to lithium silicate. The extra peak can be assigned to lithium oxide (Li_2O).[57–59] Therefore, the Li element in $Li_{5.84}SiO_z$ (LSO250-2) exists in two different environments, namely Li−O−Li (44%) and Li−O−Si (56%). The occurrence of Li−O−Li arised from the extra Li_2O subcycle in the ALD process. Both the quantitative and qualitative results of XPS are in excellent accordance with the XANES results.
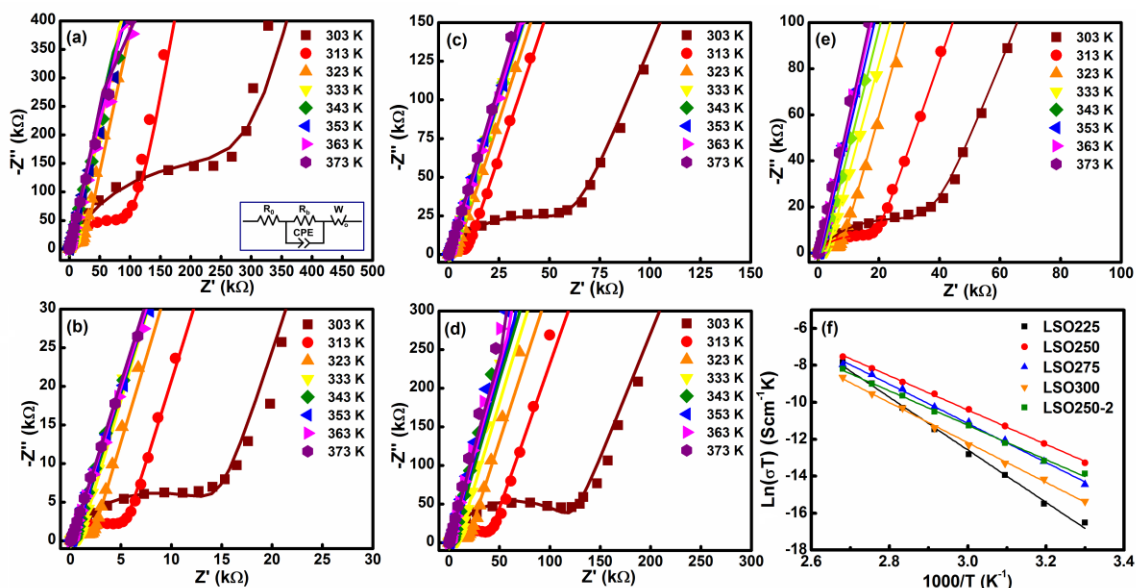
Figure 5.4 EIS plots of LSO thin films (a) LSO225, (b) LSO250, (c) LSO275, (d) LSO300, and (e) LSO250-2; (f) Arrhenius plots measured from 313 to 383 K (solid lines were simulated to fit the measured scattered points).

Ionic conductivities of LSO thin films were measured by EIS. Figure 5.4 (a-e) displays the Cole-Cole plots acquired at a temperature range from 313 to 383 K, followed by the Arrhenius plot of the ionic conductivity [Figure 5.4(f)]. At the high frequency region, one

semicircle was presented, attributed to the bulk resistance. At low frequency region, an inclined tail can be ascribed to the polarization of the electrode-electrolyte interface. One important point to note is that this feature is typical of an ionic conductor when an open circuit diffusion takes place by using an ionic blocking electrode (Au for instance).[32,60] The impedance plots were fitted using an equivalent circuit depicted in the inset of Figure 5.4(a), where R_0 and R_b denote the contact ohmic resistance and the bulk resistance of the electrolytes. A constant-phase element (CPE) was employed in the circuit, which represents the resultant bulk capacitance of the LSO thin films. W is the finite length Warburg element, occurring when charge carriers diffuse through the solid.[61]

The Li$^+$ conductivity of LSO thin films was calculated by applying the empirical R_b values into the equation, $\sigma = d/(AR_b)$ wherein $d = 130$ nm and A = sandwiched area between the gold electrodes.[21,31,32] Comparing the thin films deposited with one Li subcycle, thin films LSO225, LSO250, LSO275, and LSO300 deliver an ionic conductivity of 1.05×10^{-6}, 1.45×10^{-6}, 9.41×10^{-7}, and 4.69×10^{-7} S cm^{-1}, respectively, at the maximum measuring temperature 373 K (100 °C), among which thin film LSO250 exhibits the highest value. Similarly, at the minimum measuring temperature 303 K (30 °C), the ionic conductivity measures to be 2.18×10^{-10}, 5.72×10^{-9}, 1.73×10^{-9}, and 7.06×10^{-10} S cm^{-1} for thin films LSO225, LSO250, LSO275, and LSO300, respectively. Although the ionic conductivities are of similar level, the best ionic conductivity can still be obtained from thin film LSO250. The reason can be associated with the lithium content of the as-prepared thin films. In silicate glass solid-state electrolyte systems, the elementary structural unit (SU) is SiO_4 tetrahedron sharing bridging oxygens (BO). A continuous 3D network over the entire volume forms. Introduction of alkali oxides leads to the disruption of the Si−O−Si bonds and consequently the formation of nonbridging oxygens (NBO), which would be beneficial to the conductivity. To improve the conductivity, one critical factor is the charge carrier concentration, which is lithium in this case. Among the four lithium silicate thin films, LSO250 has the highest lithium to silicon ratio (3.74), which is also the closest stoichiometry to Li_4SiO_4.[37,39,62–64] It is worth mentioning that to a certain degree a higher content of lithium might give rise to a better ionic conductivity, primarily owing to a reduced activation energy.[62,65–68] The value of E_a was calculated from the slope of the linear lines [Figure 5.4(f)], which are 1.22, 0.80,

0.91, and 0.93 eV for LSO225, LSO250, LSO275, and LSO300, respectively. The measured values are consistent with the range of E_a of lithium silicate glasses.[37,65–67,69] This provides further evidence for the above theory that LSO250 indeed has the lowest activation energy.

Furthermore, the ionic conductivity of LSO250-2 was also evaluated and presented in Figure 5.4(e), which varied from 3.13×10^{-9} to 7.46×10^{-7} S cm^{-1} from 303 to 373 K. The ionic conductivity of LSO250-2 is lower than that of LSO250, albeit LSO250-2 has a stoichiometry of $Li_{5.84}SiO_z$ which contains much more Li than LSO250. However, the activation energy of thin films LSO250-2 is 0.799 eV, almost the same with that of LSO250 (0.797 eV to be exact). The possible reasons are the following. First, ion motion in disordered solids can be described by activated hopping between charge-compensating sites. Conventionally, point defects form based on two models which are Schottky and Frankel processes. The former one involves cation-anion vacancy pairs while the latter relates to cation or anion vacancy-interstitial pairs. The amount of the defects affects the concentration of charge carries. [62,70] When there are much more equivalent sites than the available mobile ions to fill in, increasing the mobile ion density would benefit the ionic conductivity. The creation of NBO provides extra hopping sites and lowers the activation energy. However, to a certain degree, extra lithium into the system does not necessarily mean an increase in the mobile ion concentration, but probable occupants that 'block' the possible diffusion pathways (vacancies). Meanwhile, the highest potential barrier that the ions have to conquer in diffusion could remain almost unchanged.[39,62,70] With the above being said, there is still severe paucity in the information on the mechanisms behind ion dynamics in amorphous ion conductors. Further studies and calculations are urged to advance the understanding of glassy solid-state electrolytes.

5.4 Conclusions

ALD prepared lithium silicate SSEs were achieved at 225, 250, 275, and 300 °C with LiO^{t}Bu, TEOS, and H_2O as sources. Linear growth was obained with a GPC of 0.80, 1.00, 1.26, and 1.36 Å, respectively. At a deposition temperature of 250 °C, the GPC was also obtained with increased Li_2O subcycle number, which was 2.57 Å. The presence of

Li_2O subcycle helps facilitate the growth of SiO_2. XANES analysis showed that Si in thin films share the same SiO_4 tetrahedral structure from the surface to the bulk and the thin films were amorphous. By introducing lithium oxide as the network modifier, the polymerization degree or long-range order was decreased. Extra lithium affected the bonding structures around Si. XPS results gave the ratio of Li to Si which was closed to the stoichiometry of Li_4SiO_4 except LSO250-2 with a much higher lithium content. XPS also confirmed that all the as-deposited lithium silicate thin films existed in similar chemical structure as that in standard Li_4SiO_4. Furthermore, the Li^+ conductivity of the thin film solid-state electrolytes was measured. LSO250 exhibited the best conductivity of 5.72×10^{-9} S cm^{-1} at 303 K. Incorporation of more Li improved the ionic conductivity but only to a certain degree. It is expected that the lithium silicate thin films developed by ALD can find potential applications in 3D all-solid-state batteries.

Acknowledgement

Supporting Information

The Supporting Information is available free of charge on the ACS Publications website at DOI:

10.1021/acsami.7b07113

LSO250-2 film thickness as a function of ALD cycle number, SEM of cross section of LSO250-2 on Si, deposition of LSO250 on CNTs, and XPS survey scans of LSO thin films

The authors declare no competing financial interest.

References

1   J. B. Goodenough and K.-S. Park, *J. Am. Chem. Soc.*, 2013, **135**, 1167–1176.

2   E. M. Erickson, C. Ghanty and D. Aurbach, *J. Phys. Chem. Lett.*, 2014, **5**, 3313–3324.

3   J. F. M. Oudenhoven, L. Baggetto and P. H. L. Notten, *Adv. Energy Mater.*, 2011, **1**, 10–33.

4   S. Ferrari, M. Loveridge, S. D. Beattie, M. Jahn, R. J. Dashwood and R. Bhagat, *J. Power Sources*, 2015, **286**, 25–46.

5   C. Sun, J. Liu, Y. Gong, D. P. Wilkinson and J. Zhang, *Nano Energy*, 2017, **33**, 363–386.

6   J. B. Bates, N. J. Dudney, B. Neudecker, A. Ueda and C. D. Evans, *Solid State Ionics*, 2000, **135**, 33–45.

7   M. E. Donders, W. M. Arnoldbik, H. C. M. Knoops, W. M. M. Kessels and P. H. L. Notten, *J. Electrochem. Soc.*, 2013, **160**, A3066–A3071.

8   M. Roberts, P. Johns, J. Owen, D. Brandell, K. Edstrom, G. El Enany, C. Guery, D. Golodnitsky, M. Lacey, C. Lecoeur, H. Mazor, E. Peled, E. Perre, M. M. Shaijumon, P. Simon and P.-L. Taberna, *J. Mater. Chem.*, 2011, **21**, 9876–9890.

9   Y. J. Nam, S. J. Cho, D. Y. Oh, J. M. Lim, S. Y. Kim, J. H. Song, Y. G. Lee, S. Y. Lee and Y. S. Jung, *Nano Lett.*, 2015, **15**, 3317–3323.

10   Y. Yang, Z. Peng, G. Wang, G. Ruan, X. Fan, L. Li and H. Fei, *ACS Nano.*, 2014, **8**, 7279–7287.

11   Y. Zhang, J. Lai, Y. Gong, Y. Hu, J. Liu, C. Sun and Z. L. Wang, *ACS Appl. Mater. Interfaces*, 2016, **8**, 34309–34316.

12   A. A. Talin, D. Ruzmetov, A. Kolmakov, K. McKelvey, N. Ware, F. El Gabaly, B. Dunn and H. S. White, *ACS Appl. Mater. Interfaces*, 2016, **8**, 32385–32391.

13   S. M. George, *Chem. Rev.*, 2010, **110**, 111–31.

14   X. Meng, X.-Q. Yang and X. Sun, *Adv. Mater.*, 2012, **24**, 3589–615.

15   J. Liu and X. Sun, *Nanotechnology*, 2015, **26**, 24001.

16   J. Liu, M. N. Banis, Q. Sun, A. Lushington, R. Li, T.-K. Sham and X. Sun, *Adv. Mater.*, 2014, **37**, 6472–6477.

17   X. Li, X. Meng, J. Liu, D. Geng, Y. Zhang, M. N. Banis, Y. Li, J. Yang, R. Li, X. Sun, M. Cai and M. W. Verbrugge, *Adv. Funct. Mater.*, 2012, **22**, 1647–1654.

18   C. Liu, E. I. Gillette, X. Chen, A. J. Pearse, A. C. Kozen, M. A. Schroeder, K. E. Gregorczyk, S. B. Lee and G. W. Rubloff, *Nat. Nanotechnol.*, 2014, **9**, 1031–1039.

19   M. Putkonen, T. Aaltonen, M. Alnes, T. Sajavaara, O. Nilsen and H. Fjellvåg, *J. Mater. Chem.*, 2009, **19**, 8767–8771.

20   T. Aaltonen, M. Alnes, O. Nilsen, L. Costelle and H. Fjellvåg, *J. Mater. Chem.*, 2010, **20**, 2877–2881.

21   T. Aaltonen, O. Nilsen, A. Magrasó and H. Fjellvåg, *Chem. Mater.*, 2011, 4669–4675.

22   J. Hamalainen, J. Holopainen, F. Munnik, T. Hatanpaa, M. Heikkila, M. Ritala and M. Leskela, *J. Electrochem. Soc.*, 2012, **159**, A259–A263.

23   J. Hämäläinen, F. Munnik, T. Hatanpää, J. Holopainen, M. Ritala and M. Leskelä, *J. Vac. Sci. Technol. A*, 2012, **30**, 01A106.

24   E. Østreng, H. H. Sønsteby, T. Sajavaara, O. Nilsen and H. Fjellvåg, *J. Mater. Chem. C*, 2013, **1**, 4283–4290.

25   D. J. Comstock and J. W. Elam, *J. Phys. Chem. C*, 2013, **117**, 1677–1683.

26   A. S. Cavanagh, Y. Lee, B. Yoon and S. M. George, *ECS Trans.*, 2010, **33**, 223–229.

27   E. Østreng, P. Vajeeston, O. Nilsen and H. Fjellvåg, *RSC Adv.*, 2012, **2**, 6315–6322.

28   B. Wang, J. Liu, Q. Sun, B. Xiao, R. Li, T. K. Sham and X. Sun, *Adv. Mater. Interfaces*, 2016, **3**, 1600369.

29   V. Miikkulainen, A. Ruud, E. Østreng, O. Nilsen, M. Laitinen, T. Sajavaara and H. Fjellvåg, *J. Phys. Chem. C*, 2014, **118**, 1258–1268.

30   Y.-C. Perng, J. Cho, D. Membreno, N. Cirigliano, B. Dunn and J. P. Chang, *J. Mater. Chem. A*, 2014, **2**, 9566–9573.

31   B. Wang, J. Liu, Q. Sun, R. Li and T. Sham, *Nanotechnology*, 2014, **25**, 504007.

32   J. Liu, M. N. Banis, X. Li, A. Lushington, M. Cai, R. Li, T.-K. Sham and X. Sun, *J. Phys. Chem. C*, 2013, **117**, 20260–20267.

33   A. C. Kozen, A. J. Pearse, C. Lin, M. Noked and G. W. Rubloff, *Chem. Mater.*, 2015, **27**, 5324–2331.

34   M. Nisula, Y. Shindo, H. Koga and M. Karppinen, *Chem. Mater.*, 2015, **27**, 6987–6993.

35   S. Shibata, *J. Electrochem. Soc.*, 2016, **163**, 2555–2562.

36   A. J. Pearse, T. E. Schmitt, E. J. Fuller, F. El-Gabaly, C. F. Lin, K. Gerasopoulos, A. C. Kozen, A. A. Talin, G. Rubloff and K. E. Gregorczyk, *Chem. Mater.*, 2017, **29**, 3740–3753.

37   A. Nakagawa, N. Kuwata, Y. Matsuda and J. Kawamura, *J. Phys. Soc. Japan*, 2010, **79**, 98–101.

38   T. Minami, A. Hayashi and M. Tatsumisago, *Solid State Ionics*, 2000, **136**–**137**, 1015–1023.

39   J. B. Bates, N. J. Dudney, G. R. Gruzalski, R. A. Zuhr, A. Choudhury, C. F. Luck and J. D. Robertson, *Solid State Ionics*, 1992, **53**, 647–654.

40   T. Minami, a Hayashi and M. Tatsumisago, *Solid State Ionics*, 2006, **177**, 2715–2720.

41   J. W. Klaus, O. Sneh and S. M. George, *Sci. (Washington, DC, U. S.)*, 1997, **278**, 1934–1936.

42   J. D. Ferguson, E. R. Smith, a. W. Weimer and S. M. George, *J. Electrochem. Soc.*, 2004, **151**, G528–G535.

43   Y. Du, X. Du and S. M. George, *J. Phys. Chem. C*, 2007, **111**, 219–226.

44   D. Li, G. M. Bancroft, M. Kasrai, M. E. Fleet, X. H. Feng, K. H. Tan and B. X. Yang, *Solid State Commun.*, 1993, **87**, 613–617.

45   G. S. Henderson, *J. Non. Cryst. Solids*, 1995, **183**, 43–50.

46   D. Li, G. M. Bancroft, M. E. Fleet and X. H. Feng, *Phys. Chem. Miner.*, 1995, **22**, 115–122.

47   F. Zhang, L. S. Liao, W. H. Chan, S. T. Lee, R. Sammynaiken, T. K. Sham and T. Si, *Phys. Rev. B Condens. Matter Mater. Phsys*, 2000, **61**, 8298–8305.

48   G. S. Henderson and J. C. St-Amour, *Chem. Geol.*, 2004, **213**, 31–40.

49   S. P. Thompson, *Astron. Astrophys.*, 2008, **484**, 251–265.

50   M. Yamada, a. Inaba, a. Ueda, K. Matsumoto, T. Iwasaki and T. Ohzuku, *J. Electrochem. Soc.*, 2012, **159**, A1630–A1635.

51   D. Cabaret, *J. Non. Cryst. Solids*, 2001, **289**, 1–8.

52   L. Cormier, P. Gaskell, G. Calas and a. Soper, *Phys. Rev. B*, 1998, **58**, 11322–11330.

53   V. Nazabal, E. Fargin, G. Le Flem, V. Briois, C. C. D. Moulin, T. Buffeteau and B. Desbat, *J. Appl. Phys.*, 2000, **88**, 6245–6251.

54   S. Buchner, C. Radtke and N. M. Balzaretti, *J. Inorg. Non-Metallic Mater.*, 2013, **3**, 15–21.

55   B. H. W. S. De Jong, D. Ellerbroek and A. L. Spek, *Acta Crystallogr. Sect. B*, 1994, **50**, 511–518.

56   P. C. Soares Jnr, P. A. P. Nascente and E. D. Zanotto, *Phys. Chem. Glas.*, 2002, **43**, 143–146.

57   A. C. Kozen, A. J. Pearse, C.-F. Lin, M. A. Schroeder, M. Noked, S. B. Lee and G. W. Rubloff, *J. Phys. Chem. C*, 2014, **118**, 27749–27753.

58   Y.-C. Lu, E. J. Crumlin, G. M. Veith, J. R. Harding, E. Mutoro, L. Baggetto, N. J. Dudney, Z. Liu and Y. Shao-Horn, *Sci. Rep.*, 2012, **2**, 715.

59   K. P. C. Yao, D. G. Kwabi, R. a. Quinlan, a. N. Mansour, A. Grimaud, Y.-L. Lee, Y.-C. Lu and Y. Shao-Horn, *J. Electrochem. Soc.*, 2013, **160**, A824–A831.

60   R. Murugan, V. Thangadurai and W. Weppner, *Angew. Chem. Int. Ed.*, 2007, **46**, 7778–7781.

61   J. R. Macdonald, *Ann. Biomed. Eng.*, 1992, **20**, 289–305.

62   H. L. Tuller, D. P. Button and D. R. Uhlmann, *J. Non. Cryst. Solids*, 1980, **40**, 93–118.

63   R. Prasada Rao, T. D. Tho and S. Adams, *Solid State Ionics*, 2010, **181**, 1–6.

64   H. Lammert, M. Kunow and A. Heuer, *Phys. Rev. Lett.*, 2003, **90**, 215901.

65   R. J. Charles, *J. Am. Ceram. Soc.*, 1966, **49**, 55–62.

66   B. J. Neudecker and W. Weppner, *J. Electrochem. Soc.* , 1996, **143**, 2198–2203.

67   R. J. Charles, *J. Am. Ceram. Soc. Soc.*, 2006, **46**, 460–466.

68   O. L. Anderson and D. A. Stuart, *J. Am. Ceram. Soc.*, 1954, **37**, 573–580.

69   K. Otto and M. E. Milberg, *J. Am. Ceram. Soc.*, 1968, **51**, 326–329.

70   J. C. Dyre, P. Maass, B. Roling and D. L. Sidebottom, *Reports Prog. Phys.*, 2009, **72**, 46501.

Supporting Information
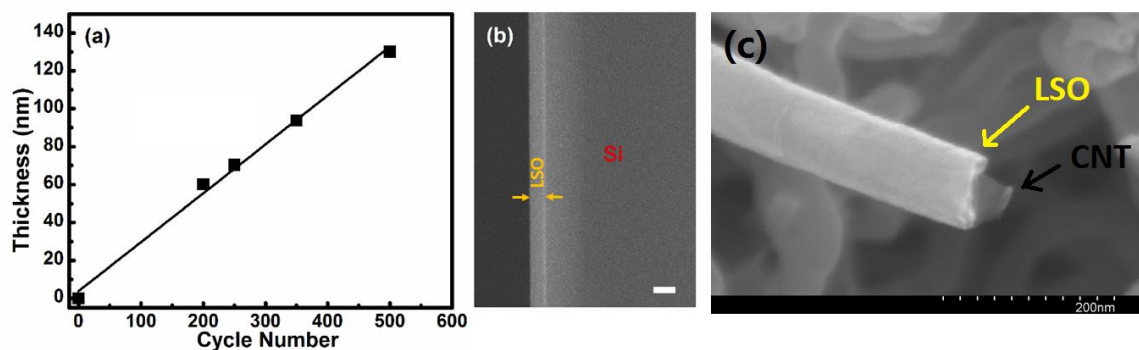
Figure 5.SI-1 (a) Thickness of the lithium silicate thin film as a function of ALD cycle number; (b) cross-section SEM picture of the ALD deposited lithium silicate thin film using on Si (100) substrate after 500 ALD cycles at 250 °C (LSO250-2).The scale bar is 200 nm. (c) SEM morphology of LSO250 on CNTs after 250 cycles
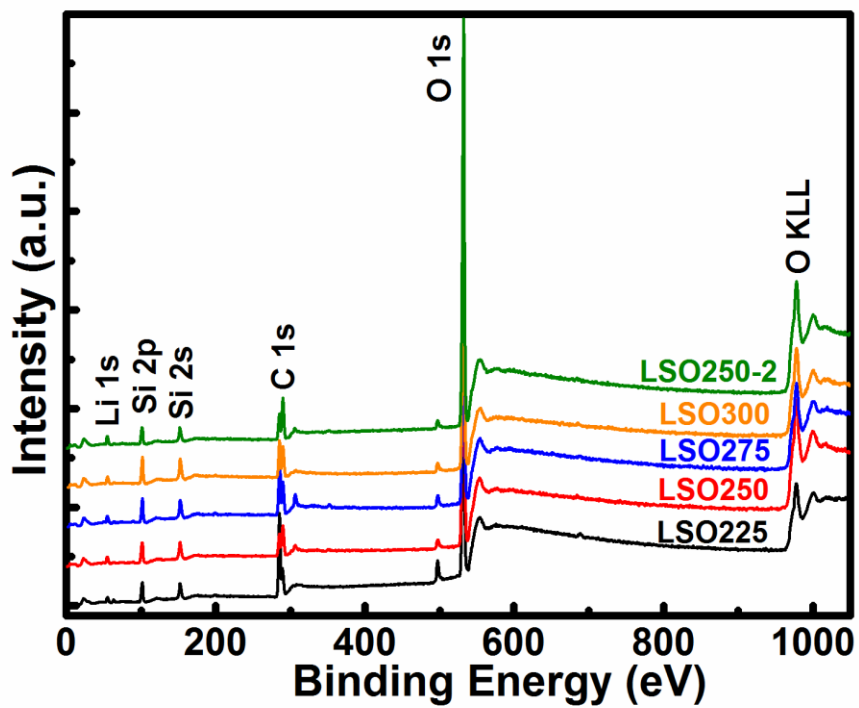
Figure 5.SI-2 XPS survey of lithium silicate thin films deposited on carbon nanotubes (CNTs)

Chapter 6

6 Atomic Layer Deposition of Lithium Niobium Oxides as Potential Solid-State Electrolytes for Lithium Ion Batteries*

The development of solid-state electrolytes by atomic layer deposition (ALD) holds unparalleled advantages towards the fabrication of next-generation solid-state batteries. Lithium niobium oxide (LNO) thin films with well-controlled film thickness and composition were successfully deposited by ALD at a deposition temperature of 235 °C using lithium tert-butoxide and niobium ethoxide as Li and Nb sources, respectively. Furthermore, incorporation of higher Li content was achieved by increasing the Li to Nb subcycle ratio. In addition, detailed X-ray absorption near edge structure (XANES) studies of the amorphous LNO thin films on the Nb L-edge revealed the existence of Nb as Nb^{5+} in a distorted octahedral structure. The octahedrons in niobium oxide thin films experienced severe distortions, which could be gradually alleviated upon the introduction of Li atoms into the thin films. The ionic conductivities of the as-prepared LNO thin films were also measured, with the highest value achieving 6.39×10^{-8} S cm^{-1} at 303 K with an activation energy of 0.62 eV

6.1 Introduction

Lithium ion batteries (LIBs) have been the subject of extensive studies in the past decades for a wide range of applications including portable electronics, electric vehicles, and grid energy storage systems. However, the increasing demands of technological advancements require safer and longer-lasting battery systems with higher energy density.[1–4] One of the most promising avenues is the development of all solid-state batteries (ASSBs). The direct replacement of flammable liquid electrolytes used in conventional LIBs with solid-state-electrolytes (SSEs) can significantly reduce the inherent safety risks which might lead to catastrophic battery failures. Additionally, SSEs provide better thermal stability, increased electrochemical stability, and in some cases, wider voltage windows.[5–7] Furthermore, SSEs allow for conceptual innovations in battery design, enabling the switch from two-dimensional (2D) liquid electrolyte batteries to three-dimensional (3D) ASSBs. In those proposed designs, the vastly increased surface area allows for higher energy densities in a limited areal footprint while the short diffusion paths can enable good power density.[8–11]

However, the fabrication process of 3D ASSBs has significant challenges that need to be addressed. The SSEs must be deposited homogeneously and uniformly over a substrate with high aspect ratio, which can only be achieved by atomic layer deposition (ALD).[12–14] Compared to physical deposition techniques like pulsed laser deposition (PLD) or sputtering, ALD is based on chemical reactions where the vapor-phase precursors are alternatively pulsed into the reaction chamber and react in a self-limiting manner. The self-limiting surface reactions enable precise control over film thickness and guarantees excellent coverage and uniformity on the substrates.[15–19] In recent times there have been significant efforts dedicated to the development of ALD processes of lithium-containing compounds for SSE materials. Lithium carbonate was first successfully synthesized by Putkonen et al., which initiated a great leap-forward in the development of lithium-containing systems by ALD.[20] Subsequently, several SSE materials such as lithium lanthanum titanate, lithium alumina, lithium tantalate, lithium phosphate, lithium lanthanum zirconia (LLZO), and lithium phosphorus oxynitride (LiPON) have been reported.[21–30] Among the inorganic SSEs, crystalline systems such as LLZO would

require drastic post heat treatment, which could lead to severe problems in the measurement of ionic conductivity and even the fabrication of ASSBs.[22,24,27] In addition, it is difficult to obtain a pure phase SSE without carefully tuning the composition of the as-prepared materials. Therefore, glassy SSEs attract more attention due to the fact that they require no further annealing. Among the potential candidates, LiPON has been one of the most popular SSEs for thin film batteries. Recently, ALD processes of LiPON thin films have been established of which the conductivity can reach as high as 10^{-7} S cm^{-1} at room temperature.[14,28–30]

Apart from the aforementioned SSE materials, lithium niobate glasses have demonstrated good ionic conductivity. Lithium ions can move isotropically in the randomly cross-linked glass networks, giving a conductivity of $10^{-5}\sim 10^{-9}$ S cm^{-1} under different synthesis conditions.[31–36] In addition, lithium niobates have been proven to be excellent interface materials for ASSBs.[37,38] In this work, we realize lithium niobium oxide thin film deposition with lithium tert-butoxide (LiO^{t}Bu) as the Li source and niobium ethoxide [Nb(OEt)$_5$] as the Nb source. Different ratios of Li to Nb subcycles presented thin films with different stoichiometries. Local electronic structures of the as-deposited thin films were studied by X-ray absorption near edge spectroscopy (XANES). Furthermore, the ionic conductivities of the ALD lithium niobium oxide thin films were measured.

6.2 Experimental

Lithium niobium oxide thin films were deposited using a Savannah 100 ALD system (Veeco/CNT division of the Veeco Instruments Inc.). For deposition of ternary compounds, the combinations of the subcycles of lithium and niobium was used. Lithium tert-butoxide [LiO^{t}Bu, (CH$_3$)$_3$COLi, Alfa Aesar, 99.9+%] and niobium ethoxide [Nb(OEt)$_5$, Et= –CH$_2$CH$_3$, Strem Chemicals Inc., 99.9+%] were used for Li and Nb sources, respectively. Deionized water was used as the oxidant for both subcycles and nitrogen as the carrier and purging gas. The system pipeline was held at 190 °C to avoid condensation of the precursors. LiO^{t}Bu and Nb(OEt)$_5$ were sublimed at 170 and 155 °C, respectively. All depositions were performed at a temperature of 235 °C. All the precursors were pulsed in for 1 s, followed by 15 s of nitrogen purge. A step wise

acetone, ethanol, and water rinse procedure was applied to clean Silicon (100) substrates. The cleaned substrates were then blown dry by nitrogen. Powder-based carbon nanotubes (CNTs) were acid-treated with nitric acid (HNO_3, 70%) for 3 hours at 120 °C, followed by washing with deionized water. After dispersing the treated CNTs in ethanol, a drop-casting method was employed on aluminum foil. The casted CNTs were dried in air overnight.

The film thicknesses were measured from the fresh-cut cross section of thin films on Si substrates using a field-emission scanning electron microscopy (Hitachi-4800). Six spots were randomly selected on each thin film to calculate the average value as the film thickness. A low-angle X-ray diffraction (XRD) (Bruker D8 Advance, Cu-Ka X-ray source) was employed to examine the phase of the thin films on Si. X-ray photoelectron spectroscopy (XPS) using a Kratos Axis Ultra Al (alpha) spectrometer was applied to determine the composition of the lithium niobium thin films on CNTs. XANES measurements were performed on the Soft X-ray Microcharacterization Beamline (SXRMB) endstation at Canadian Light Source (CLS). SXRMB endstation is equipped with a double crystal monochromator with two sets of interchangeable crystals and the operating energy range is from 1.7 to 10 keV. A set-up with the InSb (111) crystals and Si drift solid-state detector were used for the Nb L-edge XANES measurements. The detection modes were total electron yield (TEY) and X-ray fluorescence yield (FLY) with a selected energy window (e.g. Nb Lα for Nb L_3-edge). All XANES spectra were normalized to the incident photon flux and calibrated with the standard compound.

Ionic conductivities of the thin films were evaluated with electrochemical impedance spectroscopy (EIS) on a CHI electrochemistry workstation. The frequency range was from 200 k to 100 mHz with a temperature window of 303-373 K (10 K step). A cross-plane geometrical configuration was applied with the lithium niobium oxide thin films sandwiched between two Au electrodes. Each gold layer of ~50 nm was sputtered by a Polaron sputtering system under 2 kV for 9 min with a current of 20 mA. The geometric area of the thin film electrolytes between the two Au electrodes were 4×4 mm^2. The EIS plots obtained were simulated using equivalent circuits and the conductivity σ could be calculated from the simulated value of the resistance. *Ln(σT)* was plotted as a function of

1000/T. The activation energies of the thin film electrolytes were derived from the slope of the plot according to the Arrhenius equation: $\sigma T = A \cdot \exp[-E_a/(k \cdot T)]$, where T = the absolute temperature, A = a pre-exponential factor, E_a = the activation energy, and k = the Boltzmann constant.

6.3   Results and Discussion
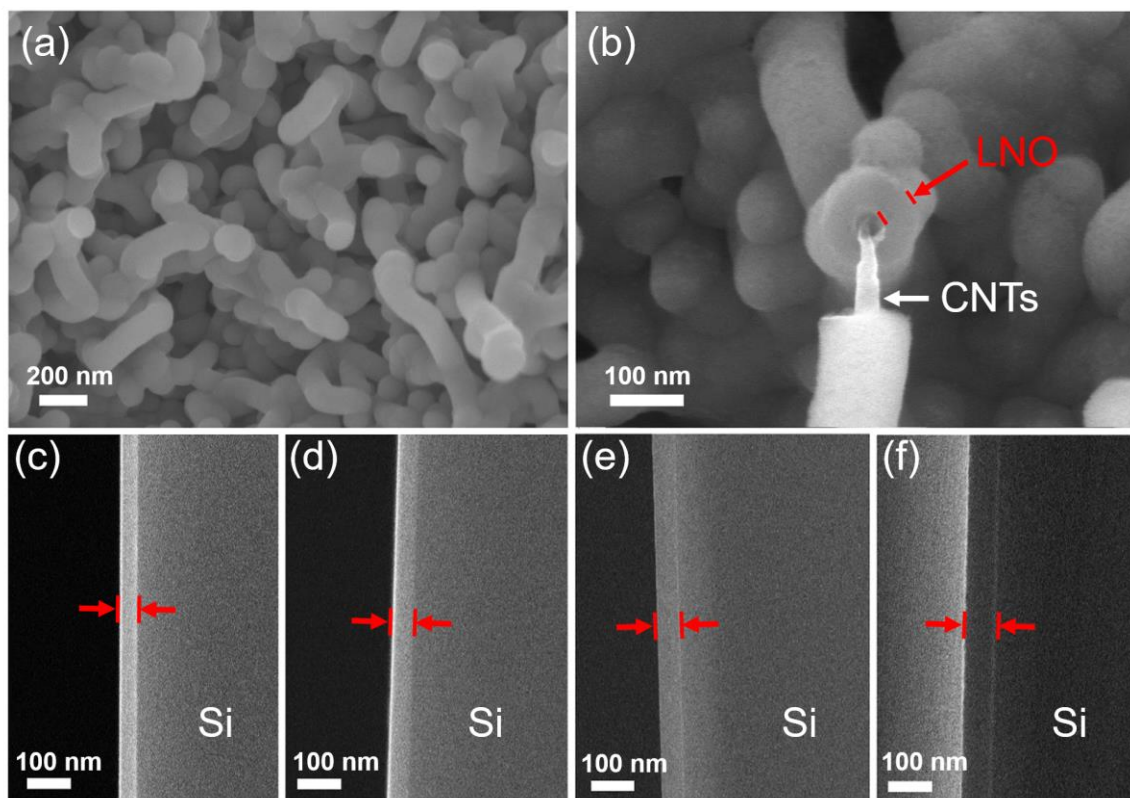
Figure 6.1 SEM morphology of lithium niobium oxide thin films after 250 cycles at 235 °C: (a, b) 1Li-1Nb on CNTs, (c-f) cross-section views of 1Li-1Nb, 1Li-2Nb, 1Li-4Nb, and 2Li-1Nb on Si substrates. LNO thin films are highlighted with red arrows.

Lithium niobium oxide (LNO) thin films were deposited on CNTs and Si substrates at a deposition temperature of 235 °C, which was chosen due to the well-established temperature for deposition of niobium oxide and is within the ALD window of the lithium subcycle.[22,27,39] Four different subcycle ratios of Li and Nb are studied: 1:1, 1:2, 1:4, and 2:1, respectively. The corresponding thin films are henceforth designated as 1Li-1Nb, 1Li-2Nb, 1Li-4Nb, and 2Li-1Nb. A complete round of deposition of both

components (Li and Nb) is one full ALD cycle. For instance, One ALD cycle for 1Li-4Nb consists of one subcycle of Li and 4 subcycles of Nb. SEM images of Figure 6.1 (a) and (b) show the resulting morphology of thin film deposition of 1Li-1Nb on CNTs after 250 ALD cycles. A conformal coating is presented on the surface of CNTs. It can be clearly seen that the CNTs are uniformly wrapped by LNO films, indicating that LNO can be deposited on high-aspect-ratio substrates. The cross-section views of LNO thin films on Si substrates are displayed in Figure 6.1 (c-f), where the LNO coating is highlighted with red arrows. Extremely uniform depositions were obtained for all four recipes.
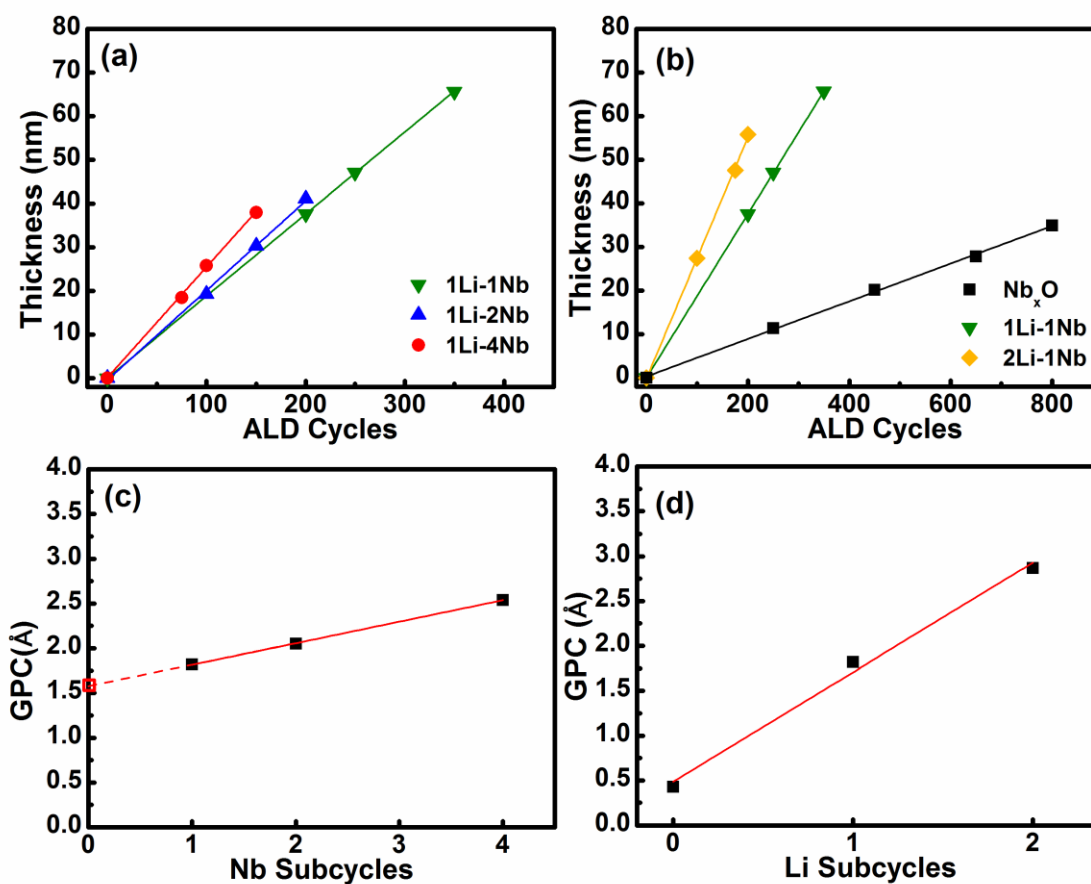
Figure 6.2 Thickness as a function of ALD cycle numbers for lithium niobium oxide thin films: (a) 1Li-1Nb, 1Li-2Nb, and 1Li-4Nb (Li subcycle kept as 1); (b) Nb$_x$O, 1Li-1Nb, and 2Li-1Nb (Nb subcycle kept as 1). GPC as a function of subcycle

number of each component: (c) Nb subcycles (Li subcycle kept as 1) and (d) Li subcycles (Nb subcycle kept as 1).

The thickness of the LNO thin films is plotted against the ALD cycle number in Figure 6.2 (a) and (b). The measured thicknesses are linearly fitted and the slopes of the lines are the growth per ALD cycle (GPC).[17,40] With no lithium subcycles, the GPC for niobium oxide (denoted as Nb_xO) was 0.43 Å, which is consistent with the results reported by Østreng et al.[39,41] The linear behavior was maintained after combination of the Li and Nb subcycles. Furthermore, self-saturated growth was observed in 1Li-1Nb when using higher pulse time (2 sec) of Li and Nb precursors, which is indicative of ALD-type growth. The GPC for 1Li-1Nb, 1Li-2Nb, 1Li-4Nb, and 2Li-1Nb was 1.82, 2.05, 2.54, and 2.87 Å, respectively, which is in agreement with the thickness measurements seen in Figure 6.1 (c-f). When the GPC is a function of the subcycle number as shown in Figure 6.2(c), one can see that the GPC increases monotonously with the number of Nb subcycles when the Li subcycle is kept constant. The y-axis intercept represents the extracted GPC of solely Li_2O in the Li subcycle (~1.6 Å), which is in accordance with previously reported values.[21,22] The same trend can be observed in Figure 6.2(d) where the GPC increases linearly with the number of Li subcycles when the Nb subcycle is held constant at 1. Therefore, it is suggested that the GPC of lithium niobium oxide thin films is a linear combination of the Li and niobium oxide subcycles. The reason for this behavior could be due to the Li subcycle, where the surface species generated after the water pulse are proposed to be hydroxide groups. Upon pulsing in $Nb(OEt)_5$, a reaction can readily take place with the surface species (-OH). Furthermore, the Nb subcycle leads to surface species terminated with the same functional groups (-OH) so that the succeeding Li subcycle can readily proceed.[22] Therefore, the growth mechanism of LNO is similar to the mechanisms of each binary oxide. Thus, the delay in growth due to the regeneration of functional groups between subcycles, which is often observed in ternary systems, could be ameliorated in this mixed system.[23,24] The self-saturating reactions of each subcycle gives rise to the linear correlation between the lithium niobium oxide thin film thickness and the ALD cycle number.
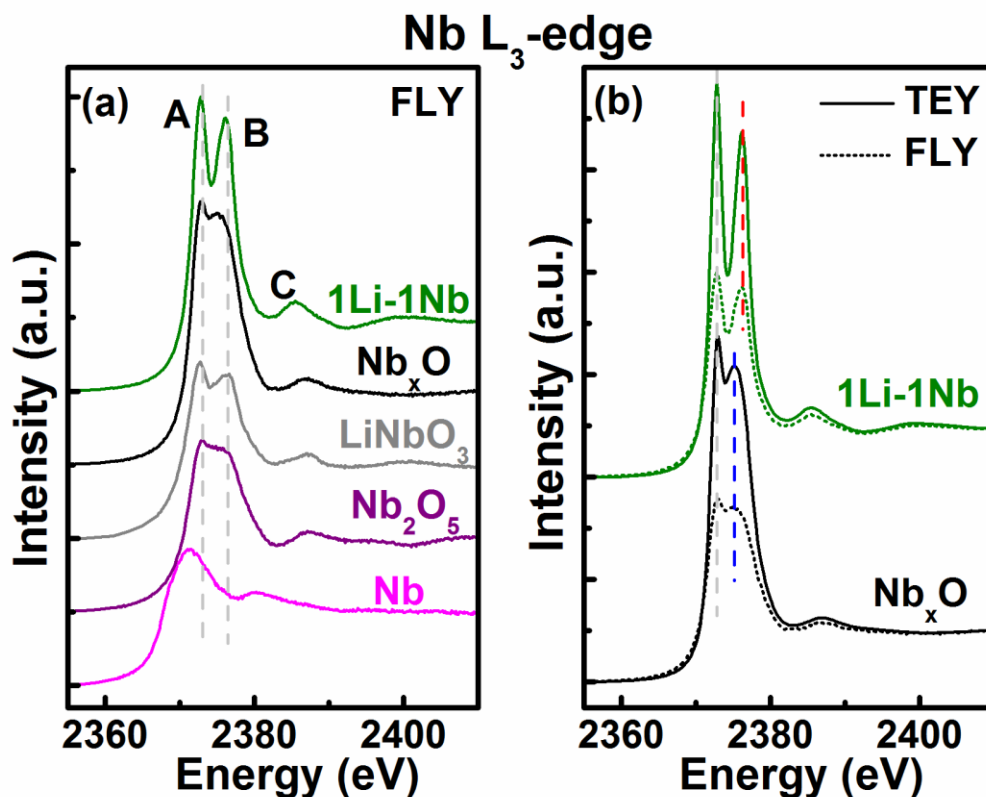
Figure 6.3 Nb L₃-edge XANES spectra: (a) fluorescent yield (FLY) XANES spectra of ALD thin films and standard powders (LiNbO₃, Nb₂O₅ and Nb); (b) total electron yield (TEY) and FLY XANES spectra of 1Li-1Nb and Nb$_x$O thin films

To study the chemical environment of the as-deposited LNO thin films, XANES at the Nb L₃-edge was conducted. The spectral features stem from the dipole excitation of core electrons to bound and quasi-bound states. Information associated with the local structure and bonding environment of the absorbing atom could be provided. The L-edge absorptions of Nb arise from allowed dipole $2p^6 4d^n \rightarrow 2p^5 4d^{n+1}$ transitions. Spin-orbit coupling of the core hole cause the splitting of the L-edge absorption into L₃ and L₂ edges, separated by roughly 94 eV. The L₃-edge involves transitions from $2p_{3/2}$ into mostly $4d_{5/2}$ final states with some $4d_{3/2}$ weighting.[42–44]

Three standard powder samples were studied as references including LiNbO₃, Nb₂O₅ and metallic Nb (Figuer 3a). Compared to the Nb L₃-edge absorption-edge spectrum of metallic Nb which exhibits only one strong resonance, a double-peaked edge structure

(peak A and B) is well resolved in the spectra of the standard oxides. This distinctive characteristic arises from the interaction of Nb with surrounding oxygen in the compound. A relative weak feature (peak C) sitting at higher energies is attributed to the transitions from $2p_{3/2}$ to the Nb 5s state.[45] Additionally, a chemical shift to higher oxidation states can be verified by the blue-shift of the edge jump threshold energy in the spectra of the oxides. The area under the curve of the whiteline (resonance at the edge) relative to the edge jump also increases significantly in the oxides, confirming the expected depletion of Nb 4d character in the oxides.

Peak A of all the standard oxides is well aligned at 2372.8 eV while that of metallic Nb is 1.4 eV lower at 2371.4 eV. Peaks A and B track the densities of states of Nb 4d character associated with the local symmetry. Peak A of 1Li-1Nb and Nb_xO thin films occur at the same energy position at 2372.8 eV with no observable shift, suggesting that Nb in 1Li-1Nb and Nb_xO is at the same oxidation state (Nb^{5+}) as in Nb_2O_5 and $LiNbO_3$. Furthermore, the spectral features of the ALD deposited thin films closely resemble those of Nb_2O_5 and $LiNbO_3$. The double-feature observed above the edge jump stems from the ligand field splitting of d-orbitals originating from the local coordination of Nb^{5+}. In addition, the relative peak intensities can be utilized to identify the unit structure as tetrahedral NbO_4 or octahedral NbO_6, where peak A would be of smaller intensity than peak B in the case of the tetrahedral unit. To supplement this information, the energy gap between the two peaks corresponds to the ligand field splitting, where the value of the gap of octahedral coordination is greater than that of tetrahedral coordination.[45,46] Furthermore, the as-deposited thin films lack long-range order since no diffraction patterns were found in low-angle X-ray diffraction. When examined closer, Nb atoms are revealed to be bonded with six oxygen atoms in octahedral structures as implied by the XANES spectra. Therefore, it is can be claimed that the Nb atoms in the ALD thin films exist as Nb^{5+} in octahedron units.[42,45–47]

Interestingly, there are some subtle differences in peak positions, as summarized in Table 1. First, one can find that peak B of the Nb_xO thin film in Figure 6.3(a) shifts to about 1.2 eV lower energy (2375.2 eV), compared to that of bulk Nb_2O_5 (2376.5 eV). However, when introducing the Li component into the ALD process, peak B of 1Li-1Nb shows a

blue-shift to 2376.1 eV, which is still 0.4 eV lower than that of $LiNbO_3$. Moreover, peak A and B are more clearly resolved in the spectrum of 1Li-1Nb than that of Nb_xO, which is similar to the conclusion when comparing the spectra of Nb_2O_5 and $LiNbO_3$. Additionally, peak C of both 1Li-1Nb and Nb_xO shifts to lower energy compared to Nb_2O_5 and $LiNbO_3$. Figure 6.3(b) presents the spectra of 1Li-1Nb and Nb_xO collected in total electron yield (TEY) and fluorescence yield (FLY) mode. TEY measures the total yield of secondary electrons (dominant), photoelectrons, and Auger electrons from the top few nanometers of the sample surface. On the other hand, FLY detects out-going fluorescent X-rays and is considered as relatively bulk sensitive.[48] The peak positions in TEY and FLY spectra coincide very well as marked by the dashed lines for each sample. Apart from the energy shifts of peak B and C, the TEY spectra of 1Li-1Nb and Nb_xO demonstrate the same patterns as the FLY, where the degree of the whiteline splitting is more apparent in the lithium-containing sample. Compared to the TEY spectra, the dampening of the split in the FLY spectra could be correlated to self-absorption (the thickness effect), where the fluorescence photons are reabsorbed by the thin films.[44] Nevertheless, the resemblance of the TEY and FLY spectra suggests similar electronic structure of Nb at the surface and in the bulk of the LNO thin films.

Table 6.1: The positions (in eV) of the peak maximum in the Nb L$_3$-edge XANES spectra

	Peak A	*Peak B*	*Peak C*
1Li-1Nb	2372.8	2376.1	2385.5
Nb$_x$O	2372.8	2375.2	2386.8
LiNbO$_3$	2372.8	2376.5	2387.3
Nb$_2$O$_5$	2372.8	2376.4	2387.2
Nb	2371.4	--	2380.2

The above discerned differences are a reflection of the fact that local, instead of long range interactions, dominate in the ALD LNO thin films. The presence of Li and O atoms around the Nb atoms leads to orbital hybridizations, modifying the local environment in

the complex. In the context of a molecular orbital scheme, the origin of peaks A and B can be ascribed to the transitions from the Nb $2p_{3/2}$ level to the unoccupied $2t_{2g}$ (π*) and $3e_g$ (σ*), in addition to the allowed transitions to the empty $3a_{1g}$ (σ*) at peak C.[45,46] In the case here, octahedral units constitute both the standards and the thin films. Although sustained in the same symmetry, the distortion might involve a change of the metal-oxygen bond length or orientation.[47] In standard $LiNbO_3$ and Nb_2O_5, the Nb atoms exist in perfectly coordinated octahedrons, while in the corresponding ALD thin films, they are found to be in a distorted octahedral environment and thus lower the energy level of the empty $3a_{1g}$ (σ*) state. As reported in literatures, the least distortion generates the largest splitting (A-B separation), as shown in the spectra of the standard samples.[45,47,49,50] Henceforth, it is proposed that the Nb and O atoms are packed into a distorted octahedral symmetry in the ALD process most likely owing to the fact that only amorphous phase is formed at the relatively low deposition temperature . When taking into consideration the radius difference between Li^+ and Nb^{5+}, the octahedron skeleton is unlikely to be changed by the introduction of Li subcycles . In addition, previous studies have shown that when the supporting surface is a basic environment, the niobium oxide can interact with the support and result in the formation of highly distorted NbO_6 octahedron. In other words, the hydroxide groups readily formed on the surface between the Li and Nb ALD subcycles could help facilitate the formation of the distortion.[51] Both distorted, the degree of distortion was modified due to the insertion of the lithium ions, comparing the spectra of 1Li-1Nb and Nb_xO. It is possible that the distortion was alleviated and thus, peaks A and B were more separated. [45,47,49,50]
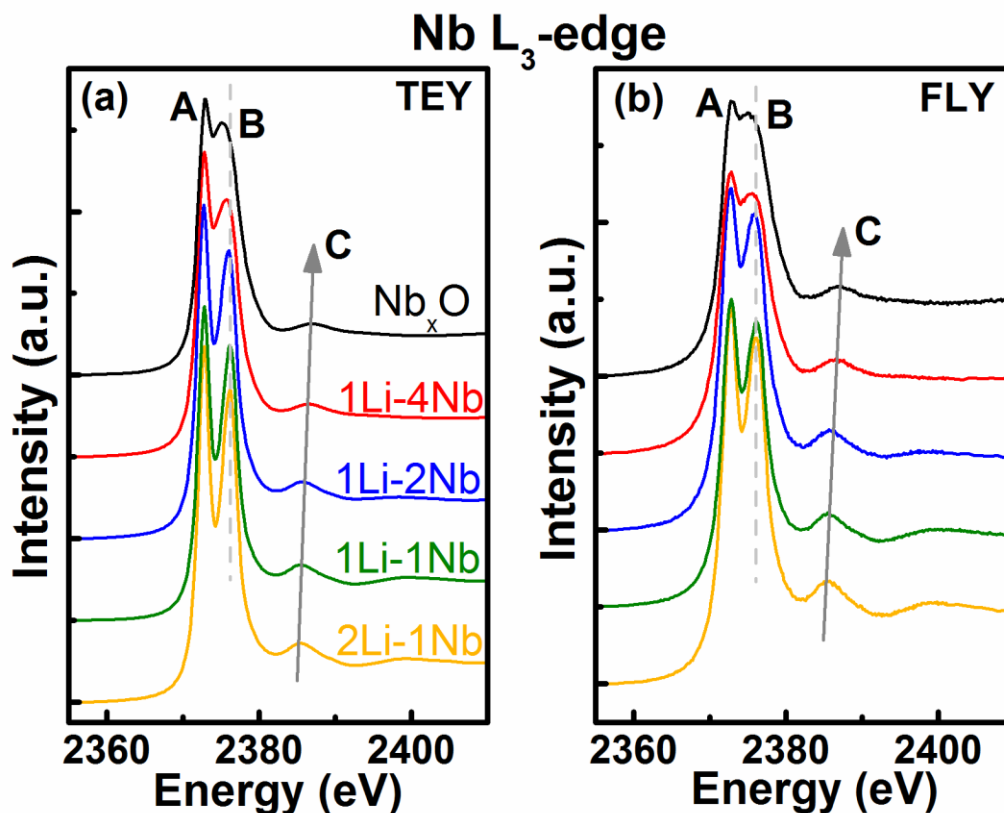
Figure 6.4 Nb L₃-edge XANES spectra of Nb$_x$O, 1Li-4Nb, 1Li-2Nb, 1Li-1Nb, and 2Li-1Nb in (a) TEY mode and (b) FLY mode

XANES studies of the thin films with varying number of subcycles (Figure 6.4) illustrates that the double-peaked whiteline and the subsequent weak peak were preserved in the spectra (both TEY and FLY) of all materials. Taking a closer look at Figure 6.4(a), the position of peak A remains constant at 2372.8 eV. The relative peak intensity of peaks A and B, and the value of the peak separation manifest that the octahedral symmetry is persistent in the as-deposited thin films in spite of the changing subcycle ratio. More strikingly, an apparent trend of evolution of the spectra was found. The separation of peaks A and B becomes narrower and the relative intensity of the gap between peaks A and B is gradually increased with a lower Li to Nb subcycle ratio from 2 (2Li-1Nb) down to 0 (Nb$_x$O), accompanied by a continuing blue-shift of peak C. The red-shift of peak B is rather delicate (0.1 eV) from 2Li-1Nb to 1Li-1Nb but reaches 0.5 eV in the spectra of 1Li-4Nb. In theory, the addition of more Li subcycles leads to the

incorporation of more Li atoms in the film composition. As discussed above, the degree of the distortion of the octahedral symmetry accounts for the shift of peak B. Thus, it is indicative that the octahedrons experience the strongest distortion in the Nb_xO thin film while the distortion is mitigated to some extent with the increasing amount of Li content in the LNO thin films. In addition, the degree of the splitting should be a sign of the ability of the ligand to split the energy levels.[49,50] The less-contrasted gap between the t_{2g} and e_g levels could possibly mean that there is an increase in the probability of the transitions to the empty space between the $2t_{2g}$ (π^*) and $3e_g$ (σ^*) states and a change in the degeneracy of the molecular orbitals. The continuing shift of peak C implies that the empty state $3a_{1g}$ (σ^*) is elevated to a higher energy level, related to the distortion with reducing lithium content in the thin films. [45,52] More importantly, the excellent agreement of the TEY and the corresponding FLY spectrum substantiates that the prominent phenomenon observed in the XANES study takes place not only on the surface but also in the bulk of the thin films.
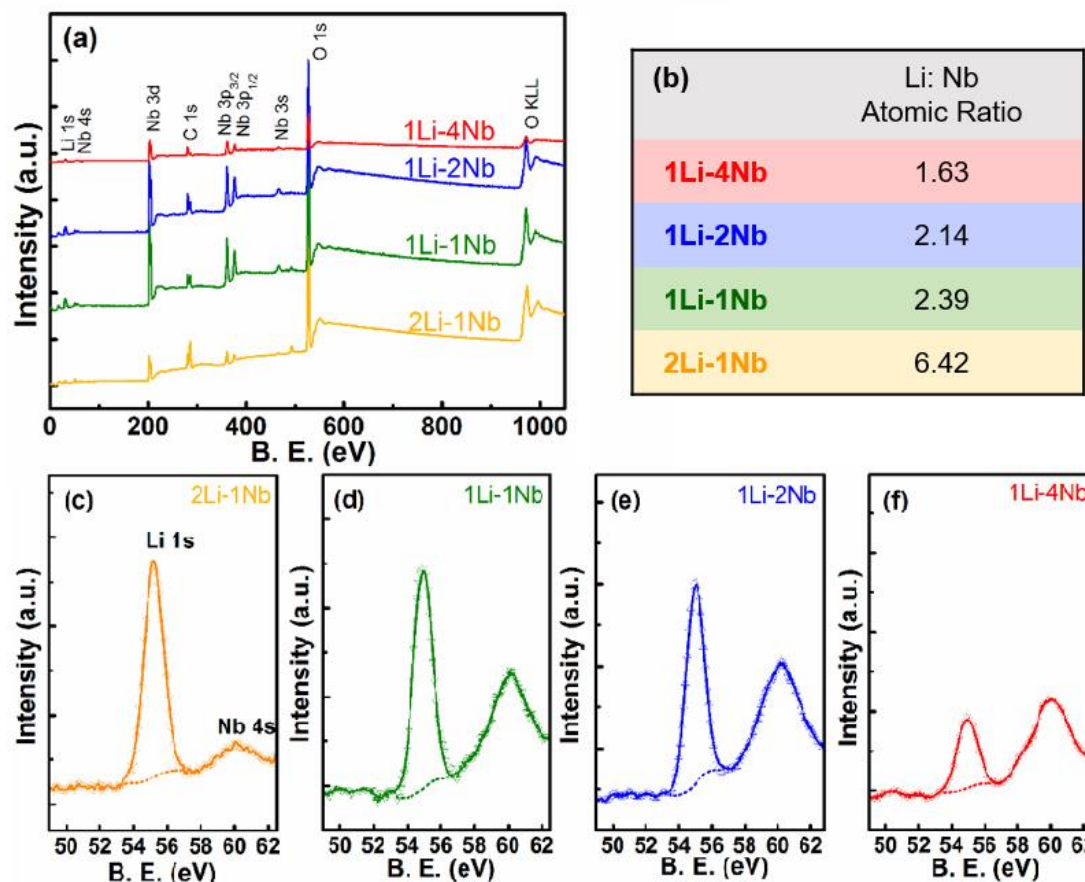
Figure 6.5 XPS spectra of the four LNO thin films on CNTs substrates: (a) survey scans; (b) compositional ratio of Li to Nb; and (c-f) deconvolution of Li 1s spectra

The above-discussed notions are on the basis that higher ratios of Li to Nb subcycles delivers higher lithium content in the thin films. To verify this, the elemental composition was determined by XPS. Figure 6.5(a) provides the survey scans of the as-deposited LNO thin films, showing the presence of Li in the thin films. The appearance of carbon signal should be due to the CNT substrates. Figure 6.5(b) lists the atomic ratio of Li to Nb in the 1Li-4Nb, 1Li-2Nb, 1Li-1Nb, and 2Li-1Nb thin films, respectively, indicating that the lithium content increased with the higher ratio of Li to Nb subcycles. High resolution XPS spectra of Li 1s are depicted in Figure 6.5 (c-f) with deconvolutions of the 1s peaks. Only one sharp and symmetric peak can be detected at 55.0 ± 0.1 eV in all four LNO thin films, revealing a single chemical state of Li$^+$ in each sample. The peak at higher binding energy belongs to the Nb 4s. The single peak can be attributed to the bonding state of Li-

O-Nb as exemplified by lithium niobate glasses found in the literatures.[53–55] The consistent peak position of Li 1s for the four LNO thin films elucidates that Li shares a similar chemical environment in the thin films with different ratios of Li to Nb subcycles.
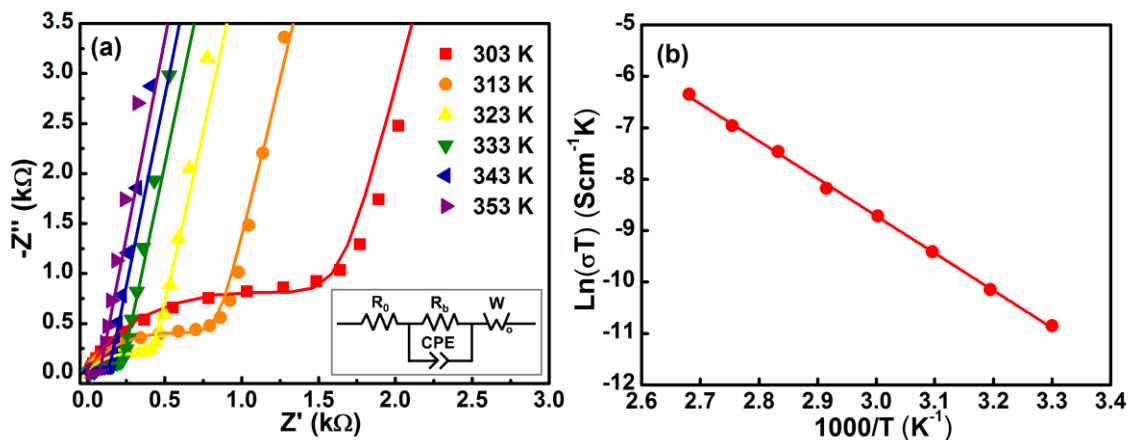
Figure 6.6 (a) Impedance plot of 1Li-4Nb thin film and (inset: equivalent circuit) and (b) Arrhenius plots of the ionic conductivity of 1Li-4Nb thin film measured between 303 and 353 K. (Scattered points are measured values and solid lines are fitted results.)

Ionic conductivity of the LNO thin films were evaluated by EIS using a cross-plane configuration. The Cole-Cole plot of 1Li-4Nb acquired at temperatures ranging from 303 to 353 K with the equivalent circuit used to fit the data is displayed in Figure 6.6(a). The impedance plots of 1Li-1Nb, 1Li-2Nb, and 2Li 1-Nb were also constructed (Supporting information). Each complex impedance curve consists of a semicircle at high frequency, which corresponds to the bulk resistance of the LNO thin films. An inclined tail can be noticed in the low frequency region due to the polarization of the electrode-electrolyte interface. Taken together, the behavior is representative of an ionic conductor in an open circuit with an ionic blocking electrode (Au in this case).[22,24,27] In the equivalent circuit, R_0 is the contact ohmic resistance and the constant-phase element (CPE) defines the bulk capacitance of the LNO thin films. W denotes the finite length Warburg element, applicable when charge carriers diffuse though a solid. The ionic conductivity of the LNO thin films were calculated using the fitted bulk resistance (denoted as R_b). The equation, $\sigma = d/(A \cdot Rb)$, was employed, wherein d = the thickness of the LNO thin film

and A = the geometric area of the lithium niobium oxide thin films between the Au electrodes. 1Li-4Nb thin film exhibited the best ionic conductivity among the four LNO thin films, which reached 6.39×10^{-8} S cm^{-1} at 303 K and 1.62×10^{-6} S cm^{-1} at 353 K. The Arrhenius plot in Figure 6.6(b) demonstrates the ionic conductivity at varying temperatures. The activation energy, E_a, was derived from the equation, $\sigma T = \sigma_c \cdot exp[-E_a/(k \cdot T)]$, where σ_c is a constant, k is the Boltzmann constant, and T is the absolute temperature. An activation energy of 0.62 eV for 1Li-4Nb thin film was extracted from the slope of the linear fitted line, which is the lowest of the four LNO thin films. The conductivity achieved is comparable to that of thin films prepared by sputtering and the activation energy falls into the range of reported values of lithium niobate glasses.[31,33,35,36] The LNO thin films by ALD can provide a moderate ionic conductivity at room temperature, which is even higher than that of other similar amorphous systems developed by ALD such as lithium aluminum oxide, lithium tantalum oxide, and lithium phosphate.[21,22,24,27] This promises the possibility of the implementation of lithium niobium oxide thin films developed by ALD as a solid-state electrolyte in all-solid-state batteries.

6.4 Conclusions

In this study, we have demonstrated a viable ALD process to deposit lithium niobium oxide thin films by combining Li (LiO^{t}Bu and H_2O) and Nb [Nb(OEt)$_5$ and H_2O] subcycles at a deposition temperature of 235 $^\circ$C. Self-limiting behavior and uniform growth on different substrates were achieved with ALD recipes composed of various subcycle ratios. Different ratios of Li to Nb subcycles could provide a tunable composition, which in turn affected the electrochemical performances and the local electronic structures. For the first time, detailed XANES studies of the ALD niobium oxide and LNO thin films were carried out focusing on the Nb L$_3$-edge. Despite the fact that the as-deposited thin films were amorphous and lacked long-range order, local octahedral units of NbO$_6$ were shown to be the building blocks of the thin films. XANES analysis indicated that the Nb in Nb$_x$O and LNO thin films exists as Nb^{5+} and the degree of distortion in the octahedral structure is dependent on the ALD subcycle ratio. Furthermore, it was found that the Nb$_x$O thin film exhibited the most distortion, and it

was shown that the distortion can be decreased to some extent with the addition of lithium content by increasing the Li to Nb subcycle ratio. The TEY and FLY spectra confirmed the consistency of the electronic structure on the surface and in the bulk of the ALD thin films. Moreover, the as-grown LNO thin film with a Li: Nb subcycle ratio of 1:4 delivered a Li^+ conductivity of 6×10^{-8} S cm^{-1} at room temperature, which provides great promise for future application as a solid-state electrolyte and interfacial engineering material in solid-state batteries.

Acknowledgement

References

1   J. B. Goodenough and K.-S. Park, *J. Am. Chem. Soc.*, 2013, **135**, 1167–1176.

2   E. M. Erickson, C. Ghanty and D. Aurbach, *J. Phys. Chem. Lett.*, 2014, **5**, 3313–3324.

3   A. Manthiram, *J. Phys. Chem. Lett.*, 2011, **2**, 176–184.

4   George Crabtree, *Nature*, 2015, **526**, 592.

5   E. Quartarone and P. Mustarelli, *Chem. Soc. Rev.*, 2011, **40**, 2525–40.

6   Y. Zhu, X. He and Y. Mo, *ACS Appl. Mater. Interfaces*, 2015, **7**, 23685–23693.

7   J. C. Bachman, S. Muy, A. Grimaud, H. H. Chang, N. Pour, S. F. Lux, O. Paschos, F. Maglia, S. Lupart, P. Lamp, L. Giordano and Y. Shao-Horn, *Chem. Rev.*, 2016, **116**, 140–162.

8   C. Sun, J. Liu, Y. Gong, D. P. Wilkinson and J. Zhang, *Nano Energy*, 2017, **33**, 363–386.

9   J. F. M. Oudenhoven, L. Baggetto and P. H. L. Notten, *Adv. Energy Mater.*, 2011, **1**, 10–33.

10   Y. Yang, Z. Peng, G. Wang, G. Ruan, X. Fan, L. Li and H. Fei, *ACS Nano.*, 2014, **8**, 7279–7287.

11   S. Ferrari, M. Loveridge, S. D. Beattie, M. Jahn, R. J. Dashwood and R. Bhagat, *J. Power Sources*, 2015, **286**, 25–46.

12   Y. Zhang, J. Lai, Y. Gong, Y. Hu, J. Liu, C. Sun and Z. L. Wang, *ACS Appl. Mater. Interfaces*, 2016, **8**, 34309–34316.

13   C. Liu, E. I. Gillette, X. Chen, A. J. Pearse, A. C. Kozen, M. A. Schroeder, K. E. Gregorczyk, S. B. Lee and G. W. Rubloff, *Nat. Nanotechnol.*, 2014, **9**, 1031–1039.

14   A. J. Pearse, T. E. Schmitt, E. J. Fuller, F. El-Gabaly, C. F. Lin, K. Gerasopoulos, A. C. Kozen, A. A. Talin, G. Rubloff and K. E. Gregorczyk, *Chem. Mater.*, 2017, **29**, 3740–3753.

15   X. Meng, X. Wang, D. Geng, C. Ozgit-Akgun, N. Schneider and J. W. Elam, *Mater. Horiz.*, 2017, **4**, 133–154.

16   H. C. M. Knoops, M. E. Donders, L. Baggetto, M. C. M. van de Sanden, P. H. L. Notten and W. M. M. Kessels, *ECS Trans.*, 2009, **25**, 333–344.

17   S. M. George, *Chem. Rev.*, 2010, **110**, 111–31.

18   X. Meng, X.-Q. Yang and X. Sun, *Adv. Mater.*, 2012, **24**, 3589–615.

19 J. Liu and X. Sun, *Nanotechnology*, 2015, **26**, 24001.

20 M. Putkonen, T. Aaltonen, M. Alnes, T. Sajavaara, O. Nilsen and H. Fjellvåg, *J. Mater. Chem.*, 2009, **19**, 8767–8771.

21 T. Aaltonen, O. Nilsen, A. Magrasó and H. Fjellvåg, *Chem. Mater.*, 2011, 4669–4675.

22 J. Liu, M. N. Banis, X. Li, A. Lushington, M. Cai, R. Li, T.-K. Sham and X. Sun, *J. Phys. Chem. C*, 2013, **117**, 20260–20267.

23 T. Aaltonen, M. Alnes, O. Nilsen, L. Costelle and H. Fjellvåg, *J. Mater. Chem.*, 2010, **20**, 2877–2881.

24 E. Kazyak, K. H. Chen, K. N. Wood, A. L. Davis, T. Thompson, A. R. Bielinski, A. J. Sanchez, X. Wang, C. Wang, J. Sakamoto and N. P. Dasgupta, *Chem. Mater.*, 2017, **29**, 3785–3792.

25 Y.-C. Perng, J. Cho, D. Membreno, N. Cirigliano, B. Dunn and J. P. Chang, *J. Mater. Chem. A*, 2014, **2**, 9566–9573.

26 Y. Cao, X. Meng and J. W. Elam, *ChemElectroChem*, 2016, **3**, 1–7.

27 B. Wang, J. Liu, Q. Sun, R. Li and T. Sham, *Nanotechnology*, 2014, **25**, 504007.

28 M. Nisula, Y. Shindo, H. Koga and M. Karppinen, *Chem. Mater.*, 2015, **27**, 6987–6993.

29 A. C. Kozen, A. J. Pearse, C. Lin, M. Noked and G. W. Rubloff, *Chem. Mater.*, 2015, **27**, 5324–2331.

30 S. Shibata, *J. Electrochem. Soc.*, 2016, **163**, 2555–2562.

31 J. Black, E. M. Conwbll, S. Electric, L. Seigle and C. W. Spencer, *Thin Solid Films*, 1992, **214**, 219–222.

32 A. M. Glass, K. Nassau and T. J. Negran, *J. Appl. Phys.*, 1978, **49**, 4808–4811.

33   N. Can, P. V. Ashrit, G. Bader, F. Girouard and V. Van Truong, *J. Appl. Phys.*, 1994, **76**, 4327–4331.

34   N. Ozer and C. M. Lampert, *Sol. Energy Mater. Sol. Cells*, 1995, **39**, 367–375.

35   L. Q. Nguyen, L. Chen and V.-V. Truong, *Thin Solid Films*, 1997, **293**, 175–178.

36   H. Xia, H. L. Wang, W. Xiao, M. O. Lai and L. Lu, *Int. J. Surf. Sci. Eng.*, 2009, **3**, 23.

37   K. Takada, N. Ohta, L. Zhang, K. Fukuda, I. Sakaguchi, R. Ma, M. Osada and T. Sasaki, *Solid State Ionics*, 2008, **179**, 1333–1337.

38   N. Ohta, K. Takada, I. Sakaguchi, L. Zhang, R. Ma, K. Fukuda, M. Osada and T. Sasaki, *Electrochem. commun.*, 2007, **9**, 1486–1490.

39   E. Østreng, H. H. Sønsteby, T. Sajavaara, O. Nilsen and H. Fjellvåg, *J. Mater. Chem. C*, 2013, **1**, 4283–4290.

40   M. Leskelä and M. Ritala, *Angew. Chem. Int. Ed.*, 2003, **42**, 5548–5554.

41   B. K. Kukli, M. Ritala, M. Leskelä and R. Lappalainen, *Chem. Vap. Depos.*, 1998, **4**, 29.

42   T. L. Gianetti, G. Nocton, S. G. Minasian, N. C. Tomson, A. L. D. Kilcoyne, S. A. Kozimor, D. K. Shuh, T. Tyliszczak, R. G. Bergman and J. Arnold, *J. Am. Chem. Soc.*, 2013, **135**, 3224–3236.

43   T. L. Gianetti, G. Nocton, S. G. Minasian, N. Kaltsoyannis, A. L. D. Kilcoyne, S. A. Kozimor, D. K. Shuh, T. Tyliszczak, R. G. Bergman and J. Arnold, *Chem. Sci.*, 2014, **0**, 1–11.

44   M. W. Ruckman, G. Reisfeld, N. M. Jisrawi, M. Weinert, M. Strongin, H. Wiesmann, M. Croft, A. Sahiner, D. Sills and P. Ansari, *Phys. Rev. B - Condens. Matter Mater. Phys.*, 1998, **57**, 3881–3886.

45   C. Sugiura, M. Kitamura and S. Muramatsu, *J. Phys. Chem. Solids*, 1988, **49**, 1095–1099.

46   Y. Kubouchi, S. Hayakawa, H. Namatame and T. Hirokawa, *X-Ray Spectrom.*, 2012, **41**, 259–263.

47   J. Cao, B. Poumellec, L. Mazerolles, F. Brisset, A. L. Helbert, S. Surble, X. He, M. Lancry and L. Pinckney, *J. Am. Ceram. Soc.*, 2017, **100**, 115–124.

48   F. Zhang, L. S. Liao, W. H. Chan, S. T. Lee, R. Sammynaiken, T. K. Sham and T. Si, *Phys. Rev. B Condens. Matter Mater. Phsys*, 2000, **61**, 8298–8305.

49   S. R. Bare, G. E. Mitchell, J. J. Maj, G. E. Vrieland and J. L. Gland, *J. Phys. Chem.*, 1993, **97**, 6048–6053.

50   H. Hu, I. E. Wachs and S. R. Bare, *J. Phys. Chem.*, 1995, **99**, 10897–10910.

51   I. Nowak and M. Ziolek, *Chem. Rev.*, 1999, **99**, 3603–3624.

52   U. Nuraini, D. Agustianawati, E. Yahya, Y. Cahyono, P. Kidkhunthod and S. Suasmoro, *Ceram. Int.*, 2017, **43**, 3664–3669.

53   N. Ozer, M. D. Rubin and C. M. Lampert, *Sol. Energy Mater. Sol. Cells*, 1996, **40**, 285–296.

54   M. Aufray, S. Menuel, Y. Fort, J. Eschbach, D. Rouxel and B. Vincent, *J. Nanosci. Nanotechnol.*, 2009, **9**, 4780–4785.

55   N. Kaufherr, D. J. Eichorst and D. A. Payne, *J. Vac. Sci. Technol. A*, 1996, **14**, 299–306.
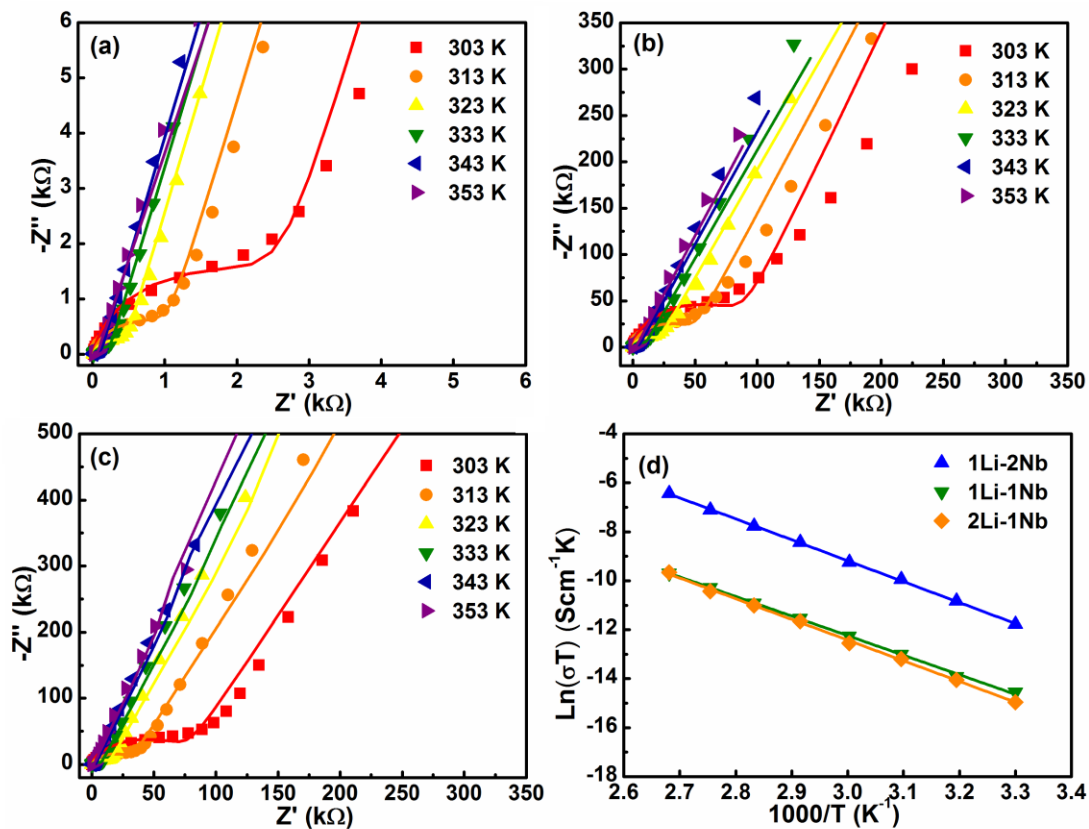
Supporting Information

Figure 6.SI-1 Impedance plot of (a) 1Li-2Nb, (b) 1Li-1Nb, (c) 2Li-1Nb thin films, and (d) Arrhenius plots of the ionic conductivity of the three thin films measured between 303 and 353 K. (Scattered points are measured values and solid lines are fitted results.

Chapter 7

7 Conclusions and Future Work

7.1 Conclusions

Lithium ion batteries are clean and recyclable energy storage system which are widely applied not only in hand-held electronic devices, but also in electric vehicles and hybrid electric vehicles. However, undergoing an extensive progress in the past decade, lithium ion batteries are now experiencing a plateau in development while higher energy density, longer cycling life, better safety, and lower cost have been urged. Among all the next-generation lithium ion batteries, all-solid-state batteries are regarded as a promising candidate where solid-state electrolyte is used, which eliminate the safety issues that are associated with the liquid electrolytes. Furthermore, the possible design of 3D structures enables higher energy density for the further application of microbatteries in various fields.

Atomic layer deposition is one unique technique to fabricate nanostructured materials as either electrodes or solid-state electrolytes for all-solid-state batteries. The grown thin films by ALD are ultra-uniform and conformal regardless of the substrate geometry. The thickness of the thin films can be precisely controlled and the chemical compositions can be tuned by changing parameters in the ALD process.

The main objective of this thesis is to develop various nanostructured materials as electrodes and solid-state electrolyte for lithium ion batteries via atomic layer deposition. Moreover, various characterization techniques, especially X-ray absorption fine structure studies were performed to understand the detailed local electronic structure of the materials.

First, an ALD process was developed to synthesize lithium phosphate thin films. A novel approach was employed, where lithium precursor (LiO^{t}Bu) directly reacted with phosphorus precursor (TMPO) without the use of water as oxidant. Uniform depositions and linear growth rate were observed at different deposition temperatures of 250, 275, and 300 ºC. Higher deposition temperatures yielded higher growth rate up to 0.74 Å per

cycle. XPS quantitative analysis showed that all the as-prepared thin films possessed a chemical composition close to the standard Li_3PO_4, while the Li/P and O/P ratio increased slightly with reduced deposition temperature. The chemical states of Li and P were the same with those in Li_3PO_4. The EIS measurements were applied to evaluate the ionic conductivity of the thin films with a through-plane setup. Lithium phosphate thin films grown at 300 $^\circ$C exhibited the best ionic conductivity of 1.73×10^{-7} S cm^{-1} at 323K with an activation energy of 0.51 eV. The room temperature ionic conductivity was extrapolated to be 3.33×10^{-8} S cm^{-1}. Therefore, lithium phosphate thin films by ALD appears to be a potential candidate as solid-state electrolyte for next-generation lithium ion batteries.

ALD is not limited to preparing solid-state electrolytes. Previous works demonstrated that it can also fabricate electrode materials such as TiO_2, SnO_2, and $LiFePO_4$. Although TiO_2 exhibits stable performance as a popular anode material, it suffers from low electronic and ionic conductivity. A rational design was proposed with CNTs as a highly electronically conductive skeleton combined with an ionically conductive material. Thereby, the ALD processes of TiO_2 (TTIP and H_2O) and lithium phosphate (LiO^{t}Bu and TMPO) were combined and the nanocomposites were deposited on CNTs at 250 $^\circ$C. The deposition temperature was selected according to the overlapped temperature range of the ALD window for both TiO_2 and lithium phosphate. Each full ALD cycle consisted of 2 TiO_2 and one lithium phosphate subcycles. A linear universal growth rate was obtained. Uniform depositions were achieved on both Si and CNTs substrates. XPS results indicated that the obtained lithium phosphate has the same chemical states with the standard material. Detailed XANES studies on Ti L-edge revealed that the chemical environment in TiO_2 component resembled that in anatase TiO_2 while showing the lack of long-range order. XRD patterns also clearly marked the presence of anatase TiO_2 for the as-deposited materials. In-situ XRD experiment at elevated temperatures proved the initial absence of lithium phosphate and the presence of anatase TiO_2. With the combustion of the carbon scaffold, better crystallinity was obtained with increased annealing temperature. HRTEM further confirmed that the nanocomposites were uniformly grown on CNTs and the nanocrystals of anatase TiO_2 existed in the matrix of amorphous lithium phosphate. The as-prepared material was tested as anode material

using Li metal as the counter electrode. CV curves clearly presented two well-defined characteristic peaks (1.7 and 2.0 V) corresponding to the redox reactions of anatase TiO_2 during charge and discharge. Highly stable cycling performance was observed maintaining a capacity of ~ 200 mA h g^{-1} after 200 cycles. Comparison of the ALD deposited TiO_2 solely on CNTs with the nanocomposites demonstrated a much improved rate capability due to the incorporation of the active electrode material into an ionically conductive matrix. This part of the thesis demonstrates the application of ALD in fabricating novel nanostructured anode materials for LIBs.

Another material, lithium silicate thin films by ALD, were explored as solid-state electrolyte for LIBs. The strategy of combining ALD binary oxides was employed where Li_2O (LiO^{t}Bu and water) and SiO_2 (TEOS and water) subcycles composed of one global ALD cycle. Lithium silicate thin films were prepared at 225, 250, 275, and 300 ^{o}C. The growth rate increased with higher deposition temperature and higher Li_2O subcycle number. The Li_2O subcycle initiated the growth of SiO_2. XANES analysis indicated that the as-prepared films were in amorphous phase and the basic unit was SiO_4 tetrahedrons. Lithium was introduced into the thin films as network modifier, and thus reduced the polymerization degree of the glass system. Additional Li would further cause change of bonding structure around Si atoms. Chemical compositions were analyzed by XPS. A Li/Si subcycle number ratio of one delivered a stoichiometry close to lithium orthosilicate (Li_4SiO_4). Extra lithium subcycles produced higher lithium content. Moreover, the best ionic conductivity was obtained from thin films deposited at 250 ^{o}C with one Li to one Si sub-cycle ratio. The room temperature ionic conductivity value was 5.72×10^{-9} S cm^{-1}, not as good as lithium phosphate but still acceptable as SSE for LIBs.

Lastly, a different metal oxide based glass system was studied as SSEs. Lithium niobium oxide was grown by ALD via combining subcycles of Li_2O and Nb_2O_5. LiO^{t}Bu and Nb(OEt)$_5$ were employed as the lithium and niobium source, respectively, at a deposition temperature of 235 ^{o}C. Uniform growth was achieved on both CNTs and Si substrates. Various subcycle number ratios of Li to Nb including 2:1, 1:1, 1:2, and 1:4 were examined in order to tune the final compositions. Linear growth was found for each procedure. Detailed XANES studies on Nb L_3-edge unveiled that NbO_6 octahedral

structure existed throughout all the as-prepared thin films, where Nb had a chemical state of 5^+. Compared to standard Nb_2O_5 and $LiNbO_3$, the octahedrons in ALD deposited ones experienced different degree of distortion. The insertion of lithium atoms by applying higher ratio of lithium subcycles gradually relieved the distortion to certain extend. In addition, the best ionic conductivity reached 6×10^{-8} S cm^{-1} at room temperature, obtained from the thin film of the 1:4 Li/Nb subcycle ratio.

To summarize, first, new ALD processes were established to synthesize materials as potential solid-state electrolytes and electrodes. The detailed structural and chemical information of the as-prepared materials were revealed using advanced characterization techniques such as XAS. The application of the developed materials can be extended to the interface modifications in solid-state battery systems. The objectives of fabricating nanostructured electrode and solid-state electrolyte materials by atomic layer deposition for next-generation LIBs were delivered and this work paves the way for the further applications of these materials in LIBs.

7.2 Future Work

Several glass systems and nanocomposites by ALD have been exploited in this thesis. Some other possible future directions to focus on has been inspired while carrying out the work, discussed as the following.

First, SSEs with higher ionic conductivity is preferred for the real application of ASSB in the future. Some systems like garnet-type $Li_7La_3Zr_2O_{12}$ (LLZO) and perovskite-type $Li_{3x}La_{(2/3)-x / (1/3) 2x}TiO_3$ (LLTO) have presented high ionic conductivity exceeding 10^{-4} S cm^{-1} at room temperature.[1,2] Using ALD as one promising approach to synthesize SSE, this group of inorganic crystalline SSE is the next one to tackle. The posed challenges remain in two aspects. The first is that most of this kind of SSEs have multiple elements (usually more than three). Some of the elements do not have overlapped ALD windows. Either new precursors should be explored or instrumentation needs to be modified. Secondly, the sequence of introducing each element into the procedure plays an important role. Another consideration is that tuning the chemical composition will probably undergo several trials and errors. The most challenging part is the post heat-

treatment. With the right atomic ratio, post-annealing is necessary to get the crystallized phase. Cracking and islanding would most likely take place which will destroy the integrity of the films. Mild annealing process can be developed or better substrates can be applied in order to solve this issue. The success of using ALD to prepare crystalline SSE will definitely be a huge lean-forward in this all-solid-state field.

Secondly, another high-performance candidate as SSEs is sulfide-based system. Compared to the former candidate, some compounds in this group are in amorphous phase and do not require a post annealing process or require only mild treatment at much lower temperatures. Systems like Li_2S-P_2S_5 glass exhibit an ionic conductivity as high as 10^{-2} S cm^{-1}.[3] Finding a proper precursor as sulfur source is the top priority. Meng et al. reported the successful deposition of metal sulfides and Li_xAl_yS SSE by ALD with the use of H_2S.[4,5] The H_2S precursor is difficult to handle and could be harmful to the deposition system. Similarly, new precursors should be developed or the apparatus should be improved. Also, sulfide systems are mostly air-sensitive. Coupling the deposition system and the characterization techniques with glove-box would be essential for the fabrication.

The third direction is regarding the interface engineering in ASSBs. ALD is capable of depositing ultrathin and conformal materials, and has been demonstrated as an effective method to prepare surface coatings for electrodes. Some of the SSE developed by ALD has proven to be excellent interfacial materials in ASSB in order to improve the electrochemical performances.[6,7] $LiNbO_3$ as a buffer layer was found to function as a passivation layer to prevent the mutual diffusion between the $LiCoO_2$ electrode and the $Li_7P_3S_{11}$ SSE, resulting in the improved lithium-ion transfer rates at the interface.[8] Therefore, the further application of the ALD synthesized SSEs as interface engineering materials is one of the directions that is worth studying.

References

1. Murugan, R., Thangadurai, V. & Weppner, W. Fast lithium ion conduction in garnet-type Li7La3Zr2O12. *Angew. Chem. Int. Ed.* **46,** 7778–7781 (2007).

2. Stramare, S., Thangadurai, V. & Weppner, W. Lithium Lanthanum Titanates: A Review. *Chem. Mater.* **15,** 3974–3990 (2003).

3. Seino, Y., Ota, T., Takada, K., Hayashi, A. & Tatsumisago, M. A sulphide lithium super ion conductor is superior to liquid ion conductors for use in rechargeable batteries. *Energy Environ. Sci.* **7,** 627–631 (2014).

4. Cao, Y., Meng, X. & Elam, J. W. Atomic Layer Deposition of LixAlyS Solid-State Electrolytes for Stabilizing Lithium-Metal Anodes. *ChemElectroChem* **3,** 1–7 (2016).

5. Dasgupta, N. P., Meng, X., Elam, J. W. & Martinson, A. B. F. Atomic Layer Deposition of Metal Sulfide Materials. *Acc. Chem. Res.* **48,** 341–348 (2015).

6. Xu, B. *et al.* Li3PO4-added garnet-type Li6.5La3Zr1.5Ta0.5O12 for Li-dendrite suppression. *J. Power Sources* **354,** 68–73 (2017).

7. Nemori, H. *et al.* Stability of garnet-type solid electrolyte LixLa3A2 -yByO12 (A = Nb or Ta, B = Sc or Zr). *Solid State Ionics* **282,** 7–12 (2015).

8. G. Pistoia, *Lithium-ion batteries: advances and applications*, 2013

Appendices

Appendix I: PERMISSION FROM IOP PUBLISHING.

**IOP Publishing LICENSE
TERMS AND CONDITIONS**

Aug 28, 2017

This is a License Agreement between BIQIONG WANG ("You") and IOP Publishing ("IOP Publishing") provided by Copyright Clearance Center ("CCC"). The license consists of your order details, the terms and conditions provided by IOP Publishing, and the payment terms and conditions.

All payments must be made in full to CCC. For payment instructions, please see information listed at the bottom of this form.

License Number	4175360965742
License date	Aug 23, 2017
Licensed content publisher	IOP Publishing
Licensed content title	Nanotechnology
Licensed content date	Jan 1, 1990
Type of Use	Thesis/Dissertation
Requestor type	Academic institution
Format	Electronic
Portion	chapter/article
Title or numeric reference of the portion(s)	Atomic layer deposition of lithium phosphates as solid-state electrolytes for all-solid-state microbatteries
Title of the article or chapter the portion is from	Atomic layer deposition of lithium phosphates as solid-state electrolytes for all-solid-state microbatteries
Editor of portion(s)	N/A
Author of portion(s)	Biqiong Wang, Jian Liu, Qian Sun, Ruying Li, Tsun-Kong Sham and Xueliang Sun
Volume of serial or monograph.	25
Page range of the portion	
Publication date of portion	28 November 2014
Rights for	Main product
Duration of use	Current edition and up to 5 years
Creation of copies for the disabled	no
With minor editing privileges	no
For distribution to	United States and Canada
In the following language(s)	Original language of publication
With incidental promotional use	no
The lifetime unit quantity of new product	Up to 499
Made available in the following markets	education, professional

The requesting person/organization is:	Biqiong Wang/ University of Western Ontario
Order reference number	
Author/Editor	Biqiong Wang
The standard identifier of New Work	ISIL
Title of New Work	DEVELOPMENT OF NANOMATERIALS FOR LITHIUM-ION BATTERIES BY ATOMIC LAYER DEPOSITION
Publisher of New Work	University of Western Ontario
Expected publication date	Dec 2017
Estimated size (pages)	196
Total (may include CCC user fee)	0.00 USD

Terms and Conditions

TERMS AND CONDITIONS
The following terms are individual to this publisher:

These special terms and conditions are in addition to the standard terms and conditions for CCC's Republication Service and, together with those standard terms and conditions, govern the use of the Works.

As the "User" you will make all reasonable efforts to contact the author(s) of the article which the Work is to be reused from, to seek consent for your intended use. Contacting one author who is acting expressly as authorised agent for their co-author(s) is acceptable. User will reproduce the following wording prominently alongside the Work:

- the source of the Work, including author, article title, title of journal, volume number, issue number (if relevant), page range (or first page if this is the only information available) and date of first publication. This information can be contained in a footnote or reference note; and
- a link back to the article (via DOI); and
- if practicable, and IN ALL CASES for new works published under any of the Creative Commons licences, the words "© IOP Publishing. Reproduced with permission. All rights reserved"

Without the express permission of the author(s) and the Rightsholder of the article from which the Work is to be reused, User shall not use it in any way which, in the opinion of the Rightsholder, could: (i) distort or alter the author(s)' original intention(s) and meaning; (ii) be prejudicial to the honour or reputation of the author(s); and/or (iii) imply endorsement by the author(s) and/or the Rightsholder.

This licence does not apply to any article which is credited to another source and which does not have the copyright line '© IOP Publishing Ltd'. User must check the copyright line of the article from which the Work is to be reused to check that IOP Publishing Ltd has all the necessary rights to be able to grant permission. User is solely responsible for identifying and obtaining separate licences and permissions from the copyright owner for reuse of any such third party material/figures which the Rightsholder is not the copyright owner of. The Rightsholder shall not reimburse any fees which User pays for a republication license for such third party content.

This licence does not apply to any material/figure which is credited to another source in the Rightsholder's publication or has been obtained from a third party. User must check the Version of Record of the article from which the Work is to be reused, to check whether any of the material in the Work is third party material. Third party citations and/or copyright notices and/or permissions statements may not be included in any other version of the article from which the Work is to be reused and so cannot be relied upon by the User. User is solely

responsible for identifying and obtaining separate licences and permissions from the copyright owner for reuse of any such third party material/figures where the Rightsholder is not the copyright owner. The Rightsholder shall not reimburse any fees which User pays for a republication license for such third party content.

User and CCC acknowledge that the Rightsholder may, from time to time, make changes or additions to these special terms and conditions without express notification, provided that these shall not apply to permissions already secured and paid for by User prior to such change or addition.

User acknowledges that the Rightsholder (which includes companies within its group and third parties for whom it publishes its titles) may make use of personal data collected through the service in the course of their business.

If User is the author of the Work, User may automatically have the right to reuse it under the rights granted back when User transferred the copyright in the article to the Rightsholder. User should check the copyright form and the relevant author rights policy to check whether permission is required. If User is the author of the Work and does require permission for proposed reuse of the Work, User should select 'Author of requested content' as the Requestor Type. The Rightsholder shall not reimburse any fees which User pays for a republication license.

If User is the author of the article which User wishes to reuse in User's thesis or dissertation, the republication licence covers the right to include the Accepted Manuscript version (not the Version of Record) of the article. User must include citation details and, for online use, a link to the Version of Record of the article on the Rightsholder's website. User may need to obtain separate permission for any third party content included within the article. User must check this with the copyright owner of such third party content. User may not include the article in a thesis or dissertation which is published by ProQuest. Any other commercial use of User's thesis or dissertation containing the article would also need to be expressly notified in writing to the Rightsholder at the time of request and would require separate written permission from the Rightsholder.

User does not need to request permission for Work which has been published under a CC BY licence. User must check the Version of Record of the CC BY article from which the Work is to be reused, to check whether any of the material in the Work is third party material and so not published under the CC BY licence. User is solely responsible for identifying and obtaining separate licences and permissions from the copyright owner for reuse of any such third party material/figures. The Rightsholder shall not reimburse any fees which User pays for such licences and permissions.

As well as CCC, the Rightsholder shall have the right to bring any legal action that it deems necessary to enforce its rights should it consider that the Work infringes those rights in any way.

For STM Signatories ONLY (as agreed as part of the STM Guidelines)

Any licence granted for a particular edition of a Work will apply also to subsequent editions of it and for editions in other languages, provided such editions are for the Work as a whole in situ and do not involve the separate exploitation of the permitted illustrations or excerpts.

Other Terms and Conditions:
STANDARD TERMS AND CONDITIONS

1. Description of Service; Defined Terms. This Republication License enables the User to obtain licenses for republication of one or more copyrighted works as described in detail on the relevant Order Confirmation (the "Work(s)"). Copyright Clearance Center, Inc. ("CCC") grants licenses through the Service on behalf of the rightsholder identified on the Order Confirmation (the "Rightsholder"). "Republication", as used herein, generally means the inclusion of a Work, in whole or in part, in a new work or works, also as described on the Order Confirmation. "User", as used herein, means the person or entity making such republication.

2. The terms set forth in the relevant Order Confirmation, and any terms set by the Rightsholder with respect to a particular Work, govern the terms of use of Works in

connection with the Service. By using the Service, the person transacting for a republication license on behalf of the User represents and warrants that he/she/it (a) has been duly authorized by the User to accept, and hereby does accept, all such terms and conditions on behalf of User, and (b) shall inform User of all such terms and conditions. In the event such person is a "freelancer" or other third party independent of User and CCC, such party shall be deemed jointly a "User" for purposes of these terms and conditions. In any event, User shall be deemed to have accepted and agreed to all such terms and conditions if User republishes the Work in any fashion.

3. Scope of License; Limitations and Obligations.

3.1 All Works and all rights therein, including copyright rights, remain the sole and exclusive property of the Rightsholder. The license created by the exchange of an Order Confirmation (and/or any invoice) and payment by User of the full amount set forth on that document includes only those rights expressly set forth in the Order Confirmation and in these terms and conditions, and conveys no other rights in the Work(s) to User. All rights not expressly granted are hereby reserved.

3.2 General Payment Terms: You may pay by credit card or through an account with us payable at the end of the month. If you and we agree that you may establish a standing account with CCC, then the following terms apply: Remit Payment to: Copyright Clearance Center, 29118 Network Place, Chicago, IL 60673-1291. Payments Due: Invoices are payable upon their delivery to you (or upon our notice to you that they are available to you for downloading). After 30 days, outstanding amounts will be subject to a service charge of 1-1/2% per month or, if less, the maximum rate allowed by applicable law. Unless otherwise specifically set forth in the Order Confirmation or in a separate written agreement signed by CCC, invoices are due and payable on "net 30" terms. While User may exercise the rights licensed immediately upon issuance of the Order Confirmation, the license is automatically revoked and is null and void, as if it had never been issued, if complete payment for the license is not received on a timely basis either from User directly or through a payment agent, such as a credit card company.

3.3 Unless otherwise provided in the Order Confirmation, any grant of rights to User (i) is "one-time" (including the editions and product family specified in the license), (ii) is non-exclusive and non-transferable and (iii) is subject to any and all limitations and restrictions (such as, but not limited to, limitations on duration of use or circulation) included in the Order Confirmation or invoice and/or in these terms and conditions. Upon completion of the licensed use, User shall either secure a new permission for further use of the Work(s) or immediately cease any new use of the Work(s) and shall render inaccessible (such as by deleting or by removing or severing links or other locators) any further copies of the Work (except for copies printed on paper in accordance with this license and still in User's stock at the end of such period).

3.4 In the event that the material for which a republication license is sought includes third party materials (such as photographs, illustrations, graphs, inserts and similar materials) which are identified in such material as having been used by permission, User is responsible for identifying, and seeking separate licenses (under this Service or otherwise) for, any of such third party materials; without a separate license, such third party materials may not be used.

3.5 Use of proper copyright notice for a Work is required as a condition of any license granted under the Service. Unless otherwise provided in the Order Confirmation, a proper copyright notice will read substantially as follows: "Republished with permission of [Rightsholder's name], from [Work's title, author, volume, edition number and year of copyright]; permission conveyed through Copyright Clearance Center, Inc. " Such notice must be provided in a reasonably legible font size and must be placed either immediately adjacent to the Work as used (for example, as part of a by-line or footnote but not as a separate electronic link) or in the place where substantially all other credits or notices for the new work containing the republished Work are located. Failure to include the required notice results in loss to the Rightsholder and CCC, and the User shall be liable to pay liquidated

damages for each such failure equal to twice the use fee specified in the Order Confirmation, in addition to the use fee itself and any other fees and charges specified.

3.6 User may only make alterations to the Work if and as expressly set forth in the Order Confirmation. No Work may be used in any way that is defamatory, violates the rights of third parties (including such third parties' rights of copyright, privacy, publicity, or other tangible or intangible property), or is otherwise illegal, sexually explicit or obscene. In addition, User may not conjoin a Work with any other material that may result in damage to the reputation of the Rightsholder. User agrees to inform CCC if it becomes aware of any infringement of any rights in a Work and to cooperate with any reasonable request of CCC or the Rightsholder in connection therewith.

4. Indemnity. User hereby indemnifies and agrees to defend the Rightsholder and CCC, and their respective employees and directors, against all claims, liability, damages, costs and expenses, including legal fees and expenses, arising out of any use of a Work beyond the scope of the rights granted herein, or any use of a Work which has been altered in any unauthorized way by User, including claims of defamation or infringement of rights of copyright, publicity, privacy or other tangible or intangible property.

5. Limitation of Liability. UNDER NO CIRCUMSTANCES WILL CCC OR THE RIGHTSHOLDER BE LIABLE FOR ANY DIRECT, INDIRECT, CONSEQUENTIAL OR INCIDENTAL DAMAGES (INCLUDING WITHOUT LIMITATION DAMAGES FOR LOSS OF BUSINESS PROFITS OR INFORMATION, OR FOR BUSINESS INTERRUPTION) ARISING OUT OF THE USE OR INABILITY TO USE A WORK, EVEN IF ONE OF THEM HAS BEEN ADVISED OF THE POSSIBILITY OF SUCH DAMAGES. In any event, the total liability of the Rightsholder and CCC (including their respective employees and directors) shall not exceed the total amount actually paid by User for this license. User assumes full liability for the actions and omissions of its principals, employees, agents, affiliates, successors and assigns.

6. Limited Warranties. THE WORK(S) AND RIGHT(S) ARE PROVIDED "AS IS". CCC HAS THE RIGHT TO GRANT TO USER THE RIGHTS GRANTED IN THE ORDER CONFIRMATION DOCUMENT. CCC AND THE RIGHTSHOLDER DISCLAIM ALL OTHER WARRANTIES RELATING TO THE WORK(S) AND RIGHT(S), EITHER EXPRESS OR IMPLIED, INCLUDING WITHOUT LIMITATION IMPLIED WARRANTIES OF MERCHANTABILITY OR FITNESS FOR A PARTICULAR PURPOSE. ADDITIONAL RIGHTS MAY BE REQUIRED TO USE ILLUSTRATIONS, GRAPHS, PHOTOGRAPHS, ABSTRACTS, INSERTS OR OTHER PORTIONS OF THE WORK (AS OPPOSED TO THE ENTIRE WORK) IN A MANNER CONTEMPLATED BY USER; USER UNDERSTANDS AND AGREES THAT NEITHER CCC NOR THE RIGHTSHOLDER MAY HAVE SUCH ADDITIONAL RIGHTS TO GRANT.

7. Effect of Breach. Any failure by User to pay any amount when due, or any use by User of a Work beyond the scope of the license set forth in the Order Confirmation and/or these terms and conditions, shall be a material breach of the license created by the Order Confirmation and these terms and conditions. Any breach not cured within 30 days of written notice thereof shall result in immediate termination of such license without further notice. Any unauthorized (but licensable) use of a Work that is terminated immediately upon notice thereof may be liquidated by payment of the Rightsholder's ordinary license price therefor; any unauthorized (and unlicensable) use that is not terminated immediately for any reason (including, for example, because materials containing the Work cannot reasonably be recalled) will be subject to all remedies available at law or in equity, but in no event to a payment of less than three times the Rightsholder's ordinary license price for the most closely analogous licensable use plus Rightsholder's and/or CCC's costs and expenses incurred in collecting such payment.

8. **Miscellaneous.**

8.1 User acknowledges that CCC may, from time to time, make changes or additions to the Service or to these terms and conditions, and CCC reserves the right to send notice to the User by electronic mail or otherwise for the purposes of notifying User of such changes or

additions; provided that any such changes or additions shall not apply to permissions already secured and paid for.

8.2 Use of User-related information collected through the Service is governed by CCC's privacy policy, available online here:

http://www.copyright.com/content/cc3/en/tools/footer/privacypolicy.html.

8.3 The licensing transaction described in the Order Confirmation is personal to User. Therefore, User may not assign or transfer to any other person (whether a natural person or an organization of any kind) the license created by the Order Confirmation and these terms and conditions or any rights granted hereunder; provided, however, that User may assign such license in its entirety on written notice to CCC in the event of a transfer of all or substantially all of User's rights in the new material which includes the Work(s) licensed under this Service.

8.4 No amendment or waiver of any terms is binding unless set forth in writing and signed by the parties. The Rightsholder and CCC hereby object to any terms contained in any writing prepared by the User or its principals, employees, agents or affiliates and purporting to govern or otherwise relate to the licensing transaction described in the Order Confirmation, which terms are in any way inconsistent with any terms set forth in the Order Confirmation and/or in these terms and conditions or CCC's standard operating procedures, whether such writing is prepared prior to, simultaneously with or subsequent to the Order Confirmation, and whether such writing appears on a copy of the Order Confirmation or in a separate instrument.

8.5 The licensing transaction described in the Order Confirmation document shall be governed by and construed under the law of the State of New York, USA, without regard to the principles thereof of conflicts of law. Any case, controversy, suit, action, or proceeding arising out of, in connection with, or related to such licensing transaction shall be brought, at CCC's sole discretion, in any federal or state court located in the County of New York, State of New York, USA, or in any federal or state court whose geographical jurisdiction covers the location of the Rightsholder set forth in the Order Confirmation. The parties expressly submit to the personal jurisdiction and venue of each such federal or state court.If you have any comments or questions about the Service or Copyright Clearance Center, please contact us at 978-750-8400 or send an e-mail to info@copyright.com.

v 1.1

Questions? customercare@copyright.com or +1-855-239-3415 (toll free in the US) or +1-978-646-2777.

Appendix II: PERMISSION FROM JOHN WILEY AND SONS.

JOHN WILEY AND SONS LICENSE
TERMS AND CONDITIONS

Aug 28, 2017

This Agreement between BIQIONG WANG ("You") and John Wiley and Sons ("John Wiley and Sons") consists of your license details and the terms and conditions provided by John Wiley and Sons and Copyright Clearance Center.

License Number	4174980954996
License date	Aug 23, 2017
Licensed Content Publisher	John Wiley and Sons
Licensed Content Publication	Advanced Materials Interfaces
Licensed Content Title	Titanium Dioxide/Lithium Phosphate Nanocomposite Derived from Atomic Layer Deposition as a High-Performance Anode for Lithium Ion Batteries
Licensed Content Author	Biqiong Wang,Jian Liu,Qian Sun,Biwei Xiao,Ruying Li,Tsun-Kong Sham,Xueliang Sun
Licensed Content Date	Aug 11, 2016
Licensed Content Pages	1
Type of use	Dissertation/Thesis
Requestor type	Author of this Wiley article
Format	Electronic
Portion	Full article
Will you be translating?	No
Title of your thesis / dissertation	DEVELOPMENT OF NANOMATERIALS FOR LITHIUM-ION BATTERIES BY ATOMIC LAYER DEPOSITION
Expected completion date	Oct 2017
Expected size (number of pages)	199
Publisher Tax ID	EU826007151
Billing Type	Invoice
Total	0.00 CAD
Terms and Conditions	

TERMS AND CONDITIONS

Terms and Conditions

license or interest to any trademark, trade name, service mark or other branding ("Marks") of WILEY or its licensors is granted hereunder, and you agree that you shall not assert any such right, license or interest with respect thereto

- NEITHER WILEY NOR ITS LICENSORS MAKES ANY WARRANTY OR REPRESENTATION OF ANY KIND TO YOU OR ANY THIRD PARTY, EXPRESS, IMPLIED OR STATUTORY, WITH RESPECT TO THE MATERIALS OR THE ACCURACY OF ANY INFORMATION CONTAINED IN THE MATERIALS, INCLUDING, WITHOUT LIMITATION, ANY IMPLIED WARRANTY OF MERCHANTABILITY, ACCURACY, SATISFACTORY QUALITY, FITNESS FOR A PARTICULAR PURPOSE, USABILITY, INTEGRATION OR NON-INFRINGEMENT AND ALL SUCH WARRANTIES ARE HEREBY EXCLUDED BY WILEY AND ITS LICENSORS AND WAIVED BY YOU.

- WILEY shall have the right to terminate this Agreement immediately upon breach of this Agreement by you.

- You shall indemnify, defend and hold harmless WILEY, its Licensors and their respective directors, officers, agents and employees, from and against any actual or threatened claims, demands, causes of action or proceedings arising from any breach of this Agreement by you.

- IN NO EVENT SHALL WILEY OR ITS LICENSORS BE LIABLE TO YOU OR ANY OTHER PARTY OR ANY OTHER PERSON OR ENTITY FOR ANY SPECIAL, CONSEQUENTIAL, INCIDENTAL, INDIRECT, EXEMPLARY OR PUNITIVE DAMAGES, HOWEVER CAUSED, ARISING OUT OF OR IN CONNECTION WITH THE DOWNLOADING, PROVISIONING, VIEWING OR USE OF THE MATERIALS REGARDLESS OF THE FORM OF ACTION, WHETHER FOR BREACH OF CONTRACT, BREACH OF WARRANTY, TORT, NEGLIGENCE, INFRINGEMENT OR OTHERWISE (INCLUDING, WITHOUT LIMITATION, DAMAGES BASED ON LOSS OF PROFITS, DATA, FILES, USE, BUSINESS OPPORTUNITY OR CLAIMS OF THIRD PARTIES), AND WHETHER OR NOT THE PARTY HAS BEEN ADVISED OF THE POSSIBILITY OF SUCH DAMAGES. THIS LIMITATION SHALL APPLY NOTWITHSTANDING ANY FAILURE OF ESSENTIAL PURPOSE OF ANY LIMITED REMEDY PROVIDED HEREIN.

- Should any provision of this Agreement be held by a court of competent jurisdiction to be illegal, invalid, or unenforceable, that provision shall be deemed amended to achieve as nearly as possible the same economic effect as the original provision, and the legality, validity and enforceability of the remaining provisions of this Agreement shall not be affected or impaired thereby.

- The failure of either party to enforce any term or condition of this Agreement shall not constitute a waiver of either party's right to enforce each and every term and condition of this Agreement. No breach under this agreement shall be deemed waived or excused by either party unless such waiver or consent is in writing signed by the party granting such waiver or consent. The waiver by or consent of a party to a breach of any provision of this Agreement shall not operate or be construed as a waiver of or consent to any other or subsequent breach by such other party.

- This Agreement may not be assigned (including by operation of law or otherwise) by you without WILEY's prior written consent.

- Any fee required for this permission shall be non-refundable after thirty (30) days from receipt by the CCC.

- These terms and conditions together with CCC's Billing and Payment terms and conditions (which are incorporated herein) form the entire agreement between you and WILEY concerning this licensing transaction and (in the absence of fraud) supersedes all prior agreements and representations of the parties, oral or written. This Agreement may not be amended except in writing signed by both parties. This Agreement shall be binding upon and inure to the benefit of the parties' successors, legal representatives, and authorized assigns.

- In the event of any conflict between your obligations established by these terms and conditions and those established by CCC's Billing and Payment terms and conditions, these terms and conditions shall prevail.

- WILEY expressly reserves all rights not specifically granted in the combination of (i) the license details provided by you and accepted in the course of this licensing transaction, (ii) these terms and conditions and (iii) CCC's Billing and Payment terms and conditions.

- This Agreement will be void if the Type of Use, Format, Circulation, or Requestor Type was misrepresented during the licensing process.

- This Agreement shall be governed by and construed in accordance with the laws of the State of New York, USA, without regards to such state's conflict of law rules. Any legal action, suit or proceeding arising out of or relating to these Terms and Conditions or the breach thereof shall be instituted in a court of competent jurisdiction in New York County in the State of New York in the United States of America and each party hereby consents and submits to the personal jurisdiction of such court, waives any objection to venue in such court and consents to service of process by registered or certified mail, return receipt requested, at the last known address of such party.

WILEY OPEN ACCESS TERMS AND CONDITIONS

Wiley Publishes Open Access Articles in fully Open Access Journals and in Subscription journals offering Online Open. Although most of the fully Open Access journals publish open access articles under the terms of the Creative Commons Attribution (CC BY) License only, the subscription journals and a few of the Open Access Journals offer a choice of Creative Commons Licenses. The license type is clearly identified on the article.

The Creative Commons Attribution License

The Creative Commons Attribution License (CC-BY) allows users to copy, distribute and transmit an article, adapt the article and make commercial use of the article. The CC-BY license permits commercial and non-

Creative Commons Attribution Non-Commercial License

The Creative Commons Attribution Non-Commercial (CC-BY-NC)License permits use, distribution and reproduction in any medium, provided the original work is properly cited and is not used for commercial purposes.(see below)

Creative Commons Attribution-Non-Commercial-NoDerivs License

The Creative Commons Attribution Non-Commercial-NoDerivs License (CC-BY-NC-ND) permits use, distribution and reproduction in any medium, provided the original work is properly cited, is not used for commercial purposes and no modifications or adaptations are made. (see below)

Use by commercial "for-profit" organizations
Use of Wiley Open Access articles for commercial, promotional, or marketing purposes
requires further explicit permission from Wiley and will be subject to a fee.
Further details can be found on Wiley Online Library
http://olabout.wiley.com/WileyCDA/Section/id-410895.html

Other Terms and Conditions:

v1.10 Last updated September 2015

Questions? customercare@copyright.com **or +1-855-239-3415 (toll free in the US) or
+1-978-646-2777.**

Appendix III: PERMISSION FROM AMERICAN SOCIETY OF CHEMISTRY.

Curriculum Vitae

Name:	Biqiong Wang
Post-secondary Education and Degrees:	City University of Hong Kong 2008-2012 B.Eng. The University of Western Ontario 2012-2017 Ph.D.
Honours and Awards:	City University of Hong Kong First Class Scholarship 2008-2012 Western Engineering Scholarship 2012-2017
Related Work Experience	Research Assistant Centre of Super-Diamond and Advanced Films (COSDAF) City University of Hong Kong 2011-2012 Summer Intern The Center for Advanced Life Cycle Engineering (CALCE) University of Maryland 2011 Teaching Assistant The University of Western Ontario 2014-2017

Publications:

1. **B. Wang**, J. Liu, Q. Sun, R. Li, T-K Sham and X. Sun, *Atomic Layer Deposition of Lithium Phosphats as Solid-State Electrolyte for All-Solid-State Microbatteiries*. Nanotechnology 25 (2014) 504007

2. **B. Wang**, J. Liu, Q. Sun, B. Xiao, R. Li, T-K Sham and X. Sun, *Titanium Dioxide/Lithium Phosphate Nanocomposite Derived from Atomic Layer Deposition as a High-Performance Anode for Lithium Ion Batteries*. Adv. Mater. Inter. (2016) 1600369

3. B. Xiao[1], **B. Wang**[1], J. Liu, K. Karthikeyan, Q. Sun, Y. Liu, G. Dadheech, M. Balogh, L. Yang, T-K Sham, R. Li, M. Cai and X. Sun, *Highly Stable $Li_{1.2}Mn_{0.54}Co_{0.13}Ni_{0.13}O_2$ Enabled by Novel Atomic layer Deposited $AlPO_4$ Coating*. Nano Energy 34 (2017) 120

4. **B. Wang**, J. Liu, M. B. Norouzi, Q. Sun, Y. Zhao, R. Li, T-K Sham and X. Sun, *Atomic Layer Deposited Lithium Silicates as Solid-State Electrolytes for All Solid-State Batteries.* ACS Appl. Mater. Interfaces 9 (2017) 31786

5. **B. Wang**, Y. Zhao, M. B. Norouzi, Q. Sun, R. Li, T-K Sham and X. Sun, *Atomic Layer Deposition of Lithium Niobates as Solid-State Electrolytes for All Solid-State Batteries.* Submitted

6. B. Xiao, H. Liu, J. Liu, Q. Sun, B. Wang, K. Kaliyappan, Y. Zhao, M. N. Banis, Y. Liu, R. Li, T-K Sham, G. A. Botton, M. Cai, and X. Sun, *Nanoscale Manipulation of Spinel Lithium Nickel Manganese Oxide Surface by Multisite Ti Occupation as High-Performance Cathode.* Adv. Mater. 2017, 1703764

7. C. Cao, S. Mukherjee, J. Liu, B. Wang, M. Amirmaleki, Z. Lu, J. Y. Howe, D. Perovic, X. Sun, C. V. Singh, Y. Sun, and T. Filleter, Role of graphene in enhancing the mechanical properties of TiO2/graphene heterostructures. Nanoscale 32 (2017) 11678

8. P. Yan, J. Zheng, J. Liu, B. Wang, X. Sun, C. Wang, and J. Zhang, *Tailoring of Grain Boundary Structure and Chemistry of Cathode Particles for Enhanced Cycle Stability of Lithium Ion Battery.* arXiv preprint arXiv:1710.06050

9. Y. Zhao, L. Goncharova, Q. Zhang, P. Kaghazchi, Q. Sun, A. Lushington, **B. Wang**, R. Li, X. Sun, *Inorganic-organic Coating via Molecular Layer Deposition Enables Long Life Sodium Metal Anode*. Nano Lett. (2017) in press.

10. Y. Zhao, L. Goncharova, A. Lushington, Q. Sun, H. Yadegari, **B. Wang**, W. Xiao, R. Li, X. Sun, *Superior Stable and Long Life Sodium Metal Anodes Achieved by Atomic Layer Deposition*. Adv. Mater. 1606663 (2017), 1

11. Q. Sun, J. Liu, X. Li, **B. Wang**, H. Yadegari, A. Lushington, M. Banis, Y. Zhao, W. Xiao, N. Chen, J. Wang, T-K Sham, X. Sun, *Atomic Layer Deposited Non-noble Metal Oxide Catalyst for Sodium-Air Batteries: Tuning the Morphologies and Compositions of Discharge Product.* Adv. Funct. Mater. 1606662 (2017), 1

12. X. Lv, J. Deng, **B. Wang**, J. Zhong, T-K Sham, X. Sun and X. Sun, *γ-Fe₂O₃@CNTs Anode Materials for Lithium Ion Batteries Investigated by Electron Energy Loss Spectroscopy.* Chem. Mater. 29 (2017) 3499

13. Z. Song, **B. Wang**, N. Cheng, L. Yang, D. Banham, R. Li, S. Ye, X. Sun. *Atomic Layer Deposited Tantalum Oxide to Anchor Pt/C for Highly Stable Catalyst in PEMFCs*. J. Mater. Chem. A 5 (2017) 9760

14. S. Deng, B. Xiao, **B. Wang**, X. Li, K. Kaliyappan, Y. Zhao, A. Lushington, R. Li, T-K Sham, H. Wang, and X. Sun, *New Insight into Stable Protective Layer for Long-life and Safe High Voltage Cathodes: Atomic Layer Deposited AlPO₄ Coating for LiNi₀.₅Mn₁.₅O₄*. Nano Energy 38 (2017) 19

15. J. Liu, **B. Wang**, M. N. Banis, Z. Wang, R. Li, J. Wang, Y. Hu, T-K Sham, X. Sun, *Investigation of amorphous to crystalline phase transition of sodium titanate by X-ray absorption spectroscopy and scanning transmission X-ray microscopy.* Can. J. Chem. (2017) DOI: 10.1139/cjc-2017-0132

16. S. Lou, X. Cheng, Y. Zhao, A. Lushington, J. Gao, Q. Li, P. Zuo, **B. Wang**, Y. Gao, Y. Ma, C. Du, G. Yin, X. Sun, *Superior Performance of Ordered Macroporous TiNb$_2$O$_7$ Anodes for Lithium Ion Batteries: Understanding from the Structural and Pseudocapacitive Insights on Achieving High Rate Capability.* Nano Energy 34 (2017) 15

17. X. Li, A. Lushington, Q. Sun, W. Xiao, J. Liu, **B. Wang**, Y. Ye, K. Nie, Y. Hu, Q. Xiao, R. Li, J. Guo, T-K Sham, X. Sun, *Safe and Durable High-Temperature Lithium-sulfur Batteries via Molecular Layer Deposited Coating*. Nano Lett. 16 (2016) 3545

18. J. Liu, **B. Wang**, Q. Sun, R. Li, T-K Sham, X. Sun, *Atomic Layer Deposition of Hierarchical CNTs@FePO$_4$ Architecture as a 3D Electrode for Lithium-Ion and Sodium-Ion Batteries.* Adv. Mater. Inter. (2016) 1600468

19. H. Yadegari, M. N. Banis, B. Xiao, Q. Sun, X. Li, A. Lushington, **B. Wang**, R. Li, T-K Sham, X. Cui, X. Sun, *Three-dimensional air electrode for sodium-oxygen battery: a mechanism study toward the cyclability of the cell*. Chem. Mater. 27 (2015) 3040

20. B. Xiao, J. Liu, Q. Sun, **B. Wang**, M. N. Banis, D. Zhao, Z. Wang, R. Li, X. Cui, T-K Sham, X. Sun, *Unravelling the role of electrochemically active FePO$_4$ coating by atomic layer deposition for increased high-voltage stability of LiNi$_{0.5}$Mn$_{1.5}$O$_4$ cathode material.* Adv. Sci. (2015) 1500022

21. Q. Sun, H. Yadegari, M. N. Banis, J. Liu, B. Xiao, **B. Wang**, S. Lawes, R. Li, X. Sun, *Self-stacked Nitrogen-Doped Carbon Nanotubes and Long-life Air Electrode for Sodium-Air Batteries: Elucidating the Evolution of Discharge Product Morphology*. Nano Energy 12 (2015) 698

22. H. Yadegari, Y. Li, M. N. Banis, X. Li, **B. Wang**, Q. Sun, R. Li, T-K Sham, X. Cui, X. Sun, *On Rechargeability and Reaction Kinetics of Sodium-Air Batteries.* Energy Environ. Sci. 7 (2014) 3747

23. X. Li, X. Li, M. N. Banis, **B. Wang**, A. Lushington, X. Cui, R. Li, T-K Sham, X. Sun, *Tailoring Interactions of Carbon and Sulfur in Li-S Battery Cathode: Significant Effects of Carbon-Heteroatom Bonds*. J. Mater. Chem. A 2 (2014) 12866

24. B. Xiao, X. Li, X. Li, **B. Wang**, C. Langford, R. Li, X. Sun, *Graphene Nanoribbons Derived from the Unzipping of Carbon Nanotubes: Controlled Synthesis and Superior Lithium Storage Performance.* J. Phys. Chem. C 118 (2014) 881

25. X. Li, J. Liu, **B. Wang**, M. N. Banis, B. Xiao, R. Li, T-K Sham, X. Sun, *Nanoscale Stabilization of Li-Sulfur Batteries by Atomic Layer Deposited Al$_2$O$_3$*. RSC Adv. 4 (2014) 27126

26. J. C. Qian, S. K. Jha, **B. Q. Wang**, E. V. Jelenkovic, I. Bello, J. E. Klemberg-Sapieha, L. Martinu, and W. J. Zhang, *High quality boron carbon nitride/ZnO-nanorods p-n heterojunctions based on magnetron sputtered boron carbon nitride films.* Appl. Phys. Lett. 105 (2014) 192104

Conference Presentations:

1. Poster, **Surface Canada 2013** (May 2013, London, Canada), *"Free-Standing Paper-Based Graphene Composites as Binder Free Anodes for Lithium Ion Batteries";*

2. Poster, **15th Topical ISE Meeting** (Apr 2014, Niagara Falls, Canada), *"Free-Standing Paper-Based Nano-Carbon Composites as Binder-Free Anode for Lithium Ion Batteries";*

3. Poster, **IMLB 2016: 18th Intl. Meeting on Lithium Batterie**s (Jun 2016, Chicago, USA), *"The Application of Atomic Layer Deposition in Lithium-Ion Batteries";*

4. Oral Presentation, **ALD 2017/ALE 2017** (Jul 2017, Denver, USA), *"Atomic Layer Deposition of Solid-State Electrolytes for All-Solid-State Lithium Ion Batteries".*